Structuration of SrTiO3 surfaces and MoS2 2D material induced by swift heavy ion irradiation at grazing incidence

Radia Rahali

▶ **To cite this version:**

Radia Rahali. Structuration of SrTiO3 surfaces and MoS2 2D material induced by swift heavy ion irradiation at grazing incidence. Physics [physics]. Normandie Université, 2024. English. NNT : 2024NORMC203 . tel-04690092

HAL Id: tel-04690092

https://theses.hal.science/tel-04690092v1

Submitted on 6 Sep 2024

HAL is a multi-disciplinary open access archive for the deposit and dissemination of scientific research documents, whether they are published or not. The documents may come from teaching and research institutions in France or abroad, or from public or private research centers.

L'archive ouverte pluridisciplinaire **HAL**, est destinée au dépôt et à la diffusion de documents scientifiques de niveau recherche, publiés ou non, émanant des établissements d'enseignement et de recherche français ou étrangers, des laboratoires publics ou privés.

Normandie Université

UNIVERSITÉ CAEN NORMANDIE

THÈSE

Pour obtenir le diplôme de doctorat

Spécialité **PHYSIQUE**

Préparée au sein de l'**Université de Caen Normandie**

Structuration of SrTiO3 surfaces and MoS2 2D material induced by swift heavy ion irradiation at grazing incidence

Présentée et soutenue par

RADIA RAHALI

Thèse soutenue le 05/02/2024

devant le jury composé de :

MME MARIE-CLAUDE CLOCHARD	Directeur de recherche au CEA - ECOLE POLYTECHNIQUE	Rapporteur du jury
M. MARTINO TRASSINELLI	Chargé de recherche HDR - UNIVERSITE PARIS 4 PARIS-SORBONNE	Rapporteur du jury
MME CLARA GRYGIEL	Directeur de recherche au CEA - Université de Caen Normandie	Membre du jury
MME MARIKA SCHLEBERGER	Professeur - Université Duisburg-Essen	Président du jury
M. HENNING LEBIUS	Directeur de recherche au CEA - Université de Caen Normandie	Directeur de thèse

Thèse dirigée par **HENNING LEBIUS** (Centre de recherche sur les ions, les matériaux et la photonique (Caen))

ED 591 PSIME

CIMAP

Abstract

Structuration of surfaces and 2D materials induced by swift heavy ion irradiation at grazing incidence.

Materials modification has enabled significant advancements in the technological fields by allowing for precise control and manipulation of material properties. To ensure successful applications, it is crucial to have techniques that offer control over the size, shape, and morphology of the structures created. This thesis explores the use of swift heavy ions (SHI) to create nano- and microstructures on the surfaces of strontium titanate ($SrTiO_3$) and molybdenum disulphide (MoS_2) under grazing incidence geometry. The results show that SHI irradiation can induce various surface modifications, such as elongated surface defects, wave-like structures, and amorphization. This research demonstrates that by adjusting the fluence and angle of incidence of the ion beam, periodic wave-like structures can be formed on the surface of $SrTiO_3$. These structures can be deepened to obtain more pronounced valley, which can be used to directly grow two-dimensional materials and obtain heterostructures with well-defined interfaces. The results also demonstrates that SHI irradiation can induce foldings in MoS_2 samples. The angle of incidence of the ion beam and the substrate used can control the defects. The choice of substrate can also influence folds density and length. It is shown that using $SrTiO_3$ as a substrate allows the folding with variable lengths without the need for specific crystallographic orientation conditions.

Structuration de surfaces et de matériaux 2D induite par irradiation aux ions lourds rapides en incidence rasante

La modification des matériaux a permis de faire des progrès significatifs dans les domaines technologiques à travers un contrôle et une manipulation précis des propriétés des matériaux. Pour garantir le succès des applications, il est essentiel de disposer de techniques permettant de contrôler la taille, la forme et la morphologie des structures créées. Cette thèse explore l'utilisation d'ions lourds rapides (SHI) pour créer des nano- et microstructures sur les surfaces du titanate de strontium ($SrTiO_3$) et du disulfure de molybdène (MoS_2) avec une géométrie d'incidence rasante. Les résultats démontrent que l'irradiation aux ions lourds rapides peut induire diverses modifications de surface, telles que chaines de nanobosses, des cratères, des structures ondulatoires et de l'amorphisation. La thèse démontre qu'en ajustant la fluence et l'angle d'incidence du faisceau d'ions, des structures d'onde périodiques peuvent être formées sur la surface de $SrTiO_3$. Ces structures peuvent avoir des tailles différentes, avec des tranchées plus ou moins prononcées. Cette structure peut être utilisée pour des dépôts de couches de matériaux bidimensionnels et obtenir des hétéro-structures avec des interfaces bien définies. Les résultats démontrent également que l'irradiation peut induire des pliages dans des échantillons monocouches de MoS_2. L'angle d'incidence du faisceau d'ions et le substrat utilisé peuvent contrôler les défauts. Le choix du substrat peut également influencer la densité et la longueur des plis. Il est montré que l'utilisation de $SrTiO_3$ comme substrat permet la création de plis de longueurs variables sans la nécessité de conditions d'orientation cristallographique spécifiques.

Mots clés : Ions lourds rapides, Matériaux 2D, MoS_2, $SrTiO_3$, microstructuration, Microscope à force atomique, spectroscopie Raman, angle rasant, SHI.

Laboratory
Centre de recherche sur les Ions, les MAteriaux et la Photonique
CIMAP - GANIL CEA/CNRS/ENSICAEN/UNICAEN
Boulevard Henri Becquerel, CS 65133 14076 Caen cedex 5, France

Contents

ACKNOWLEDGEMENTS

Je tiens tout d'abord à exprimer ma gratitude envers les membres de mon jury de thèse : Marie-Claude CLOCHARD, Martino TRASSINELLI et Marika SCHLEBERGER. Merci d'avoir accepté de consacrer de votre temps à la lecture, à l'évaluation et à l'analyse de ce travail qui découle de trois années (un peu plus) de recherches passionnantes.

Cette thèse a été menée au sein du Centre de Recherche sur les Ions, les Matériaux et la Photonique (CIMAP). Je souhaite tout naturellement remercier Amine CASSIMI, ancien directeur du CIMAP (et directeur à mon arrivée), et Isabelle MONNET, actuelle directrice, pour m'avoir accueillie au sein du CIMAP et avoir créé des conditions de travail agréables et propices à la réalisation de cette thèse. Je suis également reconnaissante envers Henning LEBIUS et Clara GRYGIEL pour m'avoir donné l'opportunité de faire une thèse dans un domaine passionnant et de m'avoir ouvert les portes de l'expérimentation! Cette expérience a été pour moi à la fois enrichissante et stimulante.

À Henning, directeur de thèse, que je remercie pour sa disponibilité, sa pédagogie et sa confiance. À Clara, co-directrice de cette thèse, merci pour ses idées, ses conseils et sa franchise! À vous deux, merci pour votre accueil chaleureux, votre orientation et vos conseils. Merci d'avoir toujours été disponible et prêt à m'aider quand j'en avais besoin (quand je finissais par le demander!) que ce soit pendant les expériences d'irradiations ou à d'autres moments. Je vous suis reconnaissante pour tout ce que vous m'avez apporté.

Je tiens à exprimer ma sincère reconnaissance à Abdenacer BENYAGOUB pour son aide, ses conseils éclairés, ses idées et nos discussions enrichissantes qui ont éclairé certains aspects de mes résultats à de nombreuses reprises. Sa contribution lors de la rédaction de l'article et son engagement lors des réponses aux évaluateurs ont été d'une aide inestimable.

Je suis profondément reconnaissante envers Marika SCHLEBERGER et son équipe pour leur collaboration et leur aide en particulier dans la préparation des échantillons de matériaux 2D. Leur accueil et les séjours au sein de leur laboratoire à l'université de Duisburg Essen m'ont permis de plonger dans le monde fascinant des matériaux 2D, de développer mes compétences en fabrication et en spectroscopie Raman. Ces expériences ont enrichi mon parcours au laboratoire, et j'en suis

très reconnaissante.

Je souhaite exprimer ma gratitude particulière à Yossarian LIEBSCH pour sa réactivité, son aide et le temps qu'il m'a accordé malgré son emploi du temps chargé ! Sa contribution à la préparation des échantillons avec le dépôt CVD, sa formation au spectre RAMAN mais également l'analyse de certains de mes échantillons lorsque je n'ai pas pu me déplacer ont été précieux. Je remercie également Lukas MADAUß pour son accueil lors de mon premier séjour et pour m'avoir initié aux différentes techniques de fabrication des matériaux 2D. Mes remerciements s'adressent à tous les membres de son groupe de recherche, malheureusement j'ai une mémoire catastrophique quand il est question de nom !

Je tiens également à remercier l'ensemble du personnel du laboratoire CIMAP. Un merci tout particulier à Jimmy Rangama pour avoir pris de son temps libre afin de concevoir avec l'imprimante 3D les supports indispensables lors de mes irradiations, sans lesquels je n'aurais pas pu exploiter autant de données.

Mes remerciements vont également à Mamour SALL, Marie Pierre CHAUVAT et Isabelle MONNET pour leur assistance en microscopie électronique à transmission et pour avoir réalisé des images de mes échantillons (une tâche assez complexe)
Je suis reconnaissante envers Stephane GUILLOUS pour nos discussions instructives et ses idées intéressantes, ainsi qu'à Yvette NGONO pour nos échanges variés pendant les déjeuners.

Ce travail n'aurait pas pu être mené à bien sans l'implication et le soutien de plusieurs membres du laboratoire, notamment l'équipe administrative, pour n'en citer que quelques-uns, Sarah Colineaux et Lucie Bercker, toujours là pour trouver des solutions à mes tracas administratifs ! Je remercie également l'équipe technique du CIMAP pour leur assistance précieuse lors des irradiations, ainsi que l'équipe technique du GANIL, qui a permis de mener à bien les expériences d'irradiation.

Je souhaite également remercier mes collègues doctorants. En particulier, Prudence, avec qui j'ai partagé mon bureau à mon arrivée et qui m'a beaucoup aidé dans mes premières démarches. À mes deux collègues de bureau actuelles, Hoda ALASSAAD pour sa joie de vivre et sa bonne humeur et Ons YAHYAOUI pour ses citations motivantes. À vous deux, merci pour votre soutien, nos discussions et nos fous rires qui m'ont grandement aidé à décompresser lorsque la pression montait ! Je n'oublie pas Rima, Massimo (avec ses histoires uniques !), Min, Anna, Cintia, Ignace, Alexis, et l'élaboration de plans pendant les déjeuners. Je souhaite une excellente continuation à tous les nouveaux.

Enfin, et non des moindres, je tiens à exprimer ma profonde gratitude envers mes parents pour leur confiance inconditionnelle, pour leur soutien et leurs encouragements tant pour mes études que mes choix de vie. Ils ont toujours été présents pour moi, malgré la distance.
Un merci particulier à mon mari, Farouk, sans qui rien n'aurait été possible, pour son soutien constant, ses encouragements et sa patience envers une doctorante souvent (dernièrement) stressée

et changeante d'humeur !
Un remerciement spécial à mon fils Adem, pour son soutien à travers les nuits blanches, les poussées dentaires, la peur de séparation, la poussée de croissance, les rhumes, les pharyngites, les otites, etc. Tu as été une source de motivation à ta manière !
Je n'oublie pas ma sœur Hiba pour son soutien et ses encouragements toutes ces années et mes frères Nidhal et Hani, pour leur soutien inconditionnel, même si nous ne sommes pas toujours d'accord sur tout.
Un grand merci à mes beaux-parents pour leur affection et leur soutien indéfectible ces dernières années. Je suis particulièrement reconnaissante à ma belle-mère pour son aide précieuse pour garder Adem durant la rédaction de ce manuscrit. À mon beau frères Samir et ma belle-sœur Amel pour leur soutien, encouragements et leur présence et à mon jeune beau-frère Bachir pour ses idées et plans ingénieux (et bizarres).
Un grand merci à mes amis, dispersés aux quatre coins du monde, pour leur soutien et leur présence toutes ces années malgré la distance.

List of Figures

Summary in French

Introduction

Ces dernières années, la recherche ne cesse d'être confrontée aux problématiques technologiques modernes. Les demandes orientées vers des applications technologiques plus performantes, moins coûteuses et plus accessibles ne cessent de croître. La recherche fondamentale autour des sciences des matériaux possède un rôle central dans ce processus de compréhension du comportement des différents matériaux, suivant leurs propriétés et leur environnement, dans le but de proposer ou d'améliorer les applications potentielles. Un intérêt particulier est donné à l'étude des surfaces et interfaces.
En effet, les chercheurs explorent diverses techniques pour créer des motifs précis et bien définis à l'échelle microscopique et nanométrique. Ces modifications de matériaux, à travers la création de défauts ainsi que la nanostructuration de surfaces, offrent la possibilité d'améliorer et de contrôler l'efficacité des propriétés physiques, chimiques, biomédicales, voire d'en créer de nouvelles. L'aspect de ce domaine qui nous intéresse porte sur la nanostructuration et la microstructuration des surfaces. Cette approche offre de nouvelles possibilités de contrôler les propriétés des surfaces, telles que la mouillabilité, l'adhérence et les propriétés électriques et optiques. Ces modifications de surface peuvent avoir un impact significatif sur la performance et la fonctionnalité des matériaux dans diverses applications, notamment le stockage de l'énergie, la catalyse et les dispositifs biomédicaux.
Diverses techniques sont testées pour créer des motifs précis et bien définis à l'échelle microscopique et nanométrique, notamment les technologies à faisceau d'ions. Plusieurs installations dans le monde ont vu le jour ces dernières années, offrant un large choix d'espèces d'ions dans une large gamme d'énergies, allant du keV au GeV. Durant cette thèse, il a été question d'utiliser des ions lourds rapides. L'irradiation avec des ions d'énergie supérieure à 0,1 MeV/u peut engendrer diverses modifications, allant de défauts à l'amorphisation.
Dans cette thèse, dans un premier temps, il est question d'étudier le comportement d'une pérovskite, à savoir le titanate de strontium ($SrTiO_3$), sous irradiation aux ions lourds rapides, en favorisant notamment une géométrie d'irradiation rasante. Cette famille de matériaux est connue pour posséder diverses propriétés : ferroélectricité, piézoélectricité, etc. L'étude de son comportement sous irradiation est une étape cruciale dans la procédure de mise en application potentielle. Dans un

second temps, l'étude est étendue à un autre type de matériaux, à savoir les matériaux 2D. Un accent particulier sera accordé au disulfure de molybdène (MoS_2), qui sera préparé par la technique de dépôt en couche vapeur sur un substrat de titanate de strontium ($SrTiO_3$) monocristallin et sur le SiO_2 amorphe, qui seront par la suite soumis à l'irradiation aux ions lourds rapides en incidence rasante.

Donc, le but de cette thèse est la modification de surface à l'aide d'irradiation aux ions lourds rapides, en faisant varier les paramètres d'irradiations en utilisant des fluences allant de basse fluence, où l'impact unique domine, à de forte fluence, où l'impact multiple se produit, donnant lieu à une amorphisation de la surface sur une certaine épaisseur. Des angles d'irradiation variant de la normale à la surface (90°) au rasant ont été utilisés. Il sera question d'étudier l'effet collectif sur le titanate de strontium seul, puis de l'utiliser comme substrat pour les matériaux 2D et de l'irradier aux ions lourds rapides, afin de mettre en avant notamment l'impact du substrat sur la création de défauts morphologiques en surface. Le contenu de la thèse se présente comme suit :

• Le chapitre 1 introduit les principes fondamentaux de l'interaction ions-matière. Une présentation des processus et paramètres pertinents qui interviennent durant les collisions entre l'ion projectile et la cible sont donnés, en passant par les modèles qui décrivent le passage de l'ion dans la matière.

• Le second chapitre sera consacré à la description des matériaux utilisés dans cette étude, à savoir le titanate de strontium ($SrTiO_3$) et le disulfure de molybdène (MoS_2). Une présentation des types de modifications obtenus dans des études antérieures lorsqu'ils sont soumis à des irradiations aux ions lourds rapides est présentée. Les différentes techniques de caractérisation (AFM, DRX, Spectroscopie Raman) ainsi que le dispositif expérimental sont présentés.

• Le troisième chapitre est dédié à la présentation des résultats expérimentaux obtenus sur le titanate de strontium de deux directions cristallographiques différentes (100) (110) irradié avec deux faisceaux d'énergies différentes, à savoir le faisceau d'ion d'ion de $^{136}Xe^{19+}$ de 0.55 MeV/u et le faisceau de $^{129}Xe^{23+}$ de 0.71 MeV. Dans un premier temps, les résultats au microscope électronique à transmission (TEM) seront présentés en mettant en avant la différence entre une irradiation à basse fluence, où l'impact unique domine, et de plus grande fluence, qui résulte au chevauchement des traces. Puis, une étude au microscope à force atomique sera présentée, mettant en avant la formation de deux structures ondulatoires à l'échelle microscopique.

• Dans le quatrième chapitre, l'étude se concentre sur l'impact de la fluence sur la modification de la surface du $SrTiO_3$ (STO). L'évolution de la structure en forme de vagues obtenue est étudiée en utilisant des fluences intermédiaires.

• Dans le dernier chapitre, il sera question de présenter les résultats obtenus sur le $MoS_2/SrTiO_3$ lorsqu'il est soumis à une irradiation aux ions lourds rapides avec une géométrie d'incidence rasante. Une comparaison des modifications obtenus sera faite avec des échantillons déposés sur un autre type de substrat, du dioxyde de silicium amorphe (SiO_2).

Généralité sur l'interaction ion matière

Les ions lourds rapides offrent une approche unique pour la modification et la formation de nano- et microstructures en surface et près de la surface. Le choix des paramètres d'irradiation, tels que l'énergie, la fluence et l'angle est crucial. Il est bien connu que lorsqu'un matériau solide est irradié avec des particules chargées, une série d'interactions a lieu avec les composants de la cible avant que l'ion ne perde son énergie et ne s'immobilise dans le matériau. Ces interactions comprennent des collisions avec les électrons et les noyaux du matériau cible, qui entraînent une perte d'énergie par le biais de processus nucléaires et électroniques. Ce transfert d'énergie induit des déplacements atomiques, des cascades de déplacements, des désordres, des ionisations ou des excitations électroniques avant leur immobilisation à une certaine profondeur, laissant des défauts permanents. En fonction des paramètres d'irradiation, des modifications structurelles jusqu'à l'amorphisation peuvent être induites le long du trajet des ions, en surface et en profondeur du matériau (pour les ions de haute énergie).
Suivant l'énergie des ions, deux processus peuvent décrire le transfert d'énergie qui a lieu de l'ion vers le matériau et le ralentissement qui s'ensuit.

• Lorsque l'énergie cinétique est dans la gamme de quelques keV, les collisions sont considérées comme élastiques. C'est-à-dire que le transfert d'énergie se produit principalement par choc nucléaire avec les atomes de la cible, sans endommager le système électronique des deux partenaires et en conservant l'énergie cinétique.

• Lorsque l'énergie de l'ion est plus importante (> 100 keV), ce sont les collisions inélastiques qui dominent. Dans ce processus, la perte d'énergie électronique est liée au collision inélastique de l'ion avec le système électronique de la cible. L'énergie cinétique totale n'est pas conservée dans ce cas-là.

Suivant la vitesse du projectile, trois cas sont considérés :

• Le domaine des hautes vitesses, dans ce cas l'ion est complètement épluché de ses électrons et l'interaction du noyau avec les électrons de la cible se fait via une interaction coulombienne.

• Le cas des vitesses intermédiaires, l'ion projectile possède une vitesse du même ordre de grandeur que les électrons du système, par conséquent il y a un échange de charge avec les atomes de la cible sans perte totale d'électron. À noter que les ions du GANIL utilisés durant cette thèse possèdent une vitesse intermédiaire et donc correspondent à ce cas où le dépôt d'énergie (le pouvoir d'arrêt) passe par un maximum appelé pic de Bragg. Puis le pouvoir d'arrêt décroit et on rentre dans le domaine des basses vitesses.

• Dans la gamme d'énergie des basses vitesses, l'ionisation est quasiment inexistante et l'ion garde la majorité de ses électrons. Linhard et al. [12] ont conclu que le pouvoir d'arrêt dépend de l'énergie de l'ion incident et est donc proportionnel à la vitesse de l'ion.

La figure 1 montre l'évolution de la perte d'énergie en fonction de l'énergie cinétique de l'ion incident. Le cas du titanate de strontium ($SrTiO_3$) d'une densité de 5.117 g cm^{-3} irradié avec un faisceau de $^{129}Xe^{23+}$ est présenté.

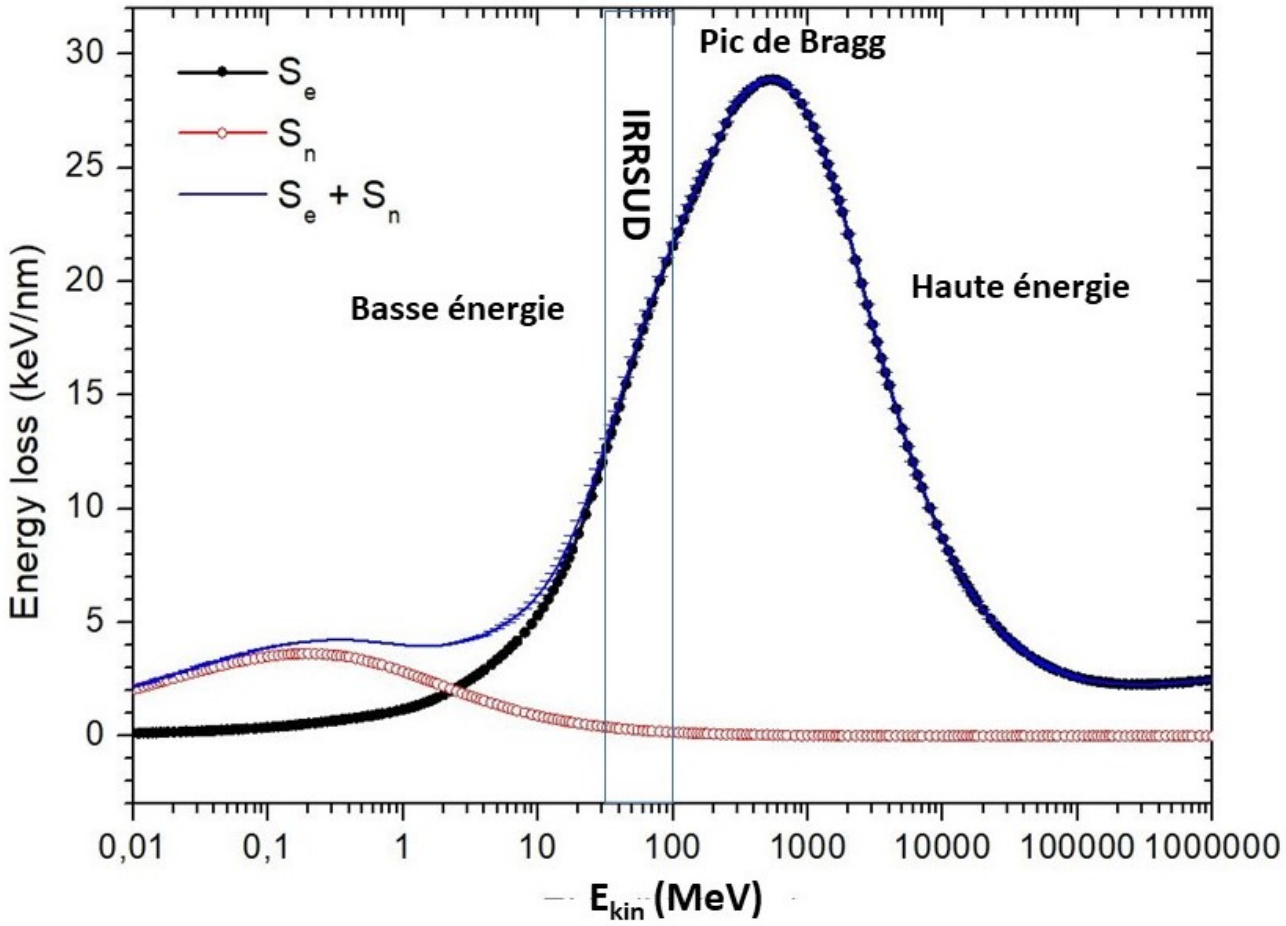

Figure 1: Evolution du pouvoir d'arrêt nucléaire et électronique dans le cas du $SrTiO_3$ irradié aux ions xénon, calculé avec le code SRIM [1].

Comme on peut le voir sur la Figure 1, dans le cas des ions lourds rapides utilisés durant cette thèse, le processus de ralentissement se produit principalement par dépôt d'énergie électronique, dans le régime des vitesses intermédiaires. Ceci donne lieu à un pouvoir d'arrêt électronique aux environs de 20 keV/nm.

Quand on parle d'interaction ion-matière, plusieurs paramètres entrent en jeu. Les plus importants dans le cas d'ions lourds sont :
• La fluence, qui représente le nombre total de particules reçues par la cible par unité de surface (ions cm^{-2}).
• Le flux (ϕ) qui correspond au nombre de particules incidentes envoyées sur la cible, par unité de

surface et par unité de temps (ions $cm^{-2}\ s^{-1}$).
• Le pouvoir d'arrêt (dE/dx) : qui est la perte d'énergie le long du parcours de l'ion : $S_{n,e} = -(dE/dx)_{n,e}$
• Le parcours projeté de l'ion est la distance parcourue par l'ion dans la cible, autrement c'est la profondeur à laquelle l'ion s'arrête (Rp).

Les faisceaux d'ions utilisés proviennent de la ligne de faisceau IRRSUD où l'énergie est comprise entre 0.3 à 1 MeV/u. L'irradiation par des ions d'énergie supérieure à 0.1 MeV/u entraîne diverses modifications allant des défauts à l'amorphisation.
Le parcours de l'ion dans le matériau cible à cette énergie engendre une zone fortement endommagée. Sous réserve d'une perte d'énergie électronique (dE/dx) seuil atteinte, cette modification se traduit par la formation d'une piste cylindrique amorphe de quelques nanomètres de diamètre dans le volume, appelée trace latente.
L'endommagement qui en résulte dépend non seulement de l'énergie mais aussi de la nature de la cible et notamment de sa structure électronique. En effet, dans le cas d'isolant ou de semi-conducteur, ces interactions donnent lieu à des défauts structuraux, tandis que dans le cas de métaux, l'énergie a tendance à se dissiper rapidement ne laissant pas le temps pour la création de défauts.

Plusieurs études ont tenté d'expliquer la formation des traces dans le volume des solides concernés suite à la perte d'énergie électronique. On retrouve notamment le modèle de l'explosion coulombienne [13] ou encore le modèle de la pointe thermique [14].

Modèle de l'explosion coulombienne

En 1965, Fleischer, Price et Walker [13] proposent ce modèle. Il part du principe qu'une trace cylindrique est créée suite au passage de l'ion dans la matière. Ce dernier induit l'éjection des électrons tout le long de son trajet, créant une zone chargée positivement. Cette accumulation de charge entraîne une répulsion coulombienne entre les ions positifs, induisant une explosion. Lorsque l'explosion se produit, les ions sont éjectés du centre de la trace, ainsi que du réseau environnant. La condition pour que le mouvement atomique soit réalisé est que le temps de retour des électrons éjectés soit supérieur à 10^{-13} s. Cette condition est remplie par les isolants et les semi-conducteurs, car la mobilité électronique y est faible contrairement aux conducteurs.

Modèle de la pointe thermique

Ce modèle, proposé pour la première fois par Dessauer en 1923 [15], puis adapté aux cas des ions lourds rapides par Toulemonde et al. [14] [16], décrit la formation d'une trace par un ion de grande énergie. Ils se basent sur le fait que l'énergie de l'ion est transférée aux électrons de la matière, qui la convertissent en énergie thermique.
Suite à une irradiation par des ions énergétiques, les électrons sont excités et ionisés. Cette énergie déposée par l'ion projectile dans le système électronique est convertie en chaleur par interaction électron-phonon. La région le long de la trajectoire des ions subit alors une augmentation de température et potentiellement une fusion, résultant en la formation d'un cylindre de quelques

nanomètres de diamètre. Après un certain temps (>100 ps), la zone refroidit et cette chaleur est dissipée par transfert vers le reste du réseau, figeant ainsi cette zone en une structure désordonnée voire amorphe (trace latente).

Résultats et discussion

La nanostructuration de surface a été largement étudiée pour créer des motifs de manière contrôlée en surface. Dans cette thèse, nous avons d'abord étudié le titanate de strontium. Les études faites sur ce matériau montrent que, pour une irradiation à basse fluence, c'est-à-dire lorsque l'impact unique domine, chaque impact d'ion engendre la formation d'une bosse en surface dans le cas d'une irradiation à 90° [6]. Cependant, lorsque l'angle est rasant, une chaîne de nano-bosses est formée en surface dans la direction du faisceau d'ion [17]. La longueur de la chaîne peut être contrôlée, tout comme l'espace entre les bosses, grâce aux paramètres d'irradiation ou encore à la direction cristallographique du matériau. Pour rappel, pour obtenir ces défauts, un seuil d'amorphisation est nécessaire, et il est de 12 keV/nm dans le cas du $SrTiO_3$ [18]. La figure 2 montre une sélection d'images AFM de surface de différents matériaux irradiés à un angle normal à la surface (90°) en (a-c) et à des angles rasants (d-f).

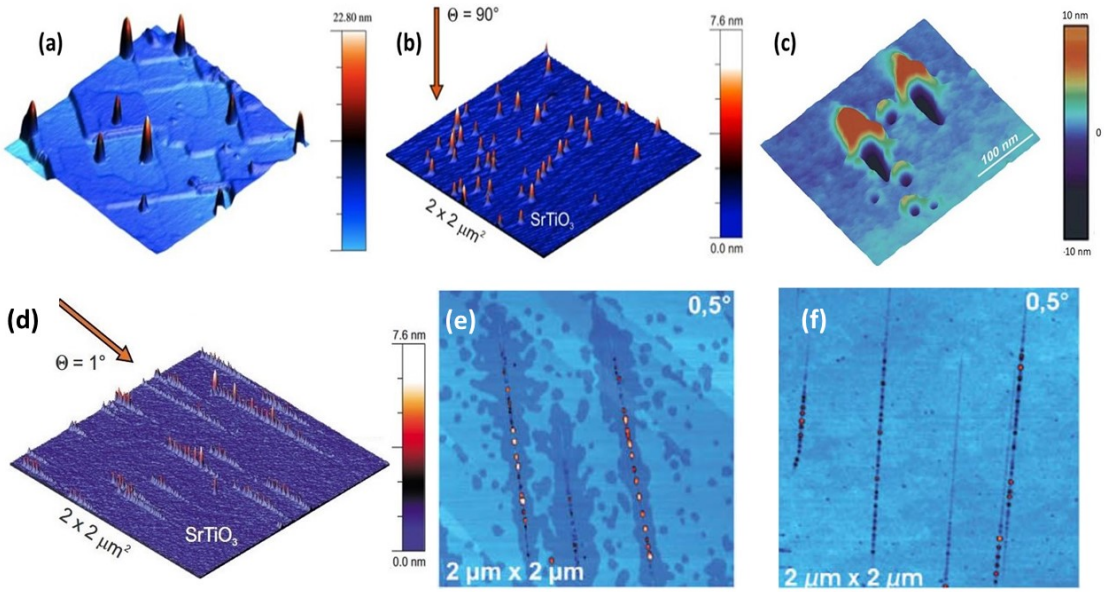

Figure 2: Images topographiques d'une surface monocristalline de LiF irradiée à $\theta = 90°$ avec des ions de Xe de 93 MeV et une fluence de 5×10^8ions cm^{-2} (a), $SrTiO_3$ (100) irradiée à $\theta = 90°$ avec des ions de ^{207}Pb de 103 MeV (b) [2]. En (c) des structures en forme de cratère sur un film de PMMA induites par une irradiation d'ions de Bi de 11.1 MeV/u sous différents angles (0°, 45° et 79° par rapport à la normale à la surface) [3]. En (d) une image AFM 3D de $SrTiO_3$ irradié à $\theta = 1°$, (e) une surface de CaF_2 irradiée avec 103 MeV $^{131}Xe^{23+}$ et (f) TiO_2 irradié avec 103 MeV $^{207}Pb^{28+}$ dans ces deux derniers cas $\theta = 0.5°$ [2] [4].

D'après Akcoltekin et al. [6] [17] cette chaîne de nanobosses en surface serait la projection d'une partie de la trace créée dans le volume. Par conséquent, le système électronique du matériau a un impact direct sur leur formation et peut être considéré comme une projection directe de la densité électronique tridimensionnelle de la cible sur la surface. Une formule a été développée qui permet de décrire la relation entre l'angle d'irradiation et la longueur des chaînes et est donnée par : $L = d/\tan\theta$ [6].
En augmentant la fluence et en irradiant à un angle normal à la surface, on obtient un recouvrement des traces. Une couche amorphe de quelques micromètres d'épaisseur se forme alors en surface [19].
L'effet de l'irradiation aux ions lourds rapides avec de faibles fluences en incidence rasante est bien connu, tout comme l'effet de fortes fluences en incidence normale. Cependant, cet effet collectif combiné à un angle rasant est beaucoup moins étudié, notamment dans le cas de matériaux monocristallins.
C'est pourquoi l'objectif de cette recherche est d'étudier l'effet de l'irradiation par des ions lourds rapides (SHI) lorsqu'une géométrie d'incidence rasante est utilisée à de fortes fluences. Plusieurs angles et fluences ont été utilisés. L'angle d'irradiation s'étend de la normale à la surface et diminue jusqu'à l'incidence rasante. L'irradiation avec cette dernière géométrie entraîne une perte d'énergie localisée près de la surface. Des échantillons de $SrTiO_3$ de direction cristallographique (100) (110) ont été utilisés. Ces échantillons proviennent de chez Crystec company à Berlin en Allemagne.

Au cours de ces expériences d'irradiation, trois types de faisceaux ont été utilisés sur la ligne de faisceaux IRRSUD. Du $^{129}Xe^{23+}$ à 92 MeV, du $^{136}Xe^{19+}$ à 75 MeV et du $^{20}Ne^{6+}$ à 20 MeV. En calculant la perte d'énergie électronique à la surface avec le code SRIM [1] (en utilisant une densité de 5.117 $g\,cm^{-3}$), cela correspond respectivement à 21 keV/nm, 19 keV/nm et 4 keV/nm. Contrairement au faisceau de néon, pour les deux faisceaux de xénon, le pouvoir d'arrêt électronique est bien supérieur au seuil de 12 keV/nm nécessaire à la formation de traces dans le $SrTiO_3$ [19]. La perte d'énergie nucléaire est presque négligeable à ces énergies, contribuant à seulement $\sim 1\%$ de la perte d'énergie totale. Elle augmente légèrement en volume pour atteindre une valeur d'environ 0.18 keV/nm pour le faisceau de xénon de 92 MeV, 0.22 keV/nm pour le xénon de 75 MeV et 0.005 keV/nm pour le faisceau de néon de 20 MeV. Le parcours projeté est de ~ 8 µm pour les ions de xénon dans le $SrTiO_3$ et de ~ 6 µm pour les ions de néon. Le tableau III.1 du chapitre 3 résume les différents paramètres d'irradiation utilisés durant cette étude. La figure I.4 montre un exemple de perte d'énergie dans le cas du $SrTiO_3$ irradié avec un faisceau de xénon de 92 MeV.

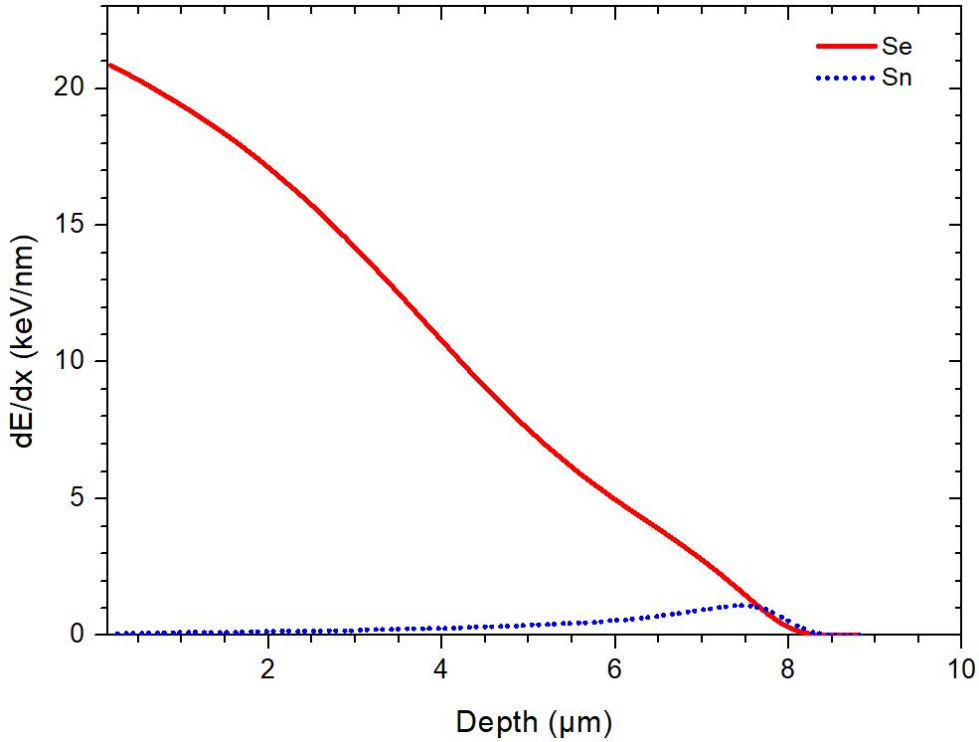

Figure 3: Perte d'énergie des ions Xe de 92 MeV en fonction de la profondeur de pénétration dans un $SrTiO_3$ monocristallin obtenue à partir des calculs SRIM [1] (La ligne bleue en pointillés représente la perte d'énergie nucléaire et la ligne droite rouge représente la perte d'énergie électronique.

Pour sonder le matériau en profondeur et étudier les déformations structurales, des analyses par diffraction aux rayons X et au microscope électronique à transmission ont été entreprises. L'analyse des diffractogrammes de rayons X a montré que l'irradiation a entraîné une perte de cristallinité et potentiellement une amorphisation. Une analyse complémentaire au microscope électronique à (TEM) a donc été entreprise pour confirmer la présence de désordre et potentiellement de changement de phase dans le titanate de strontium. La figure 4 montre des images STEM d'une coupe transversale de $SrTiO_3$ (100) préparée par FIB. Cet échantillon a été irradié à un angle nominal de 6° avec une fluence de 8×10^{13} ions cm^{-2}. On peut voir la présence de différents contrastes, qui sont synonymes de la présence de régions aux caractéristiques différentes dans l'échantillon.

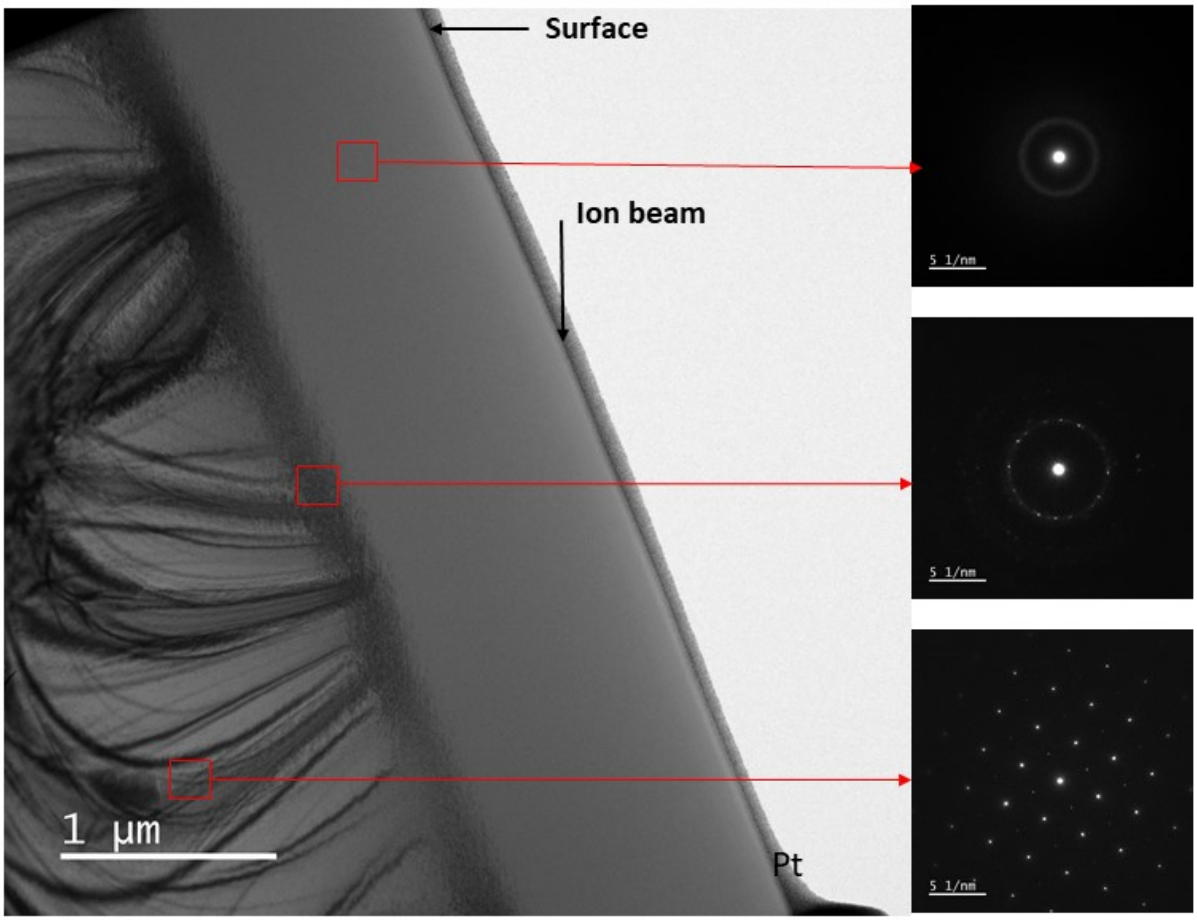

Figure 4: Image TEM d'un échantillon de $SrTiO_3$ irradié à $\theta = 6°$ avec $\phi = 8 \times 10^{13}$ ions cm^{-2}. La direction du faisceau d'ions est indiquée par une flèche noir. Dans la partie droite de l'image, trois images montrent des diagrammes de diffraction électronique de zone sélectionnée (SAED) pris à différentes profondeurs de l'échantillon.

Sur le côté droit de la figure 4, différents diagrammes de diffraction d'électrons sont pris dans différentes régions le long du trajet de l'ion dans la cible. La première image a été prise dans une région proche de la surface. On peut observer un seul anneau diffus, représentatif de la phase amorphe et de l'amorphisation du cristal par les ions incidents. Une mesure directe de la couche amorphe s'étendant de la surface au bord de la deuxième région, caractérisée par un contraste plus sombre, permet d'estimer l'épaisseur à environ 1 µm. En allant plus en profondeur, le schéma de diffraction montre un anneau diffus avec des points brillants, synonymes de la présence de désordre et d'une amorphisation partielle. En dessous de cette région et beaucoup plus profondément dans le cristal, on constate que cette région est restée monocristalline, comme le montre le dernier cliché de diffraction. Ces résultats confirment donc qu'une couche amorphe a été induite à la surface. En outre, une région avec des défauts est également créée en dessous. Ces types de déformations et de changements structurels ont déjà été observés dans le cas du $SrTiO_3$ pour une irradiation à haute fluence avec une incidence normale à la surface (90°) [19]. Ces résultats confirment donc

que la géométrie d'irradiation n'y change rien. Cependant, cela impacte l'épaisseur de la couche amorphe qui semble moins épaisse que pour une irradiation normale à la surface. Le matériau ayant été sondé en profondeur, on sait maintenant que l'irradiation à un angle rasant induit la formation d'une couche amorphe en surface, avec la présence d'une déformation dans la couche sous-jacente. La question qui se pose à présent est que se passe-t-il en surface ? Pour le savoir, des analyses au microscope à force atomique (AFM) ont été effectuées pour étudier la morphologie et la topographie de surface. Une sélection d'images a été choisie pour être présentée ici, représentant un exemple de chaque cas auquel nous avons été confrontés.

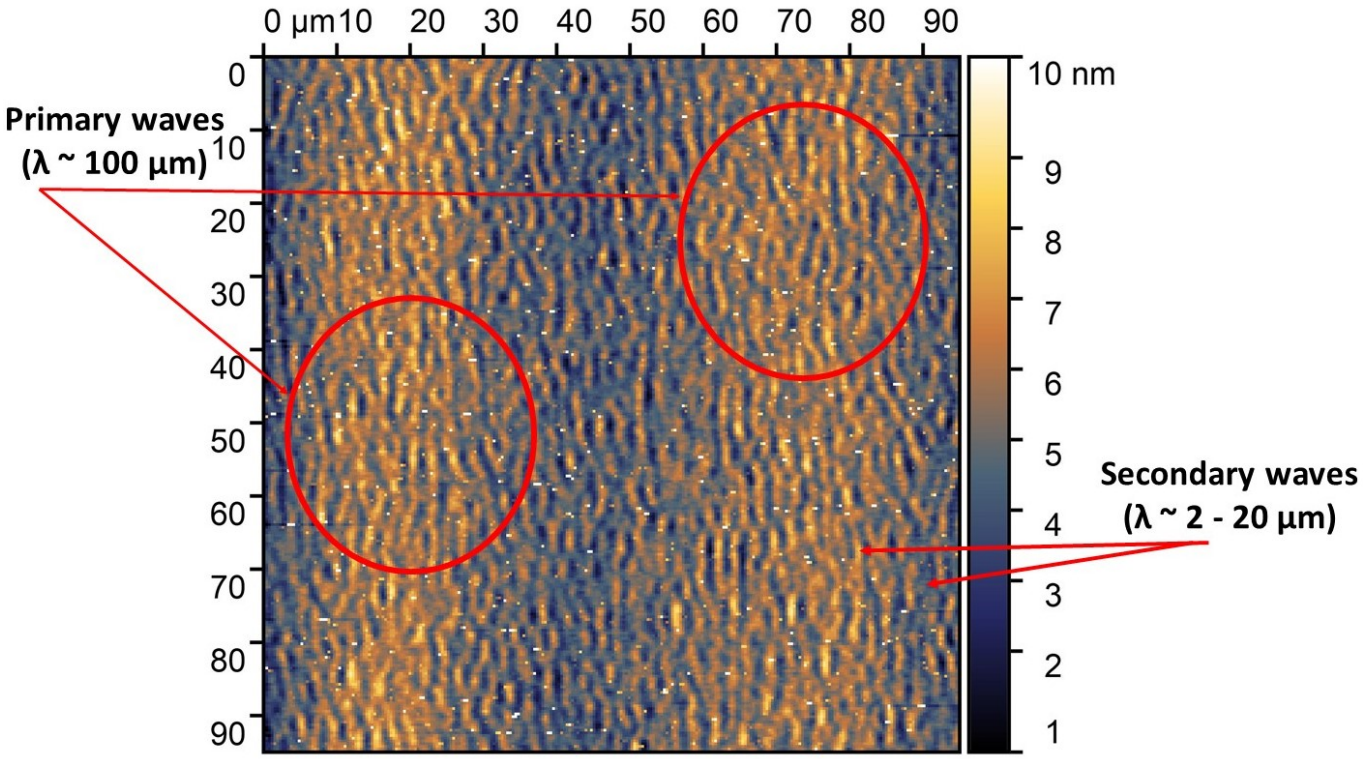

Figure 5: Image AFM de la surface de $SrTiO_3$ irradiée à un angle rasant, où deux structures périodiques ondulatoires, à savoir les ondes primaires et les ondes secondaires, sont observées et représentées par les flèches rouges.

Les premiers résultats obtenus et présentés dans le chapitre trois, dévoilent la formation de trois types de structures différentes suite à l'irradiation aux ions lourds rapides sur le de $SrTiO_3$. À savoir deux structures périodiques orientées perpendiculairement à la direction du faisceau d'ions et des nano-bosses formées sur toute la surface. Pour cette dernière structure, elle a été observée que dans une série d'échantillons. Il a donc été conclu que ce n'était qu'un cas particulier dû probablement à des échantillons contaminés avant l'irradiation.

En ce qui concerne les structures périodiques, il y a les ondes dites "primaires" et les ondes ou vagues "secondaires". Le premier type de vagues a une périodicité de l'ordre de 100 µm avec une

amplitude presque négligeable, ce qui rend leur observation et leur analyse difficiles. Cependant, cette structure n'a été observée que dans une certaine gamme de fluences. C'est-à-dire que pour leur formation, il faut une fluence assez grande pour amorphiser la surface ($> 10^{13}$ ions cm^{-2}) et assez petite pour éviter que la seconde structure ne prenne le dessus. En effet, pour des fluences plus importantes, la formation d'une seconde structure périodique, orientée également perpendiculairement au faisceau d'ion apparaît. Cette structure possède une périodicité < 10µm. La figure 5 illustre un exemple où les structures primaires et secondaires peuvent être distinguées afin de mettre en évidence les différences entre elles.

Dans le cas de l'irradiation avec un faisceau de Xe de 75 MeV, trois angles différents avec trois fluences différentes ont été utilisés. Pour une irradiation à 10.9° avec 7.66×10^{13} ions cm^{-2}, les vagues primaires ont été les seules à être observées. Dans le cas d'une irradiation à 6.1° avec 8×10^{13} ions cm^{-2}, les vagues primaires sont présentes, avec l'apparition des vagues secondaires. Tandis que pour une irradiation à 8.1° avec 1.4×10^{14} ions cm^{-2}, il n'y a que les vagues secondaires qui ont été observées.
Une valeur de fluence seuil pour la formation de la structure primaire ne peut être donnée de manière exacte étant donné que deux paramètres d'irradiation changent. La périodicité de chacune des structures a été extraite grâce à la transformée de Fourier.
La première observation revient au fait que la périodicité ne varie pas avec la direction cristallographique. Une structure périodique importante est présente avec une périodicité autour de 100 µm pour les deux directions cristallographiques et pour deux fluences différentes, à savoir 2×10^{13} ions cm^{-2} et 8×10^{13} ions cm^{-2}. On peut supposer à ce stade que cette structure, dites primaire ne s'est probablement pas développée davantage, notamment en hauteur, à cause d'une fluence insuffisante.

Sur la base de ces premiers résultats, une seconde série d'irradiation a eu lieu afin de vérifier la reproductibilité du phénomène de réorganisation de la surface en structures quasi-périodiques et d'étudier l'impact de l'énergie, de la fluence et de l'angle d'irradiation. Pour cette seconde étape, un faisceau d'ions différent a été utilisé, à savoir du $^{129}Xe^{23+}$ d'énergie 92 MeV. La perte d'énergie électronique dans ce cas est aux alentours de 21 keV/nm, ce qui est toujours supérieur à la valeur seuil d'amorphisation du $SrTiO_3$ de 12 keV/nm.
Une série d'échantillons a été irradiée à des angles allant de 1.5° à 45° à différentes fluences. Certaines différences sont perceptibles en fonction de la fluence et de l'angle utilisés. Pour une irradiation à un angle nominal de 1.5° avec 2.62×10^{13} ions cm^{-2}, à θ = 2.5° avec 3.75×10^{13} ions cm^{-2} et à 3.5° avec 6.1×10^{13} ions cm^{-2}, on obtient une surface assez rugueuse avec Rq = 6.8 nm, 2 nm et 2.2 nm respectivement. L'analyse avec la transformation de Fourier 2D confirme la présence d'une structure périodique perpendiculaire au faisceau d'ions (vagues secondaires). La présence d'une autre structure chevauchant celle-ci, la structure dite vagues primaires, est également présente mais seulement pour les échantillons irradiés à 1.5° et 3.5°.

La périodicité de chacune des ondes primaires a été extraite et est de (115 ± 4) µm pour l'échantillon irradié à 1.5° et de (102.32 ± 3) µm pour celui irradié à 3.5°. Cette structure n'a pas été observée dans le second échantillon irradié à $\theta = 2.5°$, ce qui peut être dû à une fluence pas assez

élevée pour induire le début de réorganisation de la surface. Ces résultats rappellent et confirment le type de structures observées précédemment avec le faisceau d'ions de Xe à 0.55 MeV/u. L'analyse du reste des échantillons a montré une évolution de ces structures primaires avec la fluence jusqu'à un angle d'environ 11°. Au-delà, la structure ondulatoire secondaire prend le dessus et la structure primaire n'est plus observable.

Une grande partie de cette recherche a été consacrée à l'étude de la réponse du $SrTiO_3$ à des ions lourds rapides et notamment à la formation de structures dites secondaires (vagues).
L'impact de la fluence et de l'angle d'incidence sur l'évolution des structures périodiques, en particulier les ondes secondaires, est examiné en détail. Les résultats soulignent l'importance de comprendre l'influence des paramètres d'irradiation sur la formation et l'évolution des structures de surface pour des applications potentielles.

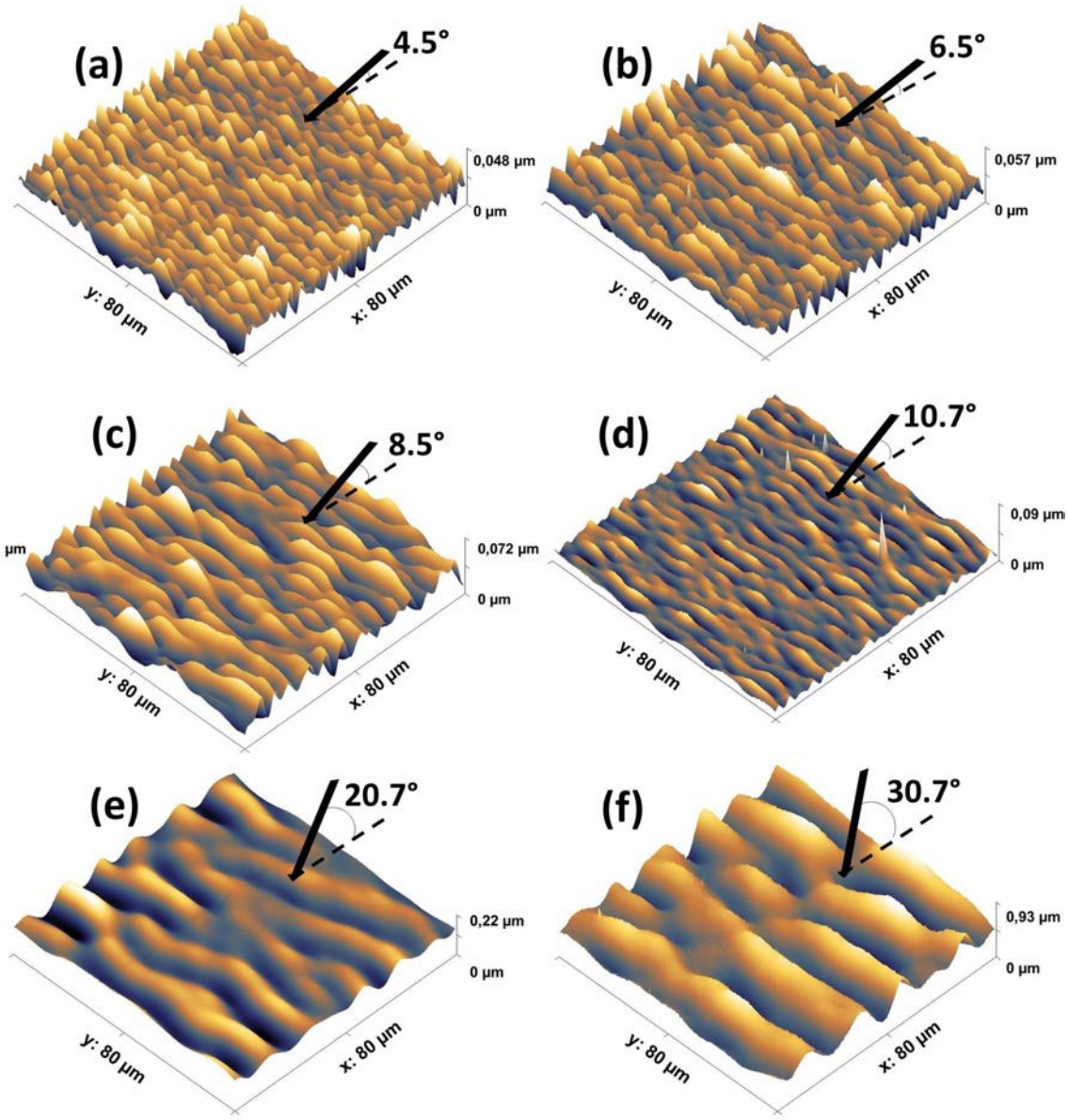

Figure 6: Images AFM $SrTiO_3(100)$ irradiées avec des ions de Xe de 92 MeV à : (a) $\theta = 4.5°$ et $\phi = 6.75 \times 10^{13}$ ions cm^{-2}, (b) $\theta = 6.5°$ et $\phi = 9.74 \times 10^{13}$ ions cm^{-2}, (c) $\theta = 8.5°$ et $\phi = 1.27 \times 10^{14}$ ions cm^{-2}, (d) $\theta = 10.7°$ et $\phi = 9.5 \times 10^{13}$ ions cm^{-2}, (e) $\theta = 20.7°$ et $\phi = 1.8 \times 10^{14}$ ions cm^{-2} et (f) $\theta = 30.7°$ et $\phi = 2.6 \times 10^{14}$ ions cm^{-2}.

Il a été constaté que le processus de réorganisation de la surface commence par la formation d'une structure primaire à des fluences d'environ 3×10^{13} ions cm^{-2}. Cette fluence n'est pas assez élevée pour finaliser la formation de structures ondulatoires de l'ordre de quelques micromètres. Étant donné que le but de cette étude est de générer des microstructures de surface et de contrôler leur forme, dans ce qui suit, l'accent sera mis sur la formation d'ondes secondaires.
Afin d'analyser le processus de formation de ces microstructures, des fluences allant jusqu'à

4×10^{14} ions cm^{-2} et des angles allant jusqu'à 45° ont été utilisés.

La figure 6 montre des images AFM de la topographie de surface de différents échantillons de $SrTiO_3$ (100) irradiés à température ambiante avec des ions Xe de 92 MeV avec des angles nominaux allant de $\theta = 4.5°$ à $\theta = 30.7°$ pour différentes fluences élevées. Les flèches noires sont là pour faciliter la visualisation de la direction du faisceau d'ions sur la surface de l'échantillon.
On observe clairement que la formation d'ondes orientées perpendiculairement au faisceau d'ions évolue avec la fluence pour les différents angles utilisés. Pour des angles relativement faibles (rasants), la périodicité reste < 10µm, comme on peut le voir sur la Fig.6 (a) où pour un angle d'incidence de 4.5°, on obtient une périodicité de (3.79 ± 0.4) µm ou encore en (c) où pour un angle de 8.5°, la périodicité est de (5.86 ± 1.1) µm.
En augmentant la fluence et l'angle d'irradiation vers la normale à la surface, ces ondes secondaires ont tendance à s'étendre dans la direction normale au faisceau d'ions et par conséquent, cette valeur augmente aussi considérablement, comme on peut le voir sur la Fig.6 (e) ou (f) où pour une irradiation à $\theta = 20.7°$ et $\theta = 30.7°$, la périodicité est respectivement de (15.54 ± 1.1) µm et (16.6 ± 0.42) µm.
Cela signifie que plus l'angle d'incidence est grand, plus la périodicité est importante. Cela implique que l'angle a un effet assez important sur la densité des ondes sur une surface donnée. Comme la périodicité augmente avec l'angle, la taille des ondes augmente et leur nombre diminue également, ce qui permet un contrôle relativement précis en fonction de l'application souhaitée.

Bien que l'effet de l'angle soit clairement visible, le fait que la fluence soit différente à chaque fois peut susciter des doutes. Pour cette raison, et comme le montre la figure 7 (a-b), une sélection de cas composée de 12 échantillons irradiés à des angles différents avec des fluences variant entre 1×10^{14} ions cm^{-2} et 3×10^{14} ions cm^{-2} est présentée. Pour plus de clarté, les valeurs de fluence sont arrondies.
La figure 7 (a) permet d'observer et de confirmer que la périodicité de ces ondulations peut être contrôlée. L'impact de l'angle sur la périodicité, malgré la fluence variable, est clairement visible, avec une périodicité plus faible au fur et à mesure que l'on s'approche des angles rasants.
Quant à la figure 7 (b), la variation de la largeur de l'onde pour des angles variant entre 4° et 45° est présentée. La largeur est définie par la moyenne de la largeur à mis hauteur (FWHM) des ondes secondaires. Elles sont déterminées à partir de coupes multiples.
Contrairement à ce qui a été observé dans des études précédentes [20], où la largeur des ondulations diminue lorsque la périodicité entre elles augmente, dans cette étude, une légère augmentation de la largeur avec l'angle d'incidence a été observée.
Cependant, outre l'effet de l'angle, la fluence joue également un rôle dans la largeur des ondes et a donc un impact direct sur la taille des vallées (séparation des ondes). Il a été observé que pour des valeurs d'angle quasi identiques, la largeur des ondes tend à diminuer avec l'augmentation de la fluence, créant ainsi un écart plus important.
D'autres études dans lesquelles des structures de surface périodiques ont été observées ont montré qu'une réorientation des ondes se produit à des angles importants [21] (c'est-à-dire que les ondulations d'abord orientées perpendiculairement au faisceau d'ions deviennent parallèles à celui-ci en augmentant l'angle d'incidence vers la normale à la surface). Dans cette étude, cependant, les

ondes restent perpendiculaires au faisceau d'ions à tous les angles jusqu'à 45.7°.
Il convient toutefois de noter que des irradiations à des angles supérieurs à 45.7° ont également été réalisées, et plus particulièrement à 90° pour des fluences variant de 5×10^{11} ions cm^{-2} à 5×10^{14} ions cm^{-2}. En analysant les différentes surfaces avec l'AFM et hormis une surface rugueuse, la transformée de Fourier n'a pas mis en évidence de formes périodiques.

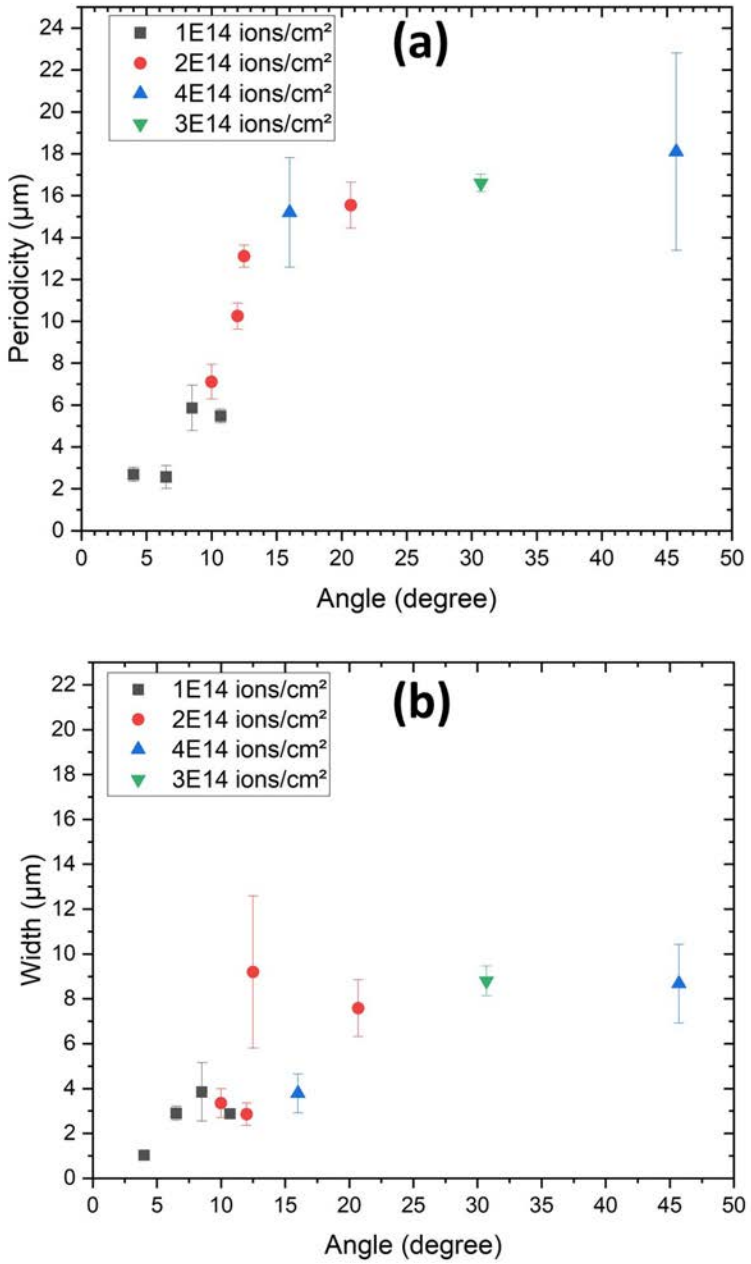

Figure 7: Évolution de la périodicité de l'ondulation (a) et de la largeur de l'ondulation (b) observées sur la surface du $SrTiO_3$ (100) irradiée avec des ions de Xe de 92 MeV en fonction de l'angle d'incidence pour différentes fluences.

Pour résumer la première partie de cette recherche, il a été démontré que l'angle affecte la périodicité (λ) des structures ondulatoires, qu'il s'agisse des ondes primaires ($\lambda > 100$ µm) ou des ondes secondaires ($\lambda < 20$ µm). Cependant, la première catégorie est limitée à des cas spécifiques : la fluence doit être suffisamment élevée pour créer une couche amorphe en surface, mais suffisamment faible pour ne pas être dépassée par la formation de structures secondaires. Compte tenu de leur taille, ce sont les ondes secondaires qui sont analysées en détail. La largeur de ces structures est également influencée par la géométrie de l'irradiation. Ainsi, lorsque l'angle augmente vers la normale à la surface, les ondes deviennent plus grandes (avec une périodicité croissante). Les vallées sont également impactées, avec une réduction de leur taille au fur et à mesure que l'angle augmente. On suppose que si la fluence n'est pas assez élevée compte tenu de l'angle, cela peut conduire à un regroupement/croisement de plusieurs ondes secondaires "petites" pour former une seule onde de plus faible amplitude. En conséquence, les défauts sont additionnés et si l'irradiation ne se poursuit pas à des fluences plus élevées, ces ondes n'auront pas le temps de finaliser leur formation en ondes bien définies. À cela s'ajoutent les différents aspects morphologiques observés, qui peuvent également être dus à la fluence variable. C'est pourquoi l'objectif du chapitre suivant est d'étudier comment évolue la réorganisation de la surface et comment la fluence impacte cela.

Évolution de la microstructure de surface de $SrTiO_3$ à $\theta = 4°$

Six échantillons de titanate de strontium ont été irradiés avec le même angle ($\theta = 4°$). La fluence utilisée était comprise entre 1×10^{13} ions cm^{-2} et 1×10^{14} ions cm^{-2}. Pour l'échantillon irradié à 1×10^{13} ions cm^{-2}, aucune structure en forme de vagues n'a été observée sur les images AFM ni avec la transformée de Fourier. Pour l'échantillon irradié à 2×10^{13} ions cm^{-2}, une structure périodique primaire est observée d'une périodicité de $\lambda \sim 80$ µm. Avec une fluence plus élevée de 4×10^{13} ions cm^{-2}, deux structures sont formées, à savoir le motif primaire avec une périodicité de $\lambda \sim 83$ µm et l'apparition de la structure d'onde secondaire qui est bien orientée perpendiculairement au faisceau d'ions avec une périodicité de $\lambda \sim 3$ µm. Ces structures dites "primaires" ont été observées pour des échantillons irradiés à 2×10^{13} ions cm^{-2}, 4×10^{13} ions cm^{-2} et 6×10^{13} ions cm^{-2}, produisant une périodicité spatiale beaucoup plus importante que les ondes secondaires. Avec l'augmentation de la fluence, la structure primaire s'estompe avec λ, atteignant environ 94 µm pour la fluence de 6×10^{13} ions cm^{-2}. À des fluences plus élevées, seule l'onde secondaire, de plus en plus prononcée, reste, comme on peut le voir sur la figure 8 (b-d).

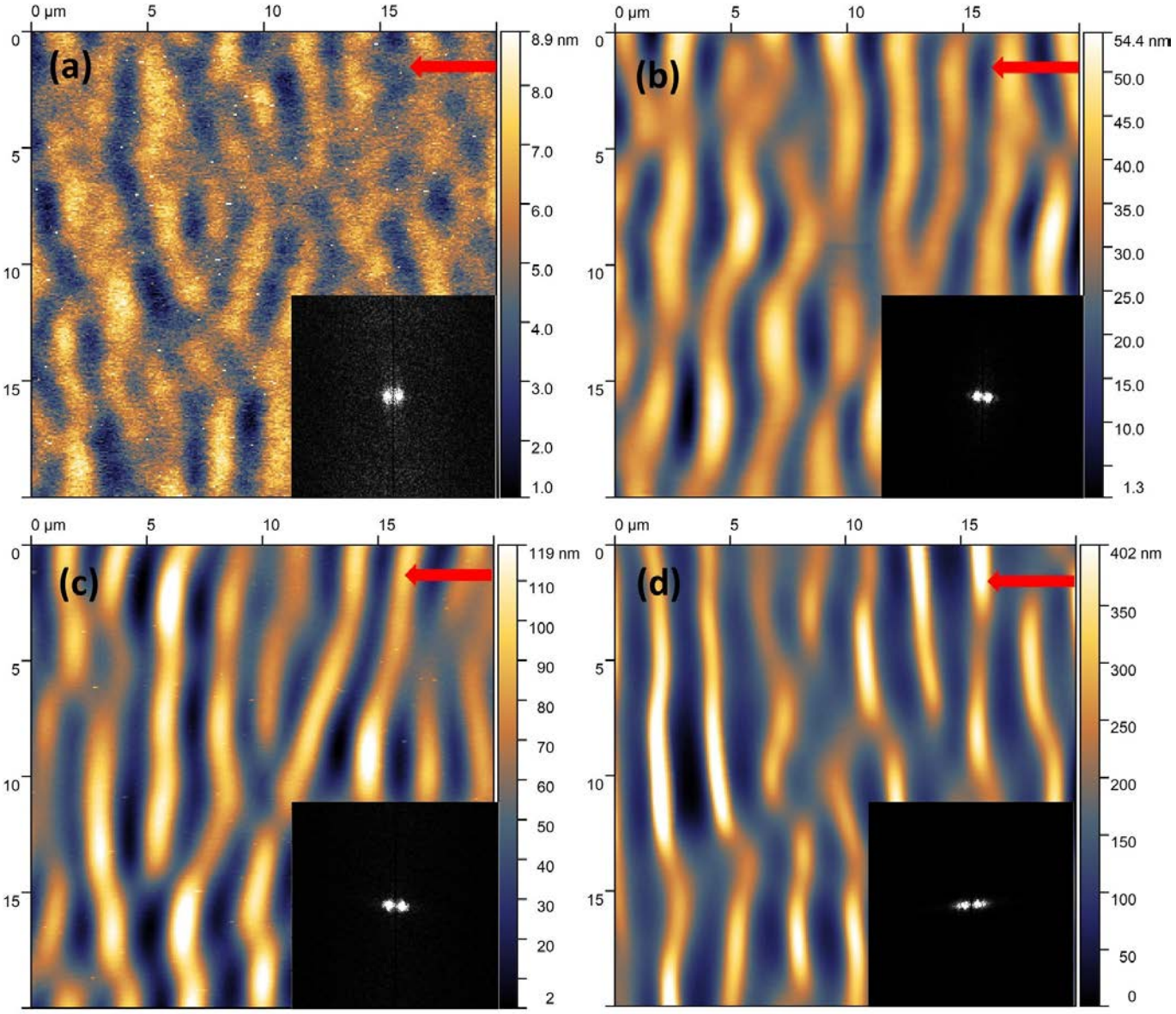

Figure 8: Images AFM de surfaces de $SrTiO_3$ (100) irradiées à 4° avec des ions Xe de 92 MeV à $\phi = 4 \times 10^{13}$ ions cm^{-2} (a), $\phi = 6 \times 10^{13}$ ions cm^{-2} (b) $\phi = 8 \times 10^{13}$ ions cm^{-2} (c) $\phi = 1 \times 10^{14}$ ions cm^{-2} (d) et leur transformation de Fourier 2D.

À partir d'une fluence de 4×10^{13} ions cm^{-2} et jusqu'à 1×10^{14} ions cm^{-2} (la fluence la plus élevée utilisée pour cet angle), la surface s'auto-organise en une structure périodique perpendiculaire au faisceau d'ions de plus en plus prononcée. La figure 8 montre l'évolution de la morphologie de la surface. La transformation de Fourier de chaque cas révèle deux points distincts, confirmant la présence d'une structure périodique en surface. La variation de la périodicité (λ) en fonction de la fluence est représentée dans la figure 9 pour l'irradiation avec principalement des angles autour de 4°. La périodicité a une valeur d'environ 3 µm et est indépendante de la variation de la fluence.

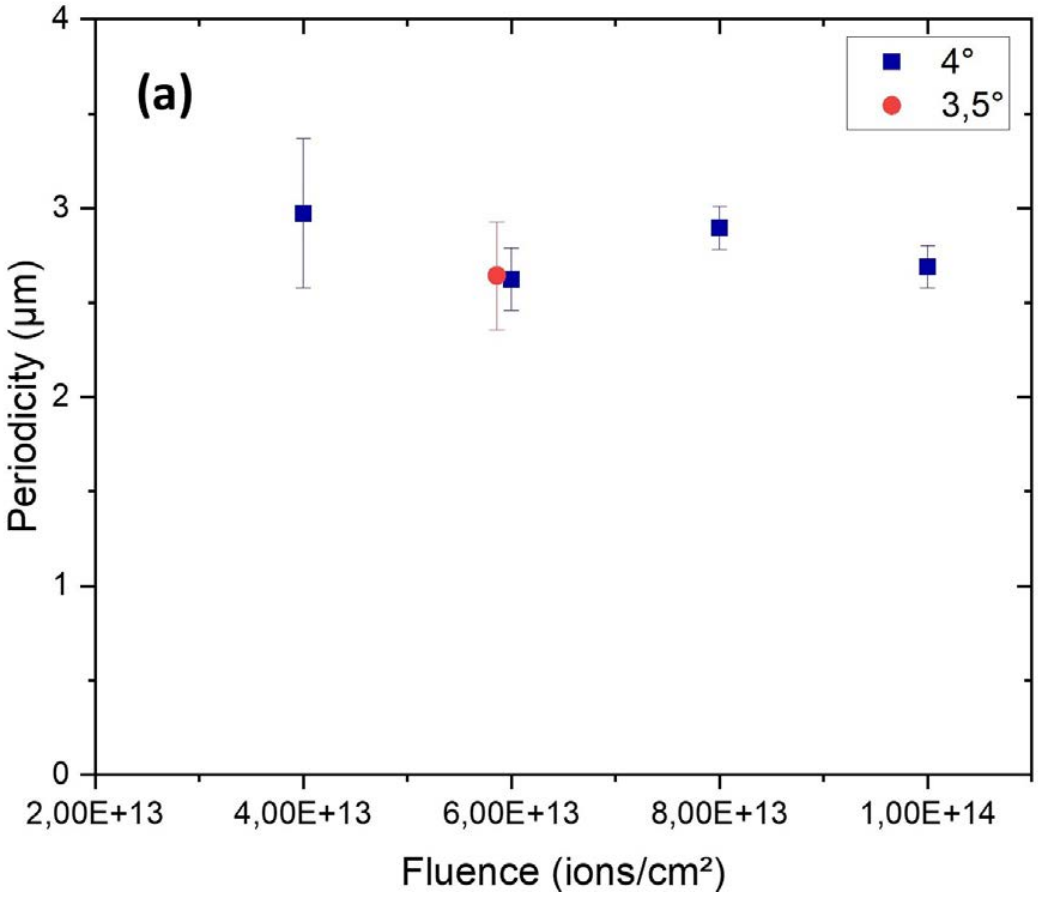

Figure 9: Évolution de la périodicité des vagues secondaires avec la fluence pour une irradiation aux ions lourds rapide de 92 MeV à 4° et 3.5°.

La figure 10 (a) montre l'évolution de la hauteur des vagues secondaires en fonction de la fluence. On constate que la hauteur des vagues augmente lorsque la fluence augmente, avec une valeur de h $\sim$ 3 nm pour une fluence de 4×10^{13} ions cm^{-2}, atteignant les 200 nm pour une fluence de 1×10^{14} ions cm^{-2}. On pourrait s'attendre à une saturation et à une stabilisation de la hauteur à une fluence donnée, mais dans ce cas particulier, la surface se développe encore à une fluence d'environ 1×10^{14} ions cm^{-2} pour un angle de 4°. Rappelons que l'analyse de la variation de la hauteur en fonction de l'angle n'a pas montré de tendance évolutive particulière. La fluence agirait donc sur la croissance de ces structures. Ceci coïncide avec ce qui a été observé précédemment dans cette étude.

Les différentes images AFM montrent qu'à mesure que la fluence augmente, les vagues ont tendance à devenir plus fines tout en conservant leur direction normale au faisceau d'ions. Quant aux vallées, elles se creusent davantage et s'élargissent, comme le montre la figure 8(a-d). Des coupes transversales de profil ont donc été réalisées, à partir desquelles les valeurs de largeur des vagues ont été dérivées sur un ensemble d'échantillons. Par largeur d'onde, on entend ici, par définition, la largeur à mi-hauteur des ondulations déterminées à partir des coupes multiples. La figure 10(b) montre une diminution de la largeur des ondes avec l'augmentation de la fluence

d'irradiation. Comme il a été observé, ce rétrécissement, qui ressemble à une contraction des ondes, s'accompagne d'un gain de hauteur à mesure que la fluence augmente. Ceci est cohérent avec ce qui a été observé dans des études précédentes pour d'autres types d'échantillons et d'énergies. Dans des études antérieures [20], cet effet de la fluence sur l'évolution de la hauteur et de la largeur des ondes a déjà été observé dans le cas de films de LiF ou de BaF_2 irradiés avec des ions lourds rapides. Cependant, la réorganisation de la surface et la formation et l'évolution des ondulations en fonction de la fluence n'ont pu avoir lieu que lorsque les échantillons ont été maintenus à la température de l'azote liquide (LNT, 77 °C) pendant l'irradiation. Dans cette étude, nous avons pu former des vagues (ondulations) à la surface d'un monocristal et les faire évoluer (taille, hauteur et périodicité) dans le temps avec différentes fluences et différents angles à température ambiante tout au long de la phase d'irradiation.

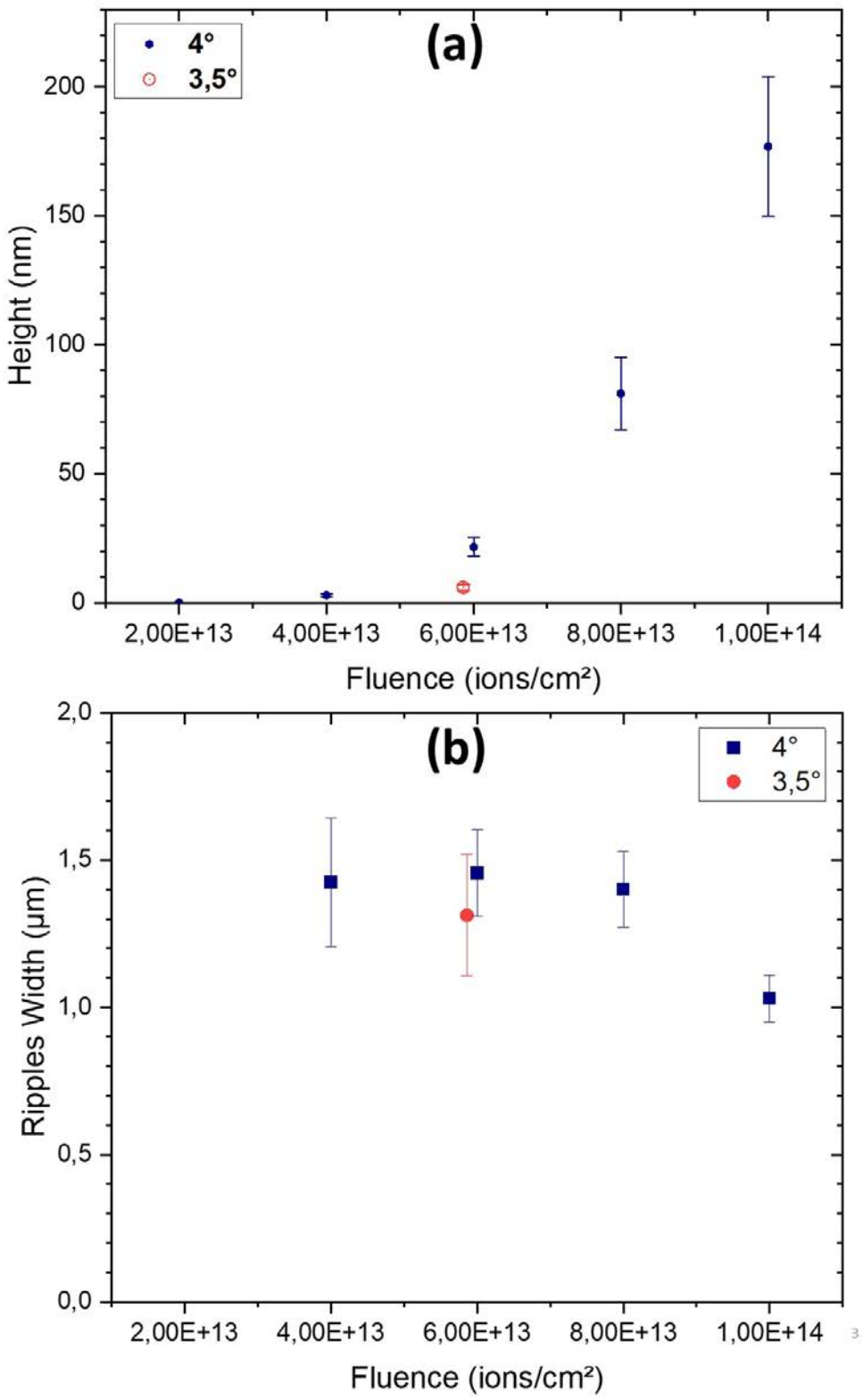

Figure 10: Evolution de la hauteur (a) et de la largeur (b) des vagues secondaires sur la surface du $SrTiO_3$ (100) irradié par des ions Xe de 92 MeV à 4° en fonction de la fluence

Effet de l'irradiation à de grands angles à haute fluence

La figure 11 montre l'image topographique de deux surfaces irradiées avec une fluence d'environ 4×10^{14} ions cm^{-2} à deux angles différents. L'échantillon irradié à $\theta = 16°$ (figure 11 (b)) présente des tranchées plus profondes et des ondes plus fines, dont la largeur diminue d'un facteur 2, contrairement à l'échantillon irradié à $\theta = 45°$ (figure 11(a)). Il convient de noter qu'à cette fluence, les trois paramètres décrivant les structures d'ondes secondaires, à savoir la hauteur, la largeur et la périodicité, sont dans le domaine micrométrique et ont des valeurs respectives de 1 µm, 4 µm et 15 µm. Une exception existe pour l'échantillon irradié à $\theta = 45°$ (figure 11(a)), où la structure ondulatoire apparaît moins structurée, avec une largeur d'environ 9 µm, une hauteur d'environ 8 nm et presque pas de vallées.
Malheureusement, par manque de temps, il n'a pas été possible d'irradier d'autres échantillons à des fluences plus élevées pour confirmer notre hypothèse. Cependant, d'après les résultats précédents sur l'influence de l'angle et de la fluence, on peut supposer qu'à cet angle, une fluence plus élevée aurait permis à la surface de former une structure plus homogène, notamment en développant les ondulations en hauteur. Cela signifie que la structuration de la surface ne s'est pas poursuivie, probablement parce que la fluence était trop faible.

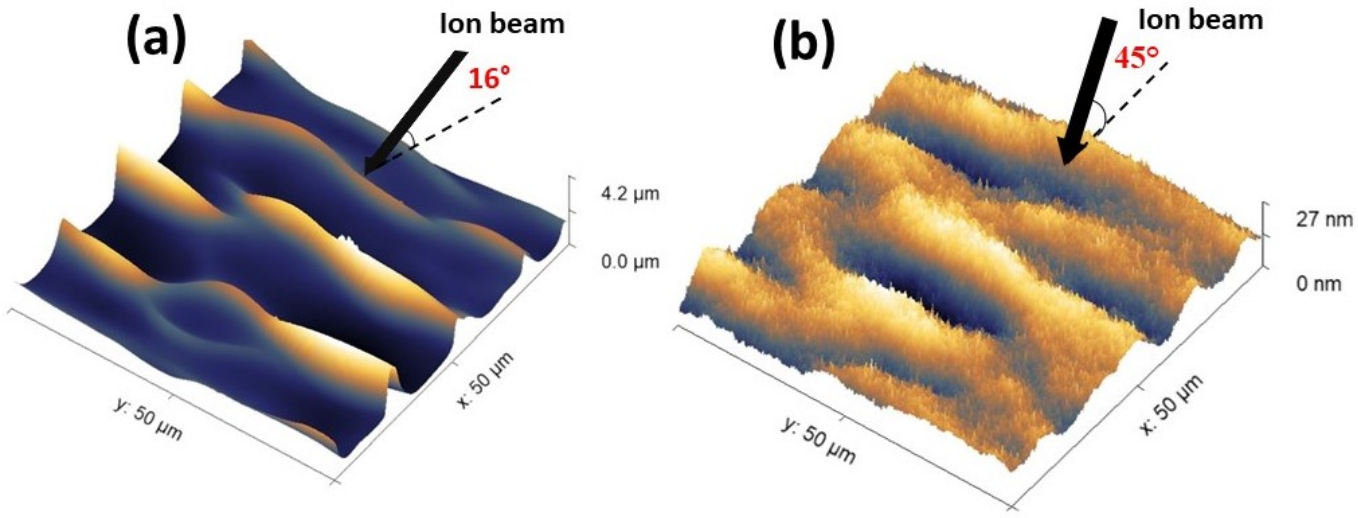

Figure 11: Images AFM de $SrTiO_3$ (100) irradié avec 92 MeV d'ions de Xe à une fluence de 4×10^{14} ions cm^{-2} à 45.7° (a) et 16° (b).

Irradiation croisée

Au cours du premier temps de faisceau, certains échantillons de $SrTiO_3$ de direction cristallographique (110) ont été irradiés avec des ions de Xe d'énergie 74 MeV à une fluence de 1.41×10^{14} ions cm^{-2} et à un angle de 8.1°. La figure 12(a) montre une image AFM de la surface après irradiation, où l'on observe la formation d'ondes secondaires perpendiculaires à la direction du faisceau d'ions (indiquée par la flèche noire). La structure périodique est confirmée par la présence de deux points distincts dans la transformée de Fourier 2D correspondante, ce qui

donne une périodicité de $\lambda \sim 5$ µm.
La surface amorphe ayant tendance à se réorganiser en une structure perpendiculaire au faisceau d'ions, il était intéressant de voir l'effet d'une irradiation croisée. Ainsi, après la première irradiation, une rotation de l'échantillon de 90° a été effectuée et une seconde irradiation a été réalisée.
La seconde irradiation a été effectuée avec des ions de Xénon d'énergie légèrement différente (92 MeV) mais toujours dans la même gamme d'énergie et toujours au-dessus du seuil de perte d'énergie électronique nécessaire à l'amorphisation. l'irradiation a été faite avec une fluence de 5.86×10^{13} ions cm^{-2} et un angle de 3.5°.
La différence d'angle et de fluence est due au fait qu'un peu plus d'un an s'est écoulé entre les deux irradiations et que des corrections ont été apportées entre-temps en calculant l'erreur d'angle. Par conséquent, la valeur de la fluence perçue par l'échantillon change également.

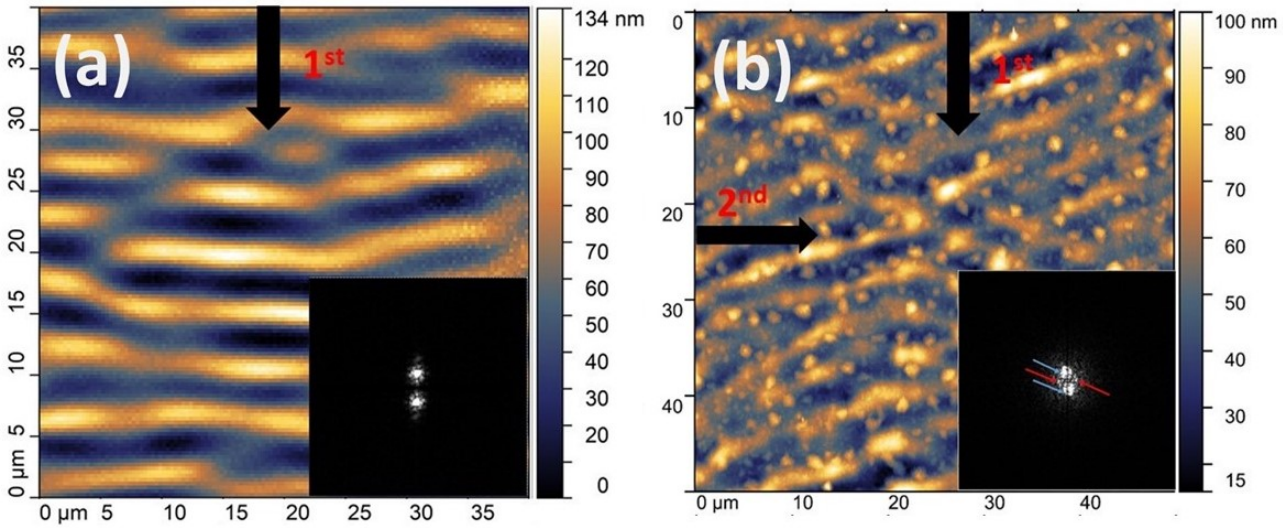

Figure 12: Images AFM de $SrTiO_3$ (110) irradié avec 0.55 MeV/u $^{136}Xe^{19+}$, $\phi = 1.41 \times 10^{14}$ ions cm^{-2} et $\theta = 8.1°$ (a), seconde irradiation avec 0.71 MeV/u $^{129}Xe^{23+}$, $\phi = 5.86 \times 10^{13}$ ions cm^{-2} et $\theta = 3°$, ainsi que la transformée de Fourier correspondante.

Afin d'avoir un point de comparaison fixe et d'éliminer les effets de l'énergie et de la fluence, qui sont différents dans les deux cas, le dépôt d'énergie total en ions keV cm^{-3} a été calculé. Cette opération a été réalisée à l'aide de la formule suivante : $E_d = Se \times$ fluence. Cela permet d'obtenir une énergie totale déposée pour la première et la deuxième irradiation d'environ 2.2×10^{22} ions keV cm^{-3} et 1.2×10^{22} ions keV cm^{-3}, respectivement.
L'analyse de la transformée de Fourier 2D de l'échantillon après la deuxième irradiation montre 4 points (voir figure 12 (b)). Les deux points indiqués par les flèches bleues de la première structure périodique semblent avoir subi une légère rotation. La périodicité dans ce cas est d'environ 5.5µm. De légers pics latéraux peuvent être identifiés (indiqués par les flèches rouges), indiquant la présence d'une structure périodique perpendiculaire au second faisceau d'ions et parallèle au premier. Ces pics donnent également une périodicité d'environ 5 µm.
L'apparition d'une deuxième paire de pics, indiquant la formation d'une structure secondaire, se

produit à la suite de la deuxième irradiation. Cette seconde irradiation agit sur la surface amorphe, non pas en réorientant (à proprement parler) les structures déjà formées, mais en annihilant la première structure et en forçant la surface à se réorganiser perpendiculairement à la direction du deuxième faisceau d'ions. Sur l'image AFM, on constate qu'à certains endroits, les ondes commencent à se briser/se fissurer, tendant à s'incliner par rapport à leur axe initial. On suppose que, comme l'énergie déposée lors de la deuxième irradiation est plus faible que lors de la première irradiation et que l'angle d'incidence est également plus faible pour la deuxième irradiation (3.5°) que pour la première (8.1°), la formation des ondes perpendiculaires au deuxième faisceau n'est pas complète, car l'énergie n'est pas assez pour forcer la dissipation totale de la première irradiation.

Mécanisme

Afin de comprendre le mécanisme derrière cette réorganisation de la surface en une structure ondulatoire périodique, une analyse générale de ce qui se produit lors de l'interaction d'un ion énergétique avec un matériau doit être revue. Comme nous l'avons expliqué précédemment, lorsque des ions énergétiques traversent des matériaux solides, une série d'interactions et de processus se produisent, en fonction de l'énergie du projectile et donc de la perte d'énergie dans le matériau. Deux processus d'interaction principaux peuvent se produire : des collisions élastiques avec les atomes de la cible (régime nucléaire), ou des collisions inélastiques avec les électrons de la cible (régime électronique). Il en résulte des déplacements atomiques, des cascades de déplacements, du désordre, des ionisations ou des excitations électroniques. Générant ainsi des modifications structurales pouvant aller jusqu'à l'amorphisation en surface du matériau et en profondeur, le long du trajet de l'ion, pour les faisceaux d'ions de haute énergie. Dans ce dernier cas, la perte d'énergie électronique est le processus de ralentissement dominant et la trajectoire du projectile est au départ plutôt rectiligne. L'énergie transférée aux électrons par l'ion incident est rapidement transmise aux autres électrons par des interactions électron-électron, puis aux atomes du réseau par des interactions électron-phonon. Ceci va conduire à une augmentation brutale de la température dans un cylindre de quelques nanomètres de diamètre autour de la trajectoire de l'ion, donnant lieu à une éventuelle fusion de ce cylindre. Ce dernier subira ensuite une phase de refroidissement en dissipant sa chaleur vers le reste de la cible par conductivité thermique. Quant à la fin du parcours de l'ion dans le matériau, les collisions nucléaires dominent et donnent lieu à des cascades de déplacement.

Des études faites sur des systèmes de couches minces, en particulier des oxydes métalliques tels que NiO [22,23], ont montré la formation de ce type de structure appelée « lamelle ». Pour expliquer leur formation en surface, une combinaison de deux processus complémentaires a été proposée. Tout d'abord, une fissuration périodique de la surface normale à la direction du faisceau d'ions est créée en raison de l'instabilité de Grinfeld [24] [25]. Ensuite, la fusion et la resolidification du matériau dans la région cylindrique créent des contraintes le long de la trajectoire de l'ion [15,26], ce qui peut induire une instabilité de la surface dans la couche de NiO. Lorsque cette contrainte dépasse la résistance de la surface à la rupture, des fissures périodiques peuvent apparaître dans le film. Il est suggéré que cette étape est suivie par une déformation plastique anisotrope (c'est-à-dire

l'effet Hammering [27–29]) qui explique l'évolution de ces fissures en structures lamellaires.
Il convient toutefois de souligner que dans notre cas, la situation est différente de celle décrite précédemment. Dans notre étude, un monocristal est utilisé sans couche mince déposée à la surface.
De plus, nous n'avons remarqué aucune à la surface, même après une irradiation à des fluences élevées. La diffraction des rayons X confirme même que le matériau reste dans un régime de déformation élastique. La question est donc de comprendre comment l'énergie extrêmement localisée déposée par les ions incidents peut induire l'auto-organisation observée à la surface d'un isolant monocristallin tel que le $SrTiO_3$.

Pendant l'irradiation du $SrTiO_3$ aux ions lourds rapides, les traces amorphes individuelles se chevauchent à mesure que la fluence augmente, ce qui conduit à la formation d'une couche amorphe d'une épaisseur de quelques micromètres (la taille varie avec la géométrie de l'angle d'irradiation). Suivie en profondeur par une couche cristalline désordonnée et, très profondément, par la matrice cristalline non irradiée (voir 4). La densité des matériaux amorphes est généralement inférieure à celle de leurs homologues cristallins.
Les valeurs rapportées pour le titanate de strontium ($SrTiO_3$) amorphe et cristallin sont respectivement de 4.2 $g\,cm^{-3}$ et de 5.1 $g\,cm^{-3}$ [22]. Pour les monocristaux de $SrTiO_3$, les propriétés mécaniques telles que le module de Young dépendent des directions cristallines. On peut néanmoins définir un module de Young moyen de 260-300 GPa. En ce qui concerne le $SrTiO_3$ amorphe, des résultats récents obtenus par nanoindentation donnent un module de Young compris entre 190 et 210 GPa [30]. Cette différence de module de Young entre la phase amorphe et le cristal n'est pas surprenante, puisque la première a une densité plus faible et que sa structure peut être considérée comme moins rigide que la phase cristalline.
D'après cette constatation et les résultats fournis par les observations au MET, nous nous trouvons dans une situation où nous avons une couche amorphe "molle" (d'une épaisseur d'environ un micromètre) sur un substrat cristallin plus rigide. On peut donc s'attendre à une expansion de la couche amorphe par rapport aux dimensions d'origine (gonflement) causée par le changement de densité induit par l'irradiation. Cependant, comme cette couche amorphe est liée au substrat cristallin, seule la dimension normale à la surface est libre de se dilater. En revanche, dans les deux autres dimensions, la couche amorphe est limitée et doit s'adapter au substrat cristallin. Cela peut induire la formation de rides à la surface afin de minimiser l'énergie du système. Au cours des irradiations suivantes, toute protubérance à la surface de l'échantillon (qui est déjà amorphe) sera soumise à une déformation plastique anisotrope, qui diminuera la dimension parallèle à la direction du faisceau et augmentera celle qui lui est perpendiculaire. Ces structures quasi-périodiques (vagues) orientées perpendiculairement au faisceau d'ions auront donc tendance à évoluer au fur et à mesure de l'irradiation, ce qui a été clairement observé dans cette étude, notamment avec l'augmentation de la hauteur et la réduction de la largeur avec l'augmentation de la fluence. Ceci est schématisé sur la figure 13.

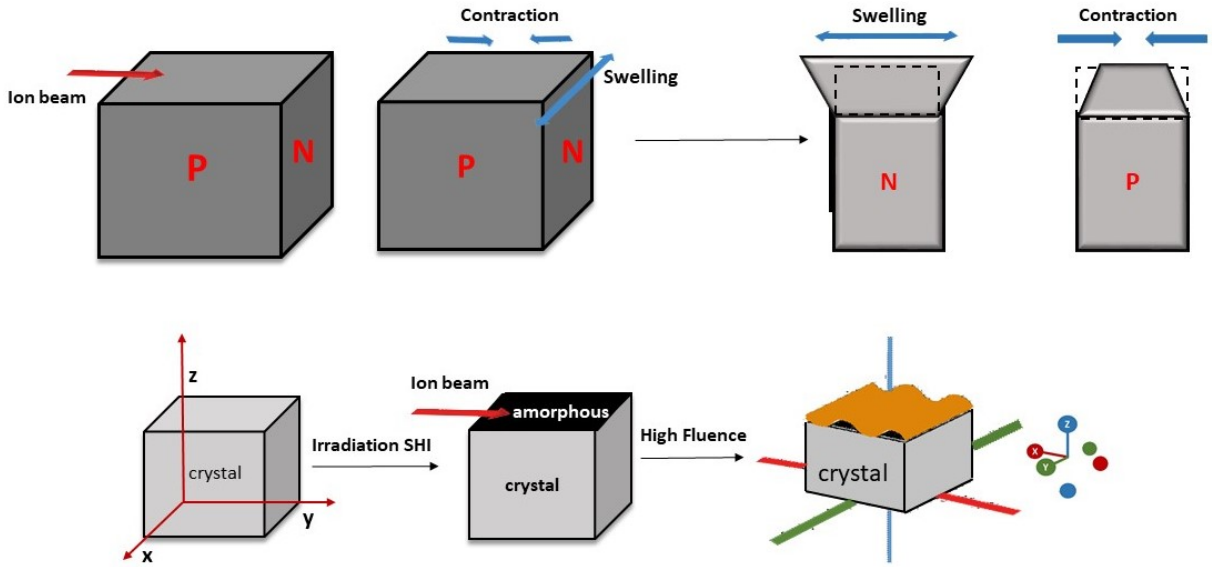

Figure 13: Illustration montrant l'effet Hammering attendu (a) dans le cas d'un échantillon amorphe, avec l'expansion attendue de la dimension perpendiculaire au faisceau d'ions (représentée ici par N) et la contraction des dimensions parallèles au faisceau d'ions (face P) et (b) dans le cas d'un film amorphe sur une couche cristalline. La couche amorphe formée à la surface est liée au substrat cristallin, elle est contrainte selon les dimensions x et y, et seule la dimension normale à la surface est libre de se dilater, d'où le développement des ondes. La direction du faisceau d'ions est indiquée par la flèche rouge

Matériaux 2D

Dans cette seconde partie de l'étude, on s'intéresse à l'impact de l'irradiation par ions lourds rapides (SHI) sur les couches de MoS_2 obtenues par dépôt chimique en phase vapeur (CVD) sur différents substrats. L'étude se concentre sur l'influence de divers facteurs tels que le type de substrat, les paramètres d'irradiation (angle d'incidence du faisceau d'ions, fluence) et l'orientation des pastilles de MoS_2 sur la probabilité de pliage. L'introduction de défauts dans les matériaux 2D affecte significativement leurs propriétés électriques, chimiques et luminescentes, élargissant ainsi leurs applications potentielles, comme catalyseurs ou membranes. Le choix du substrat influence également les propriétés des matériaux 2D et leur capacité à être utilisés dans diverses applications. Des études sur la croissance de MoS_2 sur $SrTiO_3$ ont montré une influence significative de l'interface sur les propriétés optiques et mécaniques [31].
Contrôler les défauts générés par l'irradiation aux ions est crucial pour déverrouiller le potentiel d'application des matériaux 2D. Des études montrent que l'irradiation par ions lourds conduit à des comportements uniques dans le MoS_2 par rapport au graphène. En utilisant des paramètres d'irradiation spécifiques, il est possible de réguler le pliage dans le MoS_2. Ainsi, il sera question ici de faire une étude sur l'impact de l'irradiation aux ions sur le MoS_2, en utilisant deux substrats différents et en évaluant l'influence de certains paramètres d'irradiation sur la formation de plis dans le matériau.

La spectroscopie Raman a été utilisée pour caractériser les échantillons de MoS_2 avant et après irradiation. Cette technique permet d'identifier différentes propriétés telles que le nombre de couches, les densités de défauts et les concentrations de porteurs de charge sans endommager les matériaux. Dans le cas de MoS_2 déposé sur un substrat de $SrTiO_3$, la détection des pics de MoS_2 est compliquée car ils sont masqués par les vibrations plus fortes du substrat ($SrTiO_3$), rendant difficile l'analyse de l'effet de l'irradiation sur les monocouches de MoS_2.
Le pic de photoluminescence (PL) étant sensible à la concentration de défauts dans le matériau, il peut être utilisé pour quantifier les défauts créés dans la structure cristalline du MoS_2 en fonction des paramètres d'irradiation. Le pic de la photoluminescence a montré une diminution de l'intensité avec l'augmentation de l'angle d'irradiation vers la normale de la surface, accompagnée d'un déplacement des pics vers des valeurs de fréquence plus basses. Une analyse du rapport des pics de photoluminescence (PL) avant et après irradiation a été réalisée et est présentée dans la figure 14. Lorsque l'angle d'incidence du faisceau d'ions augmente vers la normale à la surface, le rapport des pics de PL diminue jusqu'à ce qu'il atteigne une limite autour de $\theta = 1.2°$, où il augmente à nouveau. Cette diminution d'intensité suggère une augmentation de la densité des défauts. La microscopie à force atomique a été utilisée pour confirmer cette hypothèse. Cependant, il est nécessaire de réaliser d'autres séries d'irradiations pour obtenir une analyse précise des effets observés. Notamment par rapport à l'augmentation du rapport à des angles supérieurs à 2°.

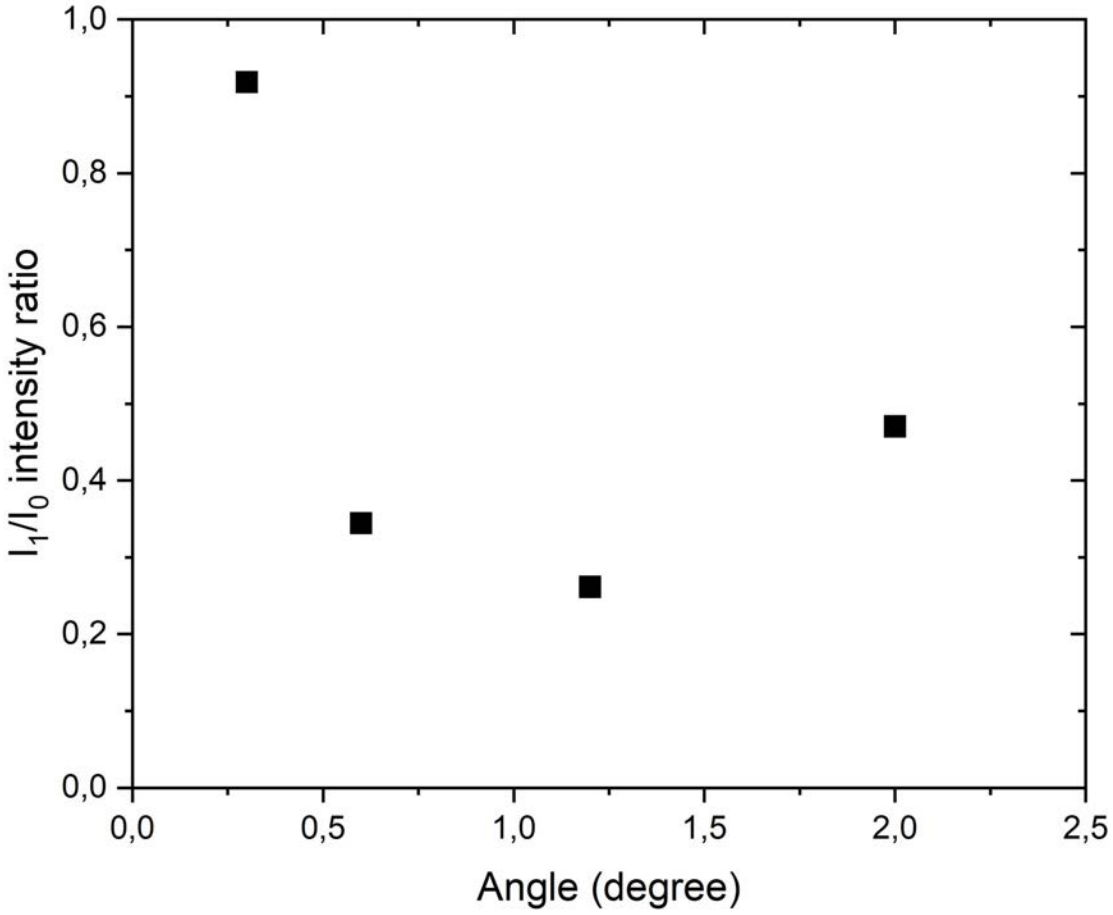

Figure 14: Rapport d'intensité I_1/I_0 du pic PL de $MoS_2/SrTiO_3$ irradié avec 5×10^9 ions cm^{-2} en fonction de l'angle d'irradiation.

La recherche met en évidence le comportement unique du MoS_2 par rapport au graphène en ce qui concerne l'introduction de défauts/structures de surface et la formation de plis. Il est noté que le pliage dans le MoS_2 est influencé par des facteurs spécifiques, notamment l'orientation des monocouches de MoS_2 par rapport à la direction du faisceau d'ions. Cette orientation est définie par la bordure des pastilles de monocouches de MoS_2.
L'étude traite également de l'impact de l'irradiation sur les spectres Raman du MoS_2, indiquant des changements dans les modes vibrationnels et la présence d'une déformation compressive induite par l'irradiation ionique. En outre, l'étude présente l'effet des angles d'irradiation sur la morphologie de la couche de MoS_2, avec des observations spécifiques liées à la densité de pliage et au chevauchement des plis à différents angles d'irradiation. Ces résultats contribuent à une meilleure compréhension du comportement du MoS_2 sous irradiation aux ions lourds rapides et de ses applications potentielles.

Analyse des surfaces de MoS_2 au microscope à forme atomique (AFM)

Analyse de monocouches de MoS_2 déposés sur du titanate de strontium

Dans cette étude, une série d'échantillons de MoS_2 déposés par CVD sur du $SrTiO_3$ monocristallin ont été irradiés avec des angles variant de 0.3° à 2° à une fluence de 5×10^9 ions cm^{-2}. Les observations effectuées par microscopie à force atomique (AFM) sur les défauts induits à la surface montrent des plis de différentes formes, tailles et orientations par rapport à la direction du faisceau d'ions. La taille et la forme des plis dépendent de l'angle d'incidence du faisceau d'ions et du type de substrat utilisé. La figure 15 montre une sélection d'images pour deux échantillons irradiés à 0.3° (a-b) et 0.6° (c-d). On constate la présence de pliage dans les deux cas.
Des études antérieures ont rapporté la résistance au pliage du MoS_2/SiO_2 après une irradiation aux ions lourds rapides à des angles rasants. Des structures en forme de incisions ont été observées dans la plupart des cas, ou des plis accompagnés de incisions, et ont conclu que pour obtenir des plis, l'axe cristallin du MoS_2 devait former un angle de 30° (ou son multiple) par rapport à la trajectoire des ions lourds [9] [32]. Cependant, dans cette étude, des pliages sont observés indépendamment de l'orientation des monocouches de MoS_2, et cette limitation associée à l'orientation de l'axe cristallin semble être contournée en utilisant le titanate de strontium comme substrat, forçant d'une certaine manière la formation de plis.

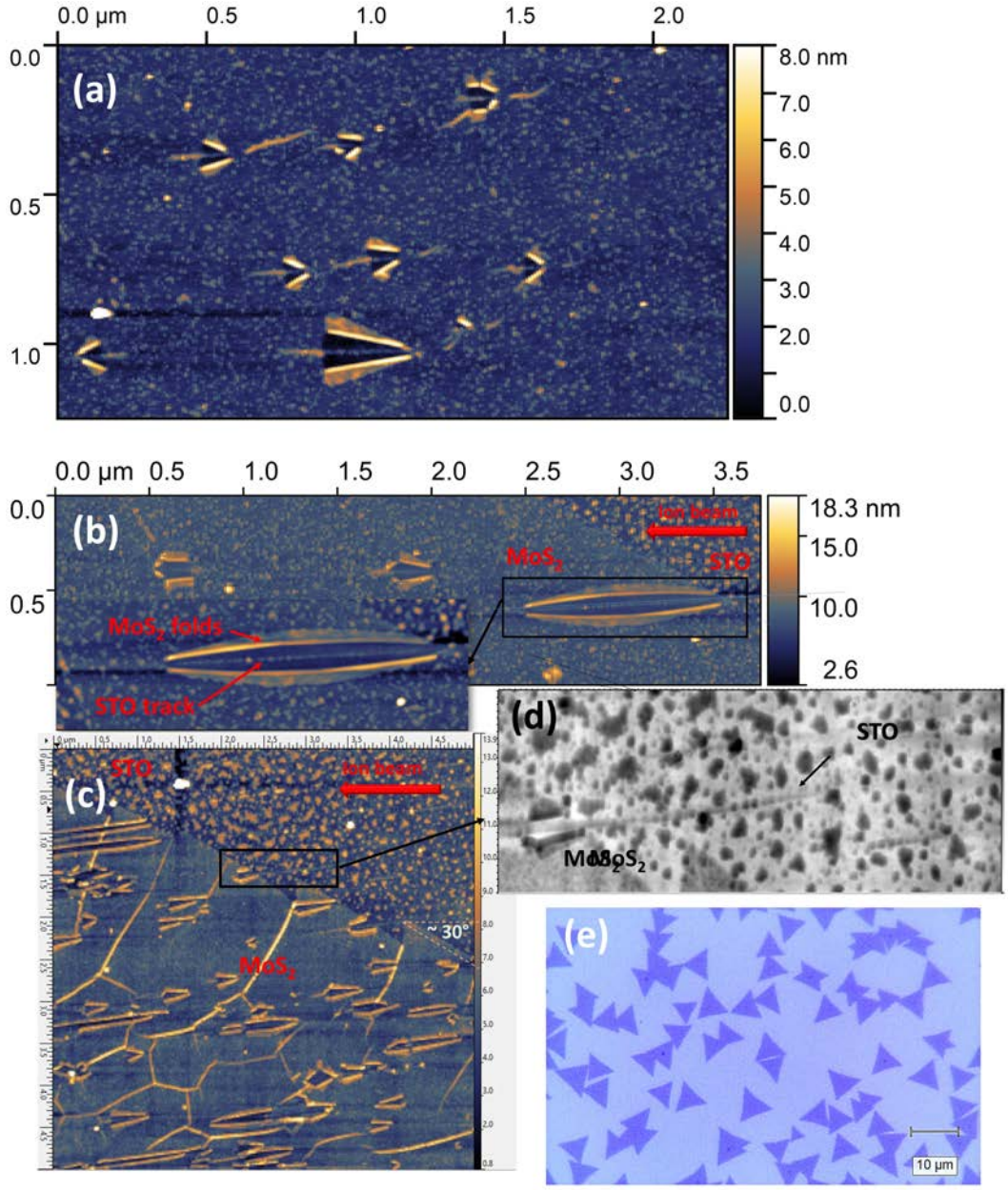

Figure 15: Images AFM de MoS_2/SiO_2 irradié avec des ions Xe de 92 MeV avec $\phi = 5 \times 10^9$ ions cm^{-2} à $\theta = 0.3°$ (a-b) 0.6° (c-d); En (f) une image au microscope optique où les pastilles de monocouches de MoS_2 sont dispersées sur la surface du substrat.

On observe que la quantité de pliage augmente avec l'augmentation de l'angle d'irradiation. D'après les images analysées, une diminution de l'angle d'incidence vers la surface entraîne une augmentation de la longueur des plis. Des plis de différentes formes et longueurs peuvent apparaître dans certaines circonstances, possiblement dus à des défauts préexistants dans le substrat ou dans le matériau 2D, influençant ainsi la direction et la forme du pliage.

Analyse de monocouches de MoS_2 déposés sur du $\alpha - SiO_2$

Une série d'échantillons de monocouches de MoS_2 déposés sur des substrats SiO_2/Si ont été soumis à une irradiation aux ions sous différents angles. Les propriétés structurales ont été analysées à l'aide de la spectroscopie Raman et de la photoluminescence, ainsi que par microscopie à force atomique (AFM).
Les résultats de la spectroscopie Raman ont montré un décalage vers des fréquences plus élevées des pics de vibration caractéristiques du MoS_2 suite à une irradiation à faible fluence. Ce décalage est interprété comme étant dû à la présence d'une contrainte compressive dans le matériau, causée par la création de défauts.
Parallèlement, l'analyse de la photoluminescence a montré une diminution progressive de l'intensité du pic de photoluminescence à mesure que l'angle d'irradiation augmentait vers la normale à la surface. Cette diminution d'intensité est typique d'une augmentation des défauts dans la structure cristalline. De plus, la largeur et la hauteur des pics de photoluminescence ont augmenté avec l'angle d'irradiation jusqu'à 0,6°, puis ont commencé à diminuer pour des angles plus importants, suggérant une plus grande sensibilité de la structure à des angles très rasants par rapport à des angles d'irradiation plus élevés. L'ensemble de ces échantillons a également été analysé par AFM pour examiner les effets des irradiations sur la structure de la surface.

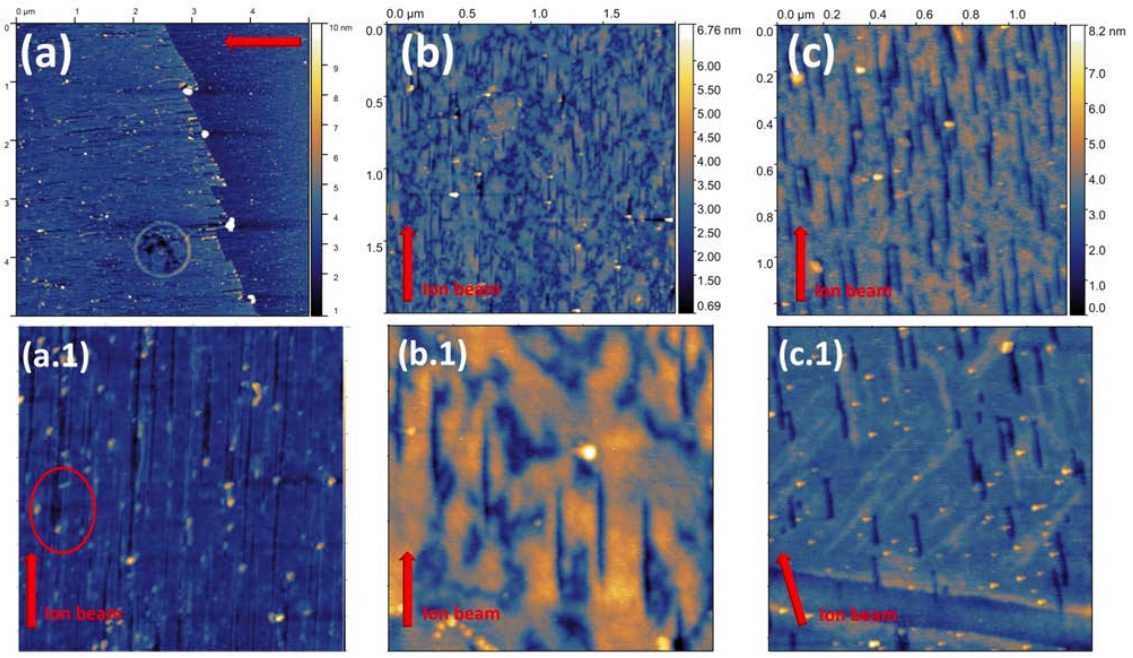

Figure 16: Images AFM de MoS_2/SiO_2 irradié avec des ions Xe de 92 MeV avec $\phi = 5 \times 10^9$ ions cm^{-2} à $\theta = 0.6°$ (a-a.1) 1.2° (b-b.1) et 2°(c-c.1).

À un angle d'irradiation de 0.3°, aucune formation de défauts n'a été observée sur la surface du MoS_2. En revanche, à des angles de 0.6°, 1.2° et 2°, des incisions lisses orientées dans la direction

du faisceau d'ions ont été observées. Ces incisions nanostructurées se forment tandis que la surface environnante demeure plane.
Lorsque le MoS_2 est irradié sur du $SrTiO_3$, cela conduit à la formation de plis, tandis que sur du SiO_2 amorphe, des incisions droites et lisses se forment, toujours orientées dans la direction du faisceau d'ions. Cette différence montre l'impact majeur du substrat sur la formation des défauts de surface.

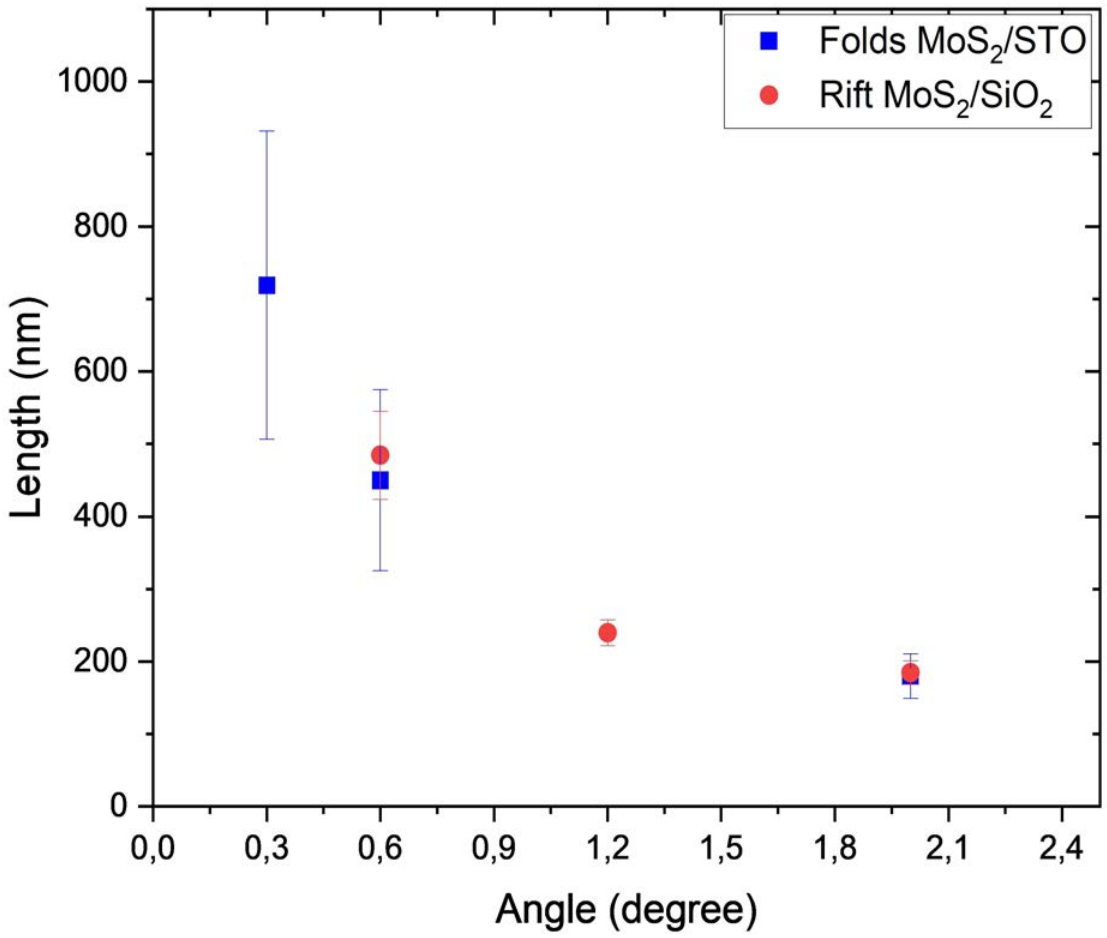

Figure 17: Mesure expérimentale de la longueur des plis (carré bleu) et de la longueur des incisions (cercle rouge) dans une monocouche de MoS_2 induite par une irradiation d'ions lourds radides (91 MeV Xe) sous différents angles d'irradiation.

La figure 17 montre l'évolution de la longueur des modifications (pliage et incision) en fonction de l'angle d'incidence du faisceau d'ions. On observe une diminution de la longueur des modifications avec l'augmentation de l'angle d'irradiation. Akcöltekin et al. [6] ont développé une équation géométrique : L = d/tan(θ) qui montre la relation entre la longueur des défauts et l'angle d'irradiation. L est la longueur du pliage/incision, θ est l'angle d'incidence du faisceau d'ions par rapport à la surface de l'échantillon, et d désigne la distance (mesurée perpendiculairement à la

surface) à partir de laquelle la surface est encore sensible au passage des ions, entraînant un changement morphologique observable en surface. Cette formule peut être utilisée pour calculer la valeur de d dans chaque cas. Pour $MoS_2/SrTiO_3$, d = (4.71 ± 0.94) nm, tandis que pour MoS_2/SiO_2, d = (3 ± 1.34) nm. Dans les deux cas, d est supérieur à l'épaisseur d'une seule couche de MoS_2, ce qui signifie que l'ion traverse la couche de MoS_2 et s'arrête à une certaine profondeur dans le substrat. Il est donc évident que l'effet des ions sur la surface, qui se traduit par la formation d'incisions et de plis, est le résultat d'un couplage entre un effet intrinsèque du matériau 2D et un effet dans le substrat pouvant être ressenti sur le matériau 2D.
Le système MoS_2 et $SrTiO_3$ a attiré une attention considérable en raison des propriétés attrayantes des deux matériaux. Contrairement aux substrats SiO_2, l'utilisation du $SrTiO_3$ comme substrat permet la création de plis de longueurs variables sans conditions d'orientation cristallographique spécifique. Cela met également en évidence l'impact du substrat et démontre qu'il constitue un atout majeur pour la création de défauts.

Introduction

Materials science research fields play a crucial role in the development of various technological applications. Through fundamental research, both experimental and theoretical, scientists aim to enhance the potential application of different materials. They strive to understand the properties and behaviors of materials at the atomic and molecular level, enabling them to design and engineer novel materials with improved performance, sustainability, and cost-effectiveness. One area of this field focuses on the nano- and micro-structuring of surfaces, as they offer new opportunities for controlling surface properties, such as wettability, adhesion, electrical and optical properties. These surface modifications can have a significant impact on the performance and functionality of materials in various applications, including energy storage, catalysis and biomedical devices.

In this context, in the recent years, ion beam technologies, which involve exposing the material to ion bombardment, have emerged as a promising tools for surface nano-structuring and defect engineering. This approach, along with other innovative techniques, allows for the manipulation of materials at the atomic and nanoscale level, resulting in materials with enhanced functionalities and performance. In recent years, various facilities around the world have made it possible to carry out irradiations with ions of different species over a wide energy range from keV to GeV. During the ion journey through the target, several interactions take place before the ion looses its energy and comes to rest within the material. These interactions include collisions with electrons and nuclei of the target material which result in energy loss through nuclear and electronic processes. In the case of swift heavy ions the interaction happens mainly with the target electronic subsystem, until the ion slows down at the end of its trajectory, where ionisation is no longer possible. The ion, then, interacts with the target atoms through elastic nuclear collisions. Irradiation with ions of energies greater than 0.1 MeV/u gives rise to various modifications ranging from defects to amorphisation. In many solids, and provided the threshold electronic energy loss (dE/dx) is reached, this results in the formation of an amorphous cylindrical track of few nanometers diameter in the bulk. It can also induce surface reorganisation and the formation of ordered nanostructures on the surface. To tailor the functionality of different materials, an understanding and knowledge of the response of materials to swift heavy ion irradiation is essential.

The aim of this research is to investigate the effect of irradiation by swift heavy ions (SHI)

when a grazing incidence geometry is used. The irradiation angle extends from the surface normal, decreasing until grazing incidence. Irradiation with the latter geometry leads to localised energy loss near the surface, resulting in elongated surface defects. These structures arise from the ions direct impact on the surface. The objective is also to examine the multiple ion impact effect on $SrTiO_3$, then use it as a substrate for 2D materials and irradiate them with swift heavy ions to highlight the effect of the substrate and the irradiation parameters on the formation of structural and morphological defects on the surface.

The structure of the thesis is as follows: The first chapter covers the fundamentals of matter-ion interaction. A presentation of the relevant processes and parameters involved during the collisions between the projectile ion and the target will be given. Additionally, the impact of irradiation on the target materials, alongside the models that describe the passage of the ion into the material, will be presented.

Chapter two will provide a description of the materials used in this study, specifically strontium titanate $SrTiO_3$ (STO) and molybdenum disulphide (MoS_2). It will cover the various modifications that have been observed upon exposure to swift heavy ion irradiation.
Besides the characterization methods—atomic force microscopy (AFM), X-ray diffraction (XRD), and Raman spectroscopy—that were employed to investigate the materials,the experimental setup used in this investigation is presented, with special emphasis on the GANIL-IRRSUD irradiation beamline with a description of the irradiation procedure used.

The third chapter is dedicated to the presentation of experimental results obtained on strontium titanate of two distinct crystallographic directions (100) (110) irradiated with two different ion beams, namely 0.55 MeV/u $^{136}Xe^{19+}$ and 0.71 MeV/u $^{129}Xe^{23+}$. An emphasis on the difference between low-fluence irradiation, where the single-ion impact dominates, and higher fluences, which result in tracks overlapping, will be presented.

The fourth chapter follows on from the study carried out in chapter three, investigating the effect of the fluence on the modification of the strontium titanate (STO) surface. Intermediate fluences are used to investigate the evolution of the surface wave-like structure obtained.

The last chapter presents the results obtained on MoS_2 deposited by CVD on strontium titanate crystalline substrates when subjected to swift heavy ion irradiation at grazing incidence geometry. The modification observed will be compared to MoS_2 samples deposited on a different kind of substrate, namely, the amorphous silicon dioxide (SiO_2).

Chapter I

State of the art

Introduction

When a solid material is bombarded with charged particles, several processes take place. Given that two systems are involved, the target material where the defects occur and the projectile ion that creates the defects through the various collisions along its path, it is essential to study and analyse the effects of the irradiation, in which all the components of the system must be treated and described.

As the ions pass through the material, a series of interactions with the target components take place. The continuous transfer of their energy to the target induces atomic displacements, displacement cascades, disorders, ionisations, or electronic excitations before it comes to rest at a certain depth, leaving behind some permanent defects. Depending on the irradiation parameters, structural modifications up to amorphization can be induced along the ion path, at the surface, and in the depth of the material (for the high energy ions). To understand what happens to matter during irradiation, one should look at the sequence of events(when it's possible) and the various parameters involved. Therefore, in this chapter, a description of the different aspects of the ion-matter interaction will be given, as well as the main characteristics and parameters of the ion-matter interaction. Since Swift Heavy Ions (SHI) are used, a particular attention will be given to this type of ion beam and the type of changes it can cause in solid targets.

Two processes can describe the transfer of energy from the ion to the material and the subsequent slowing down that occurs:

• Elastic collisions associated with nuclear shocks:
When the incident particle has a kinetic energy of less than 10 keV/u, this energy is transferred directly to the nucleus of the target atoms, inducing defects in all sorts of targets (insulators, metals, etc.). Since the electron configuration of the projectile ion and the target do not undergo large changes during the interaction, the latter can be considered and treated as a Coulomb interaction. In the case of heavy ions, their velocity is much greater than that of the target atoms, so the latter are considered immobile.
In this regime, the various deviations of atoms resulting from the ion-atom collision and the formation of defects (point defects and cascade defects) give rise to effects on the volume of the material under consideration. This leads to structural changes (swelling, phase transformation, or amorphization) [33].

• Inelastic collisions linked to electronic excitations:
In this case, the energy loss causing the slowing down of the incident ion results from its inelastic interaction with the electronic cloud of the target atoms. This process, which is dominant at high energies (> 100 keV/u) leads in an indirectly way to the formation of defects due to the electronic

excitations or even the ionisations of atoms in the vicinity of the incident ion trajectory. This type of collision, in which the total kinetic energy is no longer conserved, is particularly effective in the case of modifying insulators or metals. In contrast to nuclear collisions, here the ion follows an almost straight path, so its deflection is negligible.

Although these two energy loss processes coexist, the importance of one or the other depends not only on the nature of the projectile and the irradiation parameters, such as their energy, but also on the nature of the target.

1 Relevant parameters of the ion-matter interaction

As many parameters are involved in heavy ion irradiation, the most important ones will be discussed first, and then the most relevant ones will be detailed, i.e. stopping power and velocity.

- Fluence (F): This is the total number of particles received by the target per unit area, generally expressed in ions cm^{-2}.

$$F = \int_0^t \phi \, dt \tag{I.1}$$

- The flux (ϕ) or fluence rate: Corresponds to the number of ions sent to the target per unit area and unit time ions cm^{-2} s^{-1}

$$\phi = \frac{d\phi}{dt} \tag{I.2}$$

1.1 The stopping power of the projectile

When an ion interacts with matter, it transfers its energy to the target as it passes through the material via the various collisions. This amount of energy lost by the ion is an important parameter from the point of view of the target and the damage processes induced by irradiation. The parameter describing this amount of energy lost through both nuclear and electron collisions is called the "stopping power" and is denoted by (S).

This linear energy loss along the ion trajectory is described by the following equation:

$$S_{n.e} = -\left(\frac{dE}{dx}\right)_{n.e} \tag{I.3}$$

Where E represents the energy of the ion, x is the penetration of the ion into the solid. n and e are nuclear and electronic energy losses respectively.

This energy loss, generally expressed in keV/nm, is characteristic not only of the projectile ion and its energy, but also of the nature of the material through which it passes. As this value

represents an energy loss, a minus sign has been added to the equation.

Depending on the type of projectiles used, its characteristics determine the predominance of the collisional process involved. There are two different types of contributions: electronic stopping power and nuclear stopping power.

1.1.1 Nuclear stopping power

The nuclear energy loss is noted $S_n = -(dE/dx)_n$. In this category, during irradiation an indirect interaction between two bodies is considered. If the velocity of the projectile ion v_1 is greater than that of the target $v_2 (v_1 >> v_2)$, the target nuclei are considered to be at rest. This means that the electronic configuration of both the ion and the target remains unchanged. Allowing a treatment according to the laws of classical mechanics.

The ion-atom interaction is described in this case by the collision cross section (σ). This parameter describes the probability of an energy transfer from the projectile to the target during the interaction between the two.
According to classical Rutherford scattering, an ion of mass M_1 and atomic number Z_1 interacting with the target with kinetic energy E_1 and displacing an atom of mass M_2 and atomic number Z_2 after an energy transfer T, can be described by the collision cross section as follows [34] :

$$\sigma(E_1, T_1) = \pi \frac{(Z_1 Z_2 e^2)^2 M_1}{T^2 E_1 M_2} \tag{I.4}$$

where $e^2 = 1.44 \times 10^{-7} \text{eV.cm}^{-1}$.
Knowing that the kinetic energy transferred to the target is given by:

$$T = T_{max} \sin^2 \frac{\theta}{2} \tag{I.5}$$

Where θ is the angle of deflection of the projectile after the impact and T_{max} is the maximum energy transferred in the case of a frontal impact and expressed by:

$$T_{max} = \frac{4 M_1 M_2}{(M_1 + M_2)^2} E_1 \tag{I.6}$$

The energy loss resulting from the collisions of the ion along its path is given by:

$$-\left(\frac{dE}{dx}\right)_n = N \int_{T_{min}}^{T_{max}} T \sigma(E_1 T) dT \tag{I.7}$$

Where N represents the atomic density of the target, T_{min} and T_{max} are respectively the minimum energy (greater than zero, introduced to avoid divergence of the integral) and the maximum energy delivered during the nuclear collision between the two particles.

The potential involved in this interaction can vary depending on the velocity of the projectile relative to that of the target electrons. Ranging from a purely Coulomb interaction at high velocities, as a result, the energy loss will be given by :

$$-\left(\frac{dE}{dx}\right)_n = 2\pi N \frac{M_1(Z_1 Z_2 e^2)^2}{M_2 E_1} ln \frac{T_{max}}{T_{min}} \tag{I.8}$$

To low velocities, where the screening effect is significant.

Since in this study the interactions are considered as Coulomb interactions partially screened by the electrons of the projectile ion and the target atom. That is to say, in the case of intermediate velocities, the previous formula must be modified to take into account the effect of the electron cloud of the target and projectile atoms on the screening of the nuclei.

From the Thomas-Fermi potential, J.P. Biersack [35] gives an analytical expression of the nuclear stopping power:

$$-\left(\frac{dE}{dx}\right)_n = 4\pi N a \times \left(\frac{M_1}{M_1 + M_2}\right) \times Z_1 Z_2 e^2 \times \frac{ln\epsilon}{2\epsilon(1-\epsilon^c)} \tag{I.9}$$

With the constant $c = -1.49$ and $\epsilon = a/r_m^0 = [M_2/(M_1 + M_2)] \times [(E \times a)/(Z_1 Z_2 e^2)]$ where a is the screen radius and r_m^0 is the collision diameter.

1.1.2 Electronic stopping power

In contrast to elastic interactions, which are treated as a binary system where the energy loss is purely nuclear. Inelastic interactions involve many more particles, as the projectile ion interacts with several electrons in the target simultaneously. These electron collisions cause the ion to lose energy and, therefore, to slow down in matter to finally come to rest at the end of its trajectory. As a result, the kinetic energy is no longer conserved as the two electron configurations change through the various processes of excitation, ionisations, and electron capture.

As a result, the state of charge Z_1 changes. Bohr then proposed the following formula to calculate the effective charge Z_1*, which depends on the velocity of the projectile:

$$\frac{Z_1^*}{Z_1} = \frac{v}{v_0 Z_1^{\frac{2}{3}}} \tag{I.10}$$

Z_1^* represents the effective charge of the ion and Z_1 the atomic number of the ion. v_0 is the Bohr velocity (orbital velocity of the electron of the hydrogen atom), i.e. $v_0 = E^2/\hbar = 2.2 \times 10^6 m/s$

The electronic stopping power of ions varies according to the velocity of the projectile and therefore depending its effective charge. Three different velocity ranges are considered through the quantity $v_0 \times Z_1^{\frac{2}{3}}$ in order to obtain the electronic stopping power.

1.1.3 Projectile velocity

High-velocity $v > v_0 Z_1^{\frac{2}{3}}$ At high energies, the ion is completely stripped of its electrons and interacts with the target electrons through a purely coulombic potential. The Bethe-Bloch formula gives the electronic stopping power in this regime [36]:

$$-\left(\frac{dE}{dx}\right)_e = \frac{4\pi e^4 N}{m_e}\frac{Z_1^2 Z_2}{v^2} ln \frac{2m_e v^2}{I} \tag{I.11}$$

Where m_e is the mass of the electron, I is the average ionisation potential of the target atoms and N is the atomic density of the target.

Thus, in this range, $Se = -(dE/dx)_e$ is inversely proportional to the velocity of the ion and therefore to its energy :

$$-\left(\frac{dE}{dx}\right)_e \propto \frac{1}{v_1^2}.$$

As a result, the energy loss decreases as the velocity/energy of the projectile increases.

Note that this formula was developed for projectiles with high velocities and is therefore not valid for the GANIL heavy ions used in this thesis, whose velocity is close to the electron velocity, corresponding then to the intermediate velocity range.

Intermediate velocity regime $v \approx v_0 Z_1^{\frac{2}{3}}$ In this intermediate velocity regime, the ion has a velocity comparable to that of the electrons in the system (ion-atom). Two processes compete in this case: electron capture and ionisation of the target. As a result, the incident ion is no longer completely snatched, and its charge state fluctuates around the equilibrium state. Bethe's formula is then no longer suitable, as the stopping power becomes weaker than it predicts. Barkas [37] proposed an empirical formula for an effective charge Z_1^* to replace the charge Z in order to extend the range of validity of this formula.

$$Z_1^* = Z_1(1 - \exp\frac{-125\beta}{Z_1^{\frac{2}{3}}}) \tag{I.12}$$

where $\beta = v/c_1$

In this case, the energy deposition reaches a maximum, called the Bragg peak.

Low velocity regime $v < v_0 Z_1^{\frac{2}{3}}$ In this low velocity regime and during the interaction of the incident ion with the target atom, the ion keeps the majority of its electrons. By considering the formation of a quasi-molecule resulting from the overlapping of the electronic clouds of the components of the ion-solid system, two models have been proposed to calculate the electronic stopping power, namely the model of O.B. Firsov [38] and the model of Lindhard, Scharff, and

Shiott [12] (LSS theory).

Firsov formula :

$$-\left(\frac{dE}{dx}\right)_e = N_A \times 5,15 \times (Z_1 + Z_2) \times 10^{-15} \frac{v}{v_0} \tag{I.13}$$

Lindhard and Scharff formula:

$$-\left(\frac{dE}{dx}\right)_e = 8\pi e^2 a_0 N \frac{Z_1^{7/6} Z_2}{\left(Z_1^{2/3} + Z_2^{2/3}\right)^{3/2}} \frac{v}{v_0} \tag{I.14}$$

This formula can be expressed as a function of the kinetic energy of the incident ion:

$$-\left(\frac{dE}{dx}\right)_e = \frac{8\sqrt{2}\pi e^2 a_0 N}{v_0} \frac{Z_1^{7/6} Z_2}{\sqrt{M_1}\left(Z_1^{2/3} + Z_2^{2/3}\right)^{3/2}} E^{1/2} \tag{I.15}$$

Where Z_1 and Z_2 represent the atomic numbers of the ion and target, respectively. N is the atomic density of the target, a_0 is the Bohr radius ($a_0 = 0,529$Å) and M_1 is the mass of the ion.

It should be noted that the above formulas make it possible to obtain electronic stopping power values that are still relatively far from the experimental values. However, according to these two approaches and the two resulting equations, the electronic stopping power depends on the velocity of the incident ion and, therefore, on its energy. which means :

$$-\left(\frac{dE}{dx}\right)_e \propto v$$

The total energy loss is obtained by summing the nuclear (Sn) and electronic (Se) stopping powers:

$$-\left(\frac{dE}{dx}\right)_t = -\left(\frac{dE}{dx}\right)_e + -\left(\frac{dE}{dx}\right)_n \tag{I.16}$$

As mentioned above, during the interaction of the projectile ion with the target, its speed decreases continuously as a result of the energy loss (nuclear/electronic) that it undergoes along its trajectory, to finally at the end of its path finds itself implanted in matter.

Thanks to the total stopping power, the ion range (R), which is by definition the distance travelled by the projectile ion in the solid, can be determined by :

$$R = \int_{E_0}^{0} \frac{1}{\frac{dE}{dx}} dE \tag{I.17}$$

E_0 is the initial kinetic energy of the incident ion.

Since the projectile is constantly colliding with the target atoms, it is deflected from its trajectory and therefore follows a random path rather than a straight line. This is why the projected range (Rp) is most commonly used. This parameter corresponds to the projection of the ion's path onto its initial direction and represents the distance that the ion has travelled in the material. One can explain this as the ion penetration depth into the material measured from the surface. In the inelastic electronic collision regime, the ion trajectory can be considered rectilinear. However, in this study and as will be shown later, swift heavy ions (SHI) represent the main type of ion beam used in this thesis. These ions then follow a quasi-rectilinear trajectory at the beginning, where electronic energy loss predominates, to give way to nuclear energy loss at the end of the trajectory.

2 SRIM/TRIM calculation

The various parameters characterising the ion-atom interaction, such as the stopping power and the projected range of the ions, can be estimated using the SRIM2013 simulation software [1] based on the Monte-Carlo model, for different energies and for different types of material.

This software has two interfaces. The first, SRIM (for the stopping and range of ions in Matter), provides the following information for a given ion and target: stopping powers (electronic Se and nuclear Sn), projected ion range (Rp) and straggling (square root of the variance of Rp) as a function of ion energy. The second interface, called TRIM (for the transport of ions in matter), simulates the trajectory of the ion in the target and therefore provides the 3D distribution of the ion as a function of depth.

During this study, the SRIM/TRIM software was used to calculate the electronic and nuclear stopping power values of the various ions used. Considering the energy and mass of the incident ion and the characteristics of the various atoms composing the target material. I.1 shows the electronic and nuclear energy losses in the case of $SrTiO_3$ irradiated with $^{129}Xe^{23+}$ ions. The mass density was set at $5.117\,\mathrm{g\,cm^{-3}}$, during the calculation.

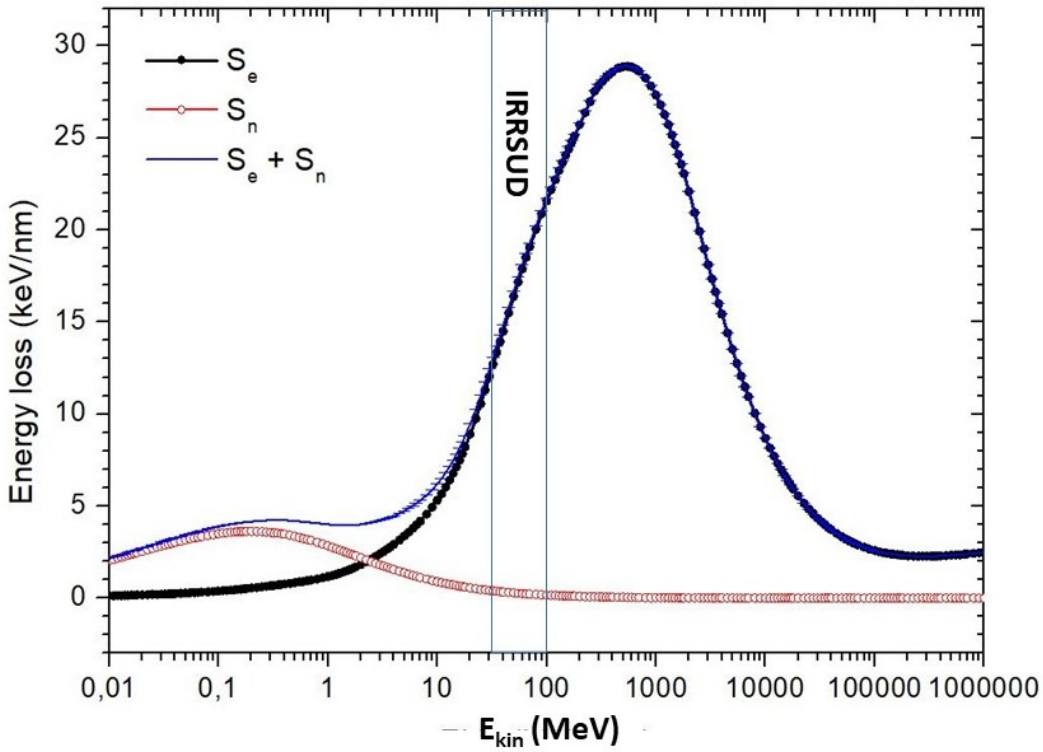

Figure I.1: Evolution of the nuclear and electronic stopping power in the case of $SrTiO_3$ irradiated with xenon ions, calculated with the SRIM code [1]

In this study, swift heavy ions (SHI) of Xenon with energies between 0.5 and 0.7 MeV/u of Xenon were used. As can be seen in figure I.1, in this energy range the energy loss is mainly due to electron collisions, then at the end of the path the nuclear energy loss dominates. The specific nature of this type of beam and the kind of modifications that can be induced will be described in more detail later in this manuscript.

3 Effect of the irradiation on the target material

In the previous section, a description of the impact of ion-solid interaction from the point of view of the projectile was given. In the following, the effects of irradiation will be examined from the target's point of view.

The characteristics of the defects that an ion can cause in a material depend not only on the irradiation parameters associated with the ion, such as energy loss, velocity, charge, etc., but also on the nature of the solid and therefore on its electronic structure.
Materials that are sensitive to radiolysis (polymers, silica, etc.) are damaged even by low-ionising radiation (X-rays, etc.) and there is no damage threshold on which the appearance of defects depends. However, very few studies have been carried out on this range of materials. In the case of materials that are insensitive to radiolysis, i.e. metals, semiconductors, and some oxides,

the defect formation process depends on both the electronic structure of the material and the various parameters associated with the projectile (energy loss, velocity, and charge of the ion). This introduces what is known as the electronic stopping power $(dE/dx)_e$ threshold, above which the material is damaged. The changes induced depend on the collision system involved in the interaction. Two processes can be distinguished: nuclear collisions, which induce the movement of solid atoms, and electronic collisions, which induce ionisation or excitation.

3.1 Modification of materials by elastic collisions

In the case of a nuclear collision, provided there is sufficient energy transfer, i.e. greater than the threshold energy for moving the target atoms E_d, the energy transmitted by the incident ion to the target atoms causes them to move from their sites. This causes either:

• Frenkel defect (interstitial-vacancy pairs) $N_d = 1$ if $E_d < E < 2E_d$.

• Or (if the energy is high enough) $E > 2E_d$, the ejection of the atom, generally called the "primary". This atom can, in turn, collide with other atoms and cause them to move (collision cascades). $N_d = E/2E_d$.

• In the case where $E < E_d$ the energy transfer causes thermal agitation of the target atom without moving it ($N_d = 0$).

Where E is the energy received by the primary atom and N_d the number of atoms displaced in the solid, described using the Kinchin and Pease relation [39].
These displacements, therefore, lead to the formation of point defects. This damage is often represented by the parameter "dpa", which is the number of displacements per atom. Using the TRIM simulation and knowing the displacement energies E_d of the target elements, one can obtain the vacancies as a function of depth.
In the case of a target with different components, the sum of the vacancies created must first be determined:

$$N(x) = \sum_{j=1}^{n} N_j(x) \tag{I.18}$$

$N_j(x)$ represents the number of gaps in atom j created at depth x.
For a given fluence and using the atomic density of the target, the distribution of atomic displacements as a function of depth can be determined:

$$dpa(x) = \varphi \times \frac{N(x)10^8}{\rho} \tag{I.19}$$

Where ρ is the atomic density of the corresponding material, expressed in atm cm^{-3} ,φ is the fluence in ions cm^{-2} and N(x) is the total number of displacements (vacancies) per incident ion and unit depth expressed in vac $ions^{-1}$ cm^{-1}.
The dpa expressed by vac atm^{-1} in our case varies with the depth of penetration of the ion into the material. This parameter will be used later to characterise the damage caused by elastic collisions (nuclear interaction).

3.2 Modification of materials by inelastic collisions

Unlike nuclear collisions, in inelastic collisions, the transfer of energy is mainly done by indirect and complex processes. When a swift heavy ion ($0.1 MeV.u^{-1}$) with an electronic stopping power greater than keV/nm penetrates a solid, the energy is transferred mainly by collision with the target's electron system. This induces ionisation and local excitations along and around the trajectory of the projectile. While in insulators and semiconductors structural defects can be created, and unless there are ions with a very high electronic stopping power, in non-radiolysable materials such as certain metals, the energy is more likely to be dissipated as thermal energy, thus preventing the formation of structural defects [34].

This strong local perturbation resulting from the ionisation density combined with an electronic energy loss threshold (depending on the type of material) gives rise to the creation of continuous or discontinuous structural defects of different sizes. These defects, which occur around the ion trajectory where the material is disordered or amorphous, are known as "tracks" or "latent tracks" with a diameter of a few nanometers and which depend on the specificity of the material and the speed of the ion. Interest in this area began around the 1950s with Young reporting tracks from fission fragments in LiF [40], followed by the first transmission electron microscopy observation of fission tracks in mica by Silk and Barnes [41].

In addition to local electronic excitations, there is also a dependence on the velocity of the projectile. In fact, the radial extent of the energy deposit in the vicinity of the ion trajectory increases with velocity [42]. Thus, the formation of the tracks and their size in the target depend on the spatial energy distribution around the trajectory of the projectile. A. Meftah et al. [5] observed a difference in the size of the defects created at low and high velocities in ferrimagnetic yttrium iron garnet Y_3FeO_{12}. Figure I.2 shows the evolution of the effective radius ($R_e = \sqrt[2]{(A\pi)}$) of the tracks created in two different speed regimes. Their study shows, in comparison with a previous low-energy study, that for the same electronic stopping power (Se), the effective trace radius (R_e) is larger at low energy due to the more localised energy deposition around the ion trajectory than at high energy.
On the right of the figure, one can see the morphology of the damage created. Beyond a threshold of electronic stopping power and following the accumulation, the damage appears in different ways and evolves with the passage from spherical discontinuous tracks along the trajectory of the ion to a continuous cylindrical structure (track) following the deposition of electronic energy, whose diameter depends strongly on the velocity of the projectile.

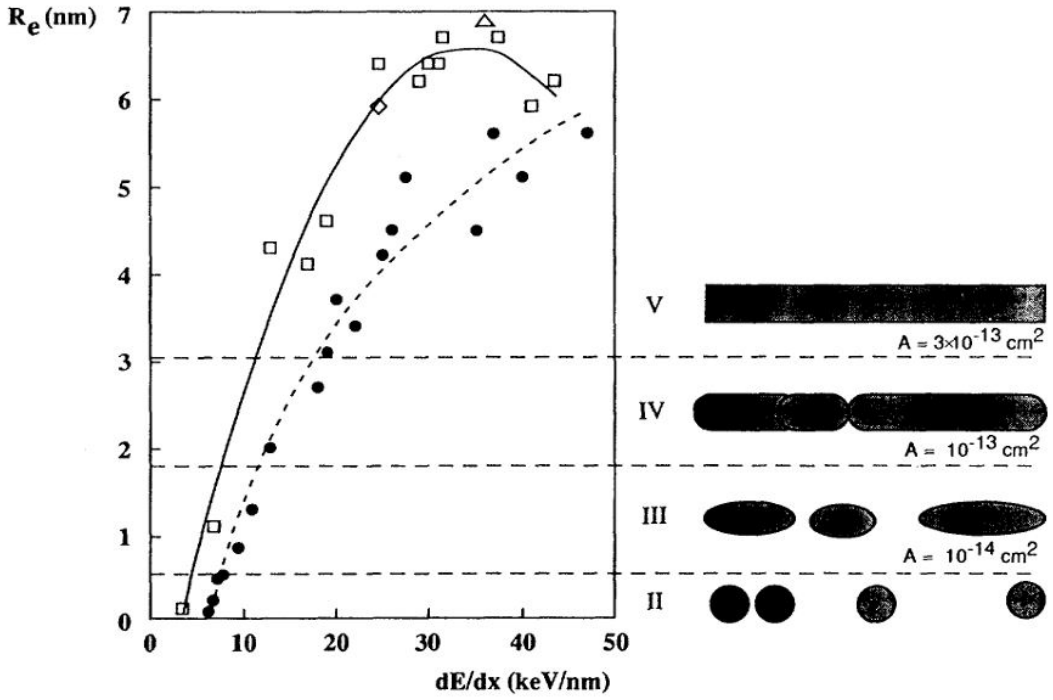

Figure I.2: Evolution of the effective radius R_e of tracks formed in Y_3FeO_{12} as a function of the electronic energy loss $(dE/dx)_e$. The black symbols correspond to the high-velocity regime, while the white squares correspond to the low-velocity regime [5]. The corresponding damage morphology is shown on the right, where several parts with different effective damage cross-section (A) are visible. In II: elongated, almost spherical defects are shown. In III: discontinuous and more elongated defects. In IV: cylindrical defects overlap to form an inhomogeneous cylinder. In V: as the electronic stopping power increases, the fragmented structures evolve to form a continuous form of amorphous material with homogeneous damage inside the cylinder. Note that the range of damage caused by nuclear collisions is not shown in the figure

The modification of materials by swift heavy ions and the formation of tracks have been the subject of various studies these last decades. Several characterization techniques have been used, ranging from Mössbauer spectroscopy, which is used to determine the effective radius, to Rutherford backscattering in channeling direction (RBS-C). However, the most widely used technique is transmission electron microscopy (TEM). With its high resolution, this technique allows the radius of the resulting track to be observed and measured directly [43] [44]. Damages induced by uranium fission fragments were first observed by TEM in mica in 1959 by Silk and Barnes [41]. Several studies followed, including chemical etching to reveal these tracks [45] and thus measure the effective radius. Provided there is a minimum of electronic energy, the formation of latent tracks is highly dependent on the irradiated material. In general, these amorphous tracks are easily formed in insulators, including oxides, ceramics, or organic materials, (SiO_2, mica, etc.) and take the form of a cylinder surrounded by a crystalline matrix [46].

In addition to the importance of the irradiation parameters mentioned above for the formation of defects and tracks, another parameter is also important, namely the excitation lifetime. When an ion collides with a solid, it transfers its energy to the target electrons, which can only convert this energy into atomic motion if the lifetime of the excited states is long enough to cause damage in the region around the ion trajectory.

3.2.1 Chronology of damage and track formation

Two processes can be distinguished in terms of time. The thermalization process, which lasts from 10^{-17} s to about 10^{-13} s. In this phase, the projectile's initial energy transfer to the target electron takes place within a radius of a few angstroms and induces ionisation and electronic excitation, generating γ electrons in a very short space of time. These excited electrons in turn collide with the electronic subsystem, resulting in a cascade of collisions within a radius of a few angstroms to a few microns. This energy distribution in the vicinity of the ion trajectory has led to the Coulomb explosion model to explain defect formation, which will be described in more detail later. Next comes the relaxation process, which involves the diffusion of electron energy to atoms in the heated lattice in the vicinity of the incident ion's trajectory between (10^{-13} – 10^{-12}s). This part will be treated with the thermal spike model. Then ($\geq$ 1 ps) the lattice cools down, freezing the formation of defects in a time lapse that differs from one material to another.

These different phases are summarised in the diagram I.3.

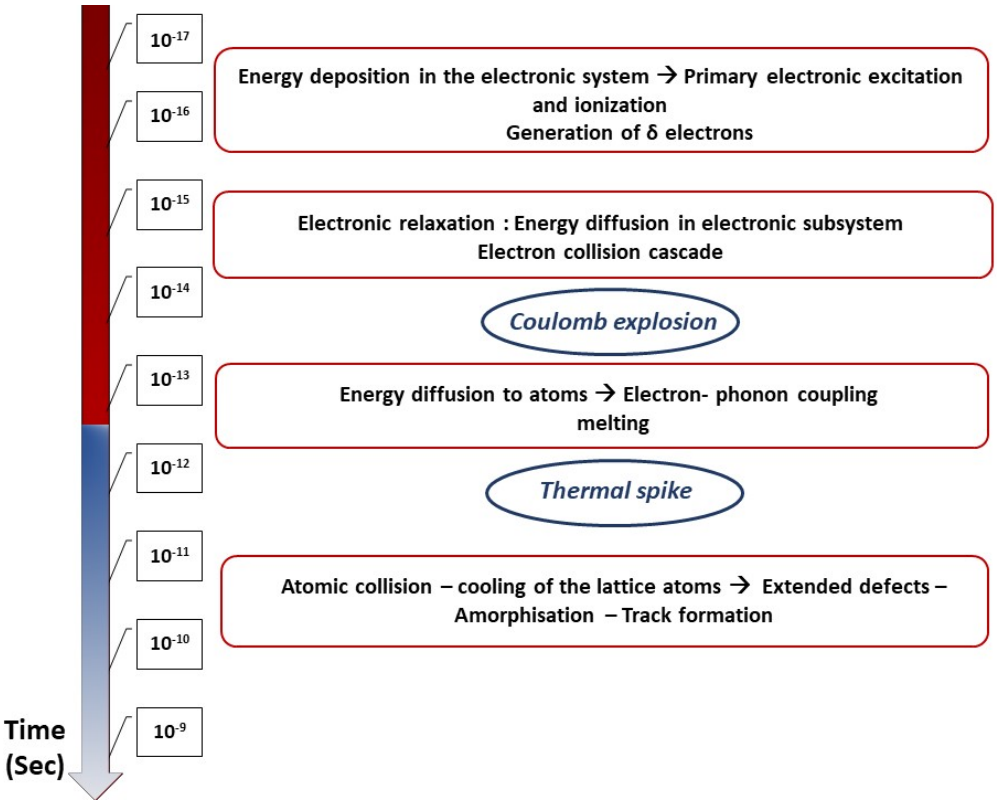

Figure I.3: Representation of the different processes involved in an ion-solid interaction that lead to the formation of the tracks

3.2.2 Ion-matter interaction models

The interpretation of the passage of the ion through the material and the transfer of energy that gives rise to structural modifications has been the subject of various studies. The mechanism of damage by electronic excitation is a complex process that is still poorly understood. Several models have been proposed to explain the processes involved in the formation of tracks in solids following irradiation with swift heavy ions. Two of them will be presented, namely the Coulomb explosion model [13] [47], which approaches the problem from the point of view of the positive charges generated along the ion trajectory, and the thermal spike model [14], which, unlike its predecessor, quantifies the effect of SHI by estimating the track radii, for example.

3.2.2.1 The Coulomb explosion model

Proposed by Fleischer, Price, and Walker [13] and extended by Lesueur and Dunlop [47], this model is based on the effect of the large electronic excitation that occurs when a high-energy ion penetrates a solid. The resulting ionisation along the ion path creates a positively charged region.

This causes a strong electrostatic repulsion between the positive ions, inducing a local explosion that results in the ejection of ions into the surrounding lattice. Atomic displacement can only be obtained if the screening time is greater than the vibration frequency of the atoms and a repulsive force exceeds a certain threshold, which depends on the elastic stiffness of the solid, i.e. its Young's modulus [13].
Knowing that the return time of the ejected electrons must be sufficiently long ($> 10^{-13}$s) to achieve atomic motion, this condition can only be met by insulators and semiconductors, unlike conductors, where the electron mobility is very high.

3.2.2.2 The thermal spike model

The thermal spike is a model that takes into account the amount of heat deposited locally as the ion passes through the material. This model was first proposed in 1923 by Desauer [15] and developed by Chadderton and Montagu-Pollock [22]. Seitz and Koehler [23], then, adapted it for other materials like metals. Several studies have followed on from this work, notably those by Meftah et al. [48] and Toulemonde [14] [16], who adapted the model to swift heavy ion irradiation (SHI). This approach assumes that the energy deposited by the projectile ion on the target electrons is transferred to the other electrons by electron-electron interactions and then transmitted to the target atoms by electron-phonon interactions. This means that the energy deposited in the electronic system is converted into heat by electron-phonon interaction in a time of between 10^{-14} – 10^{-12}s. This leads to an increase in temperature and potentially to melting of the region around and along the ion trajectory, which takes the form of a cylinder of a few nanometers in diameter. This is followed by a cooling phenomenon (cooling down) in a time > 100 ps. This heat is dissipated by transfer to the rest of the lattice through thermal conductivity, thus freezing this zone into a disordered or even amorphous structure (latent track).

The two-temperature model (TTM) [14] [49] [50] is used to calculate the resulting lattice temperatures by integrating an electron-phonon coupling parameter, using two heat diffusion equations for the electronic and phonon systems versus time t and space r:

Electrons :

$$C_e(T_e)\frac{\partial T_e}{\partial t} = \frac{1}{r}\frac{\partial}{\partial r}\left(rK_e(T_e)\frac{\partial T_e}{\partial r}\right) - g(T_e - T_a) + A(r,t) \tag{I.20}$$

Atoms :

$$C_a(T_a)\frac{\partial T_a}{\partial t} = \frac{1}{r}\frac{\partial}{\partial r}\left(rK_a(T_a)\frac{\partial T_a}{\partial r}\right) + g(T_e - T_a) \tag{I.21}$$

Where $C_{e,a}$ is the specific heat capacity, which is the heat capacity per unit volume, $K_{e,a}$ is the thermal conductivity, A(r) is the energy deposited into the electronic system, and g is the electron-phonon coupling. The thermal spike approach based on these two equations, also referred to as the inelastic thermal spike (i-TS) model [51] [52] [53] (as we refer to the thermal process acting in the inelastic collision process), has been used to explain the structural deformation leading to the formation of tracks in many types of materials, ranging from insulators [22] [54] and subsequently

developed for other materials [52] [53] [55] [56].

4 Swift heavy ions modifications

The development of large heavy-ion accelerators in the 1980s sparked interest in the scientific community, leading to extensive research in fields as diverse as materials science and biophysics [57] [26].
The growing interest in the science behind the synthesis, modification, and characterization of materials at nanometric and microscopic scales has led to the development of different types of ion beams, which differ in the type of ions used and their energies. In the case of swift heavy ions (SHI) (energy greater than 1 MeV/u), the ions have a velocity comparable to or greater than the Bohr velocity with a mass equal to or greater than that of carbon. As these ions penetrate the solid, they interact mainly with the target electrons resulting in electronic excitations and ionisations of the target atoms. As they slow down, the energy loss increases towards the Bragg maximum with a peak at energies around 1-3 MeV/u. The electronic stopping power (energy loss by inelastic collision) is dominant and varies from a few eV/nm to a few keV/nm, giving rise to nuclear energy loss at the end of the ion path, as shown in figure I.4.

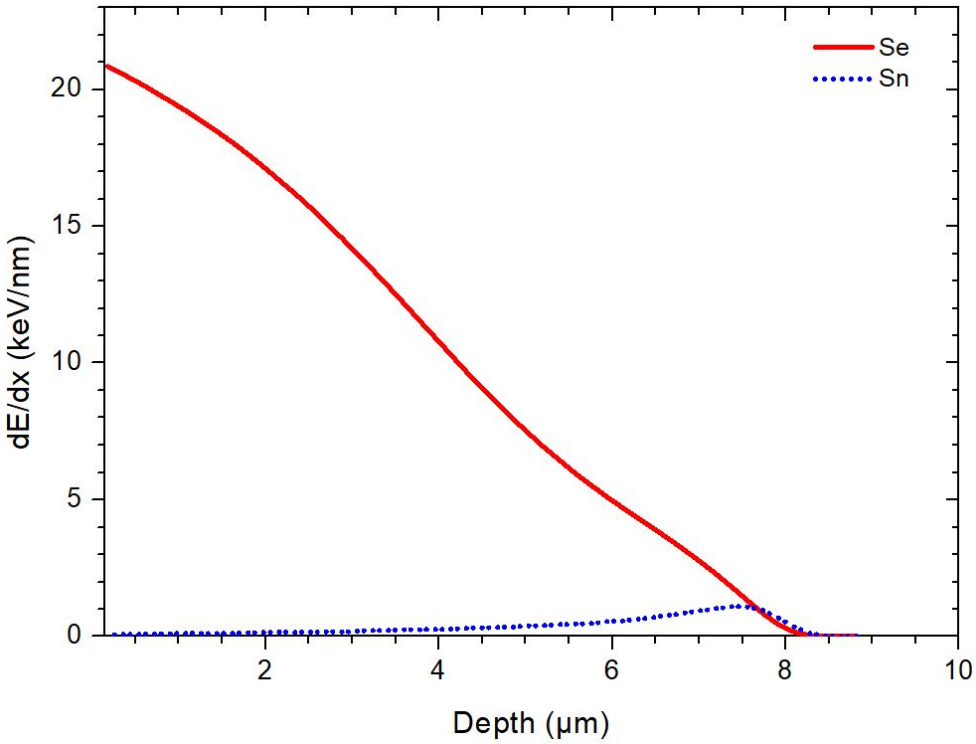

Figure I.4: Energy loss of 92 MeV Xe ions as a function of penetration depth in a monocrystalline $SrTiO_3$ obtained from SRIM calculations [1]. (Blue doted line represent nuclear energy loss and Red straight line represent Electronic energy loss)

Depending on the target materials, the mass of the projectile, and the experimental parameters, SHI irradiation can induce structural modifications at the surface as well as in the bulk of different varieties of targets. The energy deposited by the SHI in a volume around its trajectory, provided there is a certain threshold of electronic stopping power (S_e), can create a permanent cylindrical structure (track), which, depending on the material, may appear as an amorphous cylinder surrounded by a disordered crystalline area or integrated into the crystalline matrix. This threshold depends on the material and varies from 1 keV/nm for polymers up to a few tens of keV/nm for metals.
By adjusting the ion fluence and irradiation geometry, the energy deposited by the swift heavy ions in the electronic subsystem and the resulting high excitation can cause several and distinctly different types of modifications. In the low fluence regime, i.e. in the single ion impact regime, and under normal angles of incidence, each ion impact creates a track in the bulk [58]. Whereas, as shown in figure I.5 hillocks or crater-like structures can be created on the surface [59] [60] [61] [6].

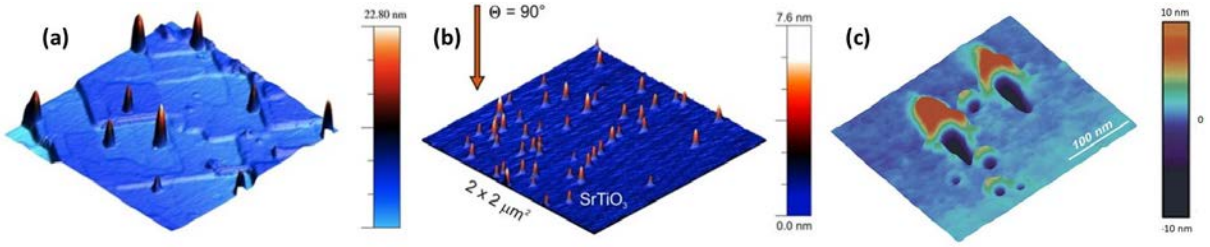

Figure I.5: 3D topography images of (a) cleaved LiF single crystal surface irradiated at $\theta = 90°$ with 93 MeV Xe ions and a fluence $5 \times 10^8 \text{cm}^{-2}$. (b) $SrTiO_3$ (100) surface irradiated under an angle of $\theta = 90°$ with 103 MeV ^{207}Pb ions [2]. (c) crater-like structures on PMMA film induced by 11.1 MeV/u Bi irradiation at different angles (0°, 45° and 79° to the surface normal) [3]
.

At a grazing angle, each ion creates a chain on the surface and in the direction of the ion beam [62] [6] [4]. These chains contain nanometer-sized hillocks that are periodically spaced. Figure I.6 shows some of the surface modifications discussed here and obtained after SHI irradiation.

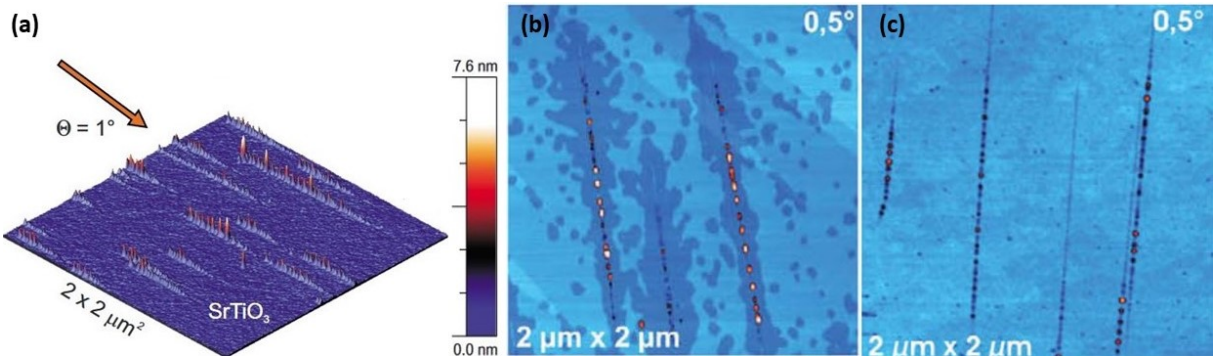

Figure I.6: AFM images of irradiated surfaces are shown in (a) a three-dimensional visualization of $SrTiO_3$ irradiated at $\theta = 1°$ with SHI. (b) Represent a CaF_2 surface irradiated with 103 MeV $^{131}Xe^{23+}$ and (c) TiO_2 irradiated with 103 MeV $^{207}Pb^{28+}$ both at $\theta = 0.5°$ [4] [2].

The chain of nano-hillocks on the surface was thought to be the projection of a part of the latent track localised into the bulk. It has been shown that, in addition to the nature of the material, irradiation parameters such as the angle of incidence have an effect on both the length of the chains and the distance between the individual hillocks forming the chains. The geometric formula for estimating and describing the angle/length relationship is given by: $L = d/\tan\theta$.
As the energy loss process is influenced by the anisotropy of the electronic structure, the distance between the nano-hillocks of a chain on the surface depends on the location of the electron density of the material and can therefore be changed by changing the angle of irradiation. Some theoretical calculations on oxidic surfaces such as $SrTiO_3$ [6] [17] [63] were performed, and they confirmed that the periodic nano-hillocks observed at the surface are influenced and can be considered as a direct projection of the three-dimensional electronic density of the target onto the surface. This can be applied to various insulating materials.
By increasing the fluence with a perpendicular incidence, the individual tracks overlap, and a surface amorphization is induced with the appearance of an amorphous layer of a few micrometres in thickness [18].
In the case of 2D materials, different kinds of modifications and defects can be created with a grazing incidence angle geometry. Incisions and folds are the most common defects induced [2] [64]. While chains of nanohillocks can be obtained in the MoS_2 bulk [64]. Their size, number and form can vary from one material to another and can therefore be controlled by varying different parameters, such as the angle of incidence, but also the surface preparation (mechanical exfoliation, chemical vapor deposition (CVD), etc.). These parameters play a key role in the characteristics of the modifications obtained, which can typically take the form of folding patterns for graphene prepared by CVD, whereas for MoS_2 this is not systematic, as certain conditions must be met. The impact of SHI on molybdenum disulphide (MoS_2) will be discussed in more detail in Chapter 2.

Chapter II

Materials and methods

1 Materials

1.1 Perovskite materials

Perovskites are materials that belong to a class of oxides sharing the same general formula, namely ABX_3. Investigated for the first time by Gustav Rose in 1839 and named after mineralogist LeV Aleksevich von Perovski [65]; It originally referred to the mineral $CaTiO_3$ (calcium titanate), whose properties and chemical composition were determined by Rose et al. [65]. The first of its sort to be discovered, and the name's genesis. This was followed by a series of synthesized perovskites whose structure can be composed of a variety of chemical components according to the following rule: A may be an alkali, alkaline earth, or rare earth, B a transition metal (both cations), and X represents oxygen, sulfur, or halogen (an anion). The physical properties of this perovskite oxide family are extremely diverse. This is why a growing amount of research is focusing on these materials. They can be employed in a variety of technological applications due to the various combinations that are conceivable and the ensuing variety of properties, such as piezoelectricity, ferroelectricity, superconductivity, etc. Since only $SrTiO_3$ (STO) is used in this study, a description of the oxide compounds will be limited to those with the general formula ABO_3.

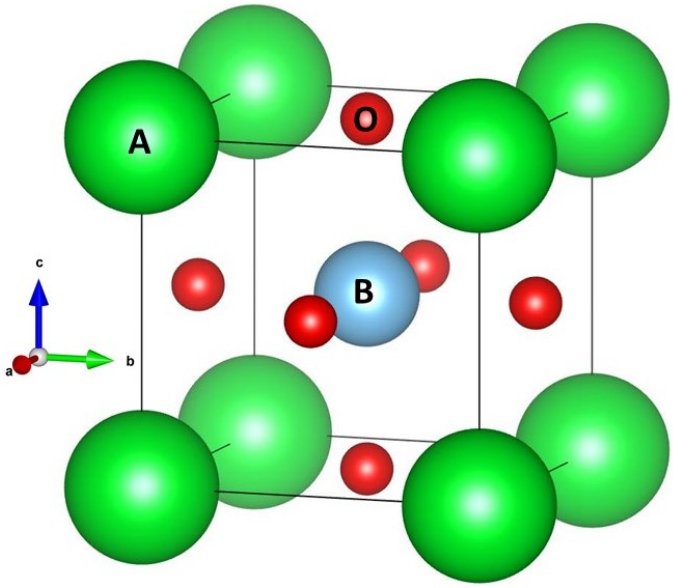

Figure II.1: Unit cell of the ABO_3 perovskite structure

Strontium titanate $SrTiO_3$-STO

$SrTiO_3$ is a ternary oxide perovskite-type inorganic material with a theoretical volumetric mass density of 5.117 g cm^{-3}. At ambient temperature and pressure, it has an ideal structure. It is known

to possess a wide bandgap of around 3.3 eV [66], making it for some an insulator and for others a remarkable semiconductor. It is described by a cubic lattice of space group $Pm\bar{3}m$ (n° 221). Its crystallographic structure consists of an alternating stack of neutrally charged SrO and TiO_2 layers spaced at 2.76 Å along the [001] crystal axis. This gives it interesting dielectric properties. It has a lattice parameter (a) of 3.905 Å [67] [68] with formal ionic charges of Sr^{2+}, Ti^{4+} and O^{2-}.
$SrTiO_3$ has been extensively studied due to its attractive properties, such as high charge storage capacity, thermoelectricity, chemical stability, low dielectric loss, and large dielectric constant at room temperature [69] [70]. These properties make it a crucial component in a vast array of applications, particularly in integrated microelectronics.
Numerous studies have been conducted on solar energy and photocatalytic water splitting for producing hydrogen [71–76]. However, a considerable challenge facing researchers is the reduction in the efficiency of its photoreaction due to its large bandgap, which affects the amount of solar energy absorbed in the ultraviolet (UV) spectrum [76]. Although this wide band gap allows for hydrogen production through photocatalytic water splitting, it can only do so in the ultraviolet range. For a more relevant application to water splitting in the visible light range, it is necessary to modulate these properties by, notably, reducing the band gap in order to broaden the range of application. Doping techniques are widely used to expand the optical absorption range [76–78]. When combined with very low temperatures, doping has shown superconductivity [79] [80]. Doping with specific electrically active species can also increase the concentration of free carriers. Controlling conductivity through doping also allows $SrTiO_3$ to expand its application range, for example as a metal oxide semiconductor field effect transistor (MOSFET), capacitor, etc. [81]. Regarding its dielectric permittivity, which is very high at room temperature, it shows significant growth when doping is combined with a temperature decrease, making this material highly attractive for microwave electronic devices [82].
With this in mind, ion irradiation is often used to induce doping, create defects, or nanostructures in $SrTiO_3$. The various defects and morphological modifications generated can affect different properties (optical, electrical, or mechanical) [83–85] by reducing, for example, the bandgap [86] aiming to enhance its performance for various applications, including optoelectronics, catalysis, energy storage, and sensors. One potential application of swift heavy ion irradiation on $SrTiO_3$ is the creation of waveguides or modification of its bandgap, leading to enhanced light absorption and emission properties [87]. An objective evaluation of such effects is necessary for further understanding and development in the field.

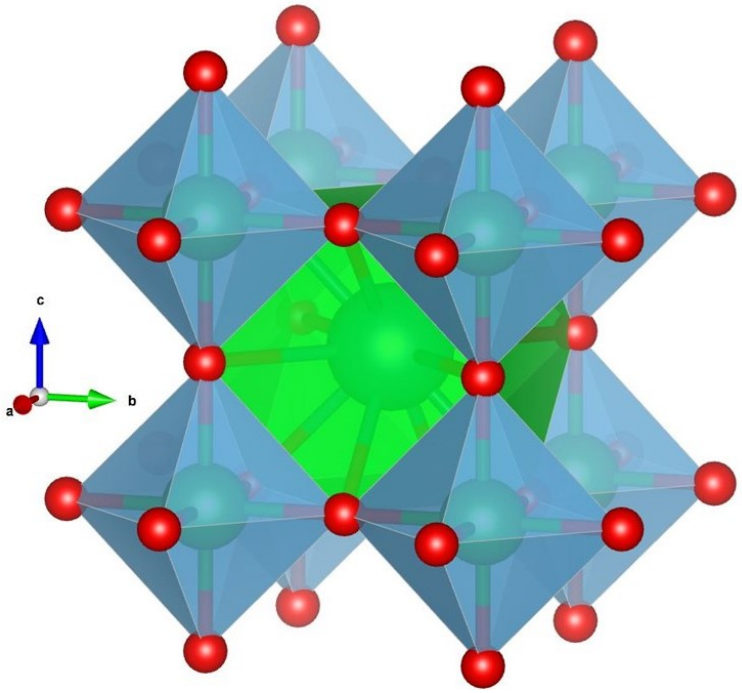

Figure II.2: Three-dimensional lattice of octahedra in $SrTiO_3$

As can be seen in Fig.II.2 its structure consists of a sequence of a three-dimensional Ti^{4+} linked to six oxygen atoms, with a Ti-O bond length equal to a/2, giving a length of 1.96Å, thus forming a corner-connected TiO_6 octahedra, represented in blue. Whereas the Sr atom is bonded to 12 oxygen atoms, forming a SrO_{12} cub-octahedra with a Sr-O bond length of around 2.7Å, represented in green.

In this thesis, a single-crystal, polished $SrTiO_3$ is used with two crystallographic direction, (100) and (110). The samples measure 5×5 mm^2 and 0.5 mm thick. They were bought from Crystec company in Germany.

1.2 The two-dimensional materials

Initially theorised to be thermodynamically unstable [88, 89], two-dimensional materials underwent a revolution after their experimental extraction by exfoliation by K. Novoselov and A. Geim in 2004 [90]. This discovery opened up a new technological frontier. They were able to generate graphene sheets with a thickness of the order of one atom by isolating a single layer of hexagonally aligned carbon atoms using an adhesive tape. This was followed by the investigation of additional 2D materials exhibiting high crystallographic quality, such as phosphorene, hexagonal boron nitride (hBN), and transition metal dichalcogenides (TMDs), e.g., molybdenum disulphide (MoS_2) and tungsten disulphide (WS_2), etc. This mechanical exfoliation can be performed on different substrates, whether crystalline or amorphous. It can also be suspended on membranes [91] [92] to minimise the impact of interatomic interactions with the substrate. The chemical vapour deposition technique (CVD) is also one of the most commonly employed methods for growing 2D materials.

These atomic-scale layered structures are gaining attention due to their remarkable inherent properties, which include mechanical, electrical, optical, and thermal ones. Significant attention was attributed to 2D semiconductors. The electronic properties of these materials can be adjusted by structural modification through strain, doping, or by controlling their dimensions [93–95]. For the 2D materials based field effect transistor (FET) devices, the electrical properties are crucial for optimising their performance. The majority of experimental and theoretical studies have focused on this, with particular interest in molybdenum disulphide (MoS_2) FETs [96] [97] and black phosphorus (BP) [98]. The choice of 2D materials is not made randomly. Indeed, thanks to their atomically thin and clean structure, the variety of band gaps, and the possible layer stacking combinations, it is possible to enhance current flow. The MoS_2/BP heterojunction has particularly shown a high on-off ratio. The performance of this type of device has been demonstrated, highlighting the effects of integrating an intermediate layer, doping, or applying stress on its performance [99–101].
Depending on the purpose of the application, one property, whether chemical or physical, will be more emphasised than the other. In electronics as well as photonics for optoelectronic components [102–104], the emphasis will be on the material's resistance, the charge carrier, and the type and concentration of doping. While in catalysis [105–108], membranes, energy storage, biomedicine, and environmental science [32] [109–111], the chemical stability aspect and the porous structure with varied sizes will be highlighted.
2D materials have made their way into the medical and biotechnology fields, most notably in the development of biosensors. The approach, as the name suggests, is based on the use of 2D materials to detect biological substances such as H_2O_2 molecules, glucose, etc., as well as DNA and proteins. In terms of solar energy, scientists have focused their research on converting energy to generate electricity through the development of photovoltaic cells. Transition metal dichalcogenides (TMDs) have shown a high power conversion efficiency, though they appear to not surpass traditional systems for the time being. Thus, further research should be conducted to find a way to increase their efficiency based on the intended purpose [112–114].
Owing to their wide range of properties, which can be modulated and enhanced for specific purposes by combining several layers of different material, complex structures with the so-called 2D heterostructures and junctions have been developed [113] [115–117].
Their inherent characteristics and properties are drastically altered and affected when their dimensional size is reduced. As a result of their thin spread over a certain area, the effect of the environment in which they are situated is not negligible. Especially when it comes to interactions between the different layers of the substrate and the two-dimensional material. Indeed, it was found that in addition to defects the substrates can also affect the electronic structure of the molybdenum disulphide (MoS_2) due to the charge transfer that takes place at the interface [118].

Molybdenum disulphide MoS_2

In this thesis, specific attention was given to the second most studied 2D material. This inorganic material, namely molybdenum disulphide (MoS_2) whose exfoliation in 2005 followed that of graphene, belongs to the transition metal dichalcogenides (TMDs) family. This group crys-

tallises in different phases and shapes. The hexagonal form is the most stable structure in which MoS_2 naturally crystallises [119]. This latter is semi-conductive and consists of an arrangement of molybdenum atom planes surrounded by two planes of sulphide atoms as illustrated in Fig.II.3. A side view of the MoS_2 structure is depicted in Fig.II.3 (a), and a top view is provided in Fig.II.3 (b). Its lattice value is 3.161 Å, and the length of the Mo-S covalent bond is 2.4 Å.
Multilayer MoS_2 or bulk is made up of layers of MoS_2 bonded together by Van der Waals forces. The structure can be trigonal (T), hexagonal (H) or rhombohedral (R). For a monolayer, two symmetries exist: hexagonal (1H) [120] and octahedral (1T). The different structures of MoS_2, whether multilayer or monolayer, or with an arrangement of monolayers offering different symmetries, result in distinct properties in each case [121] [122]. Specifically, the material's electrical properties can be altered by its symmetry. For example, the hexagonal shape exhibits semiconducting properties, whereas the octahedral structure has metallic properties. The MoS_2 also has advantageous mechanical features such as strong mechanical strength and flexibility. The number of layers has an effect on these characteristics; for example, monolayer [123] exhibits stronger strength than multilayer [123].
Electronic properties are not to be overlooked either. The $2H - MoS_2$ exhibits excellent carrier mobility. When the structure is refined down to the monolayer ($1H - MoS_2$), the large indirect band gap of $\approx$ 1.29 eV [124] rises by around 0.6 eV, resulting in a band gap transition to a direct band gap of 1.9 eV [10]. This modification also has an effect on optical properties. The number of layers of MoS_2 did, in fact, affect the photoluminescence properties. As a result, a variety of prospective applications with functionalized characteristics have arisen.

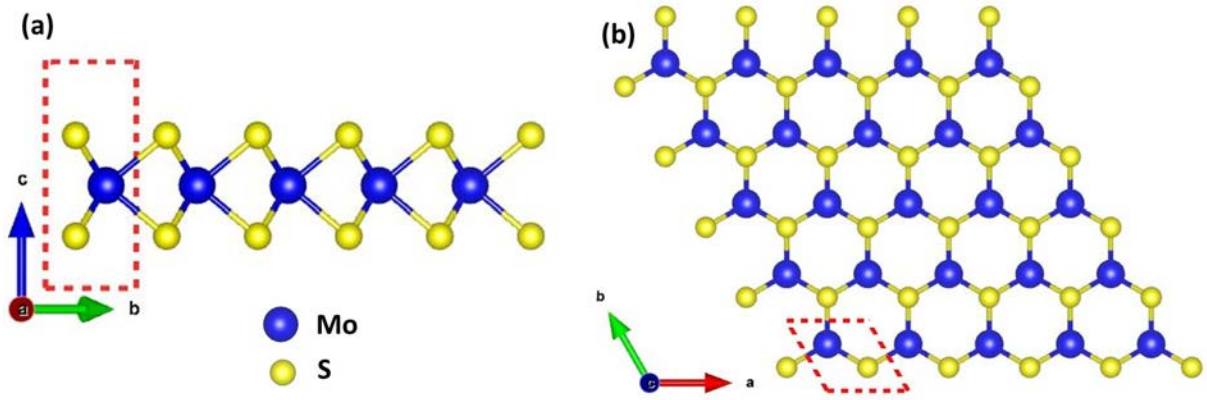

Figure II.3: Schema of the single layer $MoS_2(1H - MoS_2)$ with (a) the side view and (b) the top view of the MoS_2 lattice. The doted red line corresponds to a single unit cell. The unit cell parameter a = 3.161 Å.

One of the major challenges in reaching the considerable application potential of diverse 2D materials is determining how to controllably adjust, modify, and improve their structures in order to obtain specified and tuned properties. As previously stated, the MoS_2 has a variety of properties that are by nature sensitive to external (substrate, surrounding environment, etc.) and internal factors. Optimising these properties requires fundamental studies of the modifications and structures that can be formed in the various models and how to do them. This makes them a very interesting

candidate for irradiation studies [56] [125]. A brief review of the swift heavy ion irradiation outcomes attained so far is given later in the chapter.

2 Interaction of swift heavy ions with matter

2.1 Impact of swift heavy ions on the strontium titanate

The impact of swift heavy ion irradiation is known to cause various changes in different types of material. Strontium titanate is known to be highly responsive to the penetration and effects of SHI. Depending on the irradiation parameters, such as irradiation geometry or ion beam energy and fluence, various structural and electronic changes can occur. These range from point defects to phase transition and amorphization, or an effect on mechanical properties with changes in strength and hardness.

2.1.1 Single impact regime – for both grazing and 90° angle irradiation

At low fluence, i.e. in the single-impact regime, each ion impact generates a structural modification. For irradiation at 90°, nano-hillocks form on the surface. By decreasing the angle of incidence towards grazing angles, the appearance of the induced modifications changes with an increasingly elongated morphology until a chain composed of nano-hillocks with a certain periodicity appears, as can be seen in figure II.4. The periodicity of these nano-hillocks is linked to the spatial distribution of electrons in the target material [6]. Note that each normal or elongated hillock, each chain composed of several nano-hillcoks, is the result of the impact of an individual ion.
It has also been observed that a decrease in the angle of incidence towards the surface increases the size of these chains, up to a few micrometers in length. Figure II.4 (b) shows this dependence of chain length on angle [17]. The explanation behind this specific morphology is discussed in the first chapter.
Akcöltekin et al. investigated the influence of irradiation angle on the length of surface tracks in strontium titanium ($SrTiO_3$) irradiated at different angles [6, 17]. A geometric relation has emerged that accurately describes this dependency and can be extended to different materials:

$$L = d/tan(\theta) \tag{II.1}$$

L is the chain length, and θ represents the angle of incidence of the projectile. The parameter d corresponds to the maximum depth from which the excitation and subsequent modification can still reach the surface. When the incident ion passes through the target material, a transfer of energy occurs from the ion to the target. As explained in detail in Chapter I, in the case of swift heavy ions, the interaction occurs mainly with the electronic system of the target. This results in the formation of an amorphous cylindrical track within the bulk material and chains of nano-hillocks forming on the surface. However, as the ion penetrates deeper (but well before stopping (Rp)), the local excitation is no longer detectable on the surface. This distance 'd', which is specific to the target material, is measured perpendicular to the surface (see inset Fig.II.4(b)), for $SrTiO_3$, d = 8 nm. To better identify what defines these different parameters, an example is shown in Fig. II.4

(c), where a 3D AFM image of the surface of $MoS_2/SrTiO_3$ irradiated with swift heavy ions at a grazing angle can be observed. The formation of a chain of nanohillocks on the substrate ($SrTiO_3$) is accompanied by the folding of the single layer MoS_2. The arrows do not represent the real value of the incident angle; they are there to help visualize these various parameters. The images in Fig. II.4 (a-b) come from [6, 17].

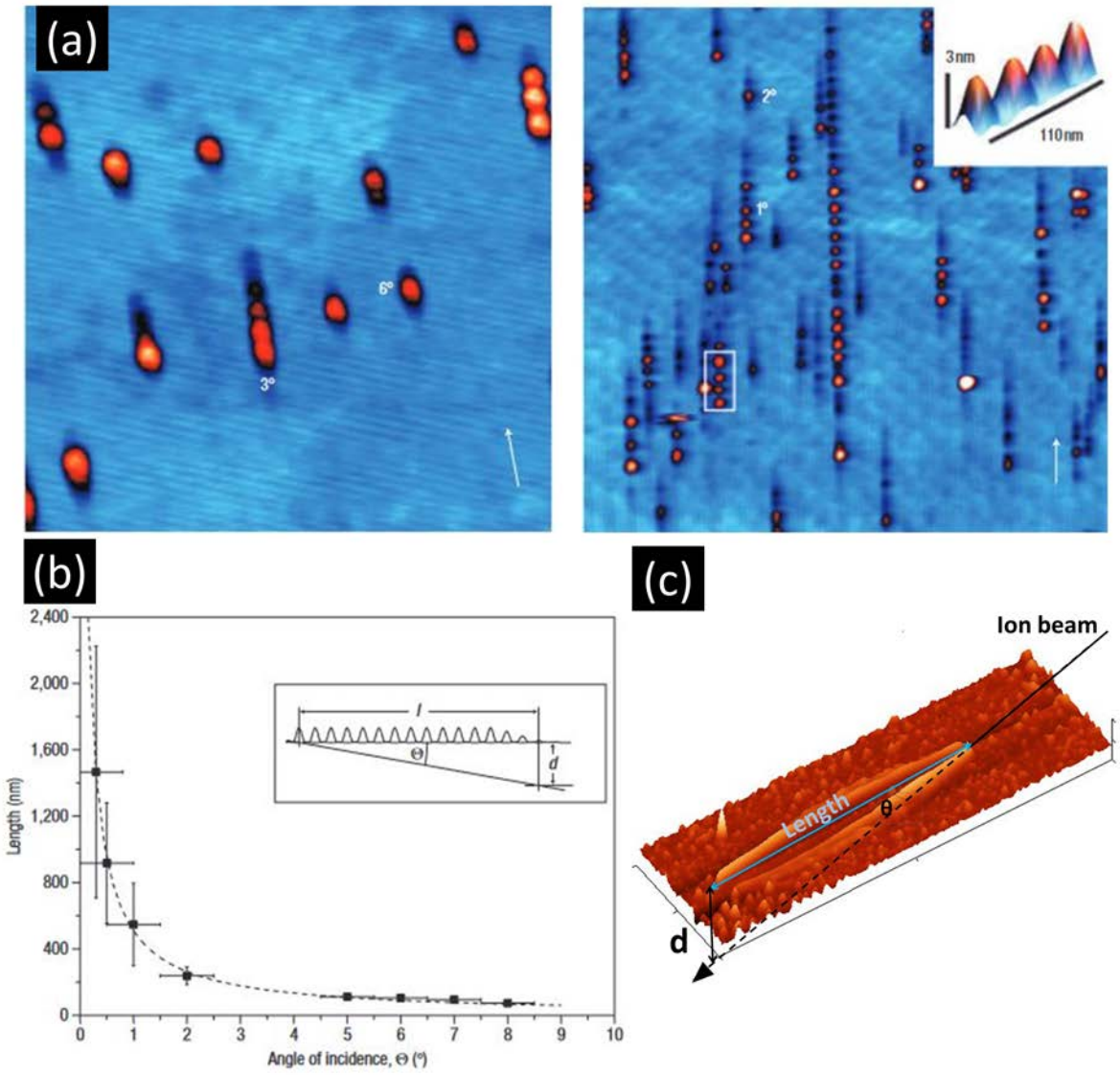

Figure II.4: Figure : (a) AFM images of $SrTiO_3$ irradiated at different angles with 92 MeV Xe ions [6]. (b) The relationship between the length of the chains and the angle of incidence is demonstrated [6] and (c) shows a 3D AFM images of $MoS_2/SrTiO_3$ sample irradiated with 92 MeV Xe ions at $\theta = 0.3°$, it was added for information purposes to help identify the different parameters mentioned

2.1.2 High fluence regime

Strontium titanate is a direct-impact amorphizable material [19], which means that it follows a direct amorphization model in which each ion generates an amorphous zone after a hit. The dependence of these changes on irradiation fluence has already been observed at both low and high energies [126] [18]. To achieve surface amorphization, it is necessary to overlap the individual tracks. With swift heavy ions (SHI) irradiation and a fluence of around 10^{13} ions cm^{-2}, overlaps start. Different regions were observed in the transmission electron microscopy (TEM) on a $SrTiO_3$ cross-section, and the threshold for amorphization in the bulk and track formation on the surface was determined to be around 12 keV/nm [18]. Although the effect of high-fluence irradiation at normal incidence is well known, its effect in grazing incidence geometry, and in particular on the different layers, is less well known. This is the reason why the impact of these two irradiation parameters combined on a single crystal is being examined in this thesis.

2.2 Impact of swift heavy ions on the two-dimensional materials

As already mentioned, 2D materials (graphene, MoS_2, WS_2, etc.) possess a wide variety of properties that can be modified and enhanced by inducing structural changes and defects. The response of 2D materials to irradiation considers many factors. The latter influence the resulting structural developments and changes (defect engineering, folding, doping, thinning, etc.), which in turn have an impact on the performance of the resulting 2D materials. Among these factors, there is the method used for this purpose; doping, laser processing, electron and ion beam irradiation, etc. The energy and beam range used (swift heavy ions, highly charged ions, focused ion beams, etc.) [127] [125] [128], the irradiation parameters (such as fluence, angle of incidence, ion energy, etc.) or the type of ion used (Xe, Ar, He, O, etc.). The target also plays a role, as the type of 2D material (graphene, TMDs group, heterostructures, etc.), the number of layers present (1L, 2L, multilayer), and the nature of substrate (Si, SiO_2, $SrTiO_3$, glass, Ni, etc.) give rise to a different response following their collision with the projectile.
Since the emphasise is on the ion beam techniques, this section will focus on the changes that can be achieved through them.
A multitude of studies have investigated the use of ions to engineer defects in different kinds of 2D materials. To this end, they have varied not only the type of substrate used, but also irradiation parameters such as energy, beam type, and angle of incidence. The following is a summary of some of the most significant studies using beams in the MeV range.

2.2.1 Two-dimensional material irradiation at non-grazing angles

Considered the first experimentally discovered 2D material, graphene has been the subject of a multitude of studies concerning defects induced by ion irradiation. Irradiation of graphene prepared by exfoliation and deposited on $SrTiO_3$ substrate, at an angle of incidence of 90° and an energy of 103 MeV [2], shows hillock-like structures of the order of a few nanometers fig.II.5 (a). These structures were observed on the substrate alone as well as beneath the graphene layer. However, no impact nor structure formation was observed on the graphene. Further studies followed, and were extended to other materials such as molybdenum disulphide MoS_2 and hexagonal boron nitride

(hBN), varying the number of layers from a single layer to a bulk material. Various beam types (SHI, FIB, HCI, etc.) have been used; nonetheless, in this study, the focus is on ion beams of swift heavy ions (SHI) energy range. Irradiation with beams of energy between 0.45 GeV and 1.23 GeV showed the appearance of hillock-like structures on the surface associated with tracks in the bulk in the case of supported single layer MoS_2 fig II.5(b) and single layer graphene but also for multilayer MoS_2 [129] [8].

The development of atomically thin materials with nanoscale pores has generated excitement within the scientific community [32] [130] due to their significant potential for various applications, which can lie within the biomedical field, with the possibility of using them for DNA sequencing [131] [132], and even in the environmental field, with applications in water desalination and ion filtration [133] [134]. Graphene is the most promising material to emerge for filtration membrane applications. This can be done whether on suspended or supported graphene [32] [135]. Using TTM-MD simulation, Vasquez et al. have shown that pores can be created in suspended graphene, following irradiation with SHI at an angle perpendicular to the surface [135], for a threshold stopping power of around 3 keV/nm. He also demonstrated the impact of electronic stopping power on pore size. Indeed, the pore size grows in direct proportion to the stopping power. But it has not yet been observed experimentally by AFM. Pores with diameters of less than 10 nm have been observed at large incidence angles of 60°, as shown in figure II.5 (c) [7].
Another phenomenon was observed on graphene irradiated at different fluences under normal incidence (90°) with 100 MeV Ag ions. Samples of three to four graphene layers were used to probe the impact on a multilayer. At low fluence, a decay of the defect rate is observed, which then increases with fluence. According to this study, at low fluence, the energy transfer between the incident ion and the target induces a defect annealing process that purifies the sample and consequently improves the quality of the crystal. While at high fluence, the increase in defect density is accompanied by graphene ablation, i.e. a reduction in the number of atomic layers [136].

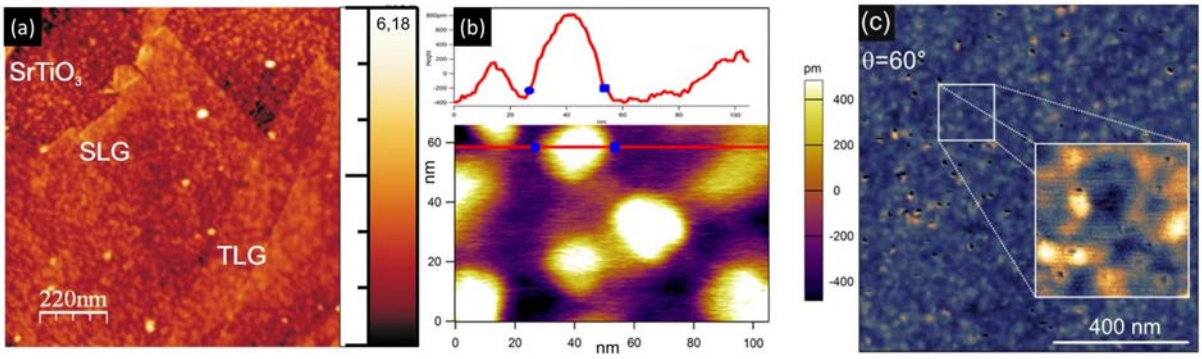

Figure II.5: AFM images of (a) graphene irradiated with 103 MeV Pb^{+29} ions, (b) single layer MoS_2 irradiated with 94 MeV Bi ions with the profile section of a hillock-shaped protrusion and (c) graphene on SiO_2 irradiated with SHI at $\theta = 60°$ where pores-like structure are visible [2] [7] [8].

In order to extend the application field and analyse the impact of an additional parameter.

Irradiations at grazing angles of incidence were undertaken, resulting in a rather unique structure at the surface, different from that obtained at normal irradiation.

2.2.2 Irradiation of 2D materials at grazing angles incidence

The irradiation geometry showed, in different materials, the impact of the incident ion angle on the type of structural defects obtained as well as on their morphology [6]. Indeed, by irradiating 2D samples with SHI in the single-impact regime and by decreasing the angle of incidence towards the surface (grazing), Akcöltekin et al. showed experimentally for the first time that irradiation of mechanically exfoliated graphene results in the formation of a structure with a typical morphology, appearing in the form of a fold. Thereafter, several studies followed, varying 2D material specimens, angles, substrates, and projectile ions. The following is a summary of the types of surface modifications obtained so far. Ochedowski et al. [9] obtained folding for each ionic impact on all graphene, MoS_2, and hexagonal boron nitride (hBN) single layers. A difference in the folding was observed in the case of MoS_2, which is accompanied by cracks, or as it is referred to, rifts. However, as the number of layers increases, the reaction differs from one material to another, especially with different foldings. In the case of graphene, both the number and length of folds decrease, while in the case of hBN, the number of layers has no impact on either the number or length of folds. The MoS_2 however, behaves differently from other materials. As the number of layers increases, the folding disappears, leaving only the rifts, whereas in bulk, a chain of nano-hillocks like that observed in the case of metallic crystal is obtained [6]. This is summarised in figureII.6 from [9] [137].

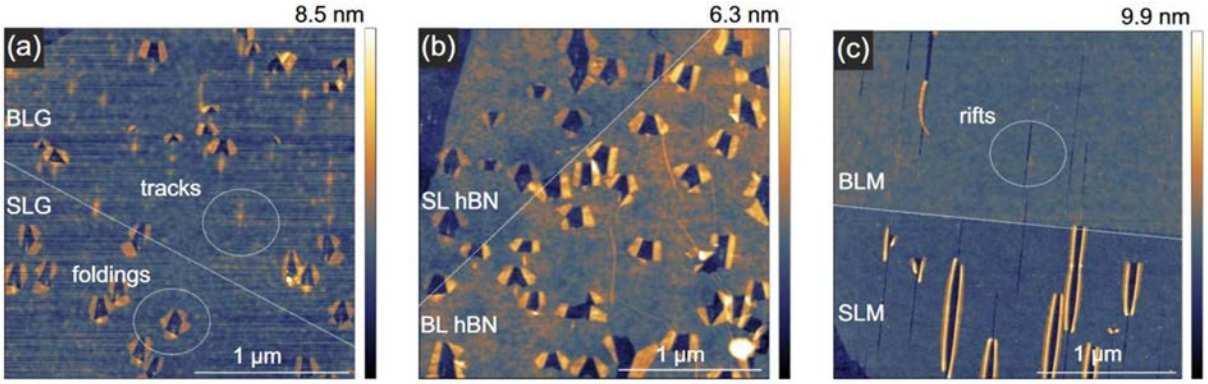

Figure II.6: AFM images of (a) single layer and bilayer graphene irradiated with 106 MeV U ions at $\theta = 1.3°$. Where for each ion impact a folding occurs in the SLG, whereas for the bilayer, a folding only occurs for every second ion impact. (b) Single and bilayers of hBN irradiated at $\theta = 1.5°$ with 106 MeV SHI. Each ion induces one folding in both case. (c) Single layer and bilayer MoS_2 irradiated at $\theta < 1°$ with 91 MeV Xe. Single layers of MoS_2 show a both folding and rifts, while the bilayer show only the rifts. Images taken from [9]

Apart from the nature of the material, by using suitable incident parameters, the number of folds can be controlled; as the number of layers increases, the number of folds decreases. The size and shape of the folds are significantly influenced not only by the angle of irradiation but also by

the deposition of electronic energy, the stopping power of which has been estimated to be around 5.1 keV nm^{-1} [7]. Indeed, it has been observed that as the angle decreases towards the grazing angle, the folding becomes larger and straighter in the direction of the ion beam. As can be seen in figure II.6 (c).

A more detailed study of the surface nanostructuring of MoS_2 deposited by exfoliation on SiO_2 showed a dependence of the probability of folding and incision formation on the angle of the SHI with the crystal axis (marked by the flake edges)of MoS_2 [64].
The response of 2D materials to irradiation is different from that of other materials, not only because of their two-dimensional structure, which limits the path and energy transfer of the ion to a single atomic layer, which in turn limits the defects that can be generated, but also because of their environment, and in particular the substrate. In the case of SHI irradiation, the projectile, in view of its projected range, passes beyond the 2D layer and reaches the substrate, forcing it to develop structural and morphological modifications that can reach, impact or even influence the behaviour of the 2D material. This is why various studies have been conducted in order to compare the outcomes of materials (graphene, MoS_2, etc.) deposited on different substrates. The differences observed mainly concern the shape and size of folds in the case of suspended and supported graphene and MoS_2 and incisions in the latter, confirming the impact of the substrate. Figure II.7 shows the different shapes of folds depending on the type of substrate used in the case of graphene [7].

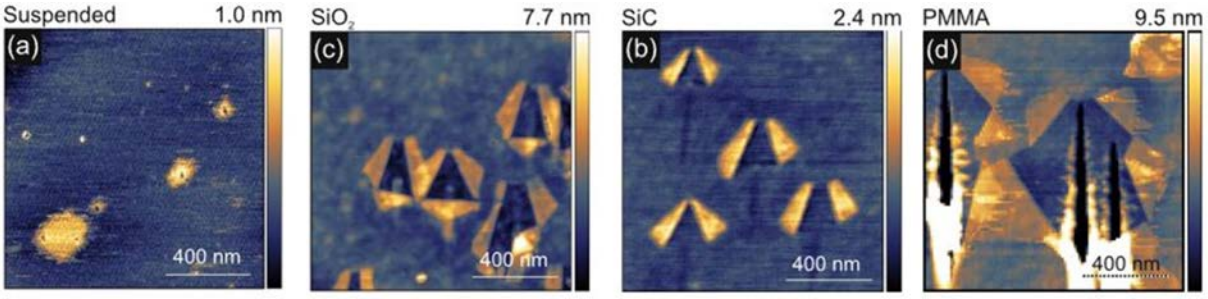

Figure II.7: AFM images of graphene irradiated by SHI at $\theta = 1.5 \pm 0.3°$ resulting in folding where (a) is a suspended graphene, (b) a graphene supported on SiO_2, (c) graphene on SiC, and (d) graphene on PMMA [7]

.

The mechanism originally proposed by Akcöltekin et al. [2] involved the impact of the substrate. They hypothesized that, after the graphene layer had been weakened by the ion beam, the creation of defects or structures on the substrate somehow pushed the 2D layer upward, eventually breaking and giving rise to the folds. Not to mention the significant impact of the intermediate water layer. Indeed, when the 2D layer is exfoliated at room temperature or transferred to a substrate, as in the case of graphene on SiO_2, or even when the sample is stored in an ambient environment, an interfacial layer consisting mostly of water is created between the 2D material layer and the substrate. The layer at the interface does not only modify the properties of two-dimensional materials but also affects the size of the modifications obtained after SHI irradiation. As observed

in the case of SHI-irradiated single layer graphene (SLG), the bend tends to open up after the sample is heated,suggesting an influence of the H_2O and O_2 interposed between the graphene layer and the substrate [138] [137]. Studies on suspended graphene [7] have shown the presence of folds on graphene after irradiation with SHI, indicating an intrinsic response of graphene to folding, with a slight impact of the environment notably impacting the size of the fold.
Throughout these results, the difficulty of creating folds on MoS_2 has been highlighted, as most studies have focused on MoS_2 deposited on SiO_2 by mechanical exfoliation. In this thesis, the study of the swift heavy ion irradiation effect at grazing incidence on MoS_2 is proposed. These samples were prepared by CVD mainly on $SrTiO_3$ and occasionally on SiO_2 for comparison.

3 Instruments and Methods

3.1 Synthesis of 2D Materials by chemical vapor deposition (CVD)

The most common process for growing monolayer or multilayer TMD materials is the chemical vapor deposition (CVD) technique. The benefit of the CVD approach is that it can be controlled by process parameterization, resulting in control over the shape of the 2D material flakes generated. The latter may be distributed as flakes or as a film extended over the full surface of the substrate.
Thanks to the collaboration with the research team of Prof. Dr. Marika Schleberger at the University of Duisburg Essen in Germany, Yossarian Liebsch and Lukas Madauß conducted all the vapour-phase deposition of MoS_2 on $\alpha - SiO_2$ and crystalline $SrTiO_3$.
The setup consisted of three isolated zones that allowed the two chemical reagents to be heated at various temperatures (100°C for sulphur and 300°C for molybdenum). Only two chambers were needed in our situation because the second chemical reactant was put immediately onto the substrate. The deposition process involves several stages. Solid chemical reactants were used: Ammonium heptamolybdate ($(NH_4)_6Mo_7O_{24}$), which is fairly dense and comes in almost powder form, and sulphur powder (S) were used as the raw materials for the molybdenum and sulphur components, respectively. Prior to deposition, the ammonium heptamolybdate is dissolved in an aqueous solution. A small amount of oxidised molybdenum is deposited at the border of the wafer. It should be noted that in the case of $SrTiO_3$ the deposition was carried out directly on the substrate since the growth was already going to be done on a crystal. Prior to $\alpha - SiO_2$ growth, a combination of Cholic acid sodium salt (1%) and AHM chemical solution (50%), diluted with 50% H_2O, is deposited on the wafer via spin coating. The substrates are subsequently placed on a support shaped like a boat (see figure II.8(b))in the second chamber. Argon gas is introduced to eliminate the oxygen before the deposition begins, and then the sulphur powder is transported from the first chamber to the second chamber, where the substrate with the molybdenum oxide/ SiO_2 is situated. Material adsorption onto the heated substrate results in diffusion, eventually leading to the formation of crystalline single crystals. In this example, the crystals formed are MoS_2 flakes in a triangular shape.
A drawing of what is described is shown in figureII.8(a). The containers in which the sulphur and the substrate with the molybdenum oxide (circled in red) are placed are shown in Fig.II.8(b).

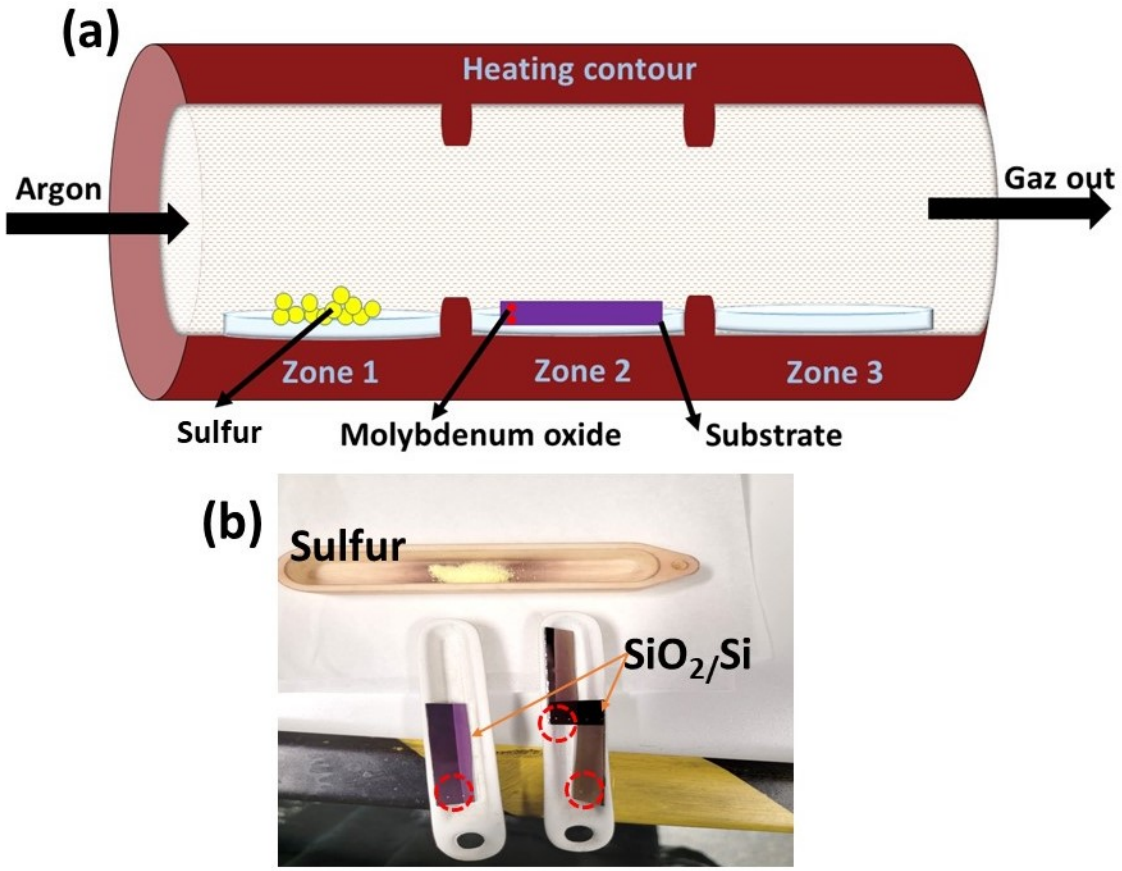

Figure II.8: Illustration of the CVD process (a). The reactants placed in two separate zones and heated to different temperatures are shown in (b).

3.2 Experimental devices

The irradiation experiments undertaken during this thesis work were carried out at the GANIL facility (Grand Accélérateur National d'Ions Lourds). This facility simultaneously produces beams of swift heavy ions in different energy regimes (high, medium and low energy) of different species (from carbon to uranium). The figure II.9 shows a diagram of the GANIL installation. The first two ion cyclotron injectors, called C01 and C02, produce ions with energies of the order of MeV per nucleon (MeV/u, where u is the atomic mass unit). The resulting beam is either driven directly to the IRRSUD (IRRadiation SUD) line for use in interdisciplinary physics experiments, or injected into a first Separated-Sector Cyclotron (CSS1), where it is accelerated to energies in the order of a few MeV/u. The beam is then sent through a stripper, which increases the charge state by stripping off a certain number of electrons. At this point, and with the help of magnetic elements, some of the ions with a higher charge state and sufficient intensity yield a more efficient deviation in the magnet drive to the medium-energy line SME (Sortie Moyenne Énergie) in the energy range from 4 to 13 MeV/u. The rest of the ions continue through the accelerator and are driven to a second cyclotron identical to the first (CSS2), which produces ions with energies ranging from 24 to 95

MeV per nucleon. They are then distributed to the various experimental rooms of the High Energy (HE) line, dedicated to specific nuclear physics applications and interdisciplinary research.

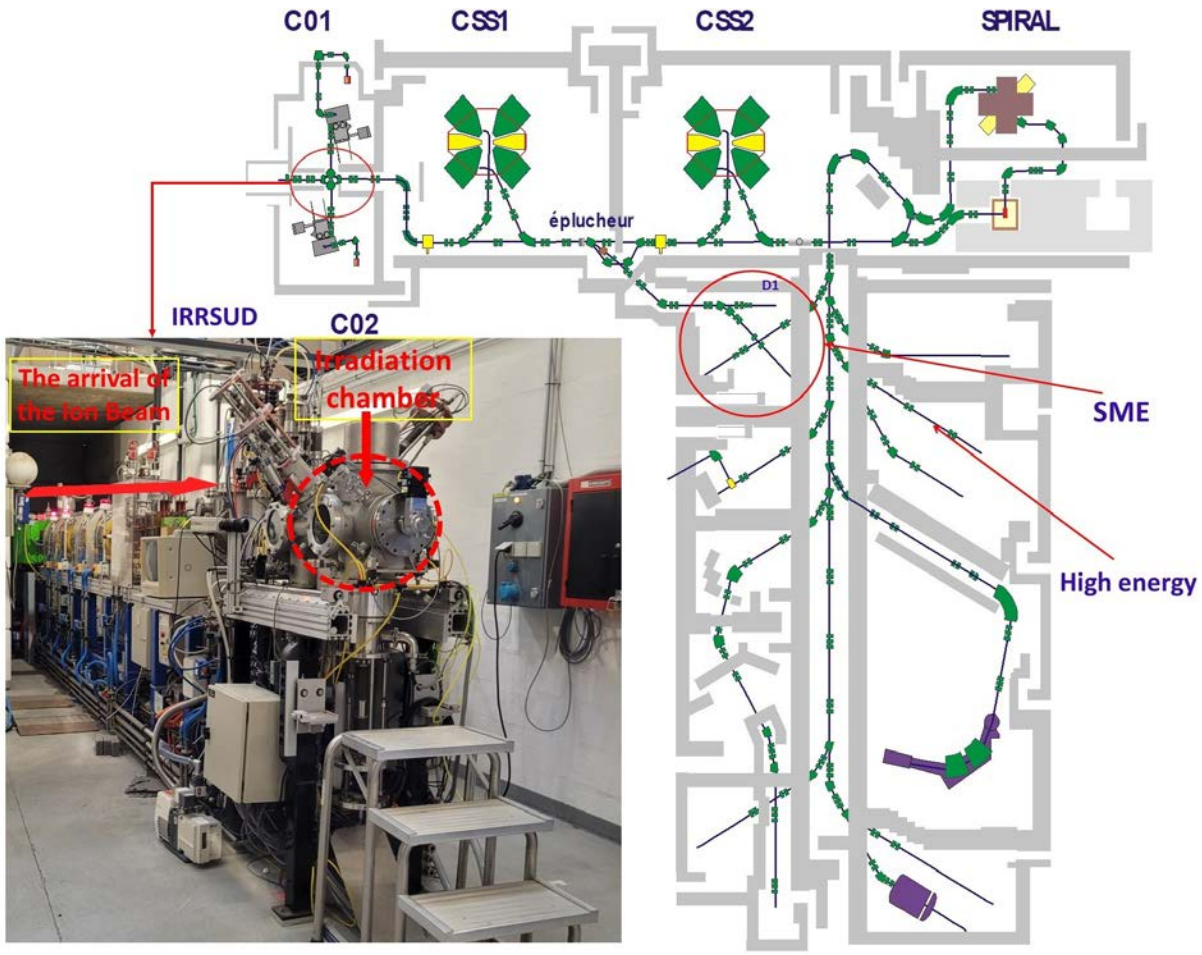

Figure II.9: A photo of the IRRSUD irradiation room is accompanied by a schema of the GANIL facility.

Irradiations were exclusively conducted at the IRRSUD beamline for this study, where the energy varies from 0.3 to 1 MeV/u depending on the beam. This line includes slits to determine the irradiation area, which can be up to 20cm^2. 16cm^2 was chosen for irradiation in this investigation. A vertical and horizontal scanning system for homogeneous irradiation of the entire selected area are also available. In the irradiation chamber (circled in red on the image), a rotating plate holder enables irradiation at different angles. Irradiation takes place at room temperature and under a high vacuum (5×10^{-6} mbar). The samples are mounted on the irradiation plates using copper or carbon tape to fix them and prevent charge accumulation. The line is also equipped with ion flux (ions cm^{-2} s^{-1}) measurement system before and during irradiation. The flux used during irradiations in this study ranged from 1×10^7 ions cm^{-2} s^{-1} for low-fluence irradiations to 7×10^9 ions cm^{-2} s^{-1} for long high-fluence irradiations.

In the following, a description of the irradiation procedure used and the steps followed during the thesis project will be discussed. In particular by emphasizing the importance of optimizing the allocated beam time according to the intended irradiation parameters.

3.3 Irradiation procedure

As it is known, the most important parameters in this type of experiment are the angle, the fluence (ions cm^{-2}) and the particle flux (ions $cm^{-2}\,s^{-1}$). If the flux is too high, there is a risk of macroscopic heating of the sample due to the deposited power and damaging it through the accumulation of charges. On the other hand, if the flux is too low, the irradiation time will increase. To achieve extremely homogenous irradiation over the entire surface in a reasonable time, some conditions have to be met. A scanning system frequency at two axes, both horizontal (400 Hz) and vertical (4 Hz), is used to ensure homogeneous irradiation. Two other conditions must be met. It is generally considered that an irradiation time >100 seconds is the minimum required for this. A compromise has to be found to have a flux high enough to irradiate in the time assigned to the experimenters and low enough not to damage our samples. Depending on the type of material being studied, one sample may be more resistant than another to high fluxes.
As strontium titanate (STO) is a fairly resistant material, the relatively high fluxes vary between 3×10^9 ions $cm^{-2}s^{-1}$ and 7×10^9 ions $cm^{-2}\,s^{-1}$ were used during this study. To get a better idea of the situation, it should be noted that irradiation times at GANIL-IRRSUD extend over 4-5 months per year. When requests for beam time are made, the committee assesses the requests, allocates and issues a certain number of UTs for each experiment request (1 UT = 8 hours). For example, for an irradiation at 5×10^{14} ions cm^{-2}, assuming that a flux of 4×10^9 ions $cm^{-2}\,s^{-1}$ is used, it would take 35 hours of the irradiation to achieve the fluence, i.e. a little over 4 UT, which in some cases could represent the time granted in total.

Note that when irradiating with a grazing angle geometry, it is necessary to correct the delivered fluence to obtain the fluence actually received by the sample. This can be achieved using the following formula:

$$\Phi_{desired} = \Phi_{delivered} \times \sin(\theta) \tag{II.2}$$

where $\Phi_{desired}$ is the real fluence received by the sample at an angle $< 90°$ and $\Phi_{delivered}$ is the fluence delivered by the machine. θ is the angle of irradiation used.
Let's take the example of an irradiation at 1°. Suppose we want to have irradiation with a real fluence (what the sample actually perceives) of about 1×10^{11} ions cm^{-2} on the sample, the sample should then be irradiated with approximatively 5.7×10^{12} ions cm^{-2}. It is the latter, with the flux used, that will therefore be considered when calculating the beam time required.

To overcome this limitation in beam time, we sought to optimise our irradiation time as much as possible. To do this, supports were manufactured using a 3D printer with a biodegradable polymer, polylactic acid (PLA), thanks to J. Rangama (CIMAP colleague).One should note that direct exposition to the ion beam was avoided, and the PLA was additionally covered in alluminium foil. Figure II.10 (a) shows a photo of one of the supports used, consisting of a sort of pillar with a surface area of 5×5mm and a different angle for each pillar. This support enabled us to

irradiate five samples at five different angles at the same time. Note that the fluence varies with the angle. Consequently, for a given fluence, the actual fluence perceived by each sample varies from one angle to another. This will be looked at in more detail later. $SrTiO_3$ samples of the same size ($5 \times 5 \times 0.5$mm) were fixed to the support with copper tape, which was in turn stuck to the irradiation plate with the same tape. In order to avoid charge accumulation and heating of the samples and the support, we covered the latter with several layers of 0.35 mm thick aluminium foil. This is more than sufficient to prevent ion penetration, which in this case is a maximum of 8µm deep. We also added steel shims to secure the support and remove as much of the charge as possible. Figure II.10 (b) shows the setup before we deposit the sample.

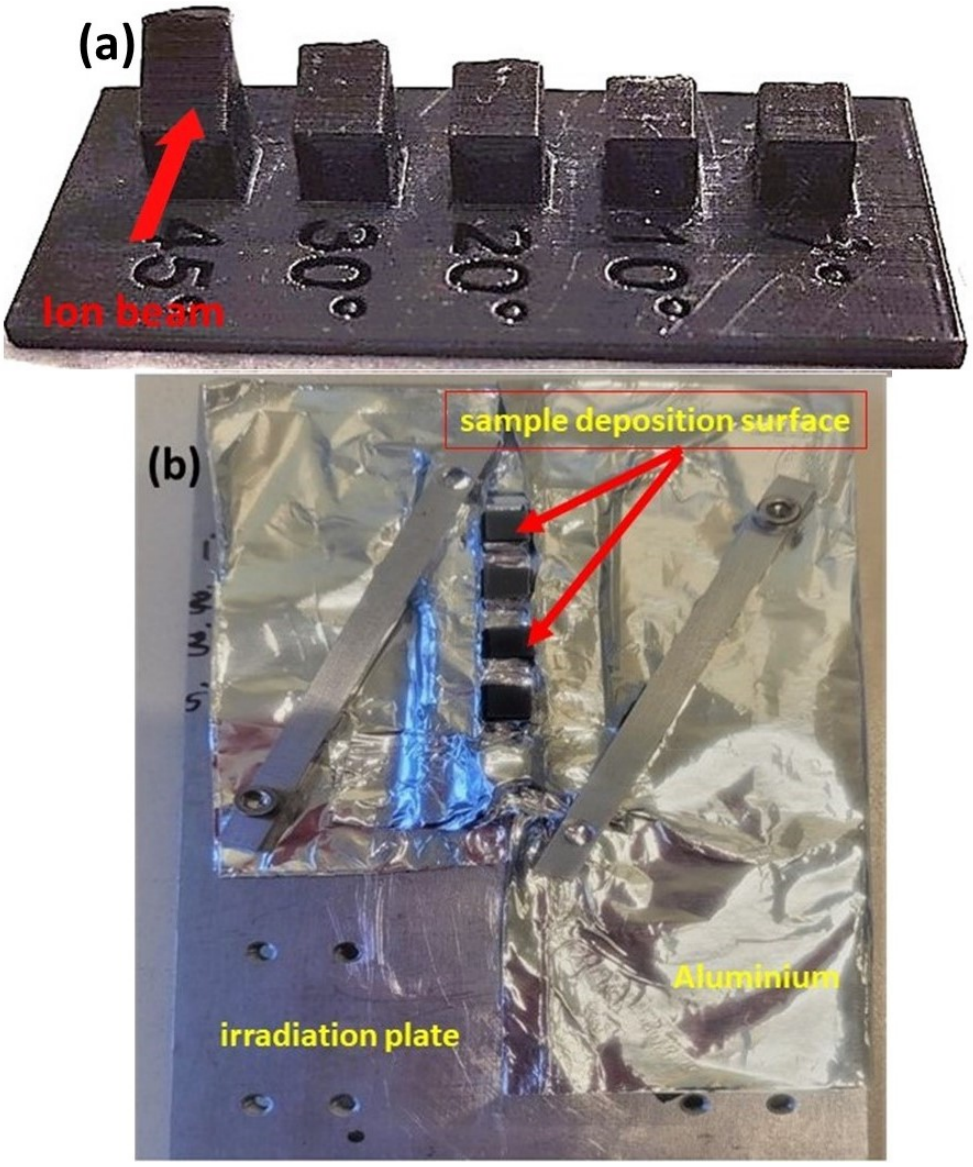

Figure II.10: (a) Support irradiation with different angles, made by 3D printing. the red arrow indicates the ion beam direction, it is a guide for the eyes but it does not represent the absolute value of the incident angle, (b) represents the support placed on the irradiation plate and covered with aluminum sheets leaving only the upper face exposed for sample depositing

Angle calibration

The irradiations undertaken in this thesis are mainly carried out at grazing incidence angles. Angle calibration is therefore essential before the start of each irradiation run, to ensure correct angle geometry. Alignment of the sample surface with the arrival of the ion beam at the desired angle is first achieved optically. Alignment of the beam line is already done with a defined axis giving

an angle of 90° to the irradiation plate. Using a telescope aligned with the optical axis of the ion beam line, the irradiation plate is rotated by 90° until it is parallel with the ion beam. At this point, the grazing angle of "zero degrees" is obtained. The second step consists of using a stepping motor (which is located below the irradiation plate) to rotate the sample holder with a precision of 0.01°, in order to get to the exact angle required. The main error bars come from the optical alignment and the rotator motor.
A final confirmation or determination step must be completed in order to ensure that the irradiation was performed at the right angle. Provided the irradiation is in the single-impact range (i.e. at low fluence), this involves using an atomic force microscope (AFM) to verify the presence of ionic impacts on the surface. Two methods can be used in this case to calculate the actual irradiation angle used. With grazing irradiation, for a given material such as $SrTiO_3$, chains of nano-hillocks appear on the surface. The length of the chains depends on the angle of incidence, as seen previously in this chapter. So, by measuring the length of the chains using a profile section on a series of chains, the angle of irradiation can be confirmed with the following formula: $l = d/\sin\theta$,
where l is the length of the chain, d the depth in the target material where the excitation is still felt at the surface, which is = 8nm for $SrTiO_3$ and θ is the irradiation angle.
If the angle is not very grazing, surface defects will look like single hillocks rather than long chains. In this case, the irradiation angle is calibrated using the surface ion impact density. From the latter, an experimental fluence is determined, and with the fluence delivered, the actual angle used can be calculated using the following formula:

$$\theta_r = sin^{-1}(\Phi_e/\Phi_d) \tag{II.3}$$

where Φ_e is the fluence calculated experimentally using the surface defect density, Φ_r is the fluence delivered, and Θ_r is the actual angle at which irradiation was performed.

3.4 Characterization methods

Following the various irradiations, the samples are characterised ex-situ using a variety of methods. Analysis and characterization techniques are crucial for learning more about how materials behave under irradiation and how it affects their properties and structure. Three complementary techniques were used in this study, depending on whether the objective was to probe the material at depth, near the surface, or at the surface. First, there is atomic force microscopy (AFM). This technique allows some local analysis to get the topography of the surfaces as well as analysis of surface morphology and nano-structuring. For in-depth analysis with a more integral and structural analysis, X-ray diffraction was mainly used in the case of $SrTiO_3$. For 2D materials, Raman spectroscopy was used to study structural changes and modifications in graphene and MoS_2. Some transmission electron microscopy (TEM) was also performed, which is also a local approach on a sample prepared with the Focused Ion Beam with a vertical cut. This allows getting very thin samples, so more information on the structure of the investigated materials and damage created by irradiation on the surface can be found. The different measurements were carried out with the help of colleagues from CIMAP, in particular Isabelle Monnet, Mamour Sall, and Marie-Pierre Chauvat. As I am not autonomous on the technique, I have chosen not to describe it.

3.4.1 Atomic force microscopy

3.4.1.1 Types of Atomic Force Microscopy measurement / Imaging techniques

The scanning tunnelling microscope (STM) was one of the first microscopes in the scanning probe microscopy family to be developed, but researchers quickly ran into an obstacle. This microscope is suitable for electrically conductive surfaces, so atomic-scale imaging of insulating materials was not possible. This is where atomic force microscopy (AFM) entered the world of non-destructive sample characterization techniques, enabling direct imaging of material surfaces. AFM (also known as scanning force microscopy (SFM)) is a versatile instrument. Created in 1986 by Binning [139], it has made it possible to overcome the condition of a conductive surface and to analyse all types of materials, including insulators. AFM can be used to study the structures and surface properties of materials on a nanometric scale in a variety of fields, including physics, chemistry, biology, and materials science.
Along with other properties, it can quantitatively measure the 3D surface structure. Electrical, conductive, magnetic, and mechanical surface properties can thus be obtained simultaneously with surface topography. Depending on the purpose of the measurement, specific tips and modes may be required. Three alternative imaging modes are available: contact mode (also known as static mode), noncontact mode (sometimes known as dynamic mode), and tapping mode (also known as dynamic intermittent contact mode in some investigations). Generally speaking, for topographical purposes, non-contact and tapping modes are preferred. In this thesis, the non-contact mode, and occasionally the tapping mode are used for the surface topography. For electrical modes, the measurement of conductivity, resistance and many other properties is possible through the various modes available (e.g., Electrostatic Force Microscopy (EFM), Kelvin Probe Force Microscopy (KPFM), Pinpoint conductive AFM, etc.), with contact mode being recommended in most cases. For measurements of mechanical properties, different modes are also available; to name a few, there is the pinpoint nanomechanical mode, force distance spectroscopy, nanoindentation, etc. By using these various modes, one may determine, for instance, the Young's modulus, the adhesion force, the hardness, etc. In most cases, the tip does not alter the surface. However, there are some circumstances in which etching and lithography can be created on the surfaces of the samples using specific tips, such as the well-known diamond tips.

3.4.1.2 Principle and Working of Atomic Force Microscopy

FigureII.11 (a) shows a schematic AFM setup. It consists of an extremely fine tip with a radius of curvature of a few nanometers, fixed at the end of a cantilever. A sample holder is placed on a piezoelectric ceramic tube. This material has the characteristic of expanding or contracting if a voltage is applied to it, and vice versa. In this way, the sample can be moved in x, y, and z directions. The device is also equipped with a laser diode reflected on the backside and at the end of the cantilever, so that it reflects exactly above the position of the tip and refracts towards the photodiode (PSD). This optical system allows for measuring cantilever deflection.
The tip, which has atoms at its end, once near the surface of the sample, undergoes interactions

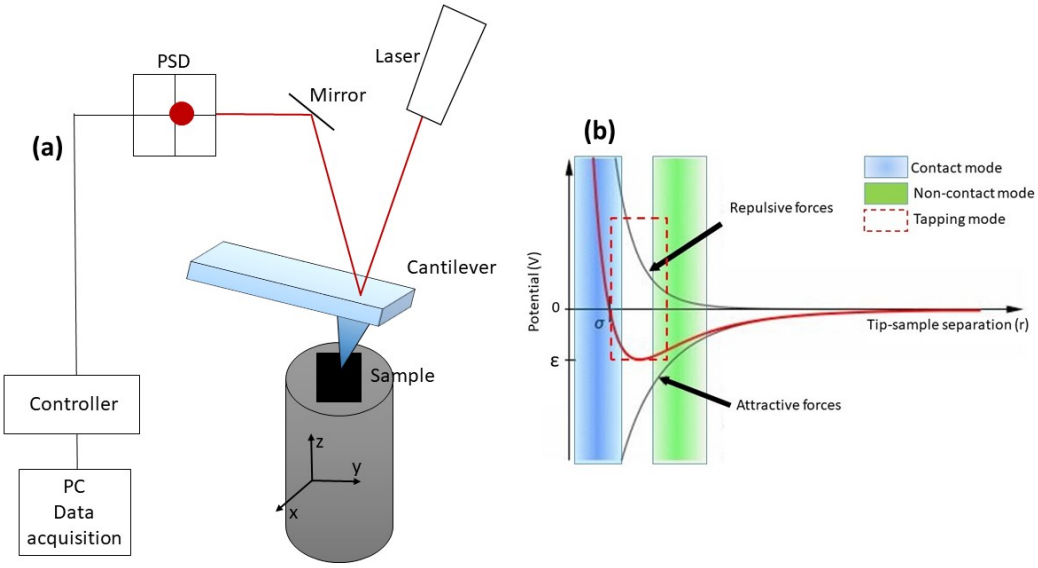

Figure II.11: (a) Scheme of an experimental AFM setup. (b) Lennard-Jones potential describing the interaction of the tip and surface atoms and the imaging mode resultant.

that generate either a repulsive force or an attractive force, depending on the distance between the tip and the surface, the environment, and the sample characteristics. These forces cause the tip to deflect and twist. As a result, laser movement is monitored by the PSD. Thanks to this feedback signal, the distance between the tip and the sample is maintained at the same distance, while the deflection of the cantilever is maintained at the same predefined force value. This signal is then translated into a topographical image.

Its working principle is based on the tip scanning the surface point-by-point. Fig. II.11 (b) shows the Lennard-Jones potential. This curve schematizes the interaction between two neutral atoms, highlighting the forces involved during the different stages of tip approach and, consequently, the different AFM operating modes. At very great distances from the surface, no forces are involved; as the tip approaches, electrostatic forces can begin to be felt (between 0.1 and 10 µm away), and at around 100 nm from the surface, adhesion and van der Waals forces begin to be felt. At a distance as close as this to the surface, other types of force can be felt, depending on the analysed system (sample) (wet, viscous, or solid). For example, when measuring in an aqueous environment, eletrostatic (screened) forces can be detected.

In the so-called dynamic mode (non-contact and tapping mode), the tip has a certain resonant frequency. The feedback maintains the amplitude/frequency at a predefined constant value throughout the scan. These two modes differ according to the distance from the surface. The non-contact mode uses attractive forces, while the tapping mode uses repulsive forces as the tip comes closer to the potential field of the sample surface. Finally, when the tip comes into contact with the surface, the repulsive forces are more important. This mode enables the extraction of certain material characteristics. The expression of the potential describing atoms' interactions is given by equation

(II.2), which shows the long-range attractiveness of the repulsive short-range force impact.

$$V(r) = 4\epsilon[(\sigma/r)^{12} - (\sigma/r)^{6}] \tag{II.4}$$

with ϵ being the depth of the potential well, σ representing the distance at which V(r) is zero (referred to as van der Waals radius), and r being the distance between the interacting species.

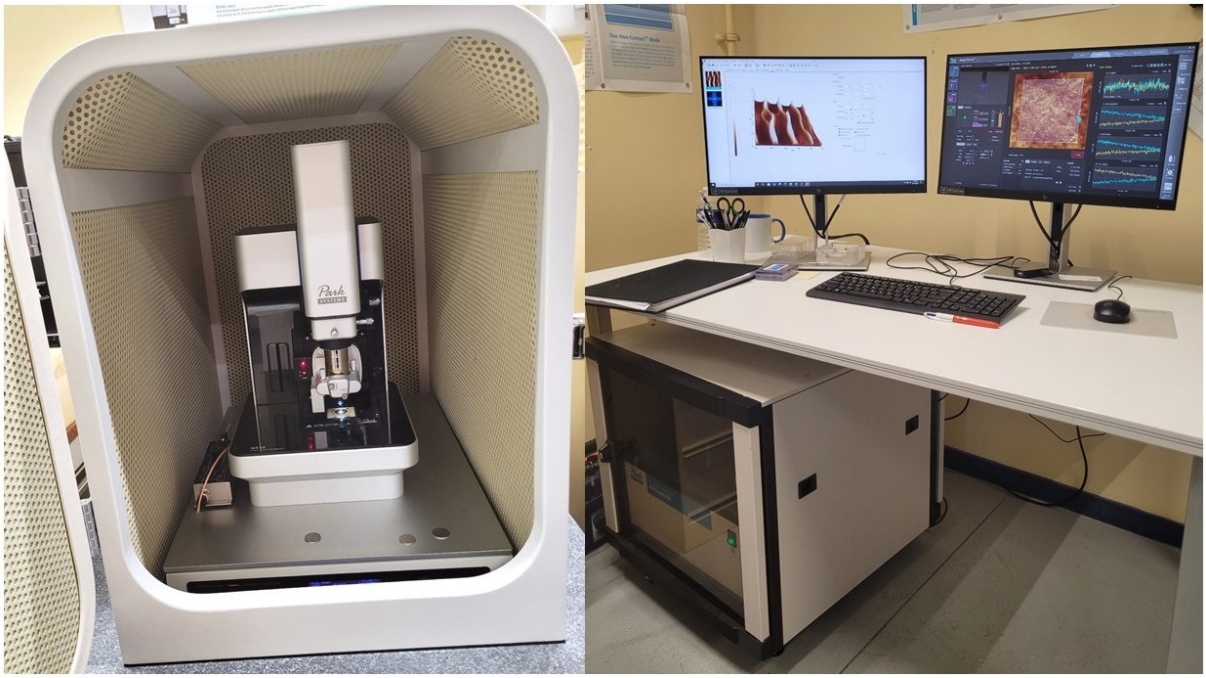

Figure II.12: The experimental set up used during this thesis is presented. This atomic force microscopy (AFM) is a Parks systems one. The whole system is in a chamber to avoid noise and other external influences on the measurement. The set up is linked to the computer where the data is stored and where the software allows to control and change the different parameters during the imaging. Note that all the images were taken in ambient air.

As with any measuring instrument, atomic force microscopy (AFM) has both advantages and disadvantages. Its strengths include the ability to measure in vacuum, liquid, or ambient air with no material restrictions. It offers nanometric resolution and 3D surface measurement. For the disadvantages, the main one is the scan size, with a maximum in Z of a few micrometres.

In this thesis, a Park Systems Nx10 atomic force microscope was used, as shown in figure II.12. To prevent external acoustic and light noise during measurements, the device contains an anti-vibration table and an acoustic enclosure. Measurements were carried out under ambient conditions. The X,Y scan areas do not exceed (100 × 100) μm^2 and a Z scan range of 15 µm. It can accommodate large samples up to 50 mm x 50 mm x 20 mm. A non-contact cantilever with a tip radius of ≈ 7 nm was used. Several parameters can affect the quality and reality of the surface structure size, including tip geometry and scan speed. For rough, high-resolution surfaces, this can

take several tens of minutes. The tool also includes a camera, which allows for the detection of the position of 2D material flakes on the substrate in real time.

3.4.2 X-ray diffraction

Prior to the Laue experiment in 1912, X-rays were not employed for crystal diffraction; in fact, the first use of X-rays was intended for industrial applications and more specifically in the medical field. The technique was later used and developed by W.L. Bragg. X-ray diffracion (XRD) has made it possible to characterise crystal structures and identify material phases. This non-destructive technique is based on the interaction of a sample's crystalline structure with electromagnetic radiation of the order of magnitude of the inter-reticular distances.
The X-ray diffraction method relies on the principle of exploiting the atomic lattice that makes up the material. These atoms form parallel crystal planes (hkl) equidistant by a distance of d_{hkl}. When these X-rays reach the target material, they may interact with the atoms making up the latter, thus deflecting their trajectories by elastic scattering. Two situations can be distinguished: the first occurs when there is the slightest phase shift between the scattered waves, so that the waves interfere destructively. The second occurs when the rays interfere constructively, i.e. when the scattered waves are in phase. The result is a diffracted wave of a certain intensity in the same direction. This occurs when the scattered rays have a step difference σ equal to the wavelength or n times the wavelength (n being an integer), i.e. :

$$\sigma = n\lambda = 2d_{hkl}sin\theta \tag{II.5}$$

with d_{hkl} the distance between two hkl planes and θ the half-angle of deflection.
This formula, known as Bragg's law, shows how the inter-reticular distances characteristic of the material under analysis can be obtained by measuring diffraction angles. Thus, the X-ray diffraction angle depends on, and is related to, the lattice spacing, provided that the wavelength used is of the same magnitude as the lattice distance. Figure II.13 shows an illustration of Bragg's law showing the constructive interference of scattered waves reflected from atoms of two atomic planes.

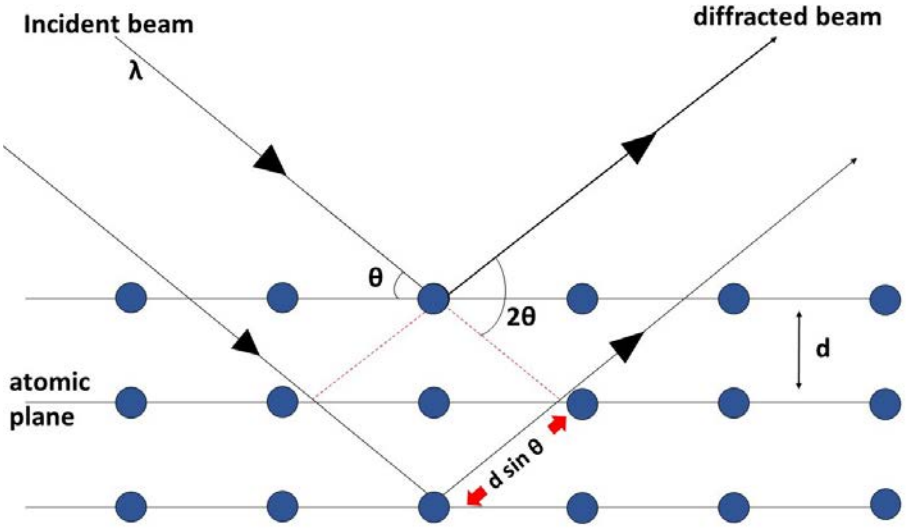

Figure II.13: Illustration of Bragg's Law for constructive interference.

During this thesis, X-ray diffraction measurements were made at ambient temperature using Bruker's Discover D8 High Resolution diffractometer. This device has an Euler platform allowing rotation along four axes, namely: $\theta, 2\theta(0-120°), \Phi(0-360°)$ and $\psi(0-90°)$ enabling the sample to be probed at different angles and at different depths in order to observe the various reflections of the crystalline planes characteristic of the analysed materials. Samples were glued to a glass plate and placed on the sample holder. X-rays were generated from a copper anode. Several optics are placed after the X-ray source and before the sample holder to optimise the X-ray beam. A Göbel mirror, with controllable slit sizes, is used to optimise the resolution of the beam, providing a parallel beam and allowing only Kα1 and Kα2 to be kept. To avoid misinterpretation of the spectra, a monochromator (based on germanium (Ge)) is used to remove the Kα2 wavelength and maintain just the Kα1 = 0.154056 nm wavelength. An absorber is also added to attenuate any excess intensity and protect the detector from damage. For the detection part, different types of detectors exist; in this study, the 1D LYNXEYE analyzer is used. It should be noted that although this device offers the possibility to make measurements in different geometric modes, in this study, the symmetrical mode geometry is the only one used with angle measurements of $2\theta - \omega$. 2θ is the incident angle of the X-ray beam, enabling it to probe the sample over several layers in depth depending on the diffraction angle. The alignment of the X-ray beam with the samples through different parameters is optimised at the beginning of the measurement, enabling comparison of the diffraction spectra of strontium titanate samples before and after irradiation.

Structural deformation measurement

The main measurement and analysis undertaken here focus on the damage and deformation of the crystal and the phase change that can occur after irradiation with swift heavy ions. The evolution of these effects with irradiation fluence is analysed, with particular attention paid to the impact of the angle of incidence of the ion beams on the different thickness layers of the mate-

rial. Knowing that the $2\theta - \omega$ diffractogram (with $\omega = 2\theta/2$) provides information and indications on the structure of the material through the lattice parameters, a change in the latter can be extracted.

Since lattice deformations are related to diffraction angles, one can get information about deformation from the peak shift 2θ by making a comparison before and after irradiation. The evolution of the lattice structure as a function of the perceived irradiation dose can thus be studied. The intensity of the diffraction spectra peaks provides information on the crystallinity of the material.

Figure. II.14 shows the reflection (200) of the diffractogramme of four $SrTiO_3$ samples of (100) crystallographic direction. One is unirradiated, and the three others were irradiated with 92 MeV Xe ions at an angle of 10.9° with three different fluences. A difference in intensity and a slight shift towards smaller 2θ angles can be observed.

It should be noted that the different diffractograms were acquired using the same acquisition parameters. An acquisition time of 2 seconds per step (for a step of 0.0002°) has been used, allowing to have an exact precision and a diffractogram in around one hour.

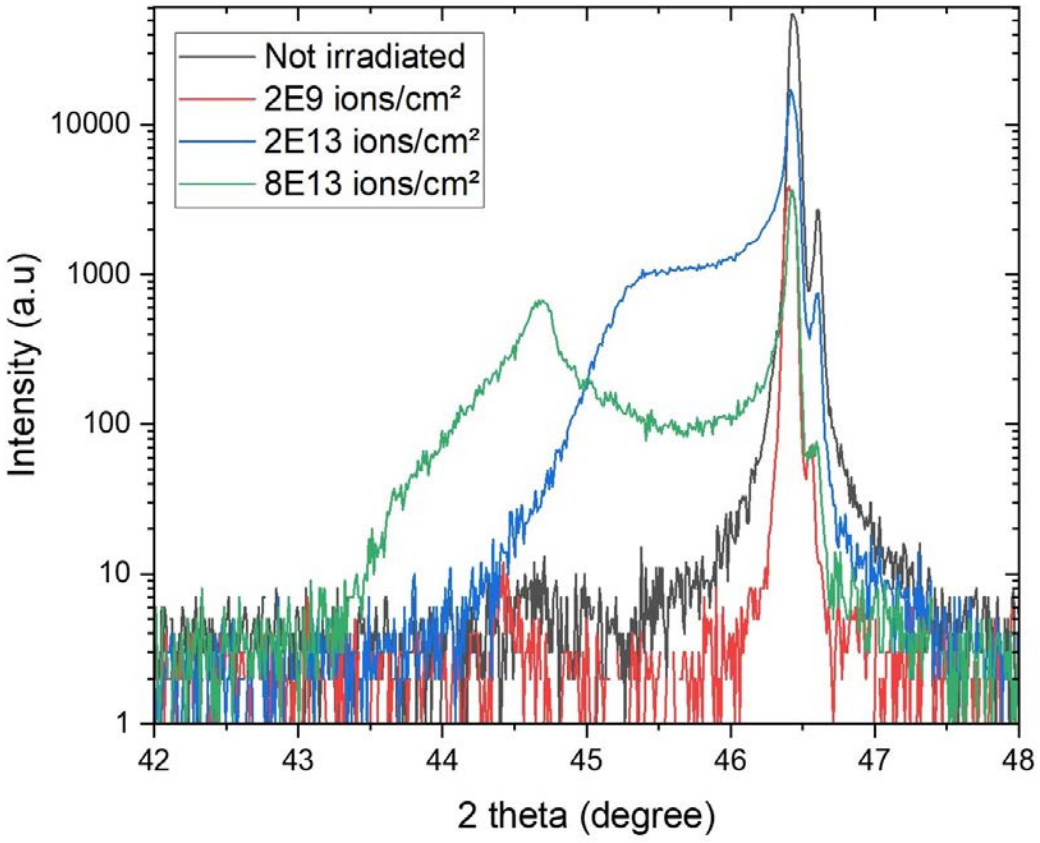

Figure II.14: X-ray patterns for (100)-$SrTiO_3$ irradiated with 92 MeV $^{129}Xe^{+23}$ ions at 10.9° with 2.16×10^9 ions cm^{-2} (red line) 1.89×10^{13}ions cm^{-2} (blue line) and 7.66×10^{13} ions cm^{-2} (green line) compared to a non-irradiated sample (dark line) with a probed depth of $\sim$ 8 µm for the (200) reflection.

The deformation ϵ of the lattice is given by:

$$\epsilon = \frac{a - a_0}{a_0} \tag{II.6}$$

"a" being the lattice parameter after deformation and "a_0" before deformation. In this way, the elastic deformation of the material can be obtained directly from the position of diffracting peaks before and after irradiation, or before and after deformation. This gives the conventional deformation of crystal:

$$\epsilon = \frac{d_{hkl} - d_{0hkl}}{d_{0hkl}} \tag{II.7}$$

X-ray diffraction (XRD) is a very powerful technique for probing matter in depth. It is often preferred for the analysis of crystalline samples such as $SrTiO_3$ because of its ability to provide information to identify the crystalline structure of the material, the size of crystals, or to detect the presence of defects. However, as the 2D materials are composed of one or a few layers of atoms, analysis with X-ray diffraction is difficult to conduct. Although X-ray diffraction is considered a non-destructive technique in most cases, in the case of 2D materials, given their thin film or sheet structure, it could, if used at very high intensities, cause damage. Raman spectroscopy is, therefore, preferred. Raman analysis is an optical excitation technique that uses only visible light. Measuring the intensity of light scattered by the material analysed is less likely to damage the material and is more sensitive to 2D structures. This technique can be used to identify the types of 2D materials, measure the thickness and quality of 2D materials, and even determine the structural properties of the material.

3.4.3 Raman spectroscopy

Raman spectroscopy is a very useful tool for studying the composition and characterising the structural properties of materials, whether organic or inorganic, in a wide variety of fields, including physics, medicine, biology, and chemistry. The Raman spectrometer's operating principle is based on the analysis of the molecular vibrations of the sample's components. Each atom gives rise to unique raman signatures depending on its state. Its principle is based on the inelastic scattering of light by the sample. When light strikes a sample, two types of scattering can take place: elastic scattering, known as Rayleigh scattering, and inelastic scattering, known as Raman scattering. The latter is named after Sir Chandrasekhara Venkata Raman, who first observed this effect in 1928 [140]. The device consists of a laser source from which monochromatic light of a certain wavelength is emitted, a sample holder, and a detection system that receives and analyses the scattered light. The latter will have a different frequency than the incident light. This difference, known as the Raman shift, is characteristic of the composition and, therefore, the structure of the substance through which it penetrates. The resulting Raman spectrum is represented by the intensity of the scattered light (Raman signal) as a function of the Raman shift. The latter enables us to extract a wide range of information, such as the type of material through the analysis of its molecular composition, its structure, or the concentration of a component in a material.
This technique is very popular when it comes to 2D materials, as it allows to quickly and easily

quantify the number of layers present in the sample [141] [10], as well as the presence of potential defects [142] [143] strain [144] or doping [145]. This data extraction is achieved by analyzing the position of peaks, which is determined by the vibrational frequency of the material's atoms. The intensity of the peaks can also provide information on the presence of defects or structural changes, which is directly proportional to Raman scattering.

Raman spectrum of molybdenum disulphide MoS_2

As we are interested in 2D materials (i.e. composed of a single layer of atoms), their characterization with a Raman spectrometer is a crucial step in determining the thickness of the layer and the potential defects and/or doping present, particularly after irradiation. Indeed, when 2D material is analysed with a Raman spectrometer, the molecular vibrations of the components are limited to in-plane motion, resulting in unique spectra that differ from bulk materials. During this thesis, molybdenum disulphide MoS_2 was extensively studied.
In the case of bulk MoS_2, four active modes are involved ($E_{1g}, E^2_{2g}, E^1_{2g}andA_{1g}$) as shown in figure.II.15 (a). However, two main bands are detectable in this study, namely the E^1_{2G} band corresponding to the in-plane vibrational frequency of molybdenum and sulfur atoms at around 385 cm^{-1} and the out-of-place A_{1g} band due to the vibration of sulfur atoms at a Raman shift of around 405 cm^{-1}.

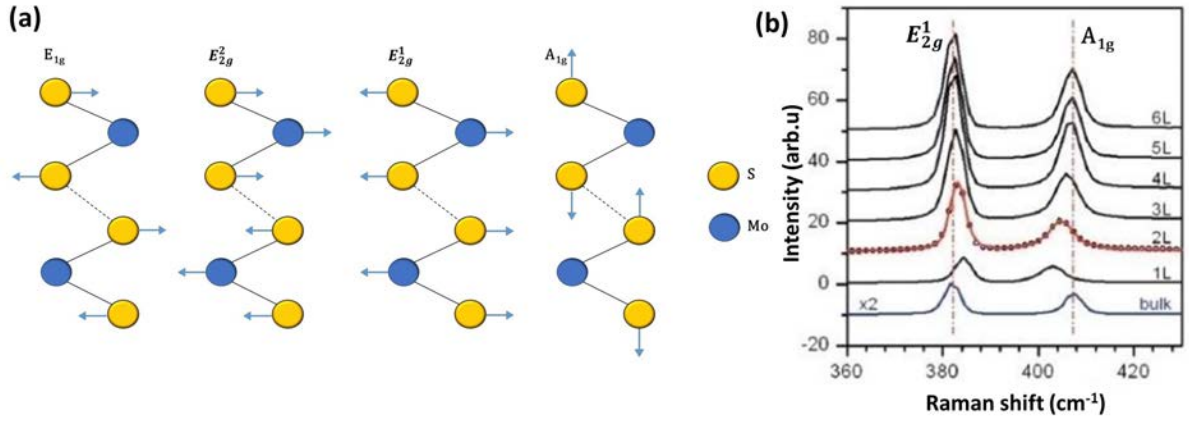

Figure II.15: (a) Atomic displacement of the four Raman active $E_{1g}, E^2_{2g}, E^1_{2g}andA_{1g}$ modes and (b) Raman spectrum of MoS_2 of different thicknesses [10]

.

Figure II.15 (b) [10] shows the difference of the Raman spectra when moving from a single-layer to a bulk material. One can note that a shift in peak position occurs as the number of layers from MoS_2 increases to bulk. This can be seen in the shift of the E^2_{g1} mode towards lower frequencies, while the A_{1g} mode shows a shift towards higher frequencies. In fact, the distance between the peaks representing the two vibration modes narrows as the number of MoS_2 layers decreases. This difference in position between the two peaks representing the two modes makes it possible to determine the thickness of the MoS_2 layers with a distance of $\sim 19\,cm^{-1}$ for single layer MoS_2 to

reach $\sim 25\,cm^{-1}$ for bulk MoS_2.

In this thesis, different samples of MoS_2 deposited on $SrTiO_3$ (STO) and SiO_2 mainly by CVD were irradiated with swift heavy ions. The fluence used varied from low, where single impacts dominate, to high fluences where overlapping impacts occur. The irradiation angle also had an impact on the modifications that could be obtained, ranging from 0.3° to 2°. The MoS_2 exhibits a certain resistance to defects when subjected to energetic irradiation. Since Raman analysis is highly sensitive to structural changes in a material, it allows to confirm the presence or absence of defects in the structure of the studied materials. This complements the analyses carried out with atomic force microscopes (AFM), where the modifications that can appear in the form of folds or cracks/rifts are not always observable. The results obtained will be presented and discussed in detail in Chapter five.

Chapter III

Effect of grazing incidence swift heavy ion irradiation on $SrTiO_3$

1 Introduction

Several studies have been carried out with the aim of creating nano-structured surfaces in various types of materials. In the present work, $SrTiO_3$ is given particular attention for this purpose. Several series of samples, the vast majority of which are oriented in the crystallographic direction (100), were irradiated with swift heavy ions (SHI). Previous studies have established that when this insulating perovskite is exposed to swift heavy ions and the required amorphization threshold of 12 keV/nm [18] is met, amorphous cylindrical tracks can appear in the bulk, accompanied by the formation of hillocks on the surface. This happens for irradiation in the single-impact regime, i.e. at low fluence and with an angle of incidence normal to the surface.
A structure with a different shape appears for irradiation under the same conditions but at a grazing angle. These structures come as chains of equally spaced nano-hillocks on the surface and a straight track in the bulk. The atomic force microscope (AFM) is frequently employed to characterise these surface hillock-like features. However, to observe the tracks and other defects induced in depth and beneath the surface, transmission electron microscopy (TEM) is usually used.
The following chapter will first present the parameters used during the different irradiation experiments. Then the results obtained on several series of polished, single-crystal strontium titanate $SrTiO_3$ (100) (110) samples from the Crystek company (Berlin - Germany) irradiated with SHI will be presented. Prior to moving on to high fluences, where the tracks overlap, the effect of low fluences, where individual impacts predominate, is looked at first.

2 Irradiation parameters

During these irradiation experiments, three types of beams on the IRRSUD beam-line were used. These were 92 MeV $^{129}Xe^{23+}$, 75 MeV $^{136}Xe^{19+}$ and 20 MeV $^{20}Ne^{6+}$. It corresponds when calculating the electronic energy loss at the surface with the SRIM code [1] (using a density of 5,117 g/cm^3) to 21 keV/nm, 19 keV/nm, and 4 keV/nm, respectively. Unlike the Neon beam, for both Xe ion beams, it is well above the stopping power threshold of 12 keV/nm needed for track formation on the $SrTiO_3$ sample [19]. The nuclear energy loss is almost negligible at these energies, contributing to only $\sim$ 1% of the total energy loss. It increases slightly in volume to reach a value of around 0.18 keV/nm for the 92 MeV Xe ion, 0.22 keV/nm for the 75 MeV Xe ion, and 0.005 keV/nm for the 20 MeV Ne ion. The projected range is $\sim$ 8 µm for the Xe ions onto de $SrTiO_3$ and 6 µm for the Ne beam.

Table III.1 summarises the various irradiation parameters and data used during this study. It should be noticed that only the one at high fluences and grazing angles of irradiation has been specifically indicated in this table.

Energy (MeV/u)	Ions species	Angle (degrees)	Fluence (ions cm^{-2})	Flux (ions cm^{-2} s^{-1})
0.55	$^{136}Xe^{19+}$	6.1	8.1×10^{13}	5×10^9
		8.1	1.41×10^{14}	
		10.9	1.89×10^{13}	
		10.9	7.66×10^{13}	
0.71	$^{129}Xe^{23+}$	1.5	2.62×10^{13}	5×10^9
		2.5	3.75×10^{13}	6.6×10^9
		3.5	6.1×10^{13}	5×10^9
		4	2×10^{13}	4×10^9
		4	4×10^{13}	4×10^9
		4	6×10^{13}	4×10^9
		4	8×10^{13}	4×10^9
		4	1×10^{14}	4×10^9
		4.5	6.75×10^{13}	6.6×10^9
		5.5	9.60×10^{13}	5×10^9
		6	3×10^{13}	7×10^9
		6.5	9.74×10^{13}	6.6×10^9
		7.7	6.86×10^{13}	4×10^9
		8	7.97×10^{13}	7×10^9
		8.5	1.27×10^{14}	6.6×10^9
		10	1.5×10^{14}	7×10^9
		10.7	9.5×10^{13}	4×10^9
		10.9	7.66×10^{13}	3×10^9
		12	2.4×10^{14}	7×10^9
		12.5	1.86×10^{14}	6.6×10^9
		16	3.9×10^{14}	7×10^9
		20.7	1.81×10^{14}	4×10^9
		30.7	2.61×10^{14}	4×10^9
		45.7	3.66×10^{14}	4×10^9

Table III.1: Irradiation parameters

3 Individual ion impact regime

The $SrTiO_3$ samples used have fairly smooth and clean surfaces, with a prominent pattern that is the terraces caused during polishing. Figure III.1 shows the surface before irradiation with the root mean square (rms) value of the surface roughness of 0.4 nm, indicating its cleanliness and smoothness without the need for initial treatment.

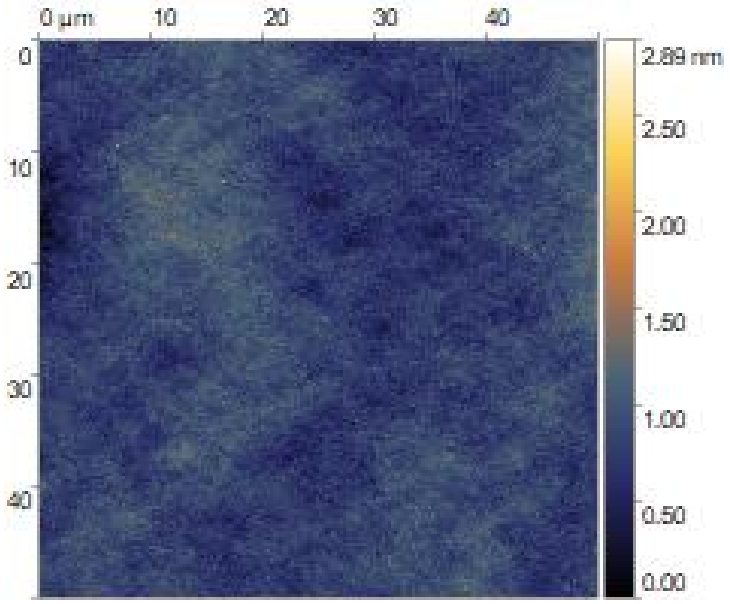

Figure III.1: (50×50) µm^2 AFM image of a non-irradiated (100)-$SrTiO_3$

The image III.2 (a) shows chains of nano hillocks obtained during irradiation with 92 MeV Xe ions at a nominal angle of 1.7° and low fluence, i.e. in the range where each ionic hit is discernible on the surface individually.
The profile of one of the chains in figure III.2 (b) gives a length of ~ 280 nm. Using the formula describing the relationship between the angle of incidence of the ions and the length of the chain: $l = d/\tan(\theta)$ [6] an angle of 1.43° is found, which, with the error bar included, is in good agreement with the irradiation angle chosen.

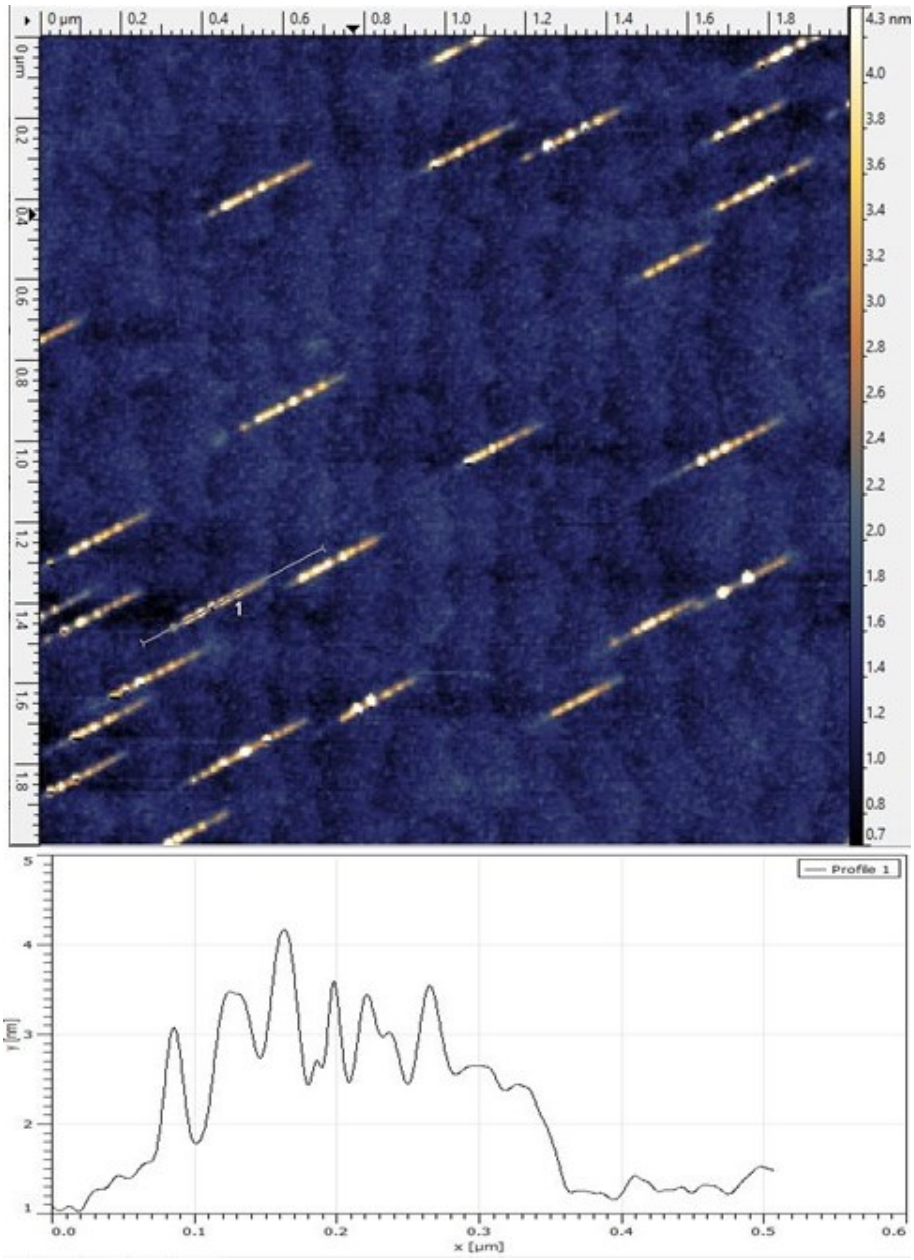

Figure III.2: (2×2) µm^2 AFM image of surface of $SrTiO_3$ irradiated with 92 MeV Xe ions at an angle $\sim 1.7°$ at low fluence. Chains of nano-hillocks measuring around 260 nm and the steps are observable on the surface. The profile of one of the chain is shown below the AFM image.

TEM analysis of irradiated $SrTiO_3$

Figure.III.3.(a) shows a SEM image of a strontium titanate sample irradiated with 92 MeV Xe ions at 3.7° with 5×10^8ions cm^{-2}. At low fluence, the individual effect of the ions can be seen with the formation of chains of nano-hillocks. For more in-depth analysis, focused ion beam scanning electron microscopy (SEM/FIB) was performed using a dual beam equipment. TEM plates were

prepared at the exact location of the chains on the surface. In fig.III.3.(b) a sample irradiated at 3.7° where a continuous track can be observed is shown (pointed with the two white arrows). However, for irradiation at a more grazing angle equal to 0.5°, as shown in III.3.(c), a discontinuous or even fragmented track appears below the surface, reminiscent of that observed on the surface under the same irradiation conditions, i.e. in the single-impact, grazing angle regime. This effect of the angle on the morphology of the modifications can be explained in the same way as for the formation of chains of nano-hillocks observed in the case of $SrTiO_3$ [6]. In this case, the deposited energy is directly related to the electron density and consequently to the formation of these chains of equally spaced nano hillocks.

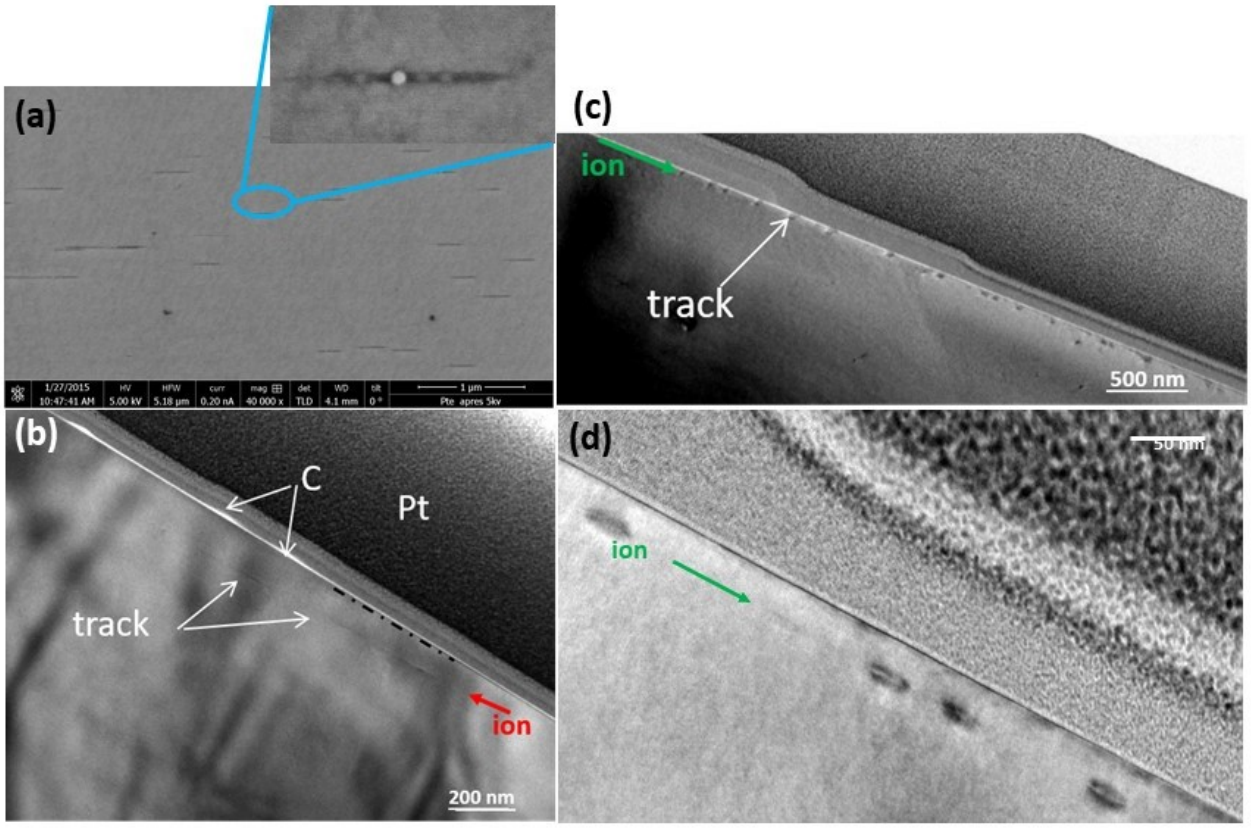

Figure III.3: (100)-$SrTiO_3$ irradiated with 92 MeV Xe ions in the individual ion impact fluence regime (a) SEM/FEG image for an irradiation at $\theta = 3.7°$; TEM cross-section images of a latent track observed for an irradiation at (b) $\theta = 3.7°$ (surface is marked with dotted line), (c) at $\theta = 0.5°$. The red and green arrows indicate the ion irradiation direction [11].

As mentioned in the previous chapter, the $SrTiO_3$ crystalline structure is composed of an atomic layer of Ti – O with a bond length of $\sim$ 1.97 Å and a layer of Sr – O spaced at around $\sim$ 2.76Å, which alternate successively. When irradiated with SHI at grazing angles, the ion penetrates the material at a defined angle and consequently passes through different regions with different electron

densities. During its journey and as it passes through the crystalline Ti – O and Sr – O planes, the ion will induce a greater energy loss in the Ti – O plane, as it contains the highest electron density than the Sr – O layer. This energy loss will occur for the nominal angle of 0.5° every 60 nm, whereas for the nominal angle of 3.7° with respect to the surface, it will occur every 6 nm [11]. Knowing the impact of the electronic spatial distribution on the energy loss process of this ion, one can assume that at the beginning of the ion trajectory and for an irradiation at a very grazing nominal angle of 0.5° amorphous spheres spaced with a radius of the order of that obtained in the cylindrical tracks, i.e. 2.4 nm, are formed. Analysis of the TEM images obtained in this case (fig.III.3(c)) gives an average distance between the spheres of about 44 nm, which gives an angle of incidence of about 0.35° which, with the set angle within the error bar estimated at 0.2°, is consistent. By increasing the angle towards the normal, as in the case of irradiation with a nominal angle of 3.7°,these amorphous spheres become more extensive and join to form a quasi-continuous track Fig. III.3(b). Moreover, in Fig.III.3 (b-d), one can notice a density contrast around the tracks; this corresponds to a deformation field in the crystalline matrix surrounding the tracks. This agrees with the observations done for $SrTiO_3$ irradiated at normal incidence [18] [19].

Studies undertaken with the same material have shown that high fluence irradiation at angles perpendicular to the surface induces defects in the crystal [18] and amorphization of the surface [19]. Considering the reported track radius of (2.4 ± 0.4) nm, the amorphous tracks will overlap as the irradiation progresses. For example, for an iradiation at 10^9ions cm^{-2}, 10 tracks can be created on $1\mu m^2$, the overlap is then 0.01 % and 50 % for a fluence of 5×10^{12}ions cm^{-2} corresponding to $\sim 5 \times 10^4$ impact/μm^2. The surface will then, for a fluence $\geq 1 \times 10^{13}$ ions cm^{-2} amorphize and form an amorphous layer of a few micrometers thick [19].

Now that the results obtained on the $SrTiO_3$ irradiated with SHI in grazing incidence at low fluence have been described, its (STO) behaviour at high fluences and the impact of this collective effect at grazing angles on its structure and morphology are the subjects of the current work and the presentation that follows.

4 Development of surface structures under multiple ion impact irradiation

An X-ray diffraction study was undertaken in order to probe the material in its entirety and to study the structural deformations that can occur after irradiation with swift heavy ions at grazing incidence. Figure. III.4 (a) shows the X-ray diffractogram patterns for 2θ incidence angles ranging from 20° to 110° and where the four characteristic peaks of $SrTiO_3$ of crystallographic direction [100] are visible. In red, there is the unirradiated sample and in blue a sample irradiated at 6° with 8×10^{13} ions cm^{-2}. In III.4 (b) and III.4 (c) the reflections (100) and (200) are depicted. These two reflections correspond to a probed depth of approximately 4 and 8 µm respectively, which corresponds to the distance travelled by the ion in the material and well beyond. In both cases, there was a clearly visible reduction in the intensity of the diffracted signal compared with

the unirradiated signal. It is known that the intensities indicate the diffracting volume within our crystal. This reduction means then, that a loss of crystallinity of the initial structure occurs. This can be a result of the irradiation inducing crystal disordering followed by surface amorphization. Additionally, a large broadening on the 2θ axis extended towards low diffraction angles is observed. This can be due to an important tensile strain induced by irradiation [19].

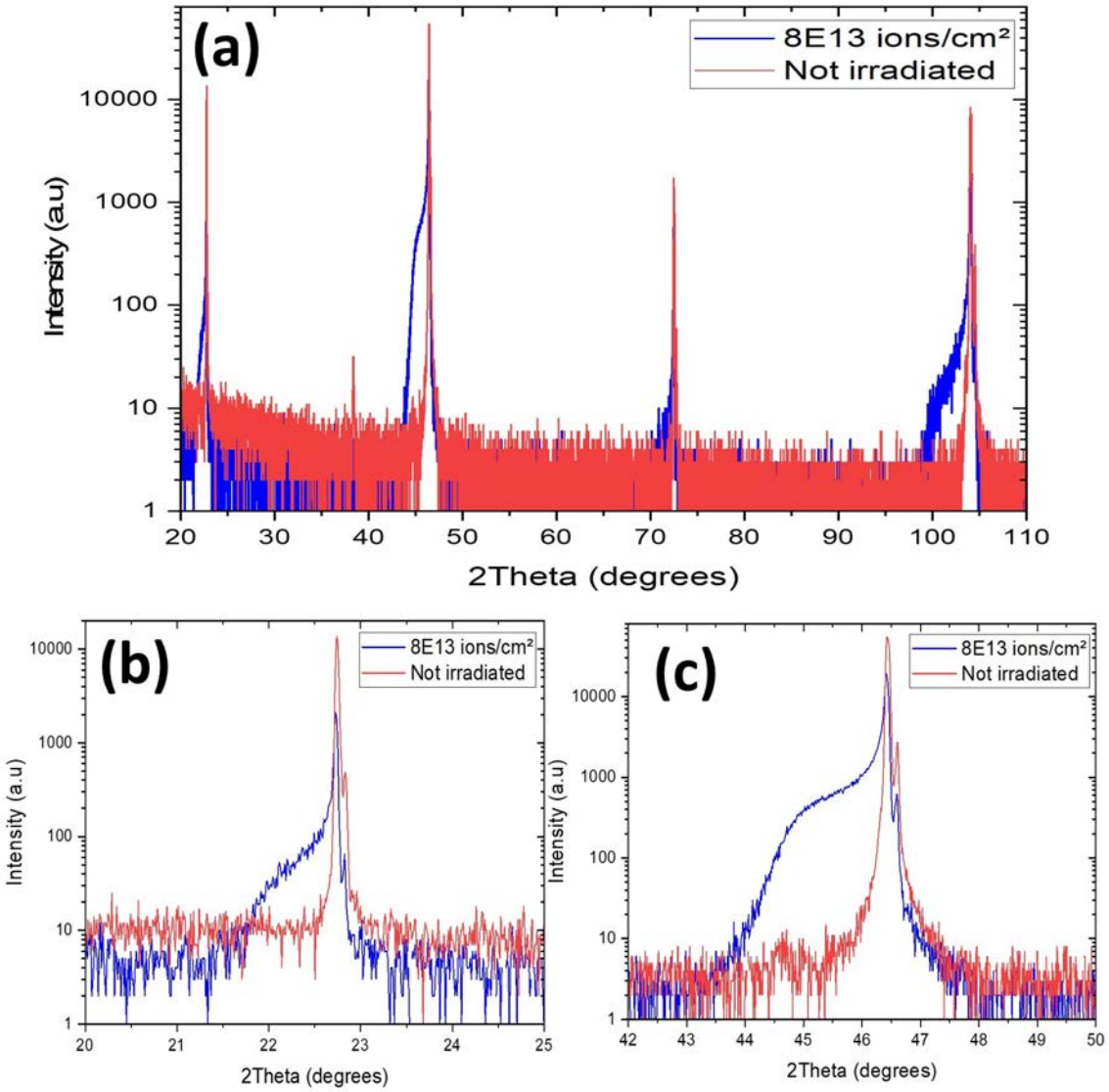

Figure III.4: X-ray patterns for (100)-$SrTiO_3$ irradiated with 75 MeV $^{136}Xe^{19+}$ ions at 6° with 8×10^{13}ions cm^{-2} compared to a non-irradiated sample with a probed depth of $\sim$ 4µm for the (100) reflection (b) $\sim$ 8µm for the (200) reflection (c)

.

These results clearly show an effect of irradiation at grazing angle on the structure of the material

investigated. To confirm the presence of disorder and the formation of an amorphous layer on the surface, transmission electron microscope (TEM) analyses were carried out on this sample. Figure. III.5 shows STEM images of a cross section of $SrTiO_3$ (100) prepared by FIB. The presence of different contrasts can be observed, which is synonymous with the presence of regions of different characteristics in the sample.

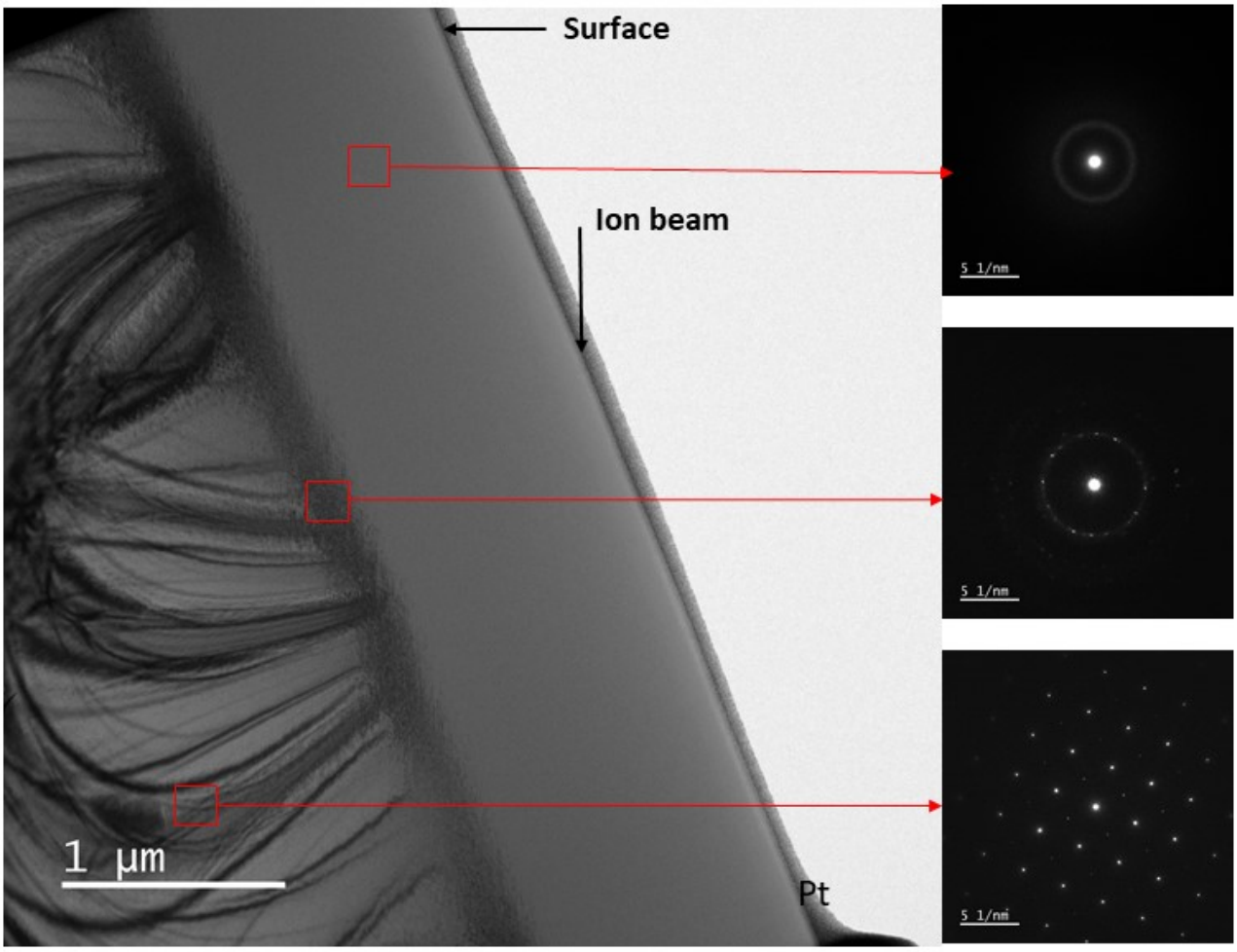

Figure III.5: TEM image of a (100)-$SrTiO_3$ sample irradiated at $\theta = 6°$ with $\phi = 8 \times 10^{13}$ions cm^{-2}. The ion beam direction is indicated with dark arrow. In the right side of the image three images show selected area electron diffraction patterns (SAED) taken at different depths of the sample.

On the right side of the image in Fig.III.5, different selected area electron diffraction (SAED) patterns are taken from different regions along the ion path in the target. The first pattern was taken in a region close to the surface. A single diffuse ring can be observed, representative of the amorphous phase and the amorphization of the crystal by the incident ions. A direct measurement of the amorphous layer extending from the surface to the edge of the second region, characterised by a darker contrast, gives a thickness of around 1.0 µm. Going deeper, the diffraction pattern shows

a diffuse ring with bright spots, synonymous with the presence of disorder and partial amorphization. Below this region and much deeper into the crystal, one can see that this region has remained single crystalline, as shown in the last diffraction pattern. These results, therefore, confirm that an amorphous layer was induced on the surface. In addition, a region with defects is also created below.

These kinds of deformations and structural changes have already been observed for high-fluence irradiation at normal incidence to the surface (90°) [19]. These results confirm that the irradiation geometry does not change this. However, the thickness of the amorphous layer is different and appears smaller than for an irradiation normal to the surface, due to the grazing aspect of the irradiation.
As the material was probed in depth, it is now known that irradiation at a grazing angle induces the formation of an amorphous layer on the surface, with the presence of a deformation in the layer beneath it. What is, then, the impact on the sample surface?
To find out, atomic force microscope analyses were carried out to image and study the morphology and topography of the surface of the investigated samples and thus see the effect of these irradiations at high fluences and grazing incidence. For clarity, only a selection of AFM images will be presented.

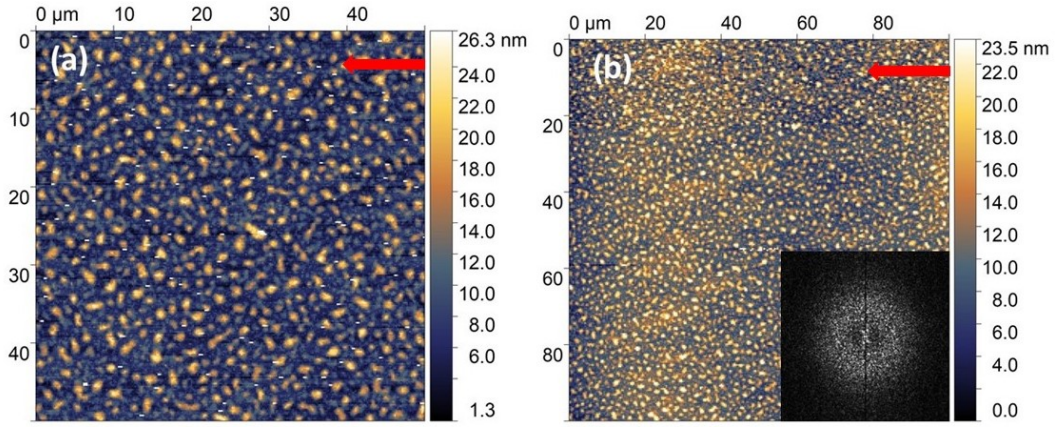

Figure III.6: AFM images of $SrTiO_3$ (100) irradiated at $\theta = 10.9°$ with $\phi = 7.66 \times 10^{13}$ions cm^{-2} with a scan of (50×50) µm^2 (a) and (100×100) µm^2 (b). The direction of the ion beam is indicated by the red arrow.

Figure III.6 shows the surface of an $SrTiO_3$ (STO) sample irradiated at a nominal angle of 10.9° with a fluence of about 7.66×10^{13}ions cm^{-2}. In fig.III.6(a), one may observe the formation of a bump-shaped structure, reminding one of hillock-like structures in the case of perpendicular irradiation. The total surface roughness here is around 5 nm. By enlarging the scan area to (100×100) µm^2 fig.III.6 (b) and performing the Fourier transformation (inset), a secondary and larger structure normal to the direction of the ion beam is present. It has a periodicity of around 100 µm and gathers all of the protrusions present on the surface. As it hangs above the other surface features, we will refer to it as the "primary structure."
By analysing the other STO samples (100) and (110), including those irradiated with a fluence

of about 2×10^{13}ions cm^{-2}, almost the same type of structure was observed. However, at lower fluences, the surface showed only the formation of hillock-like structures and not these large wave-like structures. By changing the irradiation angle and with higher fluences, as shown in Fig.III.7, AFM images of the surface of strontium titanate samples (100) irradiated with SHI at (a) 8.1° with 1.4×10^{14}ions cm^{-2} and (b) at a nominal angle of 6.1° with 8×10^{13}ions cm^{-2} are presented (note that these images were taken in ambient air with a multimode AFM). A considerably larger topographical change on the different surfaces, with the emergence of far more obvious and pronounced periodic structures, is observed. These structures have a certain amplitude and are oriented perpendicularly to the ion beam. We will refer to these structures as "secondary waves" and the space between them as "valleys." In order to see whether the crystallographic direction could have an impact on the appearance and formation of these periodic microstructures, irradiations were undertaken on $SrTiO_3$ (110) with the same parameters. Thus, these microstructures on the surface were also observable, as can be seen in Fig.III.7 (c) for an irradiation at $\theta = 8.1°$ and $\phi = 1.4 \times 10^{14}$ions cm^{-2} and (d) at $\theta = 6.1°$ with $\phi = 8 \times 10^{13}$ions cm^{-2}.

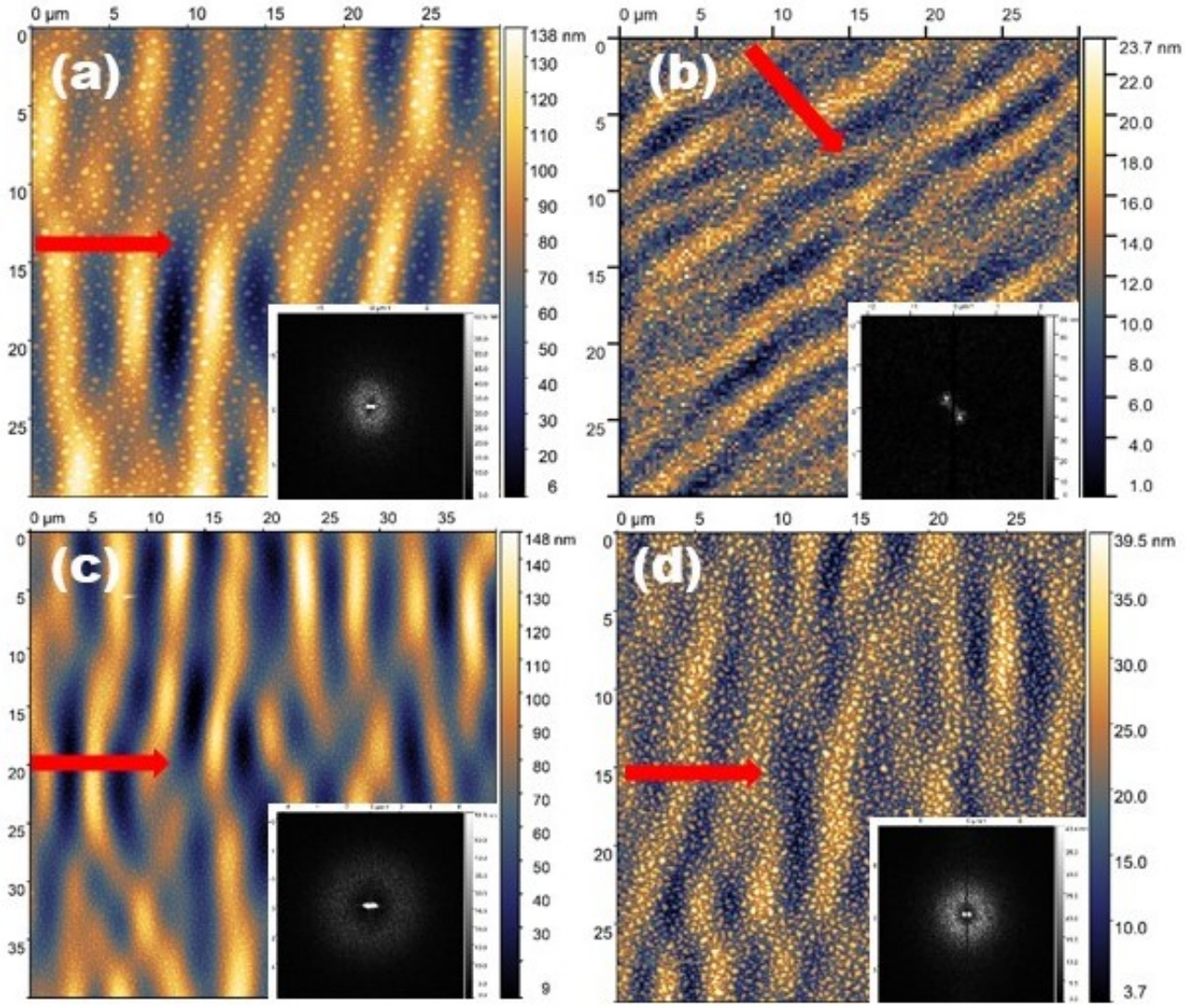

Figure III.7: AFM images of $SrTiO_3$ (100) irradiated at (a) $\theta = 8.1°$ with $\phi = 1.4 \times 10^{14}$ ions cm^{-2} and (b) at $\theta = 6.1°$ with $\phi = 8 \times 10^{13}$ ions cm^{-2} and $SrTiO_3$ (110) irradiated in (c) at $\theta = 8.1°$ and $\phi = 1.4 \times 10^{14}$ ions cm^{-2} and (d) at $\theta = 6.1°$ with $\phi = 8 \times 10^{13}$ ions cm^{-2} with the corresponding 2DFFT inset. The direction of the ion beam is indicated by the red arrow.

This type of structure is often characterised by its periodicity, or, as it is called in some studies, wavelength. This distance from the highest point of one wave to the next will be called "periodicity." There are several possible methods for accessing the geometric characteristics of an AFM image. Using image processing software such as Gwyddion or WSxM 5.0, the periodicity can be obtained using different methods. Either with the two-dimensional autocorrelation function (2D-ACF). This involves detecting a periodic signal through which the periodicity value can be obtained directly. Another method is the two-dimensional power spectral density (2D-PSD), which corresponds to the Fourier transform of the autocorrelation function. Finally, the method most commonly used for signal processing of periodic patterns is the Fourier transform. As can be seen from the different

images in the figure III.7, the two-dimensional Fourier transform (2D-FFT) inset clearly shows two spots synonymous with a periodic structure. To get more information from the 2D-Fourier transform, the profile line is plotted. Figure III.8 shows an example of the profile of the Fourier transform in Figure III.8.
Through the position of the peaks, the separation frequencies of the periodic patterns (waves) in reciprocal space can be extracted, i.e. a switch from the spatial domain to the frequency domain is done. To obtain these values, a Lorentzian fit is applied to the profile, from which the exact positions of the peaks are derived. Then, the inverse of the difference between them is calculated. The value obtained represents the periodicity (separation) of the waves observed in the AFM images.

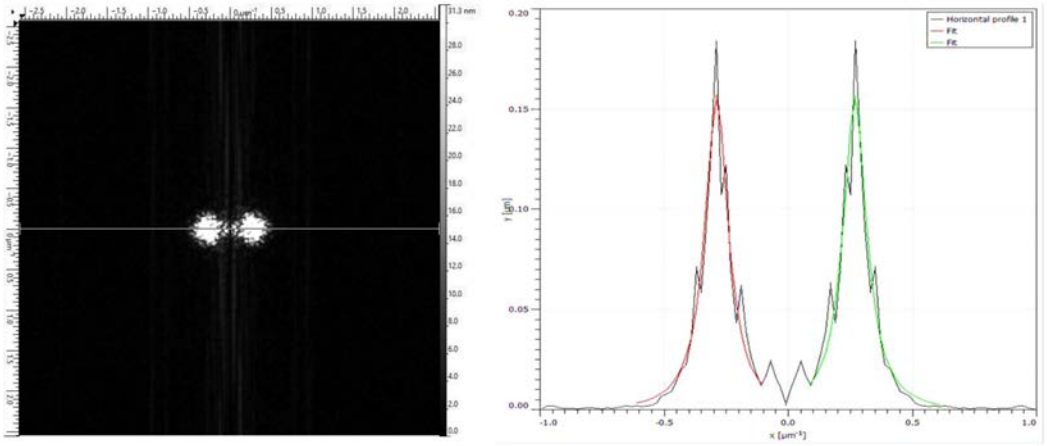

Figure III.8: The 2D Fourier transform of a periodic structure (wave) and its profile section.

The periodicity was therefore extracted for samples irradiated at three different angles, namely 6.1° , 8.1° and 10.9° for the two crystallographic directions (100) and (110). It was observed that the periodicity does not vary for the same type of sample with two different crystallographic directions. A difference is nevertheless noticeable in the wave formation for the sample irradiated at 10.9°. In figure III.6, this reorganisation of the surface into a distinct periodic shape with the so-called "secondary waves" was not observed or formed. However, a much more important periodic structure is present with a periodicity around 100 µm for the two crystallographic directions and for two different fluences, namely 2×10^{13} ions cm^{-2} and 8×10^{13} ions cm^{-2}. One can assume at this point that these primary structures are independent of the secondary wave structure. They probably did not develop further into visible structures. This is probably due to insufficient fluence, as a result of which the surface layer froze before it had time to increase in amplitude and develop into very distinct waves of a few micrometres of periodicity.
It should be noted that, in addition to the methods mentioned above, the profile taken directly from the AFM images can also provide several pieces of information, such as the height, width, and periodicity of the waves. Many of these techniques were used during image processing, depending on the number and purpose of the images. The method used each time will be specified.
Figure III.9 illustrates an example where the primary and secondary structures can be distinguished in order to highlight and summarise the differences between them.

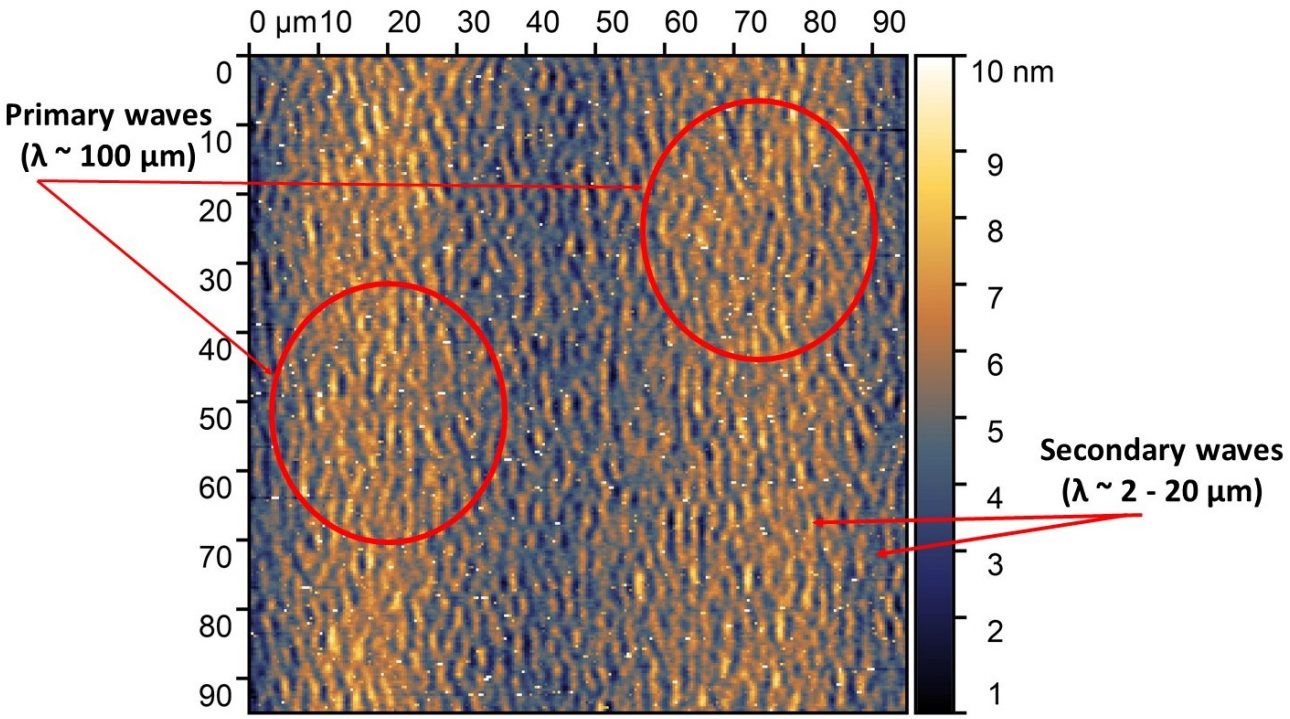

Figure III.9: AFM images of $SrTiO_3$ surface irradiated at a grazing angle where the two periodic structures, namely the primary waves and the secondary waves are depicted with the red arrows.

Figure III.10 shows the evolution of the periodicity, the height, and the width of the secondary waves with fluence for the different samples irradiated at 6.1° and 8.1°. As mentioned above, for the samples irradiated at 10.9°, since the secondary periodic structure is not correctly formed, the different parameters cannot therefore be extracted in this case. So for the sake of clarity, only the case where "secondary" waves-like structures are present will be shown. As far as these structures are concerned, their periodicity varies between 4 µm and 6 µm with a slight increase for the 8.1° compared to the 6.1°. As for the width, there is no perceptible change. However, we did notice a significant increase in the height with increasing fluence.

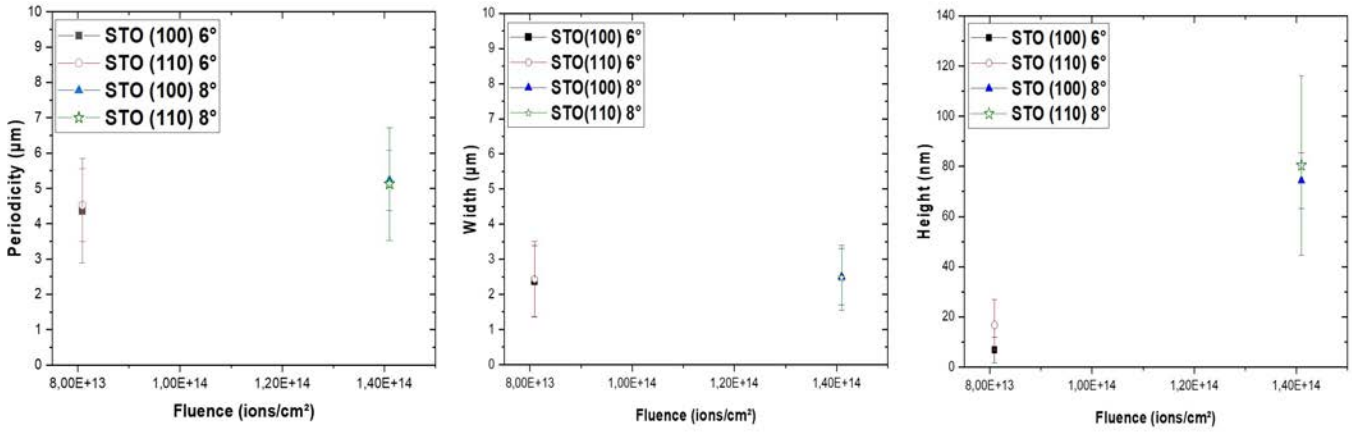

Figure III.10: Evolution of the periodicity, width and height of waves formed on $SrTiO_3$ (100) and (110) as a function of fluence for samples irradiated at $\theta = 6.1°$ and $\phi = 8 \times 10^{13}$ ions cm^{-2} and $\theta = 8.1°$ with $\phi = 1.4 \times 10^{14}$ ions cm^{-2}.

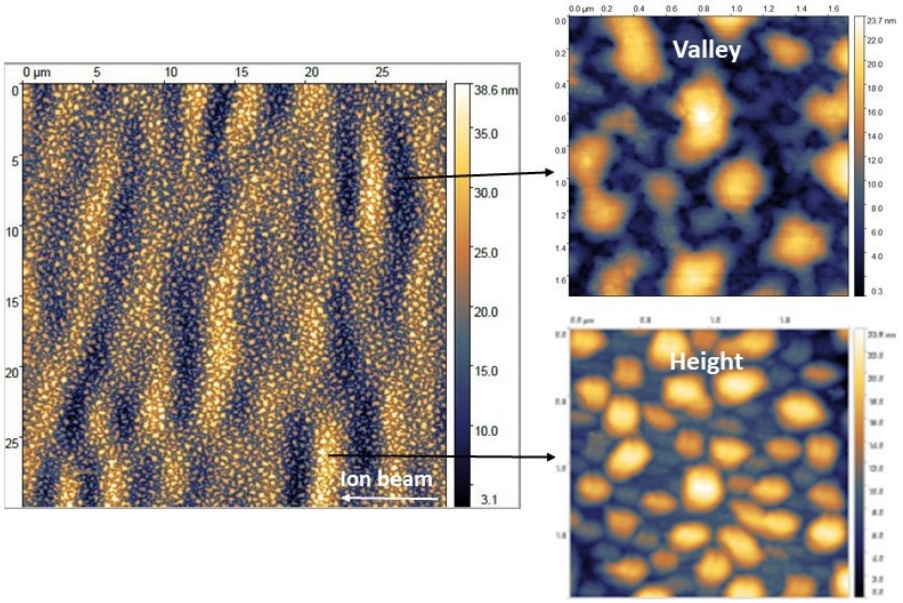

Figure III.11: AFM image of $SrTiO_3$ (110) irradiated at $\theta = 6.1°$ and $\phi = 8 \times 10^{13}$ions cm^{-2} with Xe ions of 0.55 MeV/u (a) Zoom on the valley part (b) zoom on the heights (c).

As can be seen in the figure III.11 and as discussed above, the formation of the waves is accompanied by the formation of structures such as hillocks over the entire surface of the sample. Figure III.11 shows the appearance of these round or oval-shaped protuberances at the top of the waves and in the hollows of the valleys. A detailed analysis was carried out using cross-sections of hillocks in both areas to study the evolution of these protuberances in the different irradiated samples, depending on their location, and to see if a certain trend could be found depending on

their location and the irradiation parameters. Figure III.11 (a) summarises the steps followed to obtain the data. A vertical and horizontal profile section of several hillocks in different areas of the sample was made. Then, by averaging over the whole, the variation of the different characteristics according to the irradiation parameters can be represented. In figure III.11 (b), the height of the hillocks as a function of the fluence applied is shown for the different irradiation angles. The distribution of the height is fairly random, with a slightly greater value for the protuberances in height.

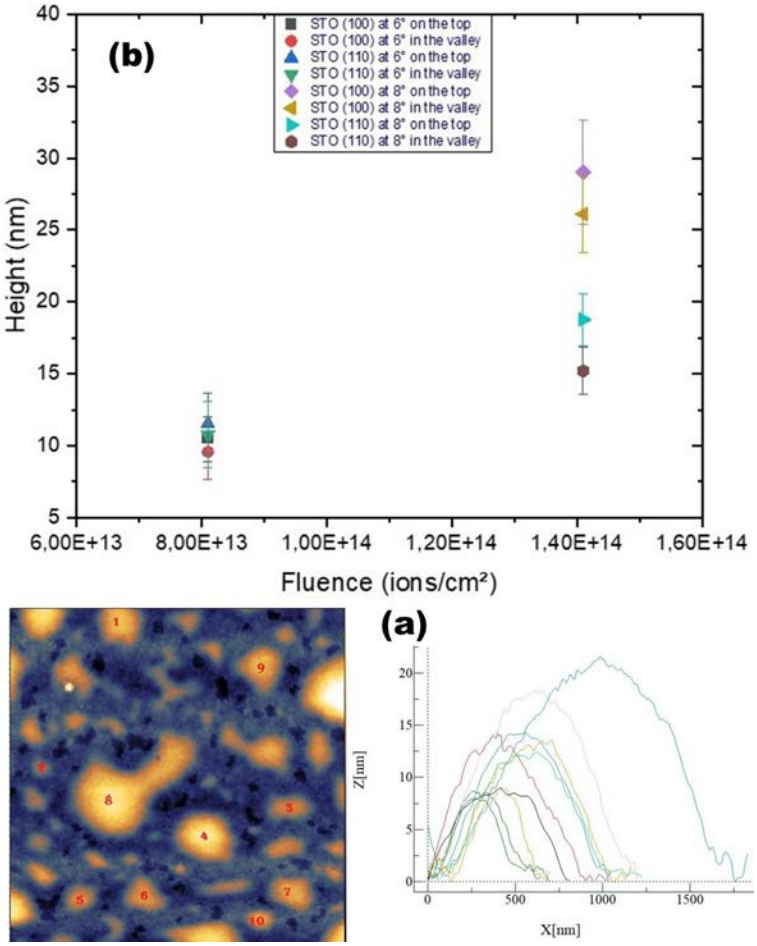

Figure III.12: (a) hillocks like structure profile section of the associated AFM image, (b) evolution of the height of the hillocks as a function of the fluence in the height and in the valleys for $SrTiO_3$ (100) and (110) irradiated at $\theta = 6.1°$ and $\phi = 8 \times 10^{13}$ ions cm^{-2} and $\theta = 8.1°$ and $\phi = 1.4 \times 10^{14}$ ions cm^{-2}.

Conclusion

Thus, in this section, the formation of three different types of structures following the SHI irradiation

of strontium titanate (100) and (110) samples at grazing angles was reviewed. These structures come in the form of microscopic waves oriented perpendicular to the ion beam and hillocks. Two types of waves were observed following high fluence irradiation. The so-called "primary waves", have a periodicity of the order of 100 µm with an almost negligible amplitude, which makes their observation and analysis difficult. The second type of wave-structure is named "secondary waves", which have a periodicity $< 10\,\mu m$. These two waves-like structures are complemented by a third features, a hillock-like structure, the size of which varies randomly. Based on these initial findings, and in order to confirm and compare the results using irradiation with higher energy while remaining in the energy range below 1 MeV/u. a second series of samples was irradiated consistently with grazing angles and fluences where the tracks overlap.

5 Surface microstructuring of $SrTiO_3$ (100)

Introduction

Another set of (100)-$SrTiO_3$ samples were irradiated with a different ion beam in this second irradiation step, $^{129}Xe^{23+}$ with an energy of 0.71 MeV/u. For the samples irradiated with 2×10^{13}ions cm^{-2} at a nominal angle of 10.9°, only the "primary" structure's presence is discernible. Its periodicity is around 100 µm. However, when irradiated at the same angle but with a higher fluence of 8×10^{13}ions cm^{-2}, as illustrated in the figure III.13, the formerly flat surface now has secondary waves beginning to form. These waves are accompanied by microstructures in the form of hillocks or bumps distributed over the entire surface. These are similar to those observed and presented previously in section 4 with the 0.55 MeV/u Xe ion beam. There is, however, an exception; after several analyses, an observation was made. These protuberances were not recurrent. As it will be presented later in this chapter for Xe SHI irradiations at 0.71 MeV/u, this is a singular effect that may be due to a series of previously contaminated samples.

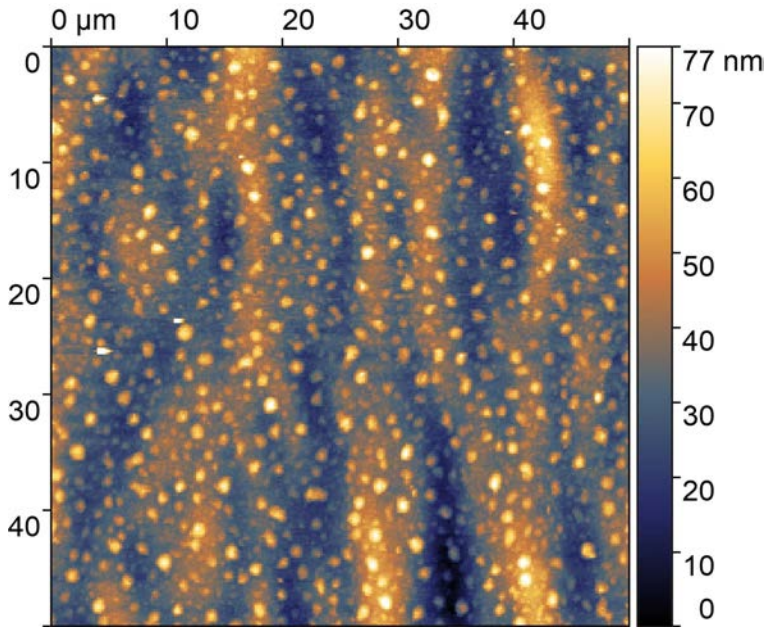

Figure III.13: (50×50) µm^2 AFM image of $SrTiO_3$ irradiated at $\theta = 10.9°$ and $\phi = 8 \times 10^{13}$ ions cm^{-2}.

5.1 Creation of two ripple forms

By irradiating strontium titanate with swift heavy ions at grazing angles of incidence, inelastic (electronic) energy loss is induced in a small nanometric volume of the ion impact in a regions close to the surface. Surface effect is then possible and has been confirmed. In order to see whether this phenomenon of reorganization of the surface into quasi-periodic structures is reproducible, a large part of this study was devoted to investigating the response of $SrTiO_3$ to swift heavy ions

(SHI) with mainly $^{129}Xe^{23+}$ beams for different angles and fluences. All this will be presented in what follows. Given that the amorphisation of the surface of the sample under SHI was confirmed, we decided to investigate the rest mainly by means of AFM measurement in order to extract data relating to the morphology of the surface microstructures and to obtain more information on the trend in their evolution.

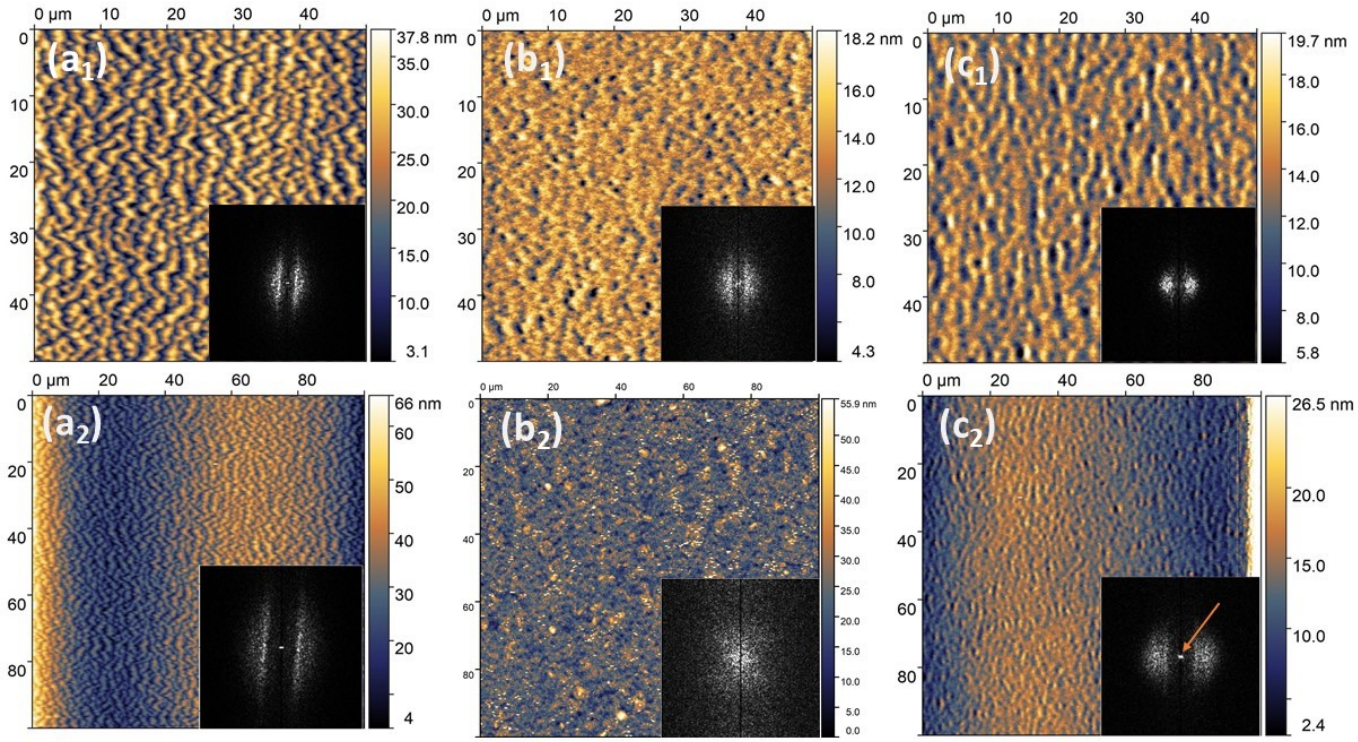

Figure III.14: AFM images of SrTiO3 (100) surfaces irradiated with 92 MeV Xe ions at $\theta = 1.5°$ with $\phi = 2.62 \times 10^{13}$ions cm^{-2} with a scan size of (50×50) µm^2 in (a_1) and (100 ×100) µm^2 in (a_2), $\theta = 2.5°$ with $\phi = 3.75 \times 10^{13}$ions cm^{-2} with a scan size of (50×50) µm^2 in (b_1) and (100 ×100) µm^2 in (b_2) and $\theta = 3.5°$ with $\phi = 6.1 \times 10^{13}$ions cm^{-2} with a scan size of (50×50) µm^2 in (c_1) and (100 ×100) µm^2 in (c_2)

Using the support described in chapter 2 and illustrated in fig.II.10, it was possible to irradiate a series of samples at angles ranging from 1.5° to 45° at different fluences. Some differences are noticeable depending on the fluence and angle used. Three examples are shown in the figure III.14, namely in (a_1, a_2) $SrTiO_3$ irradiated at a nominal angle of 1.5° with 2.62×10^{13} ions cm^{-2}, in (b_1, b_2) at $\theta = 2.5°$ with 3.75×10^{13} ions cm^{-2} and in (c_1, c_2) 3.5° with 6.1×10^{13} ions cm^{-2}. It can be seen that the surface is quite rough with Rq = 6.8 nm , 2 nm and 2.2 nm respectively. Analysis with 2D Fourier Transformation: as can be seen in the inset of the images, there are two clearly separated spots. This indicates the presence of a periodic structure perpendicular to the ion beam. The position of these peaks allows to estimate the periodicity of the patterns at (3.44 ± 0.31) µm in (a_1), (3.56 ± 0.6) µm in (b_1) and (2.64 ± 0.5) µm in (c_1).
The presence of a second pair of spots in (a_1) and (b_1) suggests the presence of a second and larger

structure. Larger AFM scans were, therefore, conducted (FigureIII.14 ($a_2 - c_2$)). They reveal the presence of another structure overlapping this one, which is also oriented perpendicular to the ion beam. Although this structure shows a very small amplitude, the corresponding 2D Fourier transforms of each of the images show the presence of two second peaks (indicated with an arrow in the Fourier transform of Fig. III.14 (c_3), whose positions give a much larger periodicity of about (115 ± 4) µm for (a_2) and (102.32 ± 3) µm for (c_3). This larger structure was not observed in the second sample irradiated at $\theta = 2.5°$, which may be due to the fluence not being high enough. This result reminds of the type of structures observed previously with the Xe ion beam at 0.55 MeV/u, which were referred to as "primary" structures. Analysis of the rest of the samples showed an evolution of these structures with fluence up to an angle of around 11°. Beyond that, the secondary wave structure takes over, and the primary one is no longer observable.

Figure III.15 (a) shows the evolution of the periodicity of primary structures as a function of fluence for different angles. As fluence increases and for increasing angles, there is a gradual decrease in periodicity. The primary structure gradually fades until it no longer appears at higher angles and fluences. In contrast, the secondary structures begin to form distinct periodic waves (Fig. III.15 (b-c)). This decrease in periodicity is accompanied by an attenuation of the Fourier transform signal of the specific spot pair for this primary periodic structure (Fig.III.15 inset(b)), until it disappears, leaving only the signal describing the periodic secondary waves (fig.III.15 inset (c)). One can also see, in the part circled in blue (Fig.III.15 (a)), an example of the effect of the angle. For almost the same fluence value, the periodicity of the primary structures decreases with increasing irradiation angle towards the surface normal. Having no other point of comparison, a trend or a specific effect of the angle on this structure cannot be deduced. The effect of angle of irradiation on the evolution of the secondary periodic waves shows the opposite effect; this will be discussed in more detail later.

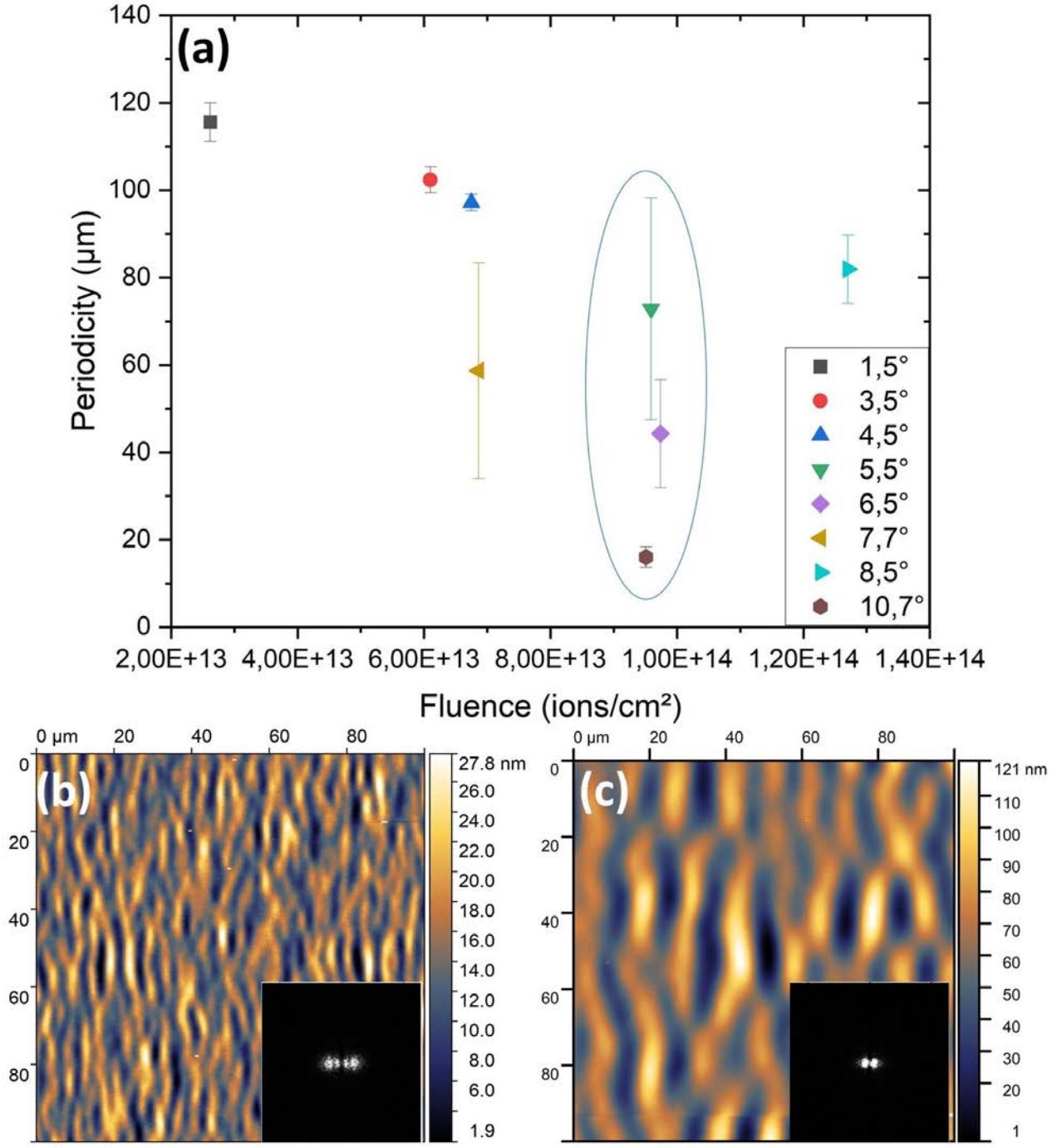

Figure III.15: (a) representation of the evolution of the primary waves periodicity as a function of fluence, for different angles. (b) and (c) AFM images of $SrTiO_3$ (100) irradiated with 92 MeV Xe ions at (b) $\theta = 10.7°$ and $\phi = 9.5 \times 10^{13}$ ions cm^{-2} and (c) at $\theta = 20.7°$ and $\phi = 1.81 \times 10^{14}$ ions cm^{-2}.

5.2 The angle-dependence of the periodicity

It was found that the surface reorganisation process starts with the formation of a primary structure at fluences of about 3×10^{13} ions cm^{-2}. This fluence is not high enough to finalise the formation of wave structures in the order of a few micrometers. Given that the aim of this study is to generate surface microstructures, including the one with the waveforms, and to control their shape, in what follows, the focus will be on the formation of secondary waves. The study continued with fluences of up to 4×10^{14} ions cm^{-2} and angles of up to 45° in order to analyse the process of formation of these microstructures and the impact of the angle and fluence used on their development and evolution. Fig.III.16 shows AFM images of the surface topography of different (100)-$SrTiO_3$ irradiated at room temperature with 92 MeV Xe with fluences and angles ranging from $\theta = 4.5°$ to $\theta = 30.7°$ for different high fluences. The black arrows indicating the direction of the ion beam are here to facilitate the visualisation of the incoming ion beam. It is clearly observable that the formation of waves oriented perpendicular to the ion beam evolves with fluence and for the different angles used. At relatively low angles (grazing) the periodicity remains $\prec 10$ µm, as can be seen in fig.III.16 (a) where for an angle of incidence of 4.5° a periodicity of (3.79 ± 0.4) µm is obtained or again in (c) where for an angle of 8.5° the periodicity is of (5.86 ± 1.1) µm. By increasing the fluence and the angle of irradiation with respect to the surface normal, these secondary waves tend to extend in the direction normal to the ion beam and consequently this value also increases considerably, as can be seen in Fig.III.16 (e) or (f) where for irradiation at $\theta = 20.7°$ and $\theta = 30.7°$ the periodicity is (15.54 ± 1.1) µm and (16.6 ± 0.42) µm respectively. This means that the larger the angle of incidence is, the larger is the periodicity. This implies that the angle has a fairly significant effect on the density of waves on a given surface. As the periodicity increases with the angle, the size of the waves increases and their number decreases as well, allowing a relatively precise control depending on the desired application.

Although the effect of the angle is clearly visible, the fact that the fluence is different each time can raise doubts. For this reason, and as shown in figure III.17 (a-b), a selection of cases made up of 12 different angles with fluences varying between 1×10^{14} ions cm^{-2} and 3×10^{14} ions cm^{-2} is presented. Note that for clarity, the fluence values are rounded. From the figure III.17(a), it can be observed and confirmed that the periodicity of these undulations can be controlled, given that the impact of the angle on the periodicity despite the variable fluence is clearly visible, with a lower periodicity as one approaches grazing angles.

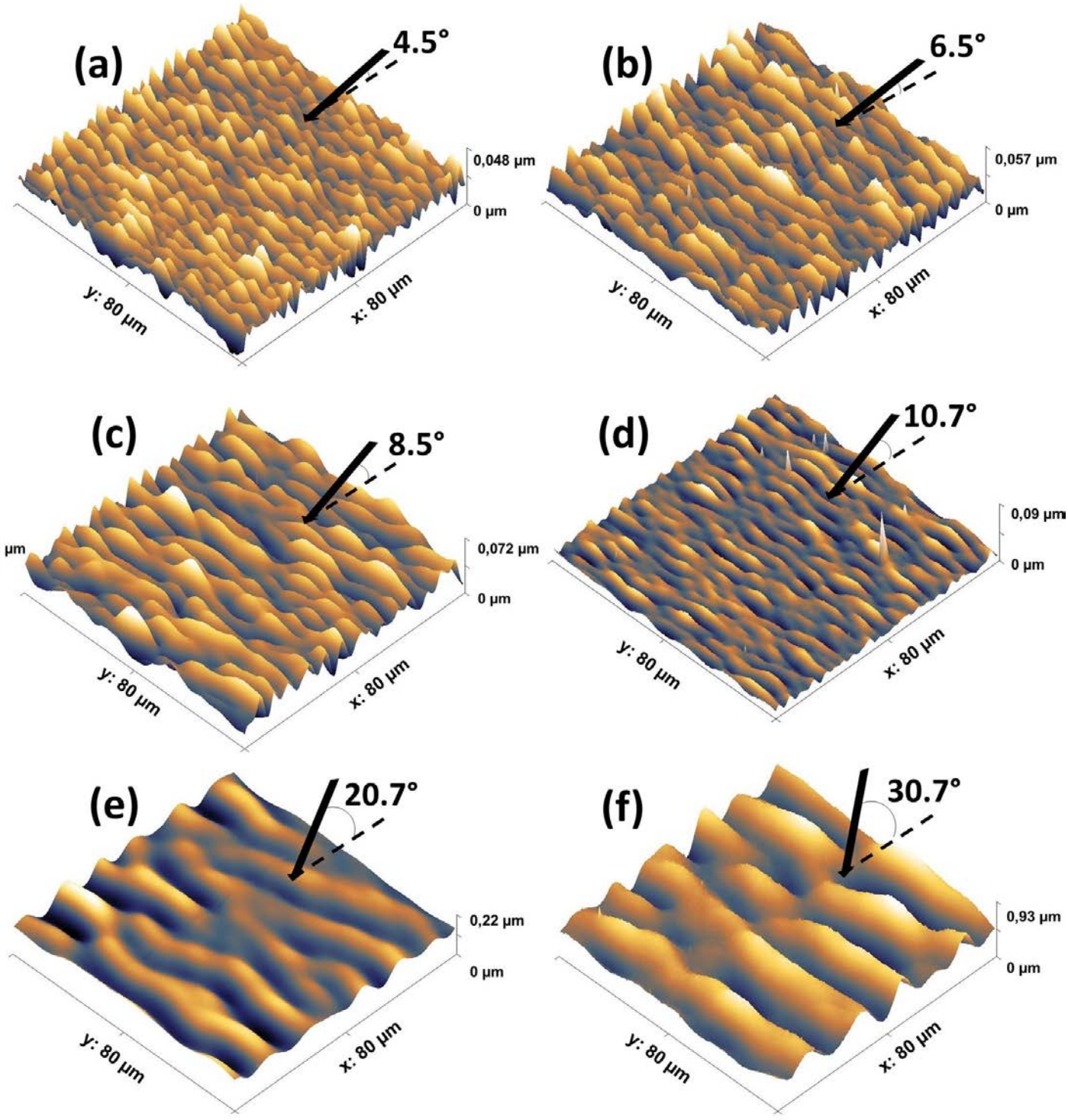

Figure III.16: AFM Images of (100)-$SrTiO_3$ surfaces irradiated with 92 MeV Xe ions at: (a) $\theta = 4.5°$ and $\phi = 6.75 \times 10^{13}$ ions cm^{-2}, (b) $\theta = 6.5°$ and $\phi = 9.74 \times 10^{13}$ ions cm^{-2}, (c) $\theta = 8.5°$ and $\phi = 1.27 \times 10^{14}$ ions cm^{-2}, (d) $\theta = 10.7°$ and $\phi = 9,5 \times 10^{13}$ ions cm^{-2}, (e) $\theta = 20.7°$ and $\phi = 1.8 \times 10^{14}$ ions cm^{-2} and (f) $\theta = 30.7°$ and $\phi = 2.6 \times 10^{14}$ ions cm^{-2}.

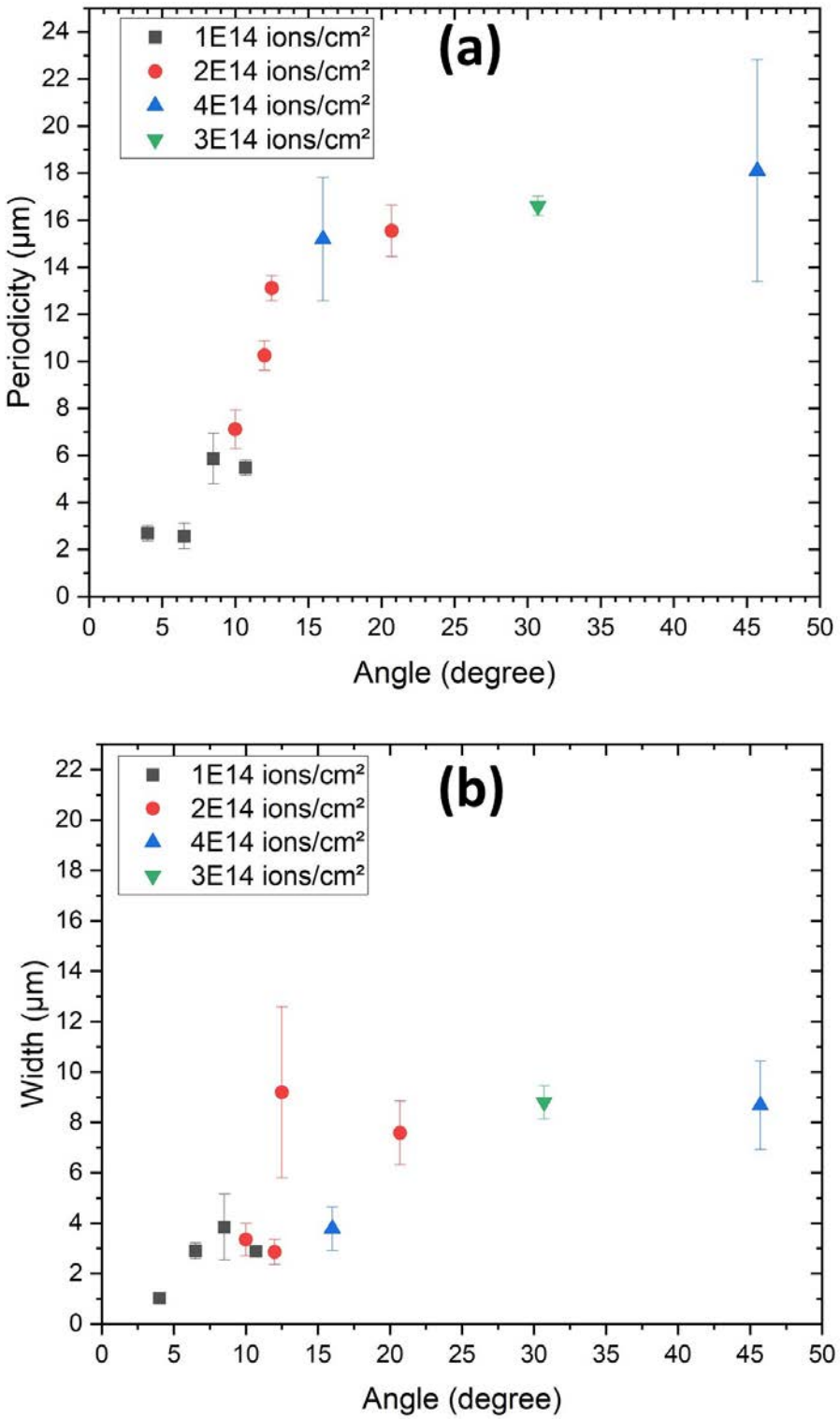

Figure III.17: (a) Evolution of the ripple periodicity and (b) the ripple width observed on (100)-$SrTiO_3$ surface irradiated with 92 MeV Xe ions according to the angle of incidence for different fluences.

Figure III.17 (b) shows the variation of the wave's width for angles varying between 4° and 45°. The width is defined by the mean FWHM of the secondary waves determined from multiple cuts. Contrary to what has been observed in previous studies [20] where the ripple width decreases as the periodicity between them increases, in this study, a slight increase in width with the angle of incidence was observed. Thus the width of the ripples and their periodicity decrease as the angle of irradiation decreases towards the surface, thus decreasing the space occupied, which makes it possible to have many more ripples on the surface whose size is greater than the size of the valleys separating them. However, apart from the effect of the angle, the fluence also plays a role in the width of the waves and therefore has a direct impact on the size of the valleys (wave separation). It has also been observed that for almost identical angle values, the width of the waves tends to decrease with increasing fluence, thus creating a larger gap.

Other studies where periodic surface structures have been observed have shown that a reorientation of the waves occurs at large angles [21] (i.e. the ripples firstly oriented perpendicular to the ion beam become parallel to it while increasing the angle of incidence towards the normal surface). In this study, however, the waves remain perpendicular to the ion beam at all angles up to 45.7°. It should be noted, however, that irradiations at angles greater than 45.7° have also been carried out, and more particularly at an angle of 90° for fluences varying between 5×10^{11} ions cm^{-2} to 5×10^{14} ions cm^{-2}. Analysing the different surfaces imaged with the AFM and apart from the rough surface, the Fourier Transform did not show any periodic forms.

6 Quantification of the ripples quality

Given the potential applications of nano-waved surfaces, particularly as substrates for different deposits, a homogeneous pattern with the minimum of disorder is therefore necessary. This is why a quantification of the defects is necessary in order to be able to find a combination of irradiation parameters that will optimise the quality of the waves and minimise the defects that may appear.
One of the techniques used for this purpose is the extraction of the degree of order of these quasi-periodic patterns on surfaces from topographic images taken with AFM. Indeed, during irradiation and as the reorganisation of the surface begins, different types of topological defects can appear since they go through several stages, as we saw earlier. At the beginning of irradiation and for intermediate fluences, the waves are not completely formed, and as the fluence increases, the structure becomes more pronounced and structured, with waves spaced by distinct valleys. These defects can appear either as a bifurcation, i.e. where the waves split into two, or as a discontinuous wave. Thus, a technique for quantifying the degree of order, or as it is sometimes called, the quality of the ripples, has been developed [146], which makes it possible to obtain the normalized density (ND) of topological pattern defects. Fig.III.18 shows the procedure for extracting these data from a $520 \times 20°$ μm^2 AFM image (Fig. III.18(a) of a sample irradiated with SHI at 4° with 6×10^{13} ions cm^{-2})and this using Gwydion software [147]. It should be noted that for each sample, several scans of different areas of the surface were carried out, from which this parameter was extracted for each one. Here (fig.III.18) only one case is shown to illustrate the steps followed.

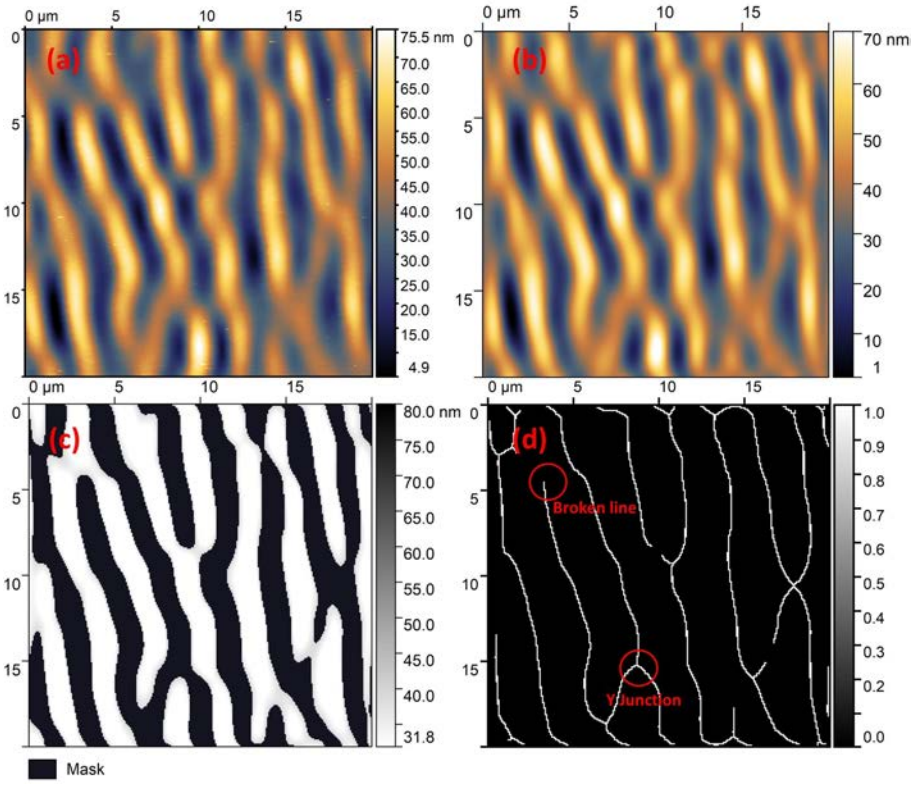

Figure III.18: (a) (20×20) µm^2 AFM image of a (100)-$SrTiO_3$ sample irradiated with 92 MeV Xe ions at $\theta = 4°$ and $\phi = 6 \times 10^{13}$ ions cm^{-2}, application of Fourier-filtering on (a), (c) application of the Otsu's threshold (binary image) on (b) and (d) thinning of the ripples to lines

The first step is performing a 2D Fourier filtering (Fig.III.18(b)). As its name suggests, this allows to filter the raw AFM images and extract only the frequency of interest. In this study and with this type of periodic pattern, it allows to get rid of noise and other surface roughness that could alter the analysis of defects and to keep only the wave structure with a certain amplitude. Then, a mask is created with Otsu's threshold [148]. This consists of levelling the topographic image by subtracting its background. Then, thanks to a threshold level, the image is converted into a black and white binary image (fig.III.18(c)). In the example presented above (Fig.III.18), heights are represented in black and valleys in white. Finally, the resulting images are thinned. This operation consists of reducing the line waves by one pixel in width (Fig.III.18 (d)).
The total raw number of defects present in our AFM images is then calculated using this last image obtained. These defects appear either as unfinished or broken lines or in the form of junctions fig.III.18 (d). The calculation is done by considering that each white pixel with more than two neighbouring white pixels or with only one neighbouring white pixel is a topological defect. Once the total number of defects is obtained and knowing the scan area of our image, the normalised density of defects is then calculated using the following formula: $N_D = (N \times \lambda^2)/A$ where N is the raw number of defects, λ the ripple periodicity (wavelength), and A the scan area of our image. Note that since the periodicity λ^2 and the area occupied by the waves A vary from one sample to another, this can complicate the comparison. The addition of these two parameters to the formula

therefore allows a comparative study of the evolution of the ripple quality as a function of irradiation parameters without the impact of λ^2 or even A. The results are interpreted using the dimensionless normalised defect density N_D obtained. Thus, when the value of $N_D = 0$, the sample is considered defect-free. When $N_D = 1$, each ripple contains one defect per length.

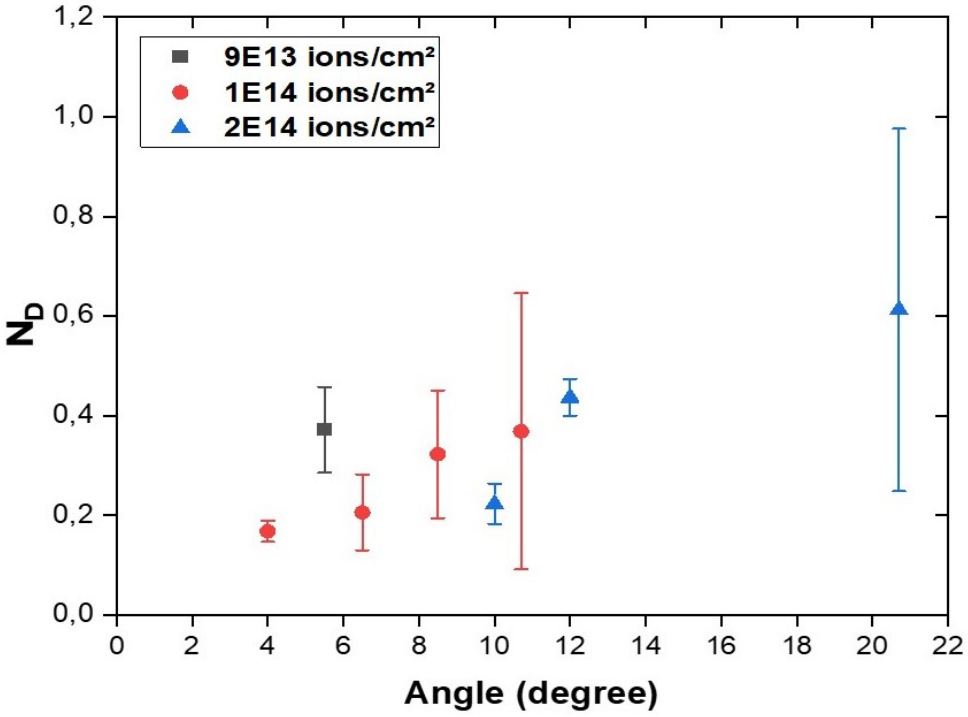

Figure III.19: Evolution of the normalized density of pattern defects N_D for 92 MeV Xe SHI irradiation $SrTiO_3$ (100) as function of angle.

In order to analyse the entire surface, several AFM images of several areas of the (100)-$SrTiO_3$ sample were processed using this approach. As we have two variable parameters, the normalised density of pattern defects N_D was calculated each time in order to analyse the evolution of the quality of these structures as a function of the angle of incidence and fluence, separately.
To do this, N_D was calculated for $SrTiO_3$ samples having almost the same fluence (note that in the figures the fluences have been rounded for better visualisation of the results) but irradiated at different and increasing angles. Fig.III.19 shows the evolution of wave quality through the number of normalised defects found for each irradiation angle. We can see that by increasing the angle, N_D increases but still remains below $N_D = 1$. This increase is expected, given that for large angles, the fluence required to form a well-defined wave structure is greater. Bearing in mind that the fluence in this study did not exceed $\phi = 4 \times 10^{14}$ ions cm^{-2} for an angle of 45.7° and where the not very well formed waves were also visible on the AFM images. It can therefore be assumed that this may be due to either an insufficient fluence for the patterns to develop into a well-defined ripple structure or that a fluence threshold has been exceeded for this angle inducing, an accumulation of defects causing the deformation of the waves-like structures.

Conclusion

It is now known, thanks to the first results obtained during this study, that the angle affects the periodicity (λ) of the waves-like structures, whether the primary waves (λ 100 µm) or the secondary waves ($\lambda < 20$µm). However, the first category is limited to specific cases: fluence has to be high enough to amorphize the surface but low enough not to be overcome by the formation of secondary structures. Also, in view of their size, the secondary waves are the ones that will be analysed in detail. The width of these structures is also impacted by the irradiation geometry. So as the angle increases towards the surface normal, the waves grow larger (with an increasing period) and the more they extend parallel to the ion beam, the more they fill the area of a given surface. This has a direct impact on the valleys, whose size will therefore be reduced as the angle increases.
It is assumed that if the fluence is not high enough given the angle, this can lead to a grouping/crossing of several "normal (small)" secondary waves to form a single wave of lower amplitude. As a result, the defects are summed up and if the irradiation does not continue at higher fluences, these waves will not have enough time to finalise their formation into well-defined waves. Add to this the different morphological aspects observed, which can also be due to the variable fluence. Because of this, the purpose of the following chapter is to investigate how changing the fluence affects the reorganisation and development of these surface patterns.

Chapter IV

Secondary waves-like structure evolution with intermediate fluences

Introduction

The effect of the angle on the evolution of the wave-like structure was demonstrated in the previous chapter. As mentioned previously, due to the short irradiation times and the fact that the irradiation was carried out at the same time at different angles, the fluence varied each time. This complicates the interpretation of the results and the study of the impact of the fluence on the formation of the waves (ripples), and their evolution with the fluence. In this section, the results obtained during a second irradiation period will be presented. During this beamtime, intermediate fluences were used in order to have a basis for comparison.

1 $SrTiO_3$ surface microstructure evolution at $\theta = 4°$

Let us start by presenting six samples of strontium titanate irradiated at the same angle ($\theta = 4°$). The fluence ranged from 1×10^{13}ions cm^{-2} to 1×10^{14} ions cm^{-2}. Since the irradiation took place at the same angle, it was not necessary to use the supports at different angles (fig.II.10). However, the same dilemma remains regarding the beamtime given and the duration of the different irradiations. Fluxes ranging from 4×10^9 ions cm^{-2} s^{-1} to 7×10^9 ions cm^{-2} s^{-1} were used. Five samples were irradiated with a fluence of 3×10^{14} ions cm^{-2}, which gives a real fluence of 2×10^{13} $ions\, cm^{-2}$ perceived by the iradiated samples, given their angle of incidence. With an average flux of 5.5×10^9 ions cm^{-2} s^{-1} the irradiation time is about 15h. The irradiation plate was then raised so as to remove the first sample from the beam scanning area and keep only the other four samples remaining. The change was made a second time to obtain a fluence of 4×10^{13} ions cm^{-2}. This maneuver continued until reaching the last sample with the highest desired fluence of 1×10^{14} ions cm^{-2}. This technique of gradually reducing the fluence value by moving the irradiation plate as we went along enabled us to irradiate continuously and optimise the irradiation time.

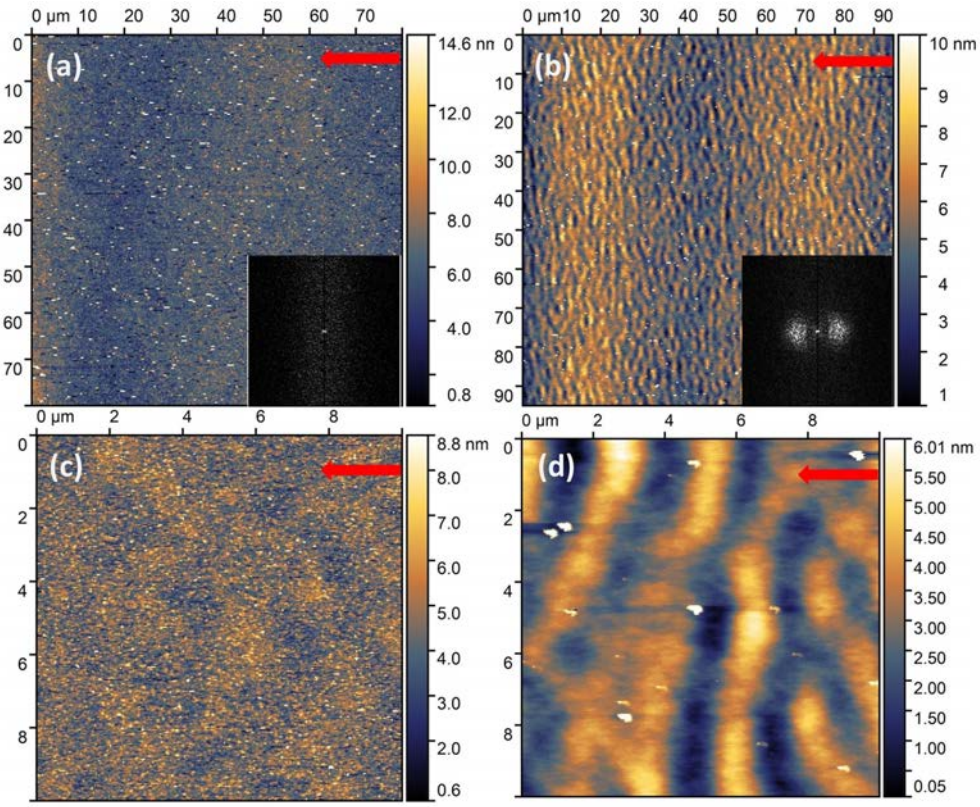

Figure IV.1: AFM images of $SrTiO_3$ (100) irradiated with 92 MeV Xe ions at $\theta = 4°$ with $\phi = 2 \times 10^{13}$ ions cm^{-2} (a) (80×80) µm^2 and (c) (10×10) µm^2,and (b)(d) with 4×10^{13} ions cm^{-2}. The direction of the ion beam is indicated by the red arrow.

For a fluence of 1×10^{13} ions cm^{-2} no wave-like structure was observed on the AFM topographic images or with their Fourier transform (not shown here). For the sample irradiated with 2×10^{13} ions cm^{-2} presented in figure IV.1 (a) with a scan of (80×80) µm^2, a structure appears similar to the primary periodic structures observed previously for low fluences. The 2D Fourier transformation yields a periodicity of $\lambda \sim 80$µm. It should be highlighted that the fluence here is referred to as low in comparison with fluences that allow the formation of periodic secondary waves. In reality, this fluence is not low, as it is still in the range of multiple impacts. This means that there is amorphization by a single ion impact giving rise to tracks, which overlap to form an amorphous layer on the surface. Zooming in to (10×10) µm^2, the scan (c) shows that the surface is quite rough with an Rq = 9.93 Å. This indicates that the surface structuring process has begun without the periodic patterns oriented perpendicular to the ion beam yet being visible. With a higher fluence of 4×10^{13} ions cm^{-2} the scan in figure IV.1 (b) shows two structures, namely the primary pattern with a periodicity of $\lambda \sim 83$ µm and the appearance of the secondary wave structure which is well oriented perpendicular to the ion beam with a periodicity of $\lambda \sim 3$ µm. These so-called "primary" structures was observed for samples irradiated at 2×10^{13} ions cm^{-2}, 4×10^{13} ions cm^{-2} and 6×10^{13} ions cm^{-2} yielding a much larger spatial periodicity than the secondary waves.
With increasing fluence the primary structure fades with λ, getting higher to about 94 µm for the

6×10^{13} ions cm^{-2} fluence. At higher fluences, only the increasingly pronounced secondary wave patterns remain, as can be seen in figure IV.2 (b-d).

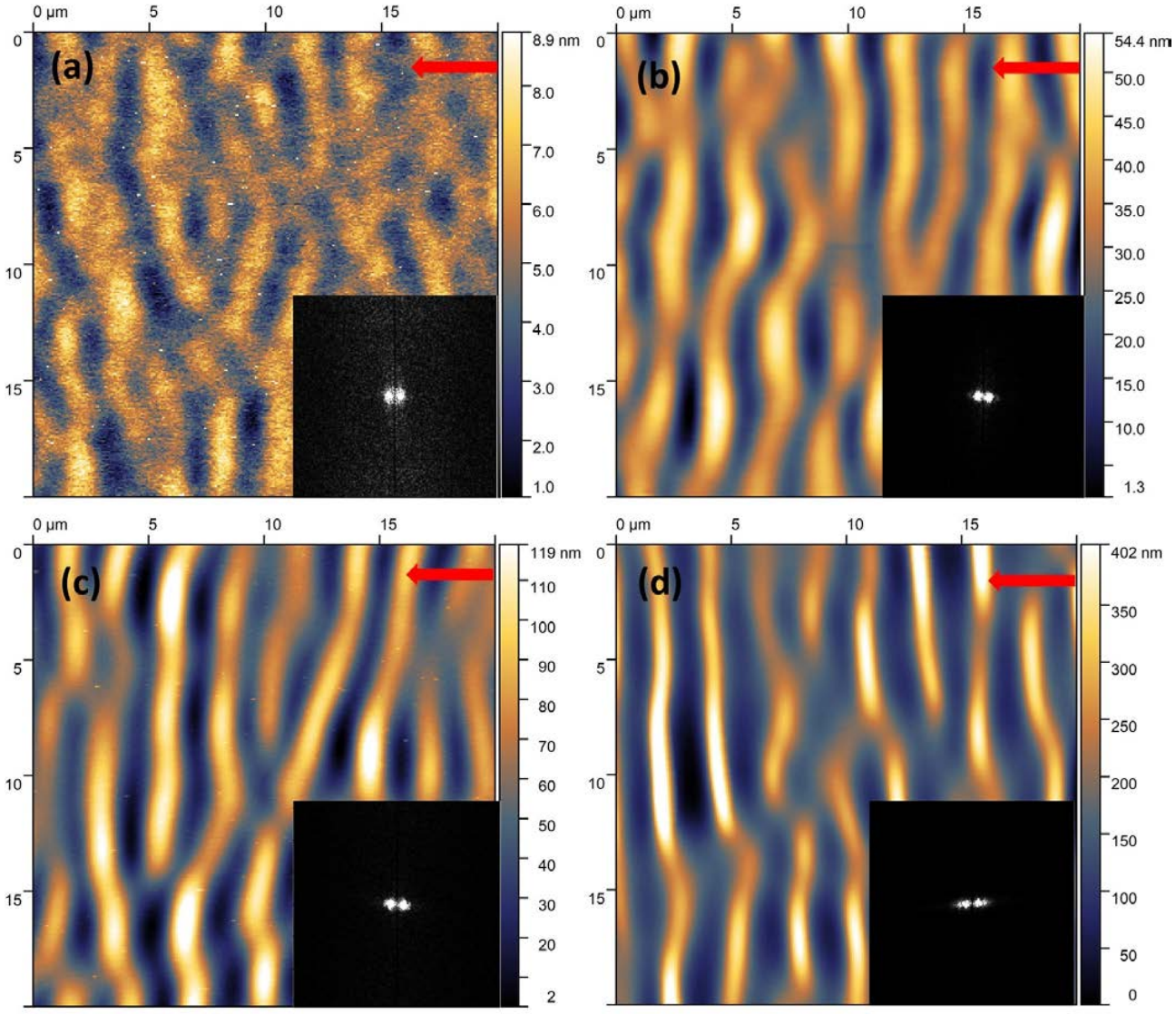

Figure IV.2: AFM image of $SrTiO_3$ (100) surfaces irradiated at 4° with 92 MeV Xe ions at (a) $\phi = 4 \times 10^{13}$ ions cm^{-2}, (b) $\phi = 6 \times 10^{13}$ ions cm^{-2}, (c) $\phi = 8 \times 10^{13}$ ions cm^{-2} and (d) $\phi = 1 \times 10^{14}$ ions cm^{-2} with their 2D Fourier transformation inset. The direction of the ion beam is indicated by the red arrow.

From a fluence of 4×10^{13} ions cm^{-2} and up to 1×10^{14} ions cm^{-2} (the highest fluence used for this angle), the surface amorphises and self-organises into a periodic structure perpendicular to the ion beam. Fig.IV.2 shows the evolution of the surface morphology, with the formation of waves becoming more pronounced with increasing fluence. The Fourier transformation of each case (inset of each image) reveals two distinct spots, confirming the periodicity of the surface structure. The

dependence of periodicity (λ) on fluence is depicted in fig.IV.3 for irradiation with 92 MeV Xe SHI mainly at angles around 4°. The periodicity has a value of about 3 µm and is independent of fluence variation. This confirms the results presented previously, where the periodicity of the secondary wave-like structure was shown to be influenced by the angle of incidence of the ion beam and not by the fluence.

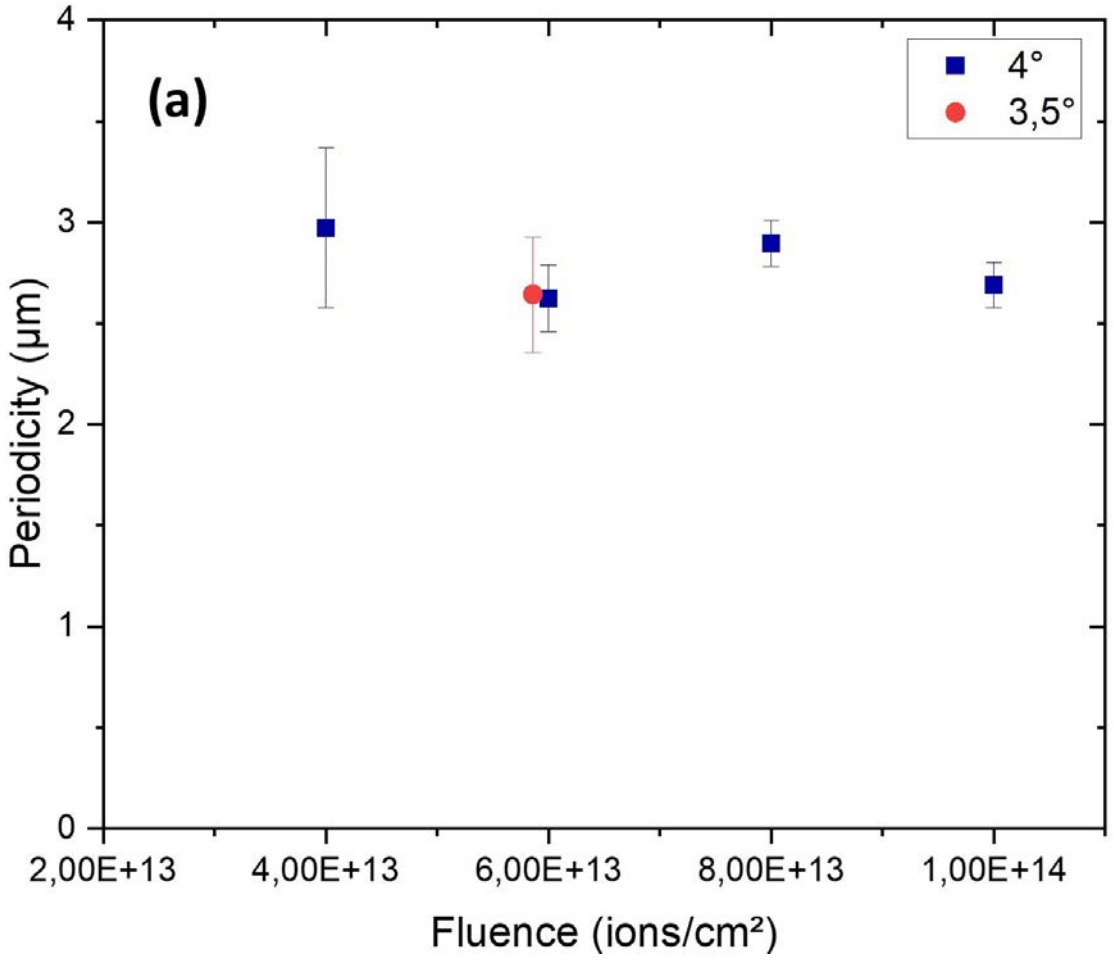

Figure IV.3: Evolution of wave periodicity with fluence for swift heavy ions irradiations at 92 MeV Xe ions at angles around 4°.

1.1 Evolution of surface roughness

A parameter that can be used to analyse the damage on the surface is the measurement of surface roughness [149]. This technique consists of characterising a surface and evaluating its roughness by measuring different parameters and variables that govern it. Several categories can be identified; the three main ones are the amplitude parameters, the spatial parameters, and the hybrid parameters. The most commonly used are the so-called amplitude parameters, which quantify the height variations on the surface. The arithmetic average height Sa (nm) and the root mean square

roughness (RMS) (Sq), provide an average measurement of the deviations from the mean plane of the surface. Note that in the case of a surface with a wavy profile, the parameter usually used is Wq, which refers to the root-mean-square ripple (wave) of the surface. The same formula is used in both Sq and Wq cases, though. In this study, the first low-fluence samples do not yet have any undulation on the surface, which is why the roughness parameter Sq is used for all cases. Although both (Sq and Sa) quantify the height variations on the surface, there is a difference in the sensitivity of the measurement. Sq provides a more accurate measurement since any effects, anomalies, or surface differences, however small, are detected.

(20×20) μm^2 AFM images were performed on seven different locations on the $SrTiO_3$ surface, and Sq was extracted from each scan. Fig. IV.4(a) shows the evolution of the surface roughness Sq, for fluences ranging from 2×10^{13} ions cm^{-2} to 1×10^{14} ions cm^{-2}. The Sq value increases exponentially with the fluence. With a Sq value of ~ 1 nm for a fluence of 2×10^{13} ions cm^{-2} to reach a value of ~ 100 nm for the highest fluence in this case, of 1×10^{14} ions cm^{-2}. This is consistent with the deformation of the surface and its reorganisation into waves of a certain amplitude.

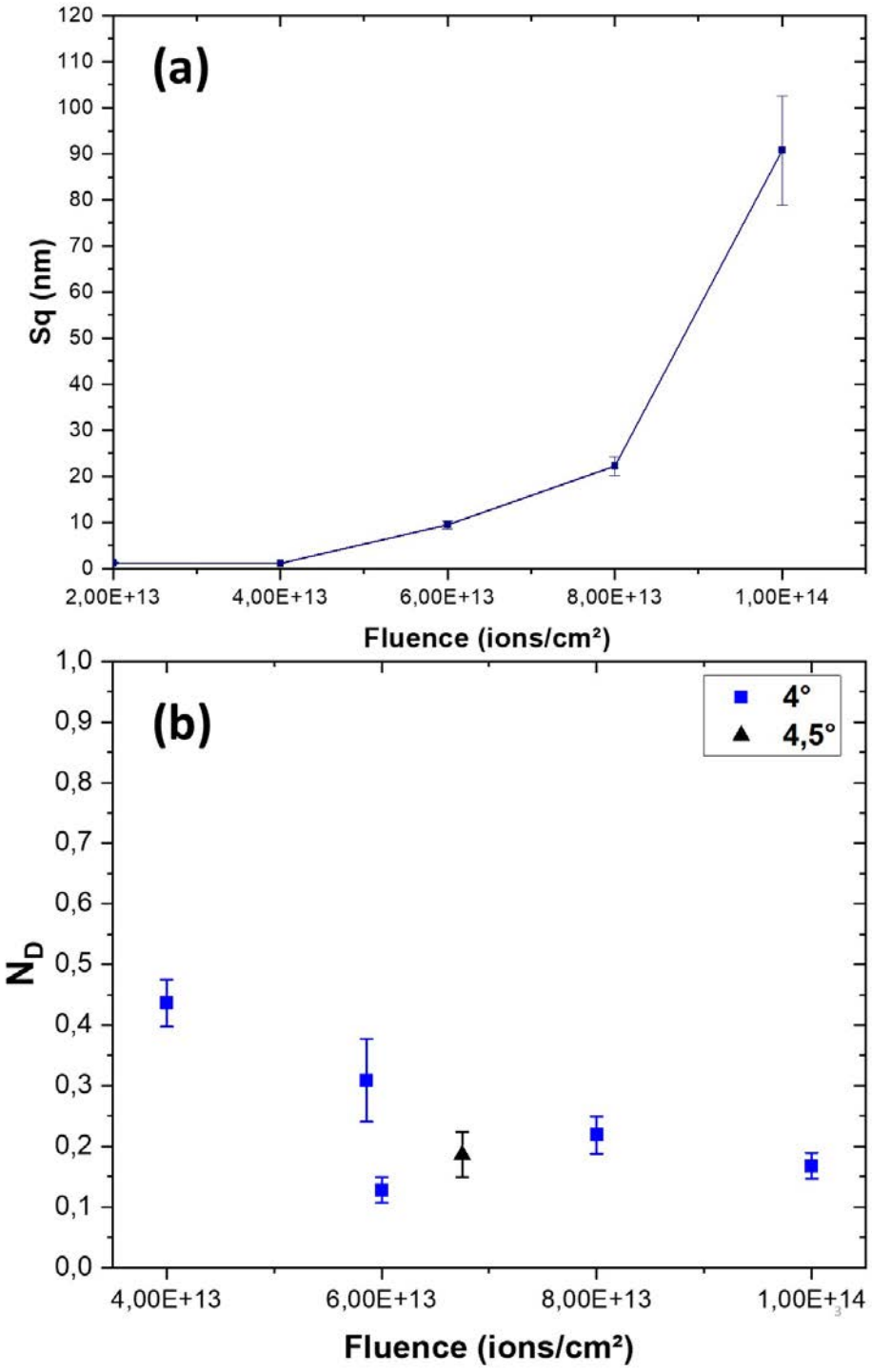

Figure IV.4: (a) Surface roughness Sq (b) evolution of the normalized density of pattern defects N_D versus fluence of $SrTiO_3$ (100) surfaces irradiated with 92 MeV Xe ions at 4°.

When considering surface roughness, one can also consider the defects that can occur. This is why the normalised density of pattern defects N_D has been calculated for samples irradiated with

fluences varying between 4×10^{13} ions cm^{-2} and 1×10^{14} ions cm^{-2} for angles around 4°, and is represented in fig.IV.4 (b). This second parameter can also help to follow the anisotropic evolution of the surface roughness into a periodic structure. It can be observed that the N_D value appears to decrease as the fluence increases. N_D reaches a minimum value of $\sim 0,1$ with a fluence of 6×10^{13} ions cm^{-2}. However, the values remain below 0.5 for all the examples, demonstrating fairly good wave quality. This decrease in N_D values with increasing fluence is in line with the observations made with AFM, and supports the hypotheses on the surface structures' evolution into wave patterns and their formation as irradiation progresses, with the impact of fluence on pattern quality. This is also in line with what has been observed in previous studies of surface structuring at low energy. Keller et al. discussed the different processes that these periodic patterns go through during their formation and evolution into ripples [150]. It has been shown that as the fluence increases, the length of the ripple increases with subsequent annealing processes, causing defect annihilation and a reduction in the normalised defect density to a certain point. Then, at higher fluences, the patterns become more disordered and many defects are formed [151]. This last case was not observed in the example presented above. This can be explained by the fact that the fluence threshold beyond which the waves become disordered and defective again was not reached.

1.2 Evolution of the wave size

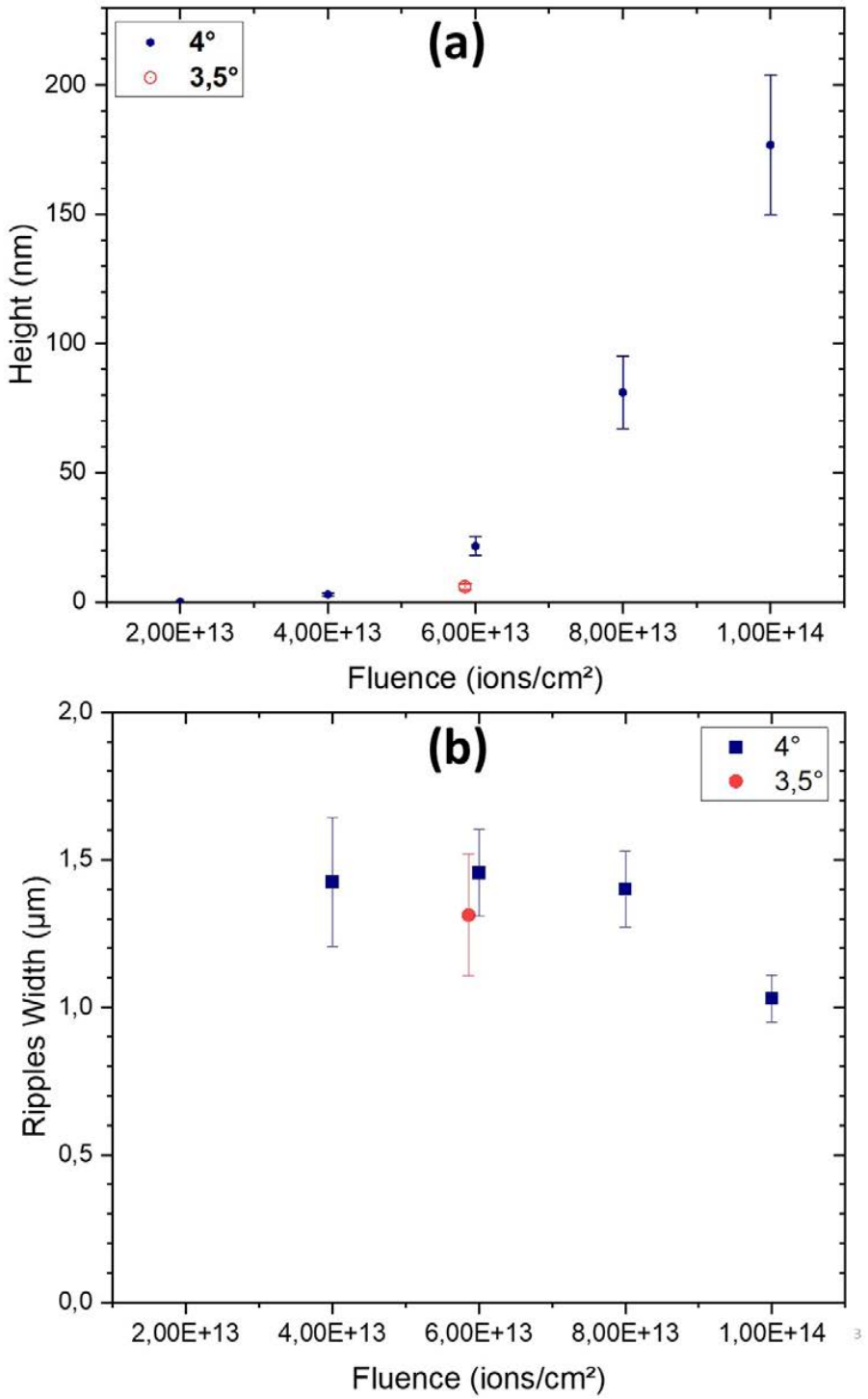

Figure IV.5: Evolution of the height (a) and width (b) of waves of $SrTiO_3$ (100) surfaces irradiated with 92 MeV Xe ions at 4° as a function of fluence.

Since Sq describes surface height variations around the mean height, and as it is increasing, the variation of the ripple height with the same fluence was then measured. Fig.IV.5 (a) shows the evolution of wave height as a function of fluence. It can be seen that the same variation in wave height occurs as the fluence is increased, with a value of h ~ 3 nm for a fluence of 4×10^{13} ions cm^{-2}, reaching h = 200 nm for a fluence of 1×10^{14} ions cm^{-2}. A saturation and stabilisation of the height at a given fluence might be expected, but in this particular case, the surface is still developing at a fluence of around 1×10^{14} ions cm^{-2} for an angle of 4°. It should be remembered that the analysis of the variation in height with angle did not show any specific evolutionary trend. So the fluence would act on the growth of these structures. This coincides with what has been observed previously in this study.
From the various AFM images, it can be seen that as the fluence increased, the waves tended to become finer while keeping their direction normal to the ion beam. As can be seen in Fig.IV.2(a-d). Profile cross-sections were therefore made, from which wave width values were derived over a set of scan samples of the entire surface. Here, by wave width one means, by definition, the average FWHM of the ripples determined from the multiple cuts. From figure.IV.5 (b) a decrease in wave width with increasing irradiation fluence is observed. As it was observed, this narrowing, looking like a contraction of the waves, is accompanied by a gain in height as the fluence increases. This is consistent with what has been observed in previous studies for other kinds of samples and energies.

In previous studies [20] this effect of the fluence on the evolution of wave height and width has already been observed in the case of LiF or BaF_2 films irradiated with SHI. However, the reorganisation of the surface and the ripple formation and evolution with fluence could only take place when the samples were kept at liquid nitrogen temperature (LNT, 77°K) during irradiation. In this study, we were able to form waves (ripples) on the surface of an original single crystal, and have them evolve (size, height, and periodicity) over time with different fluences and angles at room temperature throughout the irradiation phase.

1.3 Wide angle, high fluence

Fig.IV.6 shows the topographic image of two surfaces irradiated with a fluence of around 4×10^{14} ions cm^{-2} at two different angles. The sample irradiated at $\theta = 16°$ (fig.IV.6(b)) shows deeper trenches and thinner waves with a width that decreases by a factor of 2, unlike the sample irradiated at 45° (fig.IV.6(a)). Note that at this high fluence the micrometric range dominates for the three parameters describing the secondary wave structures, namely height, width and periodicity, which are 1 µm, 4 µm and 15 µm respectively. An exception exists for the sample irradiated at 45° (fig. (a)) where the wave-like structures appear less structured with a width of around 9 µm, a height of around 8 nm and almost no valleys. Unfortunately, due to a lack of time, it was impossible to irradiate other samples at higher fluences to confirm our hypothesis. Based on the previous results on the influence of angle and fluence, it can be assumed that at this angle, a higher fluence would have enabled the surface to form a more homogeneous structure, particularly by developing the undulations in height. This means that the surface structuring did not continue, probably because the fluence was too low.

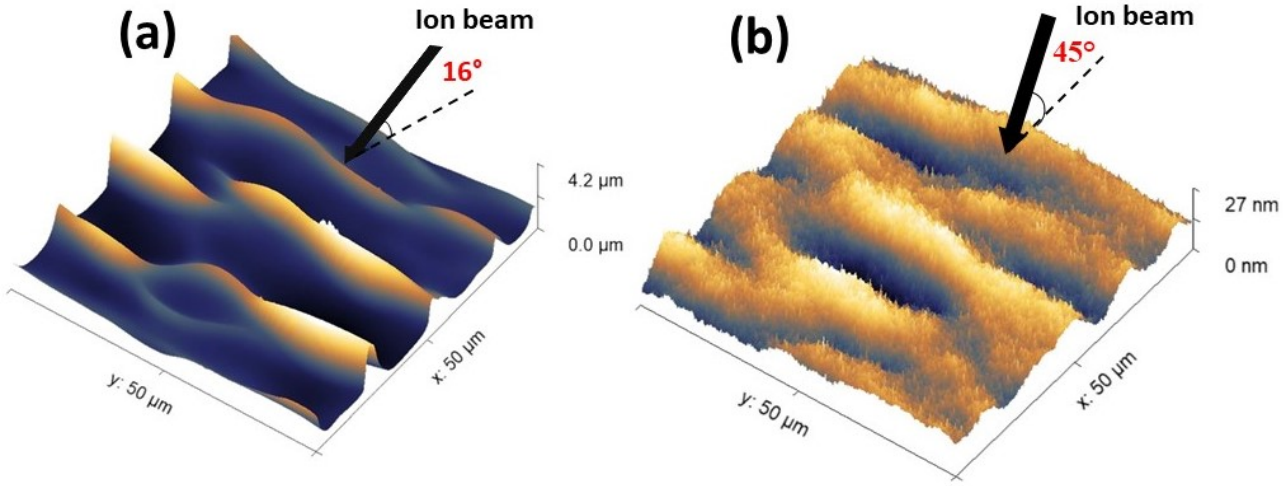

Figure IV.6: AFM images of $SrTiO_3$ (100) irradiated with 92 MeV Xe ions with 4×10^{14} ions cm^{-2} at (a) 45.7° and (b) 16°.

2 Swift heavy ion irradiation of $SrTiO_3$ with intermediate fluences and angles

As mentioned previously, the goal was to irradiate crystalline $SrTiO_3$ at angles ranging from 1.5° to 45.7°. Since there are two factors affecting the reorganisation of the surface into quasi-periodic patterns, namely the angle of incidence of the beam on the surface and the fluence, first the analysis with a variable irradiation parameter each time was presented. In the following, the results obtained for SHI irradiations with 92 MeV Xe ions for intermediate angles and fluences will be presented.

2.1 Impact of the angle

For an overall view, figure IV.7 shows all the irradiations for all angles and all fluences ranging between 3×10^{13} ions cm^{-2} and 4×10^{14} ions cm^{-2}. Fig.IV.7 shows the evolution of the periodicity IV.7 (a), the width IV.7 (b) and the height IV.7 (c), as a function of angle. The impact and influence of the angle on these last two characteristics of the secondary periodic structures is quite obvious, as long as, as expected, the height follows a non-homogeneous evolution.

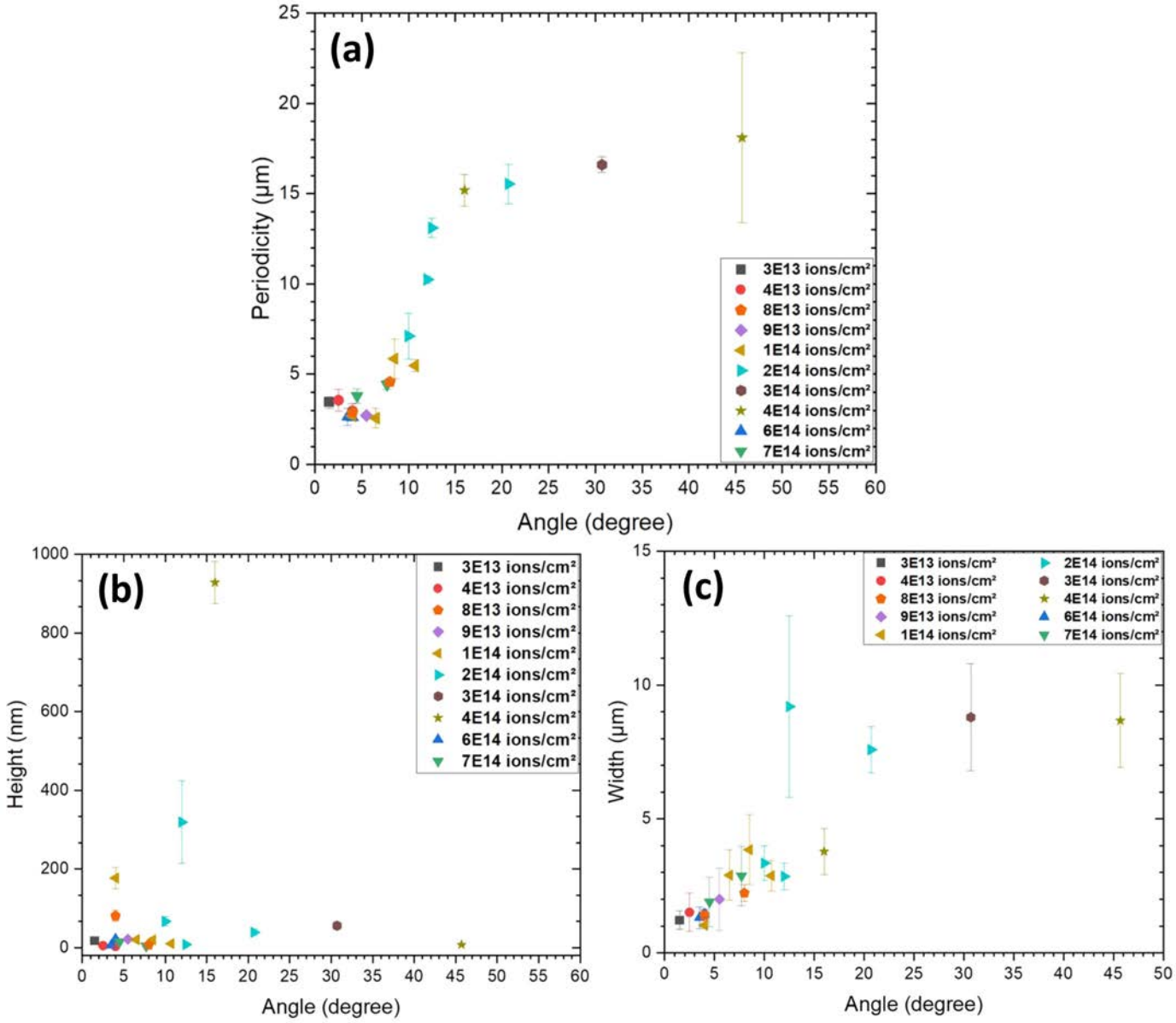

Figure IV.7: Evolution of (a) the periodicity , (b) the width and (c) the height of the waves as a function of the angle of incidence of the 92 MeV Xe ion beam for different fluences.

2.2 Impact of the fluence

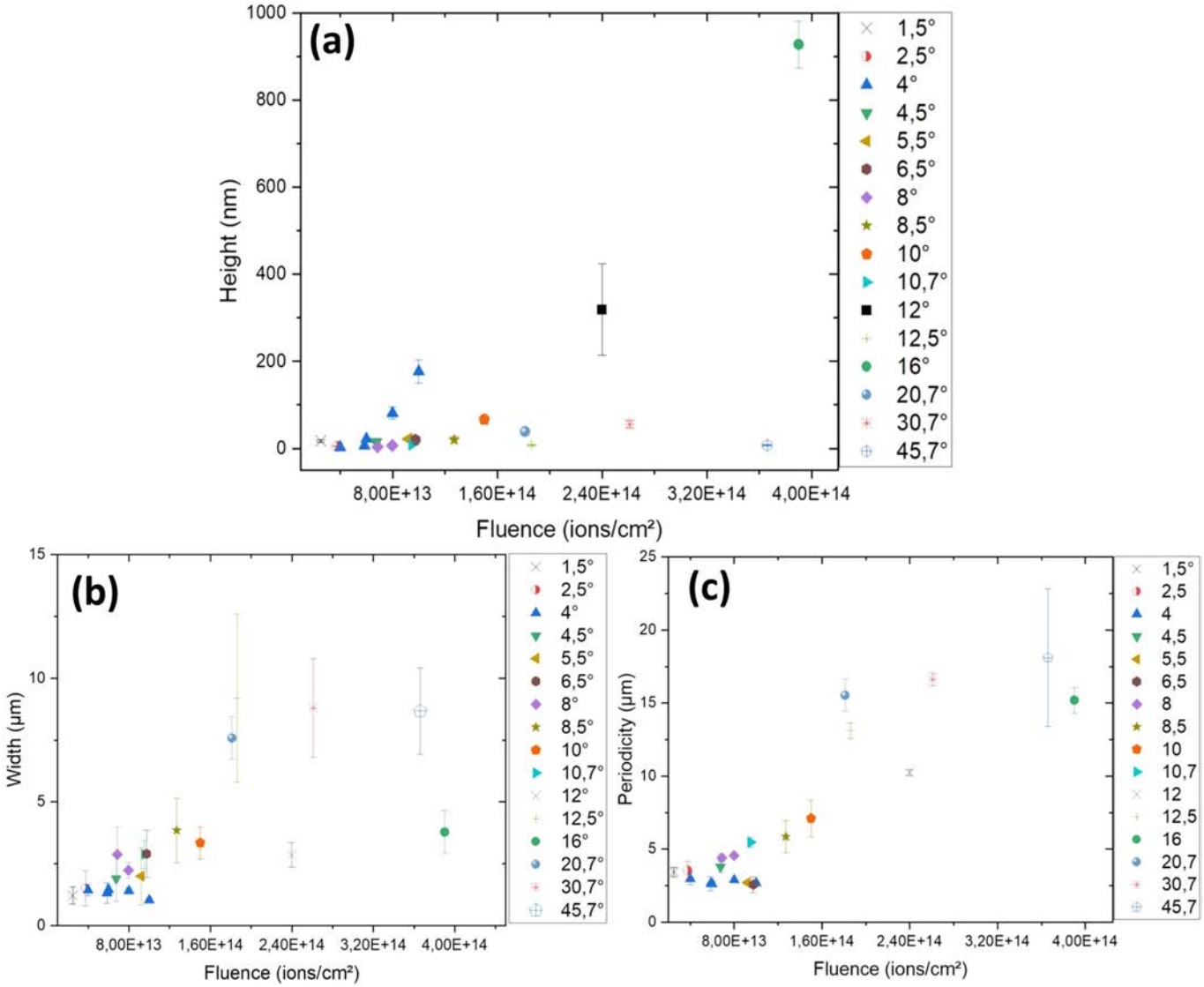

Figure IV.8: Evolution of wave height (a), width (b) and periodicity (c) as a function of fluence for different angles.

With regard to the impact of the fluence on surface structuring and wave growth, Fig. IV.8 summarises and brings together the results obtained so far for all the data acquired. A certain trend can be noted, and the impact of the fluence in particular on the height that increases as the fluence increases, which is translated by the growth of the waves in the direction normal to the surface. As far as periodicity is concerned, we can see an increase with fluence, but it should be noted that the angle differs from one case to another, so this increase is the result of the increase in the angle of incidence.

It is important to note, however, that irradiations normal to the surface (90°) were also undertaken on the same sample species with fluences varying from the single-impact regime (presence of nano-hillocks at the surface) to the multiple-impact regime (amorphization of the surface) and where no wave formation was observed or detected on the AFM topographic images.

2.3 Cross-irradiation

During the first beam time, some $SrTiO_3$ samples of crystallographic direction (110) were irradiated with Xe SHI of energy 74 MeV at a fluence of 1.41×10^{14} ions cm^{-2} and an angle of 8.1°. Figure.IV.9 (a) shows an AFM image of the surface after irradiation and where the formation of secondary waves perpendicular to the direction of the ion beam (indicated with the black arrow) is observed. The periodic structure is confirmed by the presence of two distinct spots in the corresponding 2D Fourier transform, giving a periodicity of $\lambda \sim 5$ µm. Since the amorphous surface tends to reorganise into a structure perpendicular to the ion beam, it was interesting to see the effect of cross-irradiation. So, after the first irradiation, a rotation was made on the sample through 90°, and a second irradiation was performed, in both cases at high fluence and at a grazing angle. The second irradiation was therefore carried out with Xe SHI of slightly different energy (92 MeV) but still in the same energy range and still above the electronic energy threshold Se_{th}. With a fluence of 5.86×10^{13} ions cm^{-2} and an angle of 3.5°. Regarding the energy difference, as mentioned earlier, the time and beam energy were constrained by GANIL facility availabilities. So the same sample was irradiated with two slightly different energies. As for the difference in angle and fluence, this is due to the fact that a little over a year elapsed between the two irradiations, so corrections were made in the meantime by calculating the angle error. As a result, the value of the fluence perceived by the sample also changes.

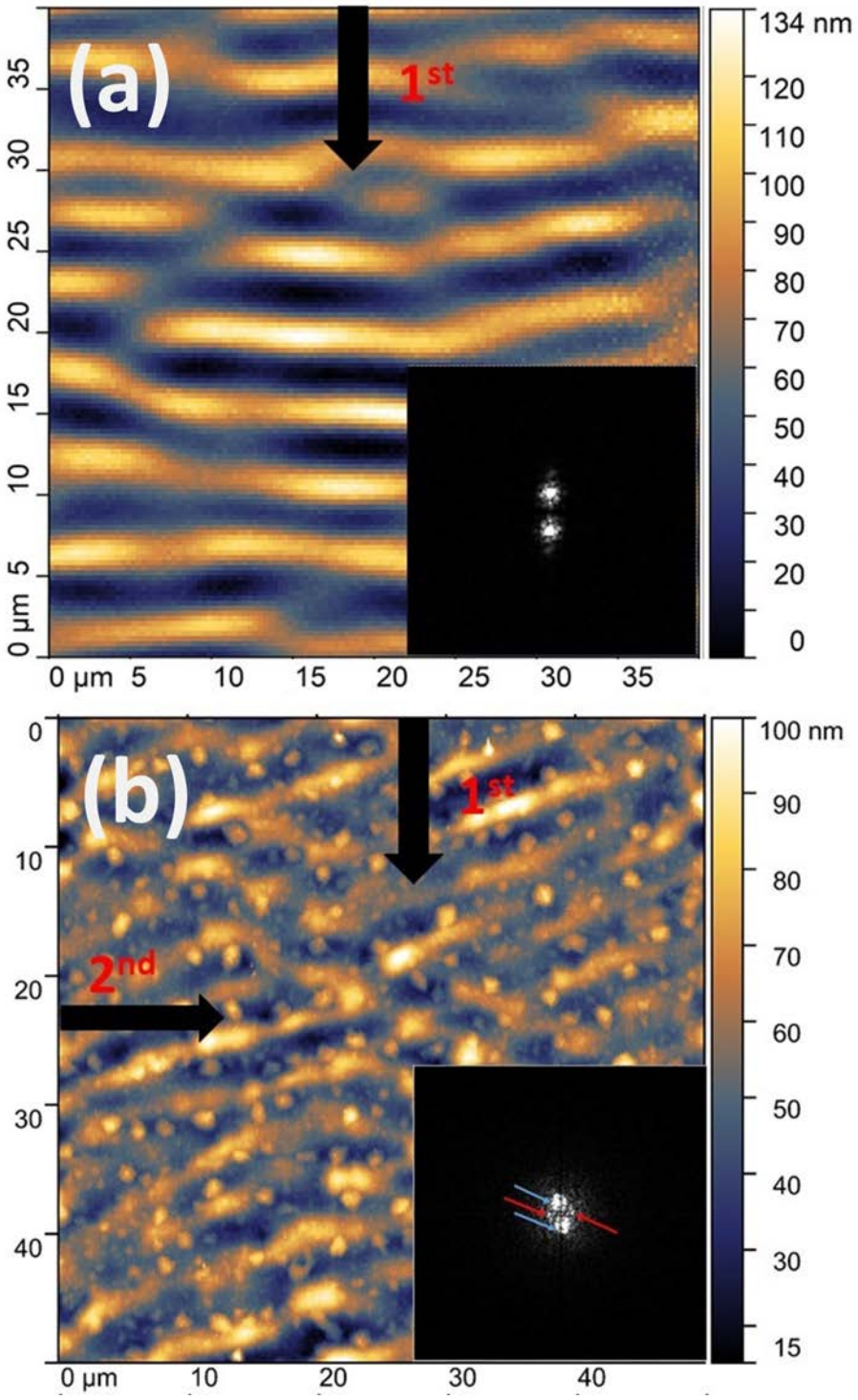

Figure IV.9: AFM images of $SrTiO_3$ (110) in (a) a (40×40) µm^2 scan of a surface irradiated with 0.55 MeV/u $^{136}Xe^{19+}$ with $\phi = 1.41 \times 10^{14}$ ions cm^{-2} at $\theta = 8.1°$ and (b) (50×50) µm^2 scan of the surface sample irradiated a second time after a rotation of 90° with 0.71 MeV/u $^{129}Xe^{23+}$ with $\phi = 5.86 \times 10^{13}$ ions cm^{-2} at $\theta = 3°$, as well as the corresponding Fourier transform inset.

In order to have a fixed point of comparison and to get rid of the effects of energy and fluence, which are different in both cases, the total energy deposit in ions.keV.cm^{-3} was calculated. This was done with the following formula: $E_d = S_e \times$ fluence. This allows to get the total deposited energy for the first and second irradiation of about 2.2×10^{22} ions keV cm^{-3} and 1.2×10^{22} ions keV cm^{-3} respectively.
The 2D Fourier transform analysis of the sample after the second irradiation shows 4 spots (see fig.IV.9 (b)). The two spots indicated by the blue arrows of the first periodic structure appear to have undergone a slight rotation. The periodicity in this case is around 5.5 µm. Slight side/horizontal peaks can be identified (indicated by the red arrows) indicating the presence of a periodic structure perpendicular to the second ion beam and parallel to the first. These peaks also give a periodicity of around 5 µm. This appearance of a second pair of peaks, indicating the formation of a secondary structure, occurs following the second irradiation. This second irradiation acts on the amorphous surface, not by reorienting (strictly speaking) the structures already formed, but by annihilating the first structure and forcing the surface to reorganise itself perpendicularly to the direction of the 2nd ion beam. From the AFM image, it can be seen that in some places the waves are starting to break/crack, tending to tilt away from their initial axis. It is assumed that because the energy deposited during the second irradiation is lower than for the first irradiation and because the angle of incidence is also lower for the second irradiation (3.5°) than for the first (8.1°), the formation of waves perpendicular to the second beam is not complete, having not enough energy to force the total dissipation of the first.

3 Discussion and mechanism

Depending on the energy of the projectile and, hence, the energy loss in the substrate, a number of interactions and reactions take place while the ion travels through the solid material. Elastic collisions with target atoms (nuclear regime) or inelastic collisions with target electrons (electronic regime) are the two basic processes that can take place, as detailed in Chapter 1. Depending on whether one or the other process prevails, these interactions can result in structural changes or even surface amorphization of the target, with the formation of an amorphous layer of a certain thickness up to amorphization in depth along the ion trajectory. Depending on the type of material employed and the energy of the excitation, these changes may result from atomic displacements, displacement cascades, disorder, ionisation, or even electronic excitations.

Understanding the process underlying the production of periodic structures, whether at high or low energy, is emphasized. The sequence of events that led to their formation will now be examined.

Since in this study electronic energy loss is the dominant slowing down process, particular interest will therefore be given to this process for the different modifications that it generates. Thus, the process at the origin of these structural modifications following the energy transfer that occurs has been successfully described with the thermal spike model. This approach based on heat transport equations was used to explain the formation of tracks in insulators [54] [58] before being generalized to other materials [52] [53] [55]. This approach considers that when the ion transfers its energy to the target electrons, an increase in temperature occurs along its trajectory, which can cause local melting of the lattice within a radius of a few nanometers. To stabilise itself, the electronic system in turn transfers this excess energy to the other electrons in the system by electron-electron interaction and then to the atoms of the lattice by electron-phonon interactions. This fusion, followed by the dissipation of energy by thermal conductivity, results in the solidification of the area along the ion's trajectory, leaving an amorphous cylindrical track with a radius of a few nm surrounded by a disturbed area. Therefore, the creation of tracks in the bulk can be explained by this two-temperature model. However, when irradiation is done at a grazing angle, as explained in Chapters 1 and 2, the changes are different, especially when it comes to the electronic structure, which is crucial for the formation of chains [6]. A successful change was thus made to the standard thermal spike model, taking into account the lack of radial symmetry along the ion path and considering that the electron density is non-homogeneous. [6]. Whereas at the beginning of the path, the energy loss is predominantly electronic, with a relatively straight path. At the end of the path, nuclear collisions dominate, giving rise to displacement cascades.

The first hypothesis puts forward the fact that the chains of nano-hillocks seen under irradiation at a grazing angle and at low fluence may be linked to the formation of high fluence waves (ripples). Given that the first waves appear in a single-impact regime, increasing the fluence would tend to bring the nano-hillocks composing the chain together to form the micrometric waves observed at high fluence. However, this hypothesis is quickly abandoned, as the range size does not seem to coincide. While the nano-hillocks and the space between them in the chains are in the nanometer range, the waves have a spacing and size in the micrometre range. Adding to this, the fact that as

the fluence increases, the tracks tend to overlap until they form an amorphous layer on the surface, so that the nano-hillocks are no longer distinguishable.

Another hypothesis puts forward the mechanism proposed for structuring surfaces at low energy (energy below 10 keV/u). In fact, nanopatterning of solid surfaces at low energy is the subject of a multitude of studies, especially for the formation of wave-shaped structures at the micrometric or even nanometric scale for applications such as nanopatterned substrates. The first ripple was observed for the first time by Alvez et al. in 1962 in the case of glass bombarded with 4 KeV [21]. Quite a few other studies followed for different types of materials such as metals [152], insulators, or semiconductors [153] [151] [150] with a particular focus on silicon. Most of those proposed at low energy involve the sputtering process, which results in the pulverisation and removal of surface material (roughening effect) followed by a smoothing effect (which may be due to ion induced diffusion or viscous flow for amorphous surfaces). Consequently, the combination between these two competing and complementary processes was considered, and this is where the Bradley-Harper model comes in [154]. The linear continuum equation of Bradley Harper was used to reproduce what was observed experimentally, such as the orientation of the ripples and their growth. But for high fluences, a saturation of the ripple pattern occurs, and it cannot be explained by this linear model. So several nonlinear models [155–158] were then introduced to explain the rest of the process, which worked pretty well. However, this process is negligible in our case compared to what happens at low energy, where the sputtering rate is higher. The fluences in this case are on the order of 1×10^{17} ions cm^{-2}, we do not exceed 4×10^{14} ions cm^{-2} with sputtering yields as calculated with SRIM [1] estimated around 0.3 atom per incident ion for the material used in this study.

This returns the discussion to irradiations within the same energy range (MeV-GeV). The first observation of surface structuring appearing as a change in dimension following irradiation with SHI was observed by Klaumunzer et al. in the case of metallic glass [27] [28]. This anisotropic growth of the thin film system was presented as a retraction of the material along the direction of the beam with a reduction in dimensions parallel to it (contraction) and its expansion perpendicular to it. This would be characterised as an increase in dimensions perpendicular to the ion beam (swelling). This is illustrated in IV.10 (a). Note that this effect can be accentuated and increased with electron energy loss. After that, several investigations have been conducted on different amorphous metallic and non-mettalic alloys. A model with quite similar behavior is then established, with the generation of disorders and defects followed by anisotropic deformation of the sample's dimensions giving rise to a morphological change in the surface with the appearance of periodic structures. To explain this phenomenon, a combination of two complementary processes has been proposed. First, as it is known and described above, a cylindrical region is generated around and along the ion trajectory. This cylindrical thermal spike tends to expand thermally, creating a molten zone and generating shear stress. This energy, once transferred to the rest of the crystal, induces a cooling phase in the cylindrical region, causing it to solidify with the associated strain increment. This subsequent melting and resolidification of the studied crystal lattice within the cylindrical region creates stress along the ion track [29] [159], which may induce surface instability in the deposited thin layer system. Periodic cracks oriented perpendicular to the ion beam direction can then appear in the film when and if this stress exceeds the resistance of the surface to fracture. This

is the phenomenon known as Grinfeld's instability [24] [25]. It is suggested that by increasing the fluence, these cracks evolve into periodic nano-pattern and lamellar structures due to anisotropic plastic deformation (i.e., the hammering effect) [28] [29].

This second stage of the surface nanostructuring process with the formation of these so-called lamella structures was observed in several studies for irradiation of halide (LiF, BaF_2) [20] and oxide (NiO) thin film systems with different substrates (SiO_2, Al, etc.) [160] [161] at off-normal incidence with SHI. These structures, characterised by their periodicity or width, also evolve with fluence, with a decrease in width as the periodicity increases. However, in this case, depending on the thickness of the film and the projected ion range, the ion can exceed the film and reach the substrate, inducing a transfer of energy from the film to the substrate through their interface. Therefore, the impact of the substrate cannot be neglected. As observed in the case of the NiO layer on an Al substrate [161] where the width of the ripples is greater with a lack of periodicity of the lamellae compared to the film deposited on SiO_2.

First of all, it is important to note that in this thesis, a different case from that previously described is discussed. In this study, the irradiation was done on only single-crystal samples without adding or depositing a thin layer on the surface. Given that X-ray diffraction shows that the material remains in an elastic strain regime, this agrees with the fact that no surface cracking was observed at any angle, even at high fluences. Therefore, one may assume that wave formation was not preceded by surface cracking. Added to this, the wave formation that occurs after SHI irradiation on $SrTiO_3$ samples takes place at high fluence, i.e. in the regime where the chains overlap as the fluence increases until they form an amorphous layer on the surface. The thickness of the latter can be controlled, particularly with the angle of incidence. In the case of $SrTiO_3$ irradiated at 6°, three layers were distinguished: an amorphous layer of about 1 µm, followed by a disordered crystalline layer, and finally the remaining crystalline layer (see FigIII.5 in Chapter 3). This phase change is accompanied by changes in physical and mechanical properties. The literature reports density values for amorphous and crystalline $SrTiO_3$ of 4.2 $g.cm^{-3}$ and 5.1 $g.cm^{-3}$, respectively [162]. Given that the density of the crystalline phase is higher than that of the amorphous phase, and from the results provided by our TEM observations, which confirm the disorder of this layer, it can therefore be considered to possess a less rigid structure than the crystalline structure. This will have an impact on the value of the Young's modulus of the two structures. Although Young's modulus for single-crystal strontium titanate depends on the crystallographic direction, we can nevertheless define an average value based on the literature, which estimates it at between 260-300 GPa for the crystalline $SrTiO_3$ and for the amorphous phase, its value can vary between 190 and 210 GPa.

By reviewing the various mechanisms proposed so far in different studies,it is possible to reject the implication and connection between the production of the ripples seen at high fluence and the chains of nano-hillocks created on the sample's surface by the collisions of individual ions at extremely low fluence, as well as the Bradley-Harper theoretical model. By considering the succession of layers of different states, one may analyse the situation where an amorphous layer is placed on a crystalline substrate, involving two systems. This leads to the hypothesis proposed here, where anisotropic plastic deformation would induce the self-organisation of the surface of a

single crystal insulator such as $SrTiO_3$. The top (amorphous) layer of our sample can be seen as a rigid layer that becomes more flexible as it is irradiated at high fluence. This layer will therefore seek to extend over a larger area than its original dimensions (swelling). However, the fact that amorphization only occurs over a certain thickness leaves the rest of the sample crystalline. So the crystalline part can be seen as a substrate to which the layer is intimately bonded and which in some way blocks its freedom of movement. Thus, the swelling of the amorphous plane is constrained by the crystalline matrix, and only the dimension normal to the surface is free to expand, while along the two other dimensions, the amorphous layer remains restrained as it has to adapt to the dimensions of the crystalline layer. This stress and the excess energy in a restricted area therefore induce the appearance of a surface structure due to anisotropic plastic deformation. This deformation appears as a decrease in the dimensions parallel to the direction of the ion beam and an increase in those perpendicular to it. These quasi-periodic structures (waves) oriented perpendicular to the ion beam will therefore tend to evolve as the irradiation continues, and this was clearly observed in this study, in particular with the increase in the height and reduction in the width of the waves with increasing fluence. This is schematized in Figure IV.10 (b).

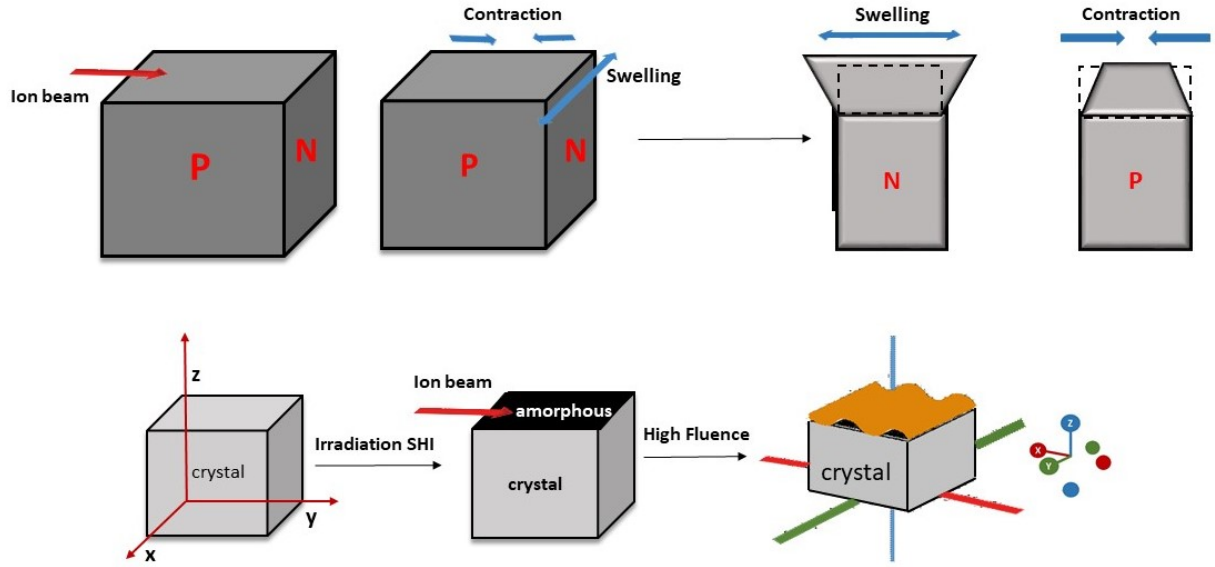

Figure IV.10: Illustration showing the expected Hammering effect (a) in the case of an amorphous sample, with the expected expansion of the dimension perpendicular to the ion beam (represented here by N) and the contraction of the dimensions parallel to the ion beam (face P) and (b) in the case of an amorphous film on a crystal layer. The amorphous layer formed on the surface is linked to the crystalline substrate, it is constrained along the x and y dimensions, and only the dimension normal to the surface is free to expand, hence the way waves develop. The direction of the ion beam is shown by the red arrow.

Chapter V

Modification of 2D materials by swift heavy ions

1 Introduction

The introduction of structural defects in order to tailor a material requires a level of precision that only a few techniques offer. One of the most effective methods is the use of swift heavy ions, which can modify the structure of the target and create specific surface structures. As described in Chapter 2, inducing defects in 2D materials has a noteworthy influence on their electrical, chemical, and luminescent properties, among others. Introducing perforations of different sizes, for example, broadens the potential applications, whether as a catalytic activity tool or as membrane [106] [135] [32] [163].
The choice of substrate has a considerable influence, in addition to creating defects to increase the variety of uses for this sort of material [164] [165] [166]. The combination of 2D materials and metallic oxide materials gives rise to heterostructures whose combined properties enable a versatile achievement of the functionality of this system. This is done with a tuning of the physicochemical properties with the tailoring of the intrinsic optical and mechanical properties. Huang et al. have demonstrated the importance of the interlayer between the 2D materials and the substrate, and more specifically for $SrTiO_3$ [31]. After chemical vapour deposition of a MoS_2 monolayer on crystalline $SrTiO_3$, they carried out various analyses to probe the optical and mechanical properties. Through photoluminescence (PL) measurements at variable temperature, the $SrTiO_3$ showed a tuning effect on the MoS_2. This is due on the one hand to a flat, clean substrate surface and an interface free from external contamination. The latter also enables direct electro-phonon coupling, improving band energy and photoluminescent properties [31].
Controlling the defects generated through the regulation of the irradiation parameters is the crucial step towards enhancing the modifications and, thus, unlocking the potential applications. Studies conducted on MoS_2 produced by CVD and irradiated with SHI showed unique behavior compared to graphene concerning the introduction of surface defects/structure [64] [137] [9]. The folding formation in MoS_2 is influenced by particular factors, including the orientation of the MoS_2 monolayer flakes relative to the direction of the ion beam. The ion beam's impact angle relative to the chrystallographic edge of the flakes must be a multiple of 30° [9] [64]. The second solution is based on forced folding using cross-irradiation [9].
In this chapter, the outcomes from exposing MoS_2 to swift heavy ion irradiation will be presented. The MoS_2 layer was grown through chemical vapour deposition (CVD) on 90 nm SiO_2/Si amorphous substrates and $SrTiO_3$ single crystalline clean and atomically flat substrates. A beam of 91 MeV Xe ions under grazing incidence angle was used. Raman spectrum analysis and AFM in non-contact mode were undertaken. The study focuses on the impact of the various factors involved, such as the type of substrate, or irradiation parameters such as the angle of incidence of the ion beam or the fluence, on the probability of folding. In particular, it shows that the condition of a specific orientation of the MoS_2 flakes for the formation of folds can be overcome.

Preparation of MoS_2 monolayer on different substrates

In order to enhance the intrinsic properties of MoS_2 deposited on a crystalline substrate, con-

trolled fabrication is essential. For this study, two different techniques were used for the growth of molybdenum disulphide (MoS_2). First, it was directly grown on SiO_2/Si amorphous and (100) $SrTiO_3$ single crystal substrates using chemical vapor deposition (CVD). This technique enables the growth of a high-quality MoS_2 layer across a vast region. Secondly, some of the samples were prepared differently. The MoS_2 was first grown by CVD on 285 nm SiO_2/Si substrates and subsequently transferred by means of polymer to the $SrTiO_3$ samples at room temperature. As illustrated in the figure V.1 outlining the steps in this process, the technique consists of depositing and spin-coating a drop of polystyrol (PS) dissolved in toluol on the supported MoS_2 grown by CVD. The sample is then heated at 85°C to dry the polystyrol. The thin PS film is scraped off to allow the water droplets placed on the cutting edges to intercalate between the polystyrol (PS) thin film and the substrate, allowing to peel off the PS/MoS_2 from the substrate. The film is then deposited on the $SrTiO_3$ substrate and heated twice, at 80° C and 150°C. The polystyrol (PS) is then dissolved by immersing the sample in a toluol bath for 30 minutes.

This synthesis was possible thanks to the collaboration with Prof. Dr. Marika Schleberger's team, specifically Dr. Lukas Madauß, and a special thanks to Yossarian Liebsch, who performed most of the MoS_2 deposition, including with the transfer technique described above.

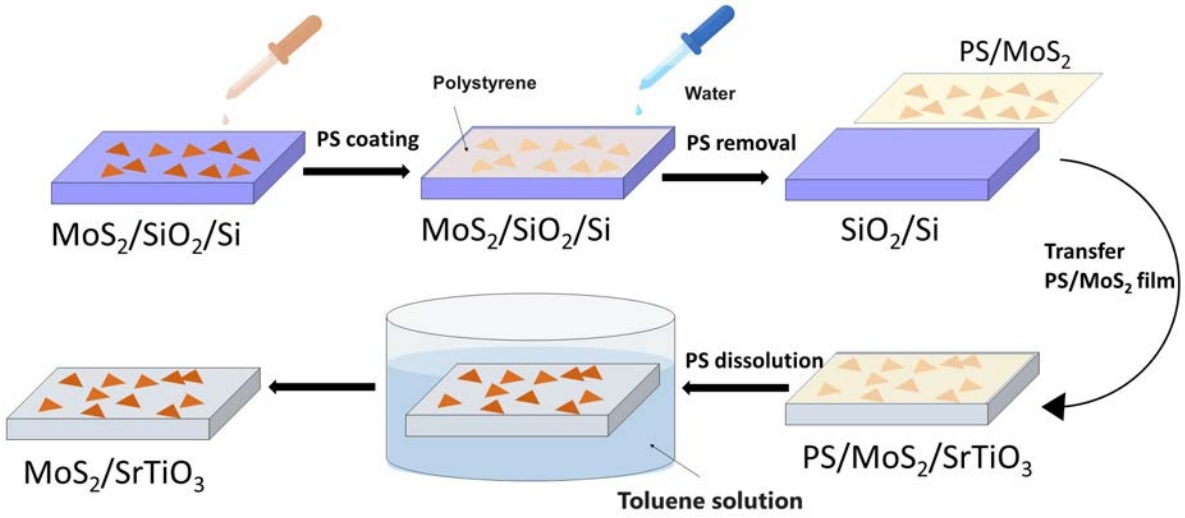

Figure V.1: Schematic representation of the steps involved in the preparation of $MoS_2/SrTiO_3$ samples by means of the transfer method.

These two techniques result in the formation of MoS_2 flakes of different shapes. Note that the MoS_2 layer does not completely cover the substrate, as it grows in the form of single flakes with sizes varying from a few dozen nanometers to a few hundred μm^2. The MoS_2 flakes crystallise in a circular pattern with an irregular edge when directly grown on $SrTiO_3$. In contrast, the transfer deposition method produces the usual triangular shape of flakes. These differences are illustrated in Figures V.2(a) and (b), respectively, which show optical microscope views of the flakes. The flakes are generally located by their optical contrast to the substrate. However, when using $SrTiO_3$ as a substrate, it is more difficult to observe them than in the case of SiO_2. There are several

factors affecting the morphological change of MoS_2 flakes. Li et al. investigated the growth of monolayer MoS_2 using modified CVD methods on glass substrates [167]. They reported the impact of different factors, such as the temperature of the sulphur source (140°C), the growth time, or even the S/Mo ratio, on the growing interface. To avoid any confusion, the study presented below was carried out on samples prepared by the transfer method, i.e. with the triangular form.

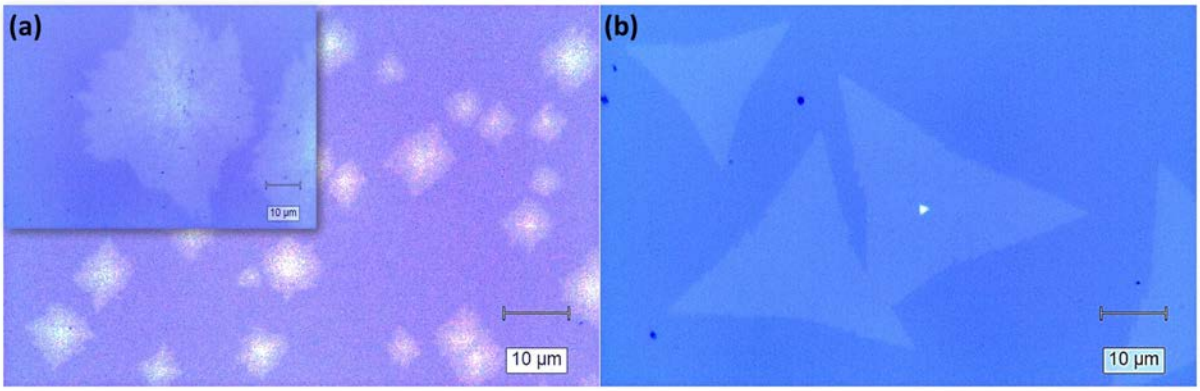

Figure V.2: Optical microscope images showing MoS_2 flakes deposited on $SrTiO_3$ substrate, (a) by a direct CVD method (b) deposited on SiO_2 then transferred to $SrTiO_3$.

2 Impact of the angle on the morphological defect induced on MoS_2

2.1 MoS_2 on $SrTiO_3$ substrates

As highlighted in Chapter 2, as 2D materials are composed of a single or a few layers of atoms, Raman spectroscopy can be considered the most appropriate method for characterising such materials. This technique enables the identification of various properties, such as layer number [10], defect densities [168], and charge carrier concentrations [169], without the risk of causing damage to the materials.

The Raman and photoluminescence measurements were carried out at room temperature using the equipment from Pr. Marika Schleberger's laboratory. The image in Fig.V.3 depicts an optical microscope view of a flake of a non-irradiated MoS_2, with the accompanying Raman spectrum; this is the commonly observed for $MoS_2/SrTiO_3$. The observed peaks of MoS_2 are typically detected in the range of 380 to 410 cm^{-1}. The signal from MoS_2 may not be detectable because of its single layer structure, as it is overpowered by the stronger background vibration of the substrate ($SrTiO_3$).

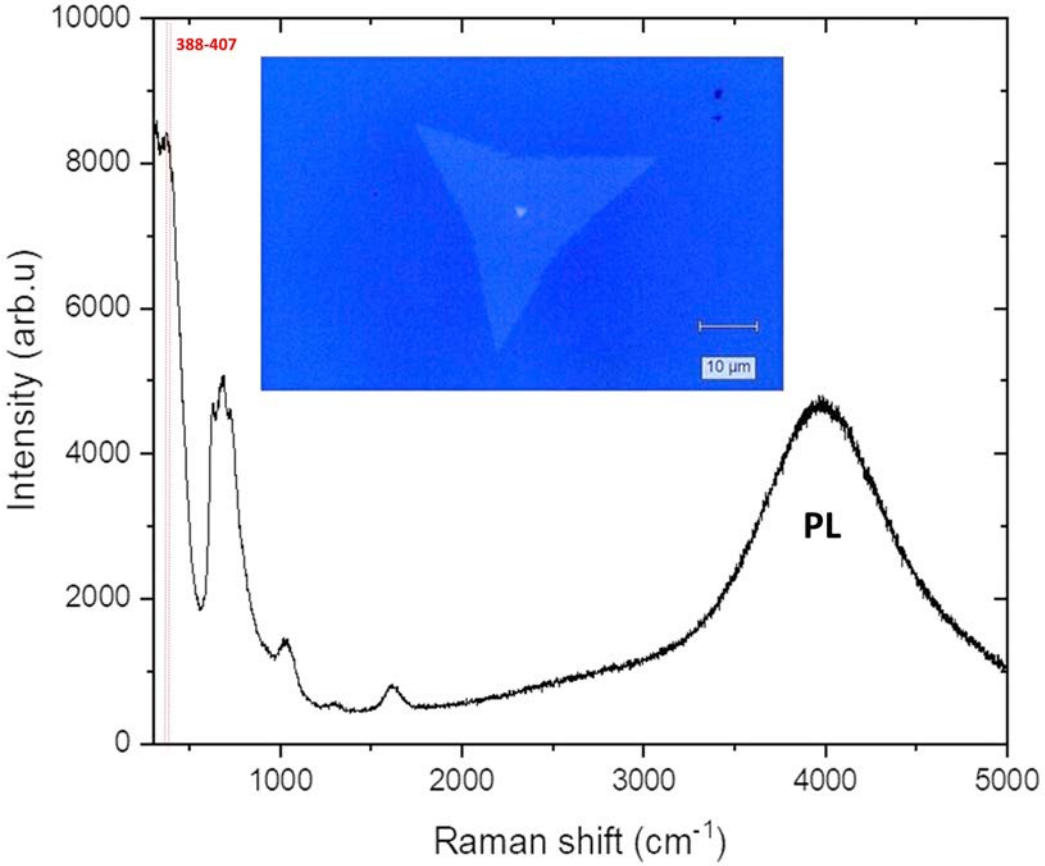

Figure V.3: Raman spectra of MoS_2 on the single crystalline $SrTiO_3$ sample with the optical image of the MoS_2 flake inset.

To confirm the position of the peaks before irradiation, a spectrum was taken from a region containing two layers of MoS_2 and compared with a spectrum of a single layer of MoS_2. As can be seen in the figure V.4, the distance between the two peaks of the 2l-MoS_2 is around 22 cm^{-1} with a clear decrease in the intensity of the photoluminescence peak. This coincides fairly well with what is expected in the presence of the MoS_2 bilayer. Considering that there is typically a 3 cm^{-1} discrepancy in width between the two peaks for the bilayer and the monolayer, these values can be regarded as a point of reference.

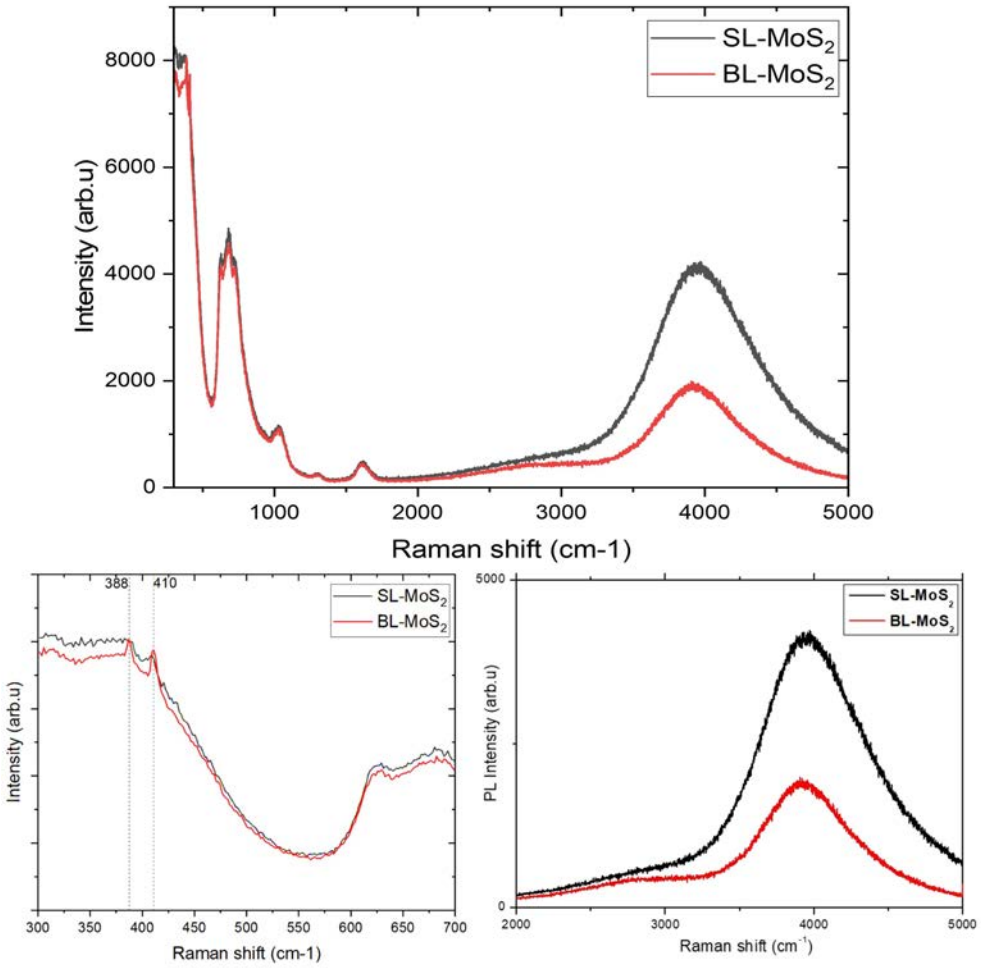

Figure V.4: Raman and Photoluminescence spectra of single and bilayer $MoS_2/SrTiO_3$ (100).

The figure V.5 shows the spectra obtained for five samples. Four were irradiated with 92 Xe ions for an increasing angle of incidence towards normal to the surface, i.e. 0.3°, 0.6°, 1.2° and 2° while keeping the same fluence, i.e. 5×10^9 ions cm^{-2} and the same flux, i.e. 5×10^8 ions cm^{-2}.s. As mentioned above, due to the substrate signal, it becomes difficult to process the Raman peaks specific to the vibration of the MoS_2 crystal lattice. An exploitation through the photoluminescence (PL) signal peak of different irradiated samples in comparison with an unirradiated sample can be undertaken. The intensity shows a tendency to decrease sharply as the irradiation angle increases towards the surface normal (fig. V.5(c)). This drop in intensity is accompanied by a shift in the peak towards lower frequency values. This may be attributed to several factors, such as structural changes that may have occurred in the material, which confirm the development of defects in the material. The decrease in intensity of the PL peaks is accompanied by their broadening, as can be seen in Fig.V.5(c-d) where the width and height of the different peaks are plotted. This broadening is proportional to the defect concentration [170] [171]. Defects present in the material have an effect on the electronic structure, which can result in decreased electrical conductivity and light scattering, leading to reduced luminescence efficiency. Studies have shown that regardless of the

sample thickness, the photoluminescence (PL) intensity spectra of MoS_2 are greatly affected by temperature [172] [173]. This is due to the impact on the recombination process of electronic holes, which ultimately reduces their intensity [172] [173]. It should be noted that after irradiation, the interaction of the 2D material with its environment, and in particular the interface coupling with substrate, can change and become more important, which could also lead to a shift and broadening of the PL peak [174] [175] [31].

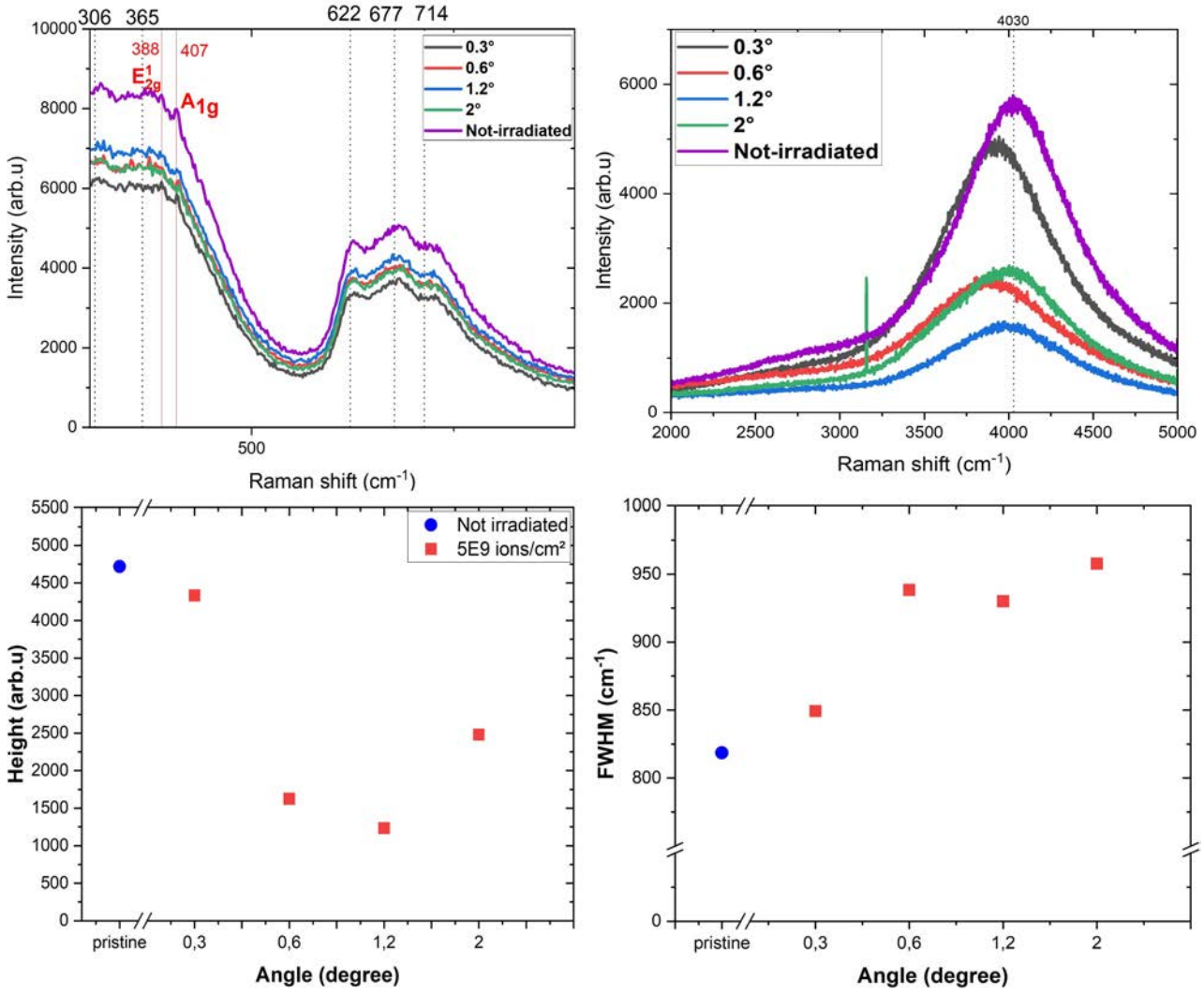

Figure V.5: Raman (a) and PL (b) spectra of $MoS_2/SrTiO_3$ (100) irradiated at 5×10^9 ions cm^{-2}. The peaks representing MoS_2, i.e. A_{1g} and E_{2g} are shown in red, and the remainder represents the vibrational signal from the substrate atoms (STO). (c) represents the variation of the height (a) width (b) of the photoluminescence peak of the $MoS_2/SrTiO_3$ (100) samples irradiated at 5×10^9 ions cm^{-2} as a function of the irradiation angle.

As the photoluminescence (PL) peak is sensitive to the concentration of defects in the material, it can be used to quantify the defects created in the MoS_2 crystal structure as a function of irradiation

parameters. An analysis of the photoluminecence (PL) peak ratio before and after irradiation was carried out and is shown in figure V.6. When the angle of incidence of the ion beam is increased towards the surface normal, the PL peak ratio decreases until it reaches a limit around = 1.2°, at which it increases again. This decrease in intensity suggests an increase in defect density. Atomic force microscopy was used to confirm this hypothesis.
There is no additional data to suggest a trend for the increase in the ratio at angles greater than 2°. This could be an individual effect for this sample, or it could indicate that an increase in defects induces an increase in the interaction between the MoS_2 layer and the interfacial layer in the region where folding and other modification have occurred. To be able to derive an accurate analysis, another series of irradiations must be performed.

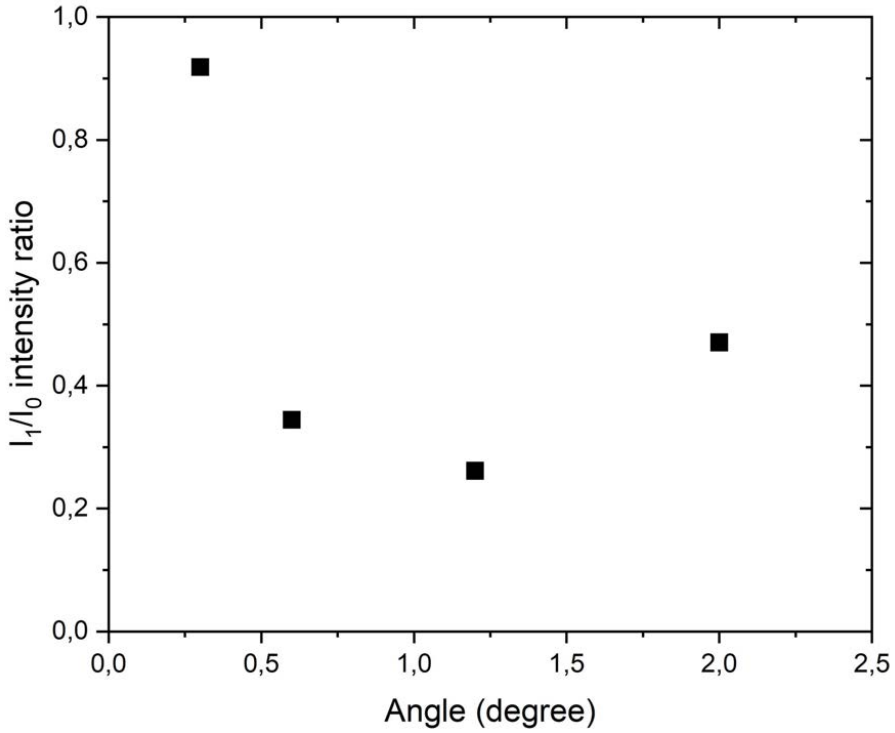

Figure V.6: I_1/I_0 intensity ratio of PL peak of $MoS_2/SrTiO_3$ irradiated with 5×10^9 ions cm^{-2} plotted as a function of the irradiation angle.

Atomic force microscopy observation of the defects induced on the surface of $MoS_2/SrTiO_3$

Several MoS_2 flakes scattered over the entire surface with different orientations with respect to the direction of the ion beam were analyzed by atomic force microscopy. The figure V.7 shows a selection of AFM images of MoS_2 single layer irradiated at a grazing angle of 0.3° with a fluence of 5×10^9 ions cm^{-2} and where the resulting morphological change can be observed. These structures appear as folds of different shape, size and direction relative to the direction of the ion beam. The orientation of the majority of the folded part with respect to the direction of the ion beam shows a

small opening at the beginning of the fold which widens towards the end of it. The folds in MoS_2 resulting from a single ion impact measure about (49 ± 4) nm in width at the beginning of the fold and roughly (134 ± 7) nm at the end of the structure. This is a little higher than what was seen in the case of graphene/$SrTiO_3$ [2]. Where for irradiation at 1° folds with dimensions of about 50-80 nm in width were observed, however the fold appeared straight and therefore the width was the same whether at the beginning or at the end of the fold [2].

Concerning the size of foldings obtained for $MoS_2/SrTiO_3$, most of the folds exhibit a length of approximately 100 nm. Occasionally, folds of different shapes may appear, as shown in figures V.7 (b-d), where, for the same irradiation parameters, folds oriented in the opposite direction to the ion beam V.7(b) or formed with four folded edges V.7(c-d) are present. The profile (fig V.7 (e)) of one of the MoS_2 folding shows two distinct edges, so the maximum height reaches around 7 nm and the thinnest layer (visible with the brighter contrast) is around 2 nm typical of an MoS_2 single layer. Much longer folds, which reach a length of 1 µm, was also observed as shown in figureV.8. Research carried out on other 2D materials such as graphene exfoliated on 90 nm SiO_2 and irradiated at 1.3° exhibit folding with a typical length of (149 ± 24) nm, and could reach (996 ± 691) nm for an angle 0.1° [9]. The irradiation of hBN at 1.5° results in folding length of (163 ± 51), while irradiating graphene/$SrTiO_3$ at 1° results in folding whose length can reach more than one µm [9]. Although the angles and fabrication techniques for the 2D layers are different from those used in this study, the evolution of the length of the folds with angle follows the same pattern and can be described by this relation: $L = d/\tan\theta$. L is the length of the fold and θ is the angle of incidence of the ion beam relative to the sample surface. The parameter d indicates the maximum depth of penetration of the SHI into the target at which the surface still reacts to the effects of the ions, which, then, corresponds to the end of the fold. Folding is also accompanied by the formation of a chain of nano-hillocks on the surface of the substrat $SrTiO_3$ after the ion impact (fig. V.8).

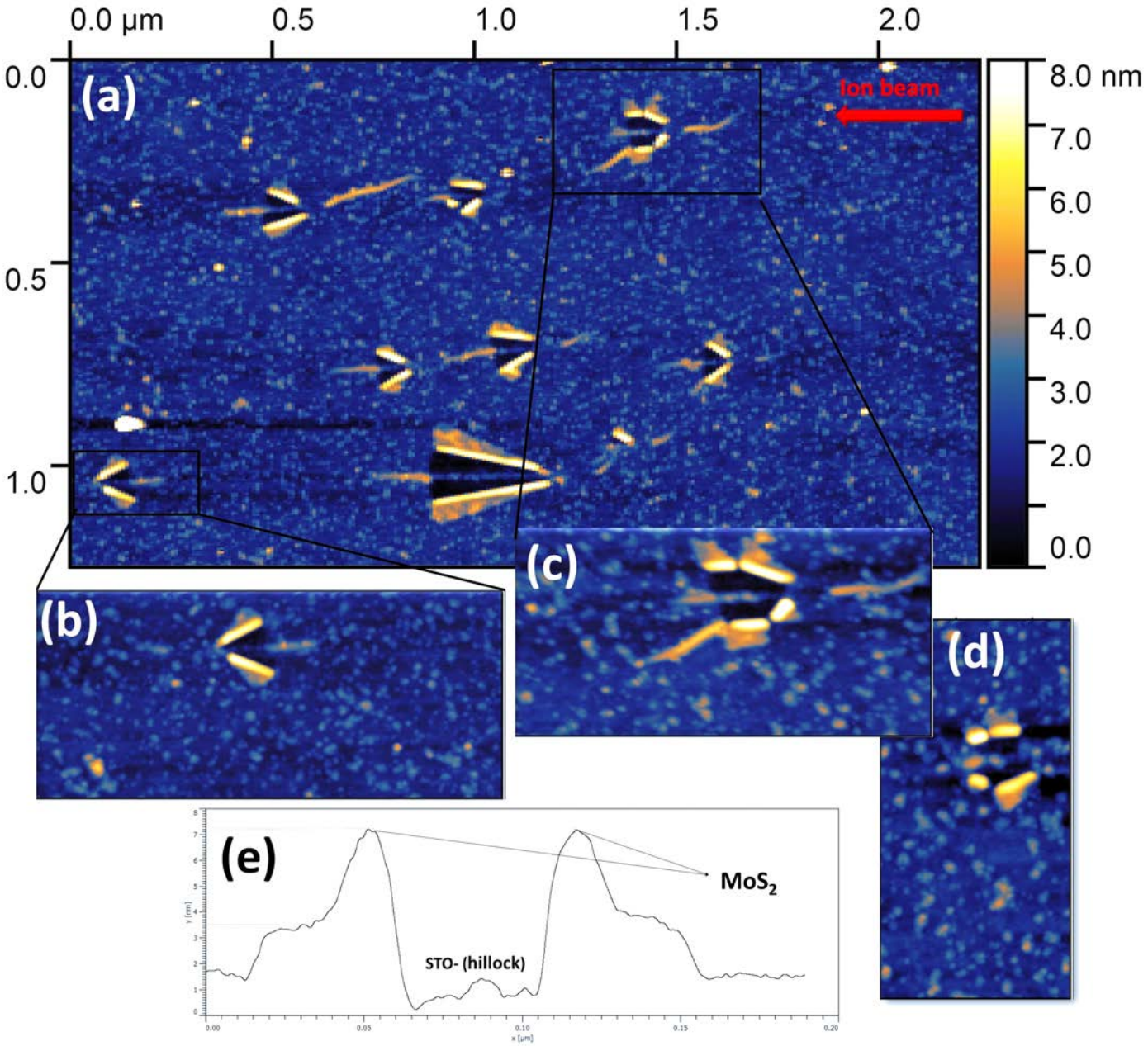

Figure V.7: AFM surface images of $MoS_2/SrTiO_3$ irradiated with $\phi = 5 \times 10^9$ ions cm^{-2} at $\theta = 0.3°$ (a) zoom on a fold reversed with respect to the direction of arrival of the ion beam (b) zoom on folds with four edges (c-d) a vertical profile section of one of the folds (e).

Studies conducted on various two-dimensional materials have demonstrated that the size and shape of folding is dependent on the angle of the incident ion beam and the type of substrate used [9] [32]. For the study carried out as part of this thesis and as mentioned above, for the same angle of irradiation (0.3°) and substrate ($SrTiO_3$), different sizes and shapes of folds were formed. For the most part, the folds measured (110 ± 10.5) nm in length. At the edges of the

MoS_2 flakes, when the ion beam hit the surface with a nominal angle of 30° or its multiple with respect to the crystallographic axis of MoS_2, their size increased by a factor of 10, while being aligned with the direction of the ion beam, as shown in figure V.8(a)(b). It should be noted that the angle measurement is subject to a relatively large error range. The angle between the ion beam direction and the edge axis of the MoS_2 single layer is determined by analysing the topographic AFM images; therefore, an effect of piezo drift during the measurements cannot be ignored.

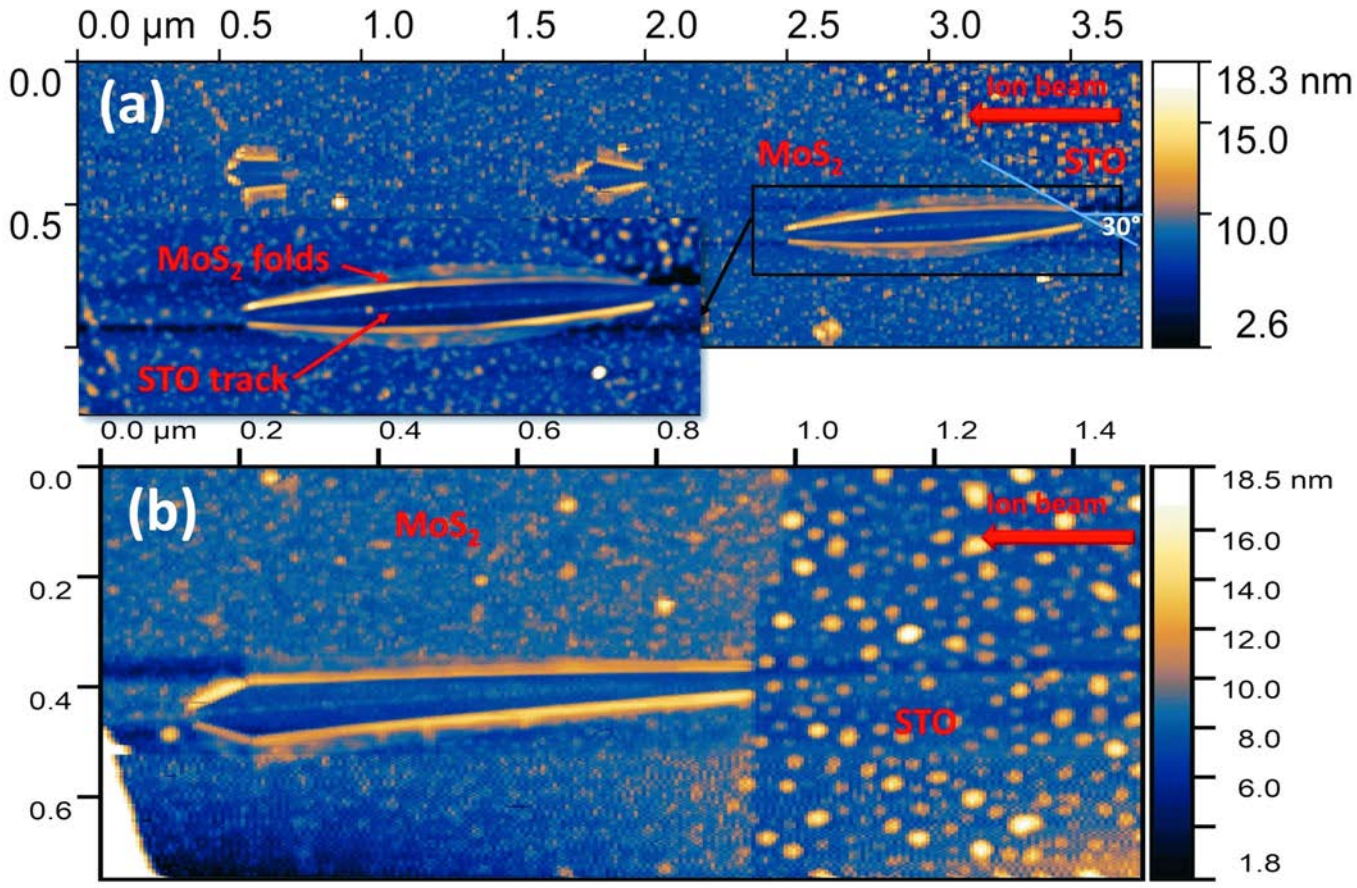

Figure V.8: AFM images of $MoS_2/SrTiO_3$ (100) irradiated with 92 MeV Xe ions with $\phi = 5 \times 10^9$ ions cm^{-2} at $\theta = 0.3° \pm 0.3°$.

Although the occurrence of folds up to 1000 nm in length corresponds to a grazing angle of $0.3° \pm 0.3°$, their formation does not appear to be systematic. As previously stated, they are most visible when the MoS_2 flakes are oriented at 30° or a multiple thereof with respect to the ion beam direction (Fig.V.8). This requirement of the direction of the MoS_2 axis with the ion beam has been stated in prior works [9] [64]. For a single layer MoS_2 deposited on SiO_2, grazing angle irradiation only resulted in folding if the specific orientation (described above) was present; otherwise, rifts were formed. This is not the case here, given that foldings are possible regardless of the orientation of the flakes; however, this condition of orientation has an impact on the size of the folds.
In contrast to the smaller folds of ($\approx$ 110 nm) observed in most of the other flakes, regardless of

their orientation to the ion beam direction, some remain even in the flakes oriented at a favourable angle.

In order to see the effect of the angle on the size, orientation, and shape of the folds, a second sample was irradiated under the same conditions with the same fluence (5×10^9 ions cm^{-2}) at an angle of ($0.6 \pm 0.3°$) with respect to the surface. The figureV.9 displays a range of AFM images of MoS_2 flakes with different orientations relative to the direction of the ion beam. The majority of the flakes, particularly those aligned at nominal angles of 30° or 50° as shown in Fig. V.9 (a-b), exhibit the formation of folds along the ion beam direction. However, an overlap of the foldings was observed, leading to the sputtering of the MoS_2 layer. In this case, the edge of the flake was oriented about 94° to the ion beam direction, as can be seen in figure V.9 (d-1,d-3). In the remaining flakes, a length measurement of the folds revealed a discrepancy in size when compared to those exposed at 0.3°, with a length of approximately 400 nm.

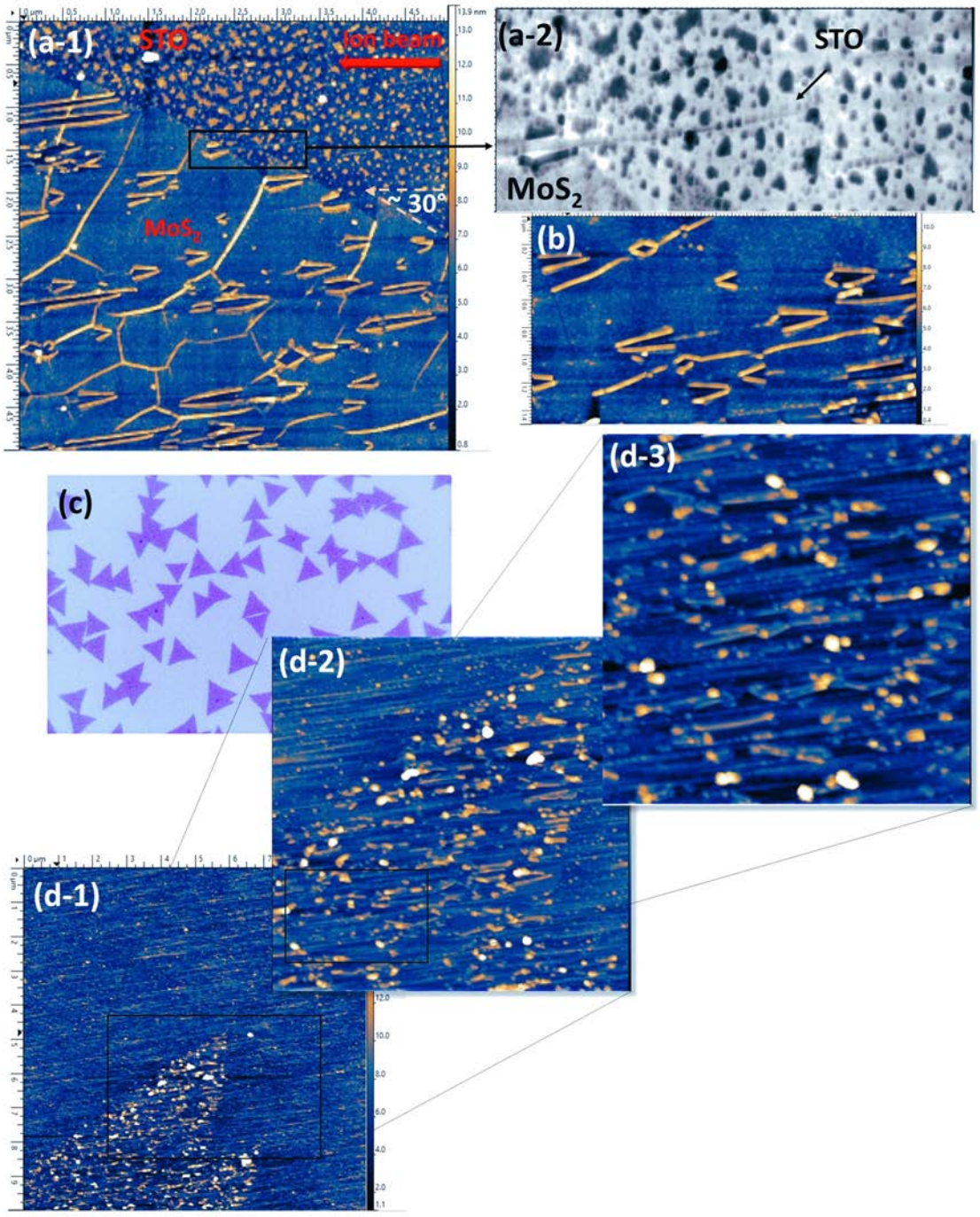

Figure V.9: AFM topography images of $MoS_2/SrTiO_3$ (100) after 91 MeV Xe irradiation with $\phi = 5 \times 10^9$ ions cm^{-2} at an angle of 0.6° ±0.3° where the axis of the flake is oriented at ≈ 30° (a-1) an image of one of the folds zoomed in with the chain of nano-hillcoks on the substrate (a-2) where foldings upon SHI impact are visible. Another example of folding on another flake (b) Optical image of CVD MoS_2 transferred onto $SrTiO_3$ substrates is shown in (c), whereas at (d-1 to d-3), an area of overlapping folds appears, giving rise to a sputtered surface.

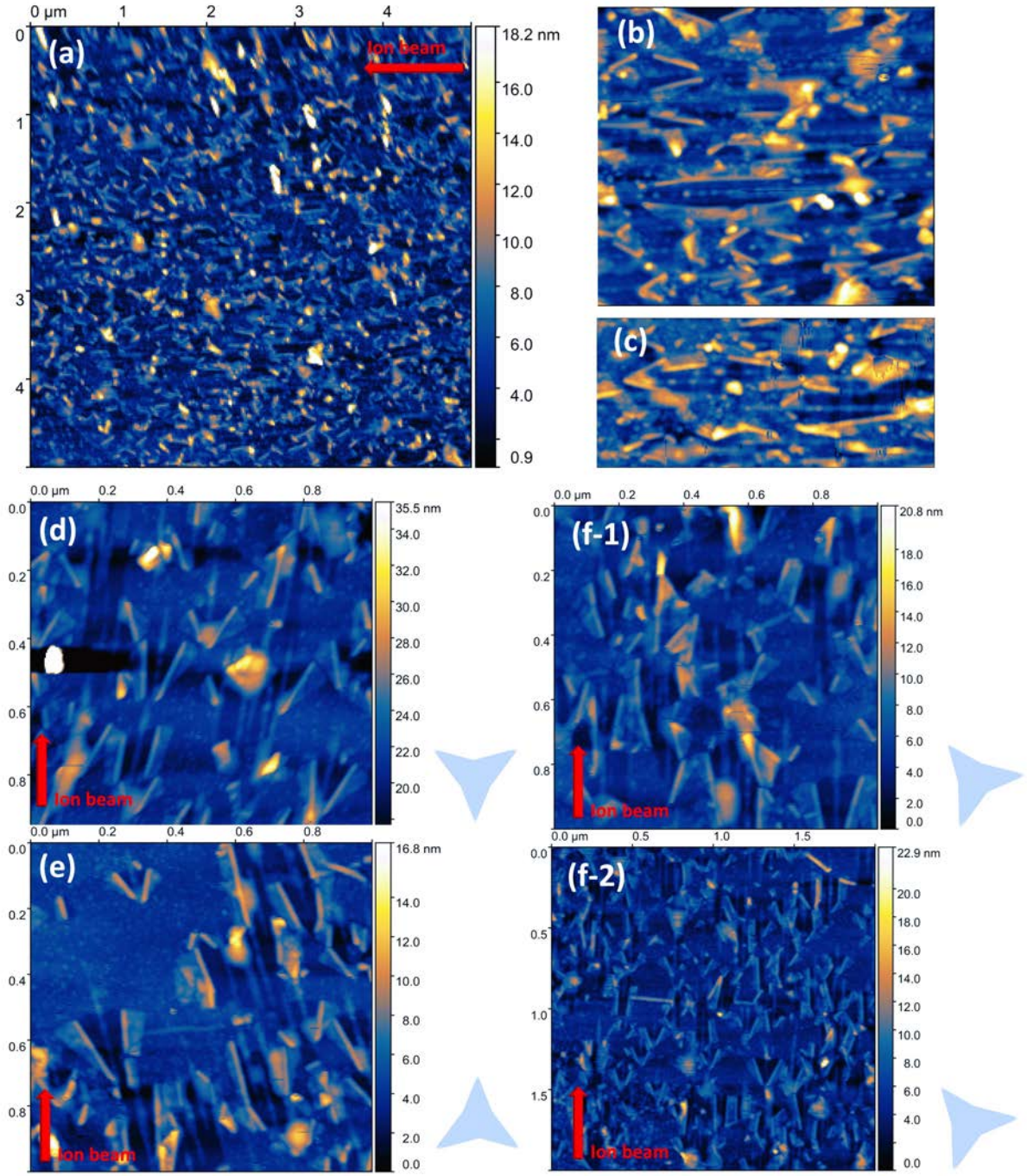

Figure V.10: Topographic AFM images revealing the folding of $MoS_2/SrTiO_3$ after irradiation with 92 MeV Xe ions with $\phi = 5 \times 10^9$ ions cm^{-2} at $\theta = 1.2°$ (a-c) and 2 ° (d-f).

Figure V.10 shows the effect of irradiations at 1.2° in (a-c) and 2° (d-f) respectively. A surprising effect was observed, while the MoS_2 layer irradiated at 1.2° appears to be completely pulverized with overlapping folds (Fig.(b-c)), the sample irradiated at 2° exhibits a reduced density of folds,

thereby preventing complete overlap and subsequent pulverization of the MoS_2 single layer. This phenomenon, unique to the 1.2° angle, is specific to this sample and the irradiation conditions that intensified the folding effect. It can be attributed to the presence of defects on the surface prior to irradiation, that is why was not included in the interpretation of the results.

Previous studies have reported resistance to folding of MoS_2/SiO_2 after irradiation with swift heavy ions at grazing angles [9] [64] [137]. In summary, they noted a lack of systematic folding in the supported MoS_2. Rift-like structures were observed in most cases, or folds accompanied by rifts. They deduced that to go beyond this limit and obtain folds, the crystalline axis of MoS_2 which is described with its edges, must form an angle of 30° or its multiple with respect to the swift heavy ion trajectory. However, in the results presented in this study, folding was observed and is present regardless of the orientation of the MoS_2 flakes. This limitation linked to the orientation of the MoS_2 crystalline axis can therefore be overcome by using strontium titanate as a substrate, which will in some way force the folding.
It should be noted that the surface folding density does not correspond with the density of incident ions. It has been observed that the folding density increases with the angle of incidence relative to the normal surface. It was also shown that when the angle of incidence decreases towards the surface, the length of the folds increases. Folds of different shapes and lengths may emerge in some circumstances. Such occurrences may be caused by the presence of pre-existing defects in the substrate or in the 2D material that direct, orient, or govern the fold and its form in some way.

2.2 Raman shift of irradiated MoS_2 on SiO_2 substrates

To find out more about the folding conditions of the supported MoS_2, another series of single layer MoS_2 samples was prepared by chemical vapour deposition, this time using 90 nm $\alpha - SiO_2/Si$ substrates. Thanks to Yossarian Liebsch from Marika Schleberger group, who carried out several depositions as well as some of the RAMAN measurements.
The same irradiation conditions and parameters were used. Figure V.11(a) depicts the Raman spectra of the previously stated samples as well as a unirradiated sample. Figure V.11 (b) shows the variation of the Raman spectra with the two prominent peaks, E^1_{2g}, corresponding to the opposite vibration of the sulphur atoms with respect to the molybdenum atoms, and A_{1g}, corresponding to the out-of-plane vibration of the sulphur atoms [176]. When subjected to low ion fluence irradiation of 5×10^9 (~50 impacts/μm^2), both the A_{1g} and E_{2g} peaks shifted towards higher frequencies. Several factors can affect the vibrational modes of the 2D materials, inducing a shift. This includes the presence, for example, of stress [177] [178] [179] or doping [180] [181]. The latter is often accompanied by a broadening of the peaks, which is not the case in this study, so this effect can be neglected. In the present study, as a blueshift of the two modes of vibration occurs, it can be attributed to the presence of compressive strain in the material, as it was reported in previous studies [182] [183] [177] [184]. Studies carried out on MoS_2 have shown that ion irradiation tends to cause defects that appear in the form of S vacancies [174] [118] [185] These vacancies may be the cause of the presence of compressive strain [186] [187].

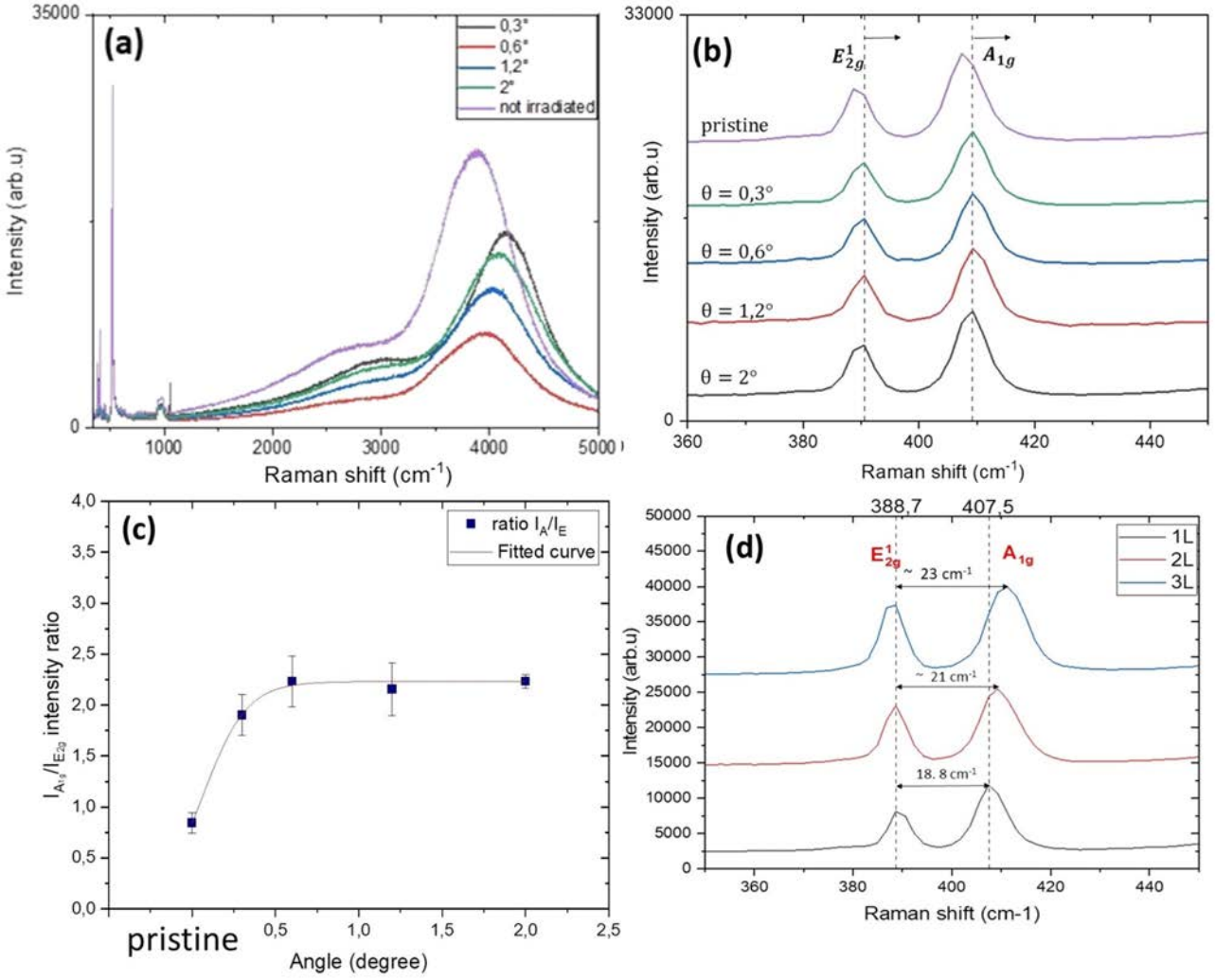

Figure V.11: Impact of angle on folding MoS_2/SiO_2. (a) Raman and PL spectra taken on the MoS_2 irradiated flakes compared with one before irradiation, (b) Raman spectra of irradiated SLM. (c) A_{1g}/E_{2g} intensity ratio plotted as a function of the angle of irradiation, (d) Monolayer, bilayer and trilayer comparative spectra.

Focusing on the two main first-order Raman bands as shown in Fig. V.11(b), the defect density in the single layer MoS_2 could be quantified by analyzing the I_A/I_E [188] ratio. From figure V.11 (c), the amount of defects corresponding to the peak intensity ratio I_A/I_E appears to increase as the grazing angle—an angle near the surface—increases towards the surface's normal. This is observed while maintaining a constant fluence of 5×10^9 ions cm^{-2}, equivalent to an average ion impact of 50 / μm^2. The intensity ratio's value rises until a nominal angle of 0.6° and thereafter saturates at roughly 2. The change in structure and atomic bonding has a significant impact on the behaviour and response of the vibrational modes (E^1_{2g}, A_{1g}) of MoS_2. Thus, the increase in the intensity ratio up to a certain value may be due to the creation of larger defects, which affect more the out-of-plane vibrations of the sulphide S atoms exposed to a certain stress than those in the

Mo-S longitudinal vibrational plane. From a nominal angle of 1.2°, a stabilisation of the variation indicates the stability of the network in its current form. This demonstrates the effect of the grazing angle on the crystal structure [189].

In addition to investigating Raman peaks, the analysis of the photoluminescence peak associated with each sample provides another means of studying defects in 2D materials and gaining insight into the effectiveness of introducing such defects.The intensity of the photoluminescence (PL) peaks shown in figure V.12 (a) appears to progressively decrease as the angle of irradiation increases towards the surface normal. To analyse this in detail, a fit was performed for each peak. The parameters of each were extracted, including the precise position of the peaks, their intensity and width. The error bars were calculated from the analysis of three distinct spectra for each angle. The results are shown in figure V.12 where in (b) the shift of the photoluminescence peak relative to its position before irradiation is represented as a function of the irradiation angle, while (c) exhibits the PL peak width variation as a function to the irradiation angle.

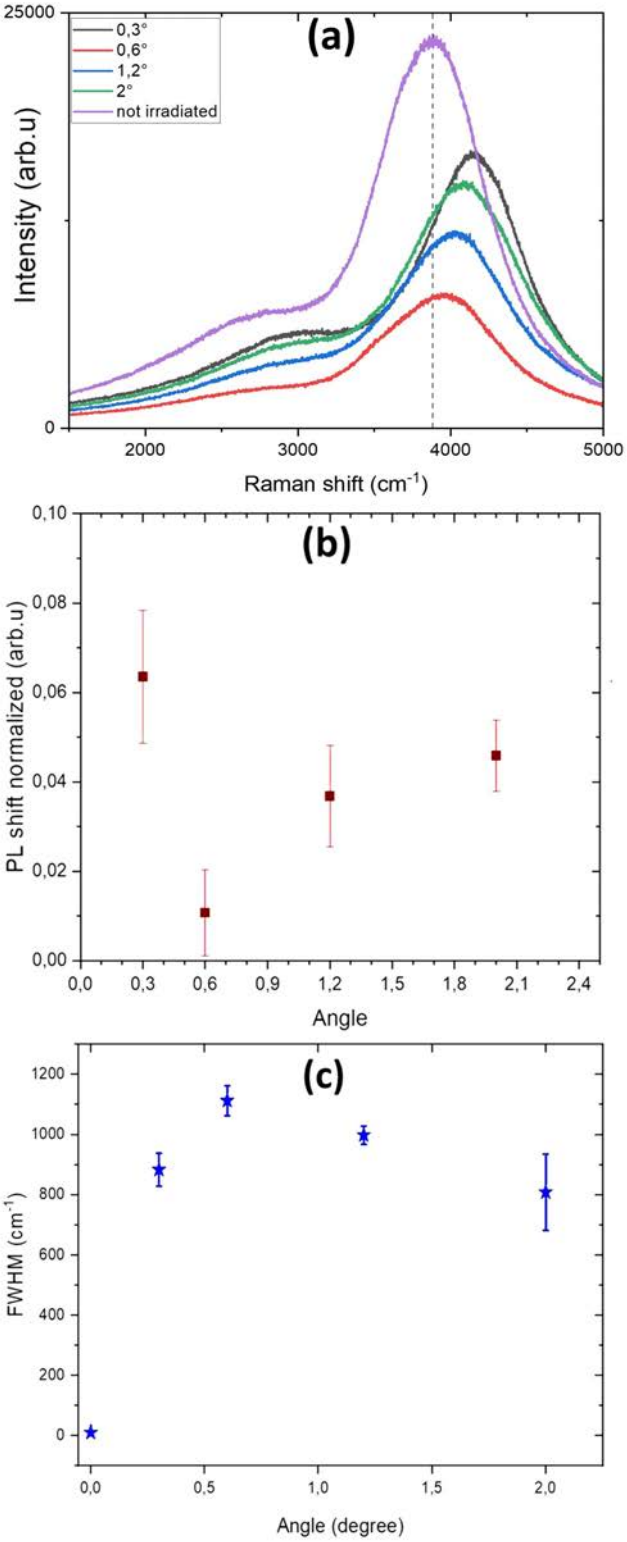

Figure V.12: (a) Photoluminescence spectra of single layer MoS_2 irradiated with 92 MeV Xe ions with a fluence of 5×10^9 ions cm^{-2}. This plot displays the shift in the peak position (b) and the variation in the peak width with respect to the irradiation angle θ.

As the defect density increases with the angle, there is a noticeable blueshift of the PL peak in comparison to the unirradiated sample. The shift is accompanied by a decrease in intensity, which is characteristic of an increase in defects in the crystalline structure. There is also a variation in the width and height of the peaks, which increases as the angle of irradiation increases towards the surface normal, up to approximately $1100\,\mathrm{cm}^{-1}$ for an irradiation angle of 0.6°, then a narrowing of the peaks begins for larger angles. This may indicate a stronger sensitivity of the structure to very grazing angles compared to irradiation angles > 1°.

All of these samples have been analysed using AFM and the results are presented below.

2.3 Morphological defect on MoS_2 on SiO_2 substrates

AFM analysis of the sample irradiated at a grazing angle of 0.3° revealed no defect formation on the MoS_2 surface despite the orientation of the flakes with respect to the ion beam direction. At angles of 0.6°, 1.2° and 2°, rifts with smooth edges oriented in the direction of the ion beam were observed. It is important to remember that by folding, one means that the layer of MoS_2 opens up and bends sideways following the ion beam direction. As a result of the doubled edges, the fold gains height, as seen in the image V.13 (a), where the profile of a fold has been obtained. While the rifts form on the MoS_2 surface, the surrounding surface remains flat; these defects take the form of nano-incisions. The profile of one of these rifts is shown in Fig. V.13(b).

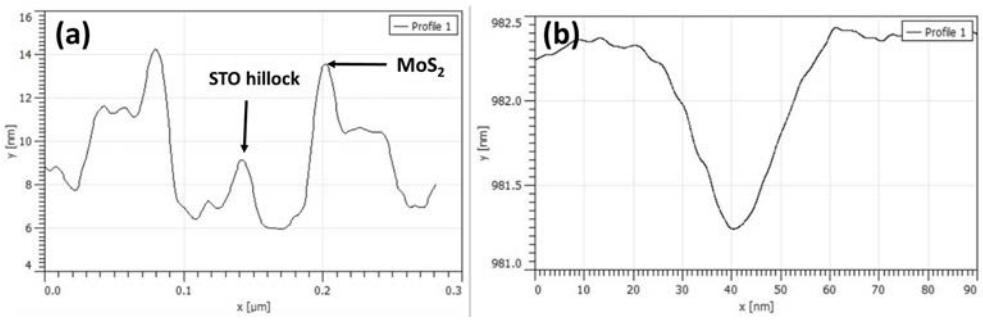

Figure V.13: Line profiles of a folding in $MoS_2/SrTiO_3$ (a) and a rift in MoS_2/SiO_2.

Figure V.14 shows the surface of the three samples irradiated at three distinct angles with 5×10^9 ions cm^{-2} and characterised by means of atomic force microscopy (AFM). The part circled in red in fig.V.14 (a.1) shows a much larger crack resulting from a double ion impact. Fig.V.14 (c.1) was made on the same MoS_2 flake as fig.V.14 (c) but situated in a bilayer location. A decrease in rift density has been observed with an impact on the shape, which appears less smooth.

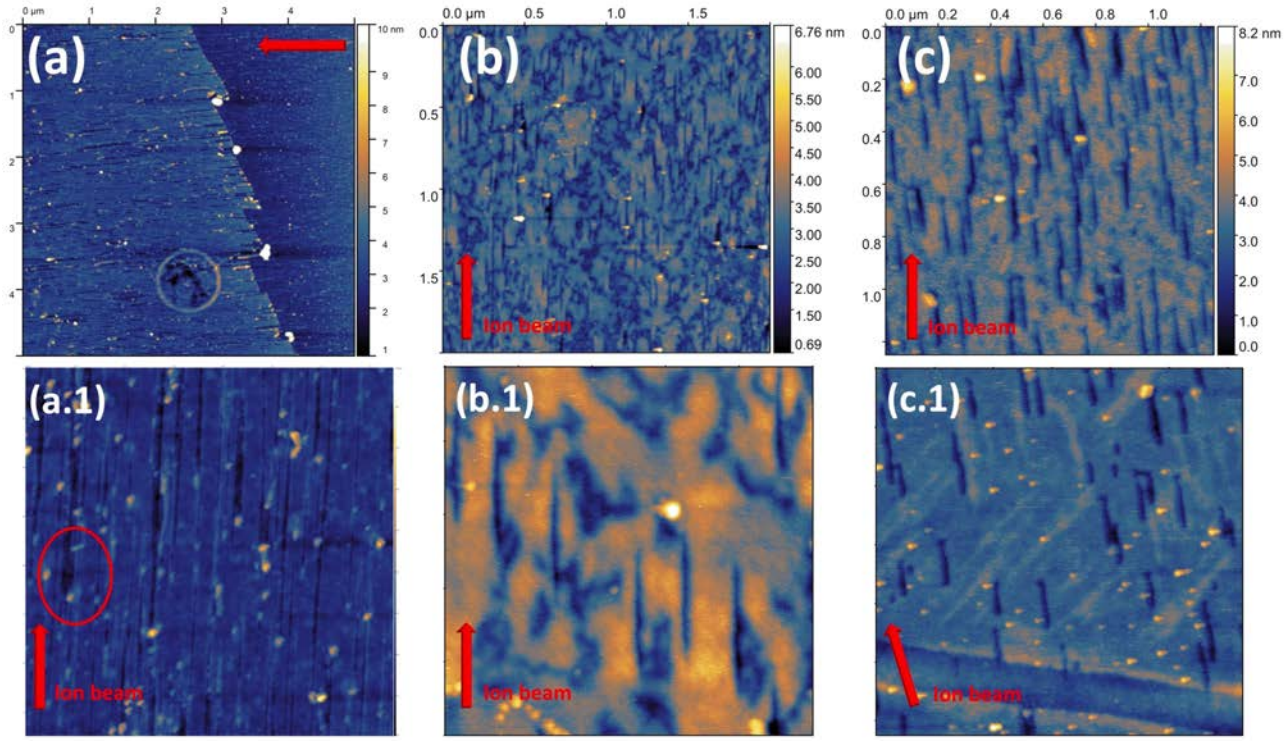

Figure V.14: AFM images of MoS_2/SiO_2 irradiated with 92 MeV Xe ions with $\phi = 5 \times 10^9$ ions cm^{-2} at $\theta = 0.6°$ (a) 1.2° (b) and 2°(c).

By varying the angle of incidence, the length of the cracks/folds can be adjusted. Figure V.15 shows an analysis of how the length of modifications (folds and cracks) is affected by the angle of incidence of the ion beam. Since we have already described in Chapter II 2.1.1 the geometrical formula II.1 which describes this dependence, we will just give a brief reminder of the meaning of the various parameters which make up this equation. L is the length of the wrinkle or crease, θ is the angle of incidence of the ion beam with respect to the sample surface, and d is the distance (measured perpendicular to the surface) from which the surface still responds to the passage of the ion, resulting in an observable morphological change on the surface. This formula can be used to calculate the value of d in each case. For $MoS_2/SrTiO_3$, d = (4.71 ± 0.94) nm, while for MoS_2/SiO_2, d = (3 ± 1.34) nm. In both cases, d is greater than the thickness of a single layer of MoS_2, which means that the ion passes through the MoS_2 layer and a certain depth of the substrate. It is therefore obvious that the effect of the ions on the surface, which results in the formation of incisions and folds, is the result of a coupling between an intrinsic effect on the 2D material and an effect in the substrate that can be felt on the surface of the MoS_2.

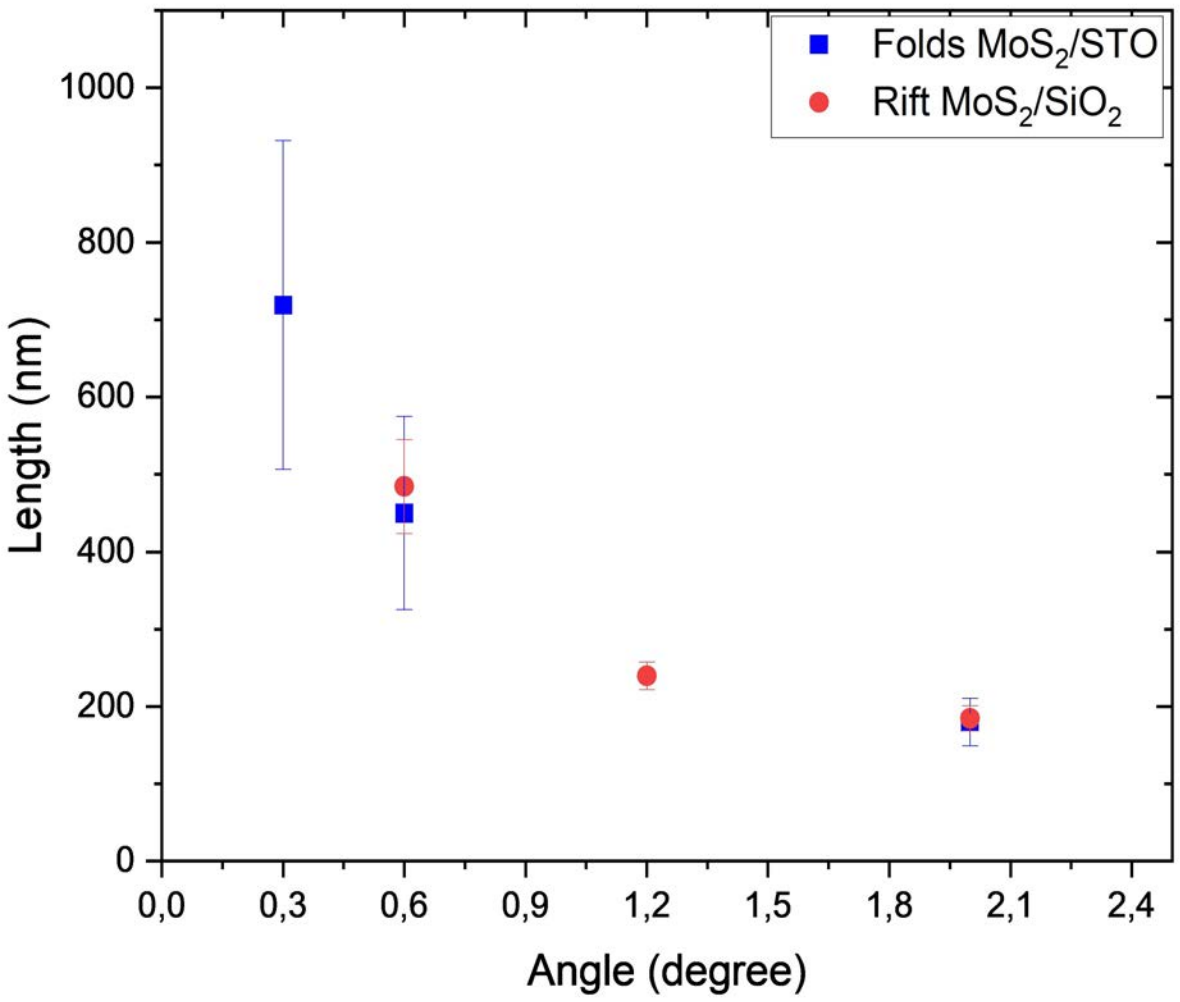

Figure V.15: Experimental measurement of fold length (blue square) and rift length (red circle) in a single layer of supported MoS_2 induced by swift heavy ion irradiation (91 MeV Xe) at various irradiation angles.

From the results presented in the 2.1 and 2.2 sections, a clear effect of the substrate can be observed, particularly on the morphology of the defects. Irradiation of deposited MoS_2 on crystalline $SrTiO_3$ results in the formation of folds, whereas using amorphous SiO_2 as a substrate leads to the creation of smooth and straight rifts, both oriented in the direction of the ion beam. The effect of the substrate on the surface modifications has been demonstrated in various studies [9]. Although there is an intrinsic response of the 2D material to the passage of ions, the substrate contributes significantly to the formation of folds and rifts.
The formation of folds and rifts in the MoS_2 single layer is a complex process influenced by various factors. As previously discussed, irradiation of $SrTiO_3$ with swift heavy ions at grazing incidence results in the formation of chains of periodically spaced nano-hillocks. The chains formed in $SrTiO_3$ contain hillocks with a height of < 10 nm [6]. $\alpha - SiO_2$, in contrast, exhibits the formation

of amorphous chains of hillocks that can be up to five times smaller in size than those observed in $SrTiO_3$ [62]. Not forgetting that in the case of amorphous SiO_2 there is the underlying crystalline Si substrate. The ions maximum depth "d" into the target refers to the location where the increase in temperature along the ions trajectory still reaches the surface and is therefore still effective, resulting in the formation of folds/rifts on the surface. It is important to note that this parameter d (on the nanometer scale) is different from the one representing the maximum depth where the ion stops in the matter, known as the projected range Rp (on the micrometre scale). The d value is much greater than the size of the MoS_2 layer, which is around 1 nm whether SiO_2 is used as the substrate or $SrTiO_3$. It is therefore clear that the ion passes through both materials. In the Section 2.1 one can see that the formation of foldings in the single layer MoS_2 is accompanied by the formation of chains of nano-hillocks on the $SrTiO_3$ (fig.V.8(a) and V.9 (a-2)), thus demonstrating the effect of the ions propagating beyond the MoS_2 layer. The impact of the substrate and the resulting surface structure can be viewed as a compressive force that acts not only on the interlayer but also exerts pressure on the extremely thin surface of the 2D material, which is already weakened by the ion's passage. Given that the structure resulting from irradiation is different for each of the substrates, this confirms that the substrate plays an important role in structure formation and surface modification. The energy range used during these irradiations gives rise to modifications resulting mainly from interaction in the electronic stopping regime (Se). As discussed in Chapter 1 section 3.2.2, the thermal spike model has successfully explained the formation of these surface tracks [50]. This may indicate that a thermal mechanism is also at the origin of the formation of folds/rifts in the MoS_2 single layer. Ochedowski et al. [9] suggested a mechanism for rift formation in 2D crystals, whereby a thermal spike in the substrate material leads to temperatures exceeding the sublimation point of a single layer of MoS_2. This leads to pressure on the 2D material layer, resulting in the appearance of rifts [64]. The authors suggest that this process is responsible for the observed rift formation in such crystals. The role of the interface is not negligible either. In this investigation, despite depositing directly on the SiO_2 substrates, the transfer of MoS_2 on the $SrTiO_3$ was accomplished at room temperature. Add to this the fact that they were stored in ambient air prior to irradiation and a water-layer interface could have been formed. Ochedowski et al. [9] have demonstrated that the presence of water not only contributes to fold formation but also plays a role in the development of rifts.

Conclusion

To summarise the results presented in this chapter, irradiation of MoS_2 single layers with swift heavy ions at grazing incidence resulted in the creation of defects with different densities in the material. The study investigated the effects of defects induced by Xe ion beams on the Raman spectrum and photoluminescence (PL) peak. The analysis revealed clear shifts in the Raman mode as well as broadening accompanied by a shift in the PL peak upon irradiation. These changes and this evolution are a characteristic signature of the creation of defects in the MoS_2 structure following irradiation and could be associated with a strain localised around defects. A variation in the density of defects as a function of the angle of incidence was observed.
In addition to the creation of structural defects, swift heavy ions (SHI)-induced morphological de-

fects on the surface were also investigated using the atomic force microscope (AFM). Swift heavy ions irradiation of MoS_2/SiO_2 resulted in the formation of straight rift-like structures along the ion beam direction on the surface. On the other hand, when MoS_2 supported on $SrTiO_3$ is irradiated, the surface underwent noticeable modification, appearing as nanometer-length folding. The system comprising MoS_2 and $SrTiO_3$ has gained significant attention due to the attractive properties of both materials. In contrast to MoS_2/SiO_2, $SrTiO_3$ substrates allow for the creation of folds with varying lengths without requiring any crystallographic orientation conditions. This also points out the impact of the substrate and demonstrates that it is a major asset for defect creation. The size and shape of surface morphological modifications can be tuned by the choice of substrate material and angle of incidence.

The results demonstrate that atomic-scale structural and surface modifications in MoS_2 may be brought about by inducing morphological changes at the nanoscale in a controlled manner. On the surface, these modifications may result in a localised improvement in the optical and electrical characteristics. Studies have shown that, when compared to MoS_2 multilayer, the stacking of two MoS_2 single layers resulting from foldings exhibits weaker interlayer coupling [170] [190] [191]. This has a direct impact on the MoS_2 band structure and its electrical structure [192] [193] [194]. It was also observed that the photoluminescence advantage of a single layer was kept despite a shift to an indirect bandgap, according to analysis of the photoluminescence spectrum. The presence of folds or fractures affected the optical absorption by enhancing its photoluminescent properties [170] [190].
The catalytic sector is another area where 2D materials are often used. Compared to the basal plane surface, the MoS_2 surface's edge exhibited significant catalytic activities [106] [107] [195]. The development of active sites through edge defects allows to improve the intrinsic activity of crystalline MoS_2 with an application for the hydrogen evolution reaction (HER) [196] [197] [195] [106].

Summary

During this thesis, the research focuses on the nano- and micro-structuring of surfaces induced by irradiation with swift heavy ions at grazing incidence, which is presented as a promising approach for the engineering of materials in controlled ways. Depending on the fluence used, surface structuring through material modification can be achieved by individual impact, i.e. at low fluence, or by multiple impacts, i.e. at high fluence.
It is known that irradiation with low fluences, where individual impacts predominate, creates chains of nanohillocks on the surface. Transmission electron microscope (TEM) measurements on single crystalline $SrTiO_3$ samples irradiated at grazing angles showed the same effect beneath the surface, where an angle effect can be observed, resulting in the formation of intermittent tracks. The findings are closely connected to the electronic structure of $SrTiO_3$. Further, irradiation at higher fluences generates structural damage with the formation of an amorphous layer on the surface, which shows a dependence of the thickness on the geometry of the irradiation angle.

The analysis of the morphological change of the surface by means of atomic force microscopy (AFM) has shown the formation of different types of structures on strontium titanate surfaces when irradiated with swift heavy ions at grazing angles. A reorganisation of the surface into a wave-like structure oriented perpendicular to the ion beam was observed for the first time in this material. Three types of structures were identified: primary waves, secondary waves, and hillocks. Image processing techniques were used to analyse the AFM images, and the different characteristics of these structures were analysed based on irradiation parameters such as the angle of irradiation and the fluence. The primary waves were found to have a periodicity of about 100 µm, whereas the secondary waves had a periodicity of less than 10 µm. The hillocks exhibit random size variation and are observed only in a few samples; hence, this was attributed to a unique effect that could have resulted from a contaminated sample series. The study of the evolution of these structures with fluence revealed that the secondary waves increased in height while the primary ones disappeared.

A study of the impact of fluence (the number of ions per unit area) and angle of incidence on the evolution of periodic structures is essential for a potential application. Particular attention is given to secondary waves. The study examines how the height, width, and periodicity of these waves are affected by the irradiation parameters. The experiments show that the size and characteristics of the

waves change with varying fluence and angle, indicating a strong correlation between these factors and the formation of surface structures. The results also indicate that for the same grazing angle the periodicity remains constant, whereas the height varies. Employing higher fluences results in an increase in wave growth, which can even lead to very fine pillar-shaped structures. While the angle increases towards the surface normal, the periodicity increases. Control over surface wave density is therefore possible

Cross-irradiation experiments have been conducted to investigate the impact of irradiation from various directions. The aim was to gain an understanding of the process that leads to the reorganisation of the surface into a periodic structure. It appears that, after the second irradiation, a reorientation, or, more specifically, a wave-like structure oriented perpendicular to the second ion beam, is beginning to form.
To better understand the origin of the formation of these waves on the surface and, thus, to be able to control them for potential applications, it is essential to analyse the mechanism at the origin of this reorganisation. Analysis and comparison with various other studies, which assessed distinct materials, different energies, and, in some cases, different irradiation conditions, has been carried out with an overview of the different mechanisms concerned. To explain the formation of periodic structures on the surface of single-crystalline $SrTiO_3$, a two-system model is proposed. The anisotropic plastic deformation present in the amorphous layer is suggested to be the driving force behind the development of the observed wave-shaped structures on the surface. Upon high irradiation, a layer of amorphous material is formed on the surface while the remaining bulk of the crystal maintains crystalline order.

Some experiments were also conducted on two-dimensional materials, specifically molybdenum disulphide (MoS_2) deposited via the chemical vapour deposition (CVD) technique on two distinct substrates: strontium titanate ($SrTiO_3$) and SiO_2. The modification of 2D materials using swift heavy ions was discussed. Besides the importance of inducing defects to enhance their properties and broaden their potential applications, the choice of substrate is also emphasized. Furthermore, the materials' response to swift heavy ion irradiation is investigated, with a focus on grazing irradiation geometry and the impact of the substrate. The MoS_2 samples underwent structural changes upon irradiation with swift heavy ions, which consisted of foldings. These folds exhibit different shapes, sizes, and orientations relative to the direction of the ion beam along the crystalline axis of MoS_2 identified with its edges. The density and length of the folds varied depending on the ion beam's incidence angle and the substrate used. It was demonstrated that choosing $SrTiO_3$ as a substrate allowed the creation of folds with varying lengths without requiring specific crystallographic orientation conditions. The modification of MoS_2 samples by swift heavy ions presents potential for tailoring the material's properties for a variety of technological purposes.

In summary, we have presented a method for structuring a monocrystalline $SrTiO_3$ surface in a controlled manner. This wave-like structure can be deepened to obtain more pronounced trenches. This structure can be used to directly grow two-dimensional materials and thus obtain a heterostructure with a well-defined and controllable interface. The surface undulation allows a combination of the characteristics of the two materials, where adapting the parameters according to

the intended application would be possible. As defect engineering is used to improve the properties of different materials, and in particular surface structure engineering, the use of substrates with a structured surface, in particular in the form of waves, makes it possible to preferentially expose 2D layer areas.

The optical characteristics of MoS_2 deposited on both flat and patterned $SrTiO_3$ substrates were found to be significantly influenced by the substrate surface [31, 175]. MoS_2 showed strong photoluminescence on flat surfaces; however, its local photoluminescence on a structured surface decreased considerably near the substrate valleys compared to that on the straight ridge height. This step on the $SrTiO_3$ substrate showed also an impact on electrical conductivity [175].

It would be interesting to investigate this effect with other 2D materials to see how these structures affect their properties. This would additionally benefit one of the active edge locations when combined with the 2D material's surface structure, especially for catalytic applications, as previously discussed. Additional research using other scanning microscopy and spectroscopy (XPS) techniques is required to obtain detailed information regarding the alteration of surface properties following irradiation, specifically the impact of a more wave-like structure as compared to a straight one. The varying height and size of the structured substrate surface may also amplify or diminish these characteristics, so it is worth it to investigate.

Bibliography

[1] J. F. Ziegler, M. D. Ziegler, and J.P. Biersack. SRIM – the stopping and range of ions in matter (2010). *Nuclear Instruments and Methods in Physics Research Section B: Beam Interactions with Materials and Atoms*, 268:1818–1823, 2010.

[2] S. Akcöltekin, H. Bukowska, T. Peters, O. Osmani, I. Monnet, I. Alzaher, B. Ban d'Etat, H. Lebius, and M. Schleberger. Unzipping and folding of graphene by swift heavy ions. *Applied Physics Letters*, 98:103103, 2011.

[3] R. M. Papaléo, R. Leal, C. Trautmann, and E.M. Bringa. Cratering by MeV–GeV ions as a function of angle of incidence. *Nuclear Instruments and Methods in Physics Research B*, 206:7–12, 2003.

[4] S. Akcöltekin E. Akcöltekin, T. Roll, H. Lebius, and M. Schleberger. Patterning of insulating surfaces by electronic excitation. *Nuclear Instruments and Methods in Physics Research*, 267:1386–1389, 2009.

[5] A. Meftah, F. Brisard, J. M. Costantini, M. Hage-Ali, J. P. Stoquert, F. Studer, and M. Toulemonde. Swift heavy ions in magnetic insulators: A damage-cross-section velocity effect. *Physical Review B*, 48(2):920–925, 1993.

[6] E. Akcöltekin, T. Peters, R. Meyer, A. Duvenbeck, M. Klusmann, I. Monnet, H. Lebius, and M. Schleberger. Creation of multiple nanodots by single ions. *Nature Nanotechnology*, 2:290–294, 2007.

[7] O. Ochedowski, O. Lehtinen, U. Kaiser, A. Turchanin, B. Ban-d'Etat, H. Lebius, M. Karlušić, M. Jakšić, and M. Schleberger. Nanostructuring graphene by dense electronic excitation. *Nanotechnology*, 26:465302, 2015.

[8] H. Guo, Y. Sun, P. Zhai, H. Yao, J. Zeng, S. Zhang, J. Duan, M. Hou, M. Khan, , and J. Liu. Swift-heavy ion irradiation-induced latent tracks in few- and mono-layer MoS_2. *Appl. Phys.A*, 122:375, 2016.

[9] Oliver Ochedowski. *Modification of 2D-Materials by Swift Heavy Ion Irradiation*. PhD thesis, Fakultät für Physik der Universität Duisburg-Essen, August 2014.

[10] C. Lee, H. Yan, L. E. Brus, T. F. Heinz, J. Hone, and S. Ryu. Anomalous lattice vibrations of single- and few-layer MoS_2. *ACS Nano*, 4,5:2695–2700, 2010.

[11] R. Rahali, H. Lebius, A. Benyagoub, E. Gardes, S. Guillous, I. Monnet, M. Sall, M.P. Chauvat, D. Marie, and C. Grygiel. $SrTiO_3$ surface micro-structuring with swift heavy ions in grazing incidence geometry. *Materialia*, 27:101696, 2023.

[12] J. Lindhard, M. Scharff, and H. E. Schioett. Range concepts and heavy ion ranges notes on atomic collisions, II. *Kgl. Danske Videnskab. Selskab. Mat. Fys. Medd.*, 14, 1963.

[13] R.L. Fleischer, P.B. Price, and R.M. Walker. Solid state detectors. *Ann. Rev. Nuc. Sci*, page 15, 1965.

[14] M. Toulemonde, C. Dufour, and E. Paumier. Transient thermal process after a high-energy heavy-ion irradiation of amorphous metals and semiconductors. *Phys. Rev. B*, 46:14362–14369, 1992.

[15] Fr. Dessauer. Über einige wirkungen von strahlen. i. *Zeitschrift für Physik*, 12:38–47, 1923.

[16] M. Toulemonde, J.M. Costantini, Ch. Dufour, A. Meftah, E. Paumier, and F. Studer. Track creation in SiO_2 and $BaFe_{12}O_{19}$ by swift heavy ions: a thermal spike description. *Nuclear Instruments and Methods in Physics Research Section B: Beam Interactions with Materials and Atoms*, 116:37–42, 1996.

[17] E. Akcöltekin1, S. Akcöltekin1, O. Osmani, A. Duvenbeck1, H. Lebius, and M. Schleberger. Swift heavy ion irradiation of $SrTiO_3$ under grazing incidence. *New Journal of Physics*, 10:053007, 2008.

[18] M. Karlusic, S. Akcöltekin, O. Osmani, I. Monnet, H. Lebius, M. Jaksic, and M. Schleberger. Energy threshold for the creation of nanodots on $SrTiO_3$ by swift heavy ions. *New journal of physics*, 12:043009, 2010.

[19] C. Grygiel, H. Lebius, S. Bouffard, A. Quentin, J. M. Ramillon, T. Madi, S. Guillous, T. Been, P. Guinement, D. Lelièvre, and I. Monnet. Online in situ x-ray diffraction setup for structural modification studies during swift heavy ion irradiation. *Review of Scientific Instruments*, 83:013902, 2012.

[20] M. Kumar, R.K. Pandey, P. Rajput, S.A. Khan, U.B. Singh, D.K. Avasthi, and A.C. Pandey. SHI induced surface re-organization of non-amorphisable nanodimensional fluoride thin films. *Phys. Chem. Chem. Phys*, 19:23229–23238, 2017.

[21] M. Navez, C. Sella, and D. Chaperot. Etude de l'attaque du verre parbombardement ionique. *C. R. Acad. Sci. Paris*, 254:240–248, 1962.

[22] L. T. Chadderton and H. M. Montagu-Pollock. Fission fragment damage to crystal lattices: heat-sensitive crystals. *Proceedings of the Royal Society of London. Series A. Mathematical and Physical Sciences*, 274:239–252, 1963.

[23] F. Seitz and J.S. Koehler. *Solid state physics*, volume 2. Academic Press, London/New York, 1956.

[24] M. A Grinfeld. Instability of the interface between a nonhydrostatically stressed elastic body and a melt. *Dokl. Akad. Nauk. SSSR*, 290:1358–1363, 1986.

[25] D. J. Srolovitz. On the stability of surfaces of stressed solids. *Acta Metallurgica*, 37:621–625, 1989.

[26] M. Toulemonde, C. Trautmann, E. Balanzat, K. Hjort, and A. Weidinger. Track formation and fabrication of nanostructures with mev-ion beams. *Nuclear Instruments and Methods in Physics Research Section B: Beam Interactions with Materials and Atoms*, 216:1–8, 2004.

[27] S. Klaumünzer and G. Schumacher. Dramatic growth of glassy $Pd_{80}Si_{20}$ during heavy-ion irradiation. *Phy. Rev. Lett*, 51:1987, 1983.

[28] S. Klaumünzer, M-D Hou, and G. Schumacher. Coulomb explosions in a metallic glass due to the passage of fast heavy ions. *Phy. Rev. Lett*, 57:850, 1986.

[29] H. Trinkaus and A. I. Ryazanov. Viscoelastic model for the plastic flow of amorphous solids under energetic ion bombardment. *Phys. ReV.Lett*, 74:5072, 1995.

[30] D. J. Prakash, Y. Chen, M. L. Debasu, D. E. Savage, C. Tangpatjaroen, C. Deneke, A. Malachias, A. D. Alfieri, O. Elleuch, K. Lekhal, I. Szlufarska, P. G. Evans, and F. Cavallo. Reconfiguration of amorphous complex oxides: A route to a broad range of assembly phenomena, hybrid materials, and novel functionalities. *Small. J*, 18:2105424, 2022.

[31] C. Huang, J. Fu, M. Xiang, J. Zhang, H. Zeng, and X. Shao. Single-layer MoS_2 grown on atomically flat $SrTiO_3$ single crystal for enhanced trionic luminescence. *ACS Nano*, 15:8610–8620, 2021.

[32] L. Madauß, J. Schumacher, M. Ghosh, O. Ochedowski, J. Meyer, H. Lebius, B. Ban-d'Etat, M. E. Toimil-Molares, C. Trautmann, R. G. H. Lammertink, M. Ulbricht, and M. Schleberger. Fabrication of nanoporous graphene/polymer composite membranes. *The Royal Society of Chemistry*, 9:10487–104+3, 2017.

[33] L. Thomé, A. Debelle, F. Garrido, S. Mylonas, B. Décamps, C. Bachelet, G. Sattonnay, S. Moll, S. Pellegrino, S. Miro, P. Trocellier, Y. Serruys, G. Velisa, C. Grygiel, I. Monnet, M. Toulemonde, P. Simon, J. Jagielski, I. Jozwik-Biala, L. Nowicki, M. Behar, W.J. Weber, Y. Zhang, M. Backman, K. Nordlund, and F. Djurabekova. Radiation effects in nuclear materials: Role of nuclear and electronic energy losses and their synergy. *Nuclear Instruments and Methods in Physics Research Section B: Beam Interactions with Materials and Atoms*, 2013.

[34] C. Lehmann. *Interaction of radiation with solids and elementary defect production*. Number 10 in Defects in crystalline solids. North-Holland ; Elsevier North-Holland, 1977.

[35] J.P. Biersack. Range of recoil atoms in isotropic stopping materials. *Zeitschrift für Physik A Hadrons and nuclei*, 211(5):495–501, 1968-10.

[36] H. Bethe, F. Hund, N. F. Mott, W. Pauli, A. Rubinowicz, G. Wentzel, and A. Smekal. *Quantentheorie*. Springer Berlin Heidelberg, 1933.

[37] W. H. Barkas. *Nuclear research emulsions*. New York : Academic Press, 1963.

[38] B. Firsov. A qualitative interpretation of the mean electron excitation energy in atomic collisions. *Soviet Physics JETP*, 36 (9)(5), 1959.

[39] G. H. Kinchin and R. S. Pease. The displacement of atoms in solids by radiation. *Reports on Progress in Physics*, 18:1, 1955.

[40] D. A. Young. Etching of radiation damage in lithium fluoride. *Nature*, 182:375–377, 1958.

[41] E. C. H. Silk and R. S. Barnes. Examination of fission fragment tracks with an electron microscope. *Philosophical Magazine*, 4:970–972, 1959.

[42] Gevrais Benoit. *Etude du dépôt d'énergie des ions lourds dans les solides par simulation monte-carlo*. PhD thesis, université de Caen Normandie, 1993.

[43] F. Studer, M. Hervieu, J. M. Costantini, and M. Toulemonde. High resolution electron microscopy of tracks in solids. *Nuclear Instruments and Methods in Physics Research Section B: Beam Interactions with Materials and Atoms*, 122(3):449–457, 1997.

[44] C. Houpert, F. Studer, D. Groult, and M. Toulemonde. Transition from localized defects to continuous latent tracks in magnetic insulators irradiated by high energy heavy ions: A HREM investigation. *Nuclear Instruments and Methods in Physics Research Section B: Beam Interactions with Materials and Atoms*, 39:720–723, 1989.

[45] P. B. Price and R. M. Walker. Observation of fossil particle tracks in natural micas. *Nature*, 196:732–734, 1962.

[46] P. Kluth, C. S. Schnohr, O. H. Pakarinen, F. Djurabekova, D. J. Sprouster, R. Giulian, M. C. Ridgway, A. P. Byrne, C. Trautmann, D. J. Cookson, K. Nordlund, and M. Toulemonde. Fine structure in swift heavy ion tracks in amorphous SiO_2. *Phys. Rev. Lett.*, 101:175503, 2008.

[47] D. Lesueur and A. Dunlop. Damage creation via electronic excitations in metallic targets part I experimental results an II : A theoretical model. *Radiation Effects and Defects in Solids*, 126(1-4):123–128 and 163–172, 1993.

[48] A. Meftah, J.M. Costantini, N. Khalfaoui, S. Boudjadar, J.P. Stoquert, F. Studer, and M. Toulemonde. Experimental determination of track cross-section in $Gd_3Ga_5O_{12}$ and comparison to the inelastic thermal spike model applied to several materials. *Nuclear Instruments and Methods in Physics Research Section B: Beam Interactions with Materials and Atoms*, 237:563–574, 2005.

[49] M.l. Kaganov, I. M. Lifshitz, and L. v. Tanatarov. Relaxation between electrons and the crystalline lattice. *Soviet Physics JETP*, 4:173–178, 1957.

[50] M. Toulemonde, C. Dufour, and E. Paumier. The ion-matter interaction with swift heavy ions in the light of inelastic thermal spike model. *Acta Physica Polonica A*, 109:311–322, 2006.

[51] C. Trautmann, C. Dufour, E. Paumier, R. Spohr, and M. Toulemonde. Track etching in amorphous metallic $Fe_{81}B_{13.5}Si_{3.5}C_2$. *Nuclear Instruments and Methods in Physics Research Section B: Beam Interactions with Materials and Atoms*, 107:397–402, 1996.

[52] C. Dufour, A. Audouard, F. Beuneu, J. Dural, J. P. Girard, A. Hairie, M. Levalois, E. Paumier, and M. Toulemonde. A high-resistivity phase induced by swift heavy-ion irradiation of Bi: a probe for thermal spike damage? *Journal of Physics: Condensed Matter*, 5(26):4573–4584, 1993.

[53] M. Toulemonde, C. Dufour, A. Meftah, and E. Paumier. Transient thermal processes in heavy ion irradiation of crystalline inorganic insulators. *Nuclear Instruments and Methods in Physics Research Section B: Beam Interactions with Materials and Atoms*, page 10, 2000.

[54] I. M. Lifshits, M. I. Kaganov, and L. V. Tanatarov. On the theory of radiation-induced changes in metals. *Journal of Nuclear Energy. Part A. Reactor Science*, 12(1):69–78, 1960.

[55] Z. G. Wang, C. Dufour, E. Paumier, and M. Toulemonde. The se sensitivity of metals under swift heavy-ion irradiation: a transient thermal process. *Journal of Physics: Condensed Matter*, 6:6733, 1994.

[56] Z. G. Wang, C. Dufour, E. Paumier, and M. Toulemonde. The se sensitivity of metals under swift heavy-ion irradiation: a transient thermal process. *Journal of Physics: Condensed Matter*, 7:2525, 1995.

[57] P. Apel. Swift ion effects in polymers: industrial applications. *Nuclear Instruments and Methods in Physics Research Section B: Beam Interactions with Materials and Atoms*, 208:11–20, 2003.

[58] L.T. Chadderton. Nuclear tracks in solids: registration physics and the compound spike. *Radiation Measurements*, 36:13–34, 2003.

[59] R. M. Papaléo, L. S. Farenzena, M. A. de Araujo, and R. P. Livi. Surface tracks in polymers induced by MeV heavy-ion impacts. *Nuclear Instruments and Methods in Physics Research B*, 151:135–139, 1999.

[60] N. Khalfaoui, C. C. Rotaru, S. Bouffard, M. Toulemonde, J. P. Stoquert, F. Haas, C. Trautmann, J. Jensen, and A. Dunlop. Characterization of swift heavy ion tracks in CaF_2 by scanning force and transmission electron microscopy. *Nuclear Instruments and Methods in Physics Research B*, 204:819–828, 2005.

[61] A.S. El-Said, M. Cranney, N. Ishikawa, A. Iwase, R. Neumann, K. Schwartz, M. Toulemonde, and C. Trautmann. Study of heavy-ion induced modifications in BaF_2 and LaF_3 single crystals. *Nuclear Instruments and Methods in Physics Research B*, 2018:492–497, 2004.

[62] A. M. J. F. Carvalho, M. Marinoni, A. D. Touboul, C. Guasch, H. Lebius, M. Ramonda, J. Bonnet, and F. Saigne. Discontinuous ion tracks on silicon oxide on silicon surfaces after grazingangle heavy ion irradiation. *Applied Physics Letters*, 90:073116, 2007.

[63] O. Osmani, A. Duvenbeck1, E. Akcöltekin, R. Meyer, H. Lebius, and M. Schleberger. Calculation of electronic stopping power along glancing swift heavy ion tracks in perovskites using ab initio electron density data. *Journal of physics: Condensed matter*, 20:315001, 2008.

[64] L. Madauß, O. Ochedowski, H. Lebius, B. Ban d'Etat, C. H. Naylor, A. T. C. Johnson, J. Kotakoski, and M. Schleberger. Defect engineering of single- and few-layer MoS_2 by swift heavy ion irradiation. *2D Materials*, 4:015034, 2017.

[65] G. Rose. Beschreibung einiger neuen mineralien des urals. *Ann. Phys. Chem.*, 124:551–573, 1839.

[66] J. A. Noland. Optical absorption of single-crystal strontium titanate. *Physical review*, 94:724, 1954.

[67] M. Schmidbauer, A. Kwasniewski, and J. Schwarzkopf. High-precision absolute lattice parameter determination of $SrTiO_3$, $DyScO_3$ and $NdGaO_3$ single crystals. *Acta Crystallogr.B*, 68:8–14, 2012.

[68] R. B. Comes, S. Y. Smolin, T. C. Kaspar, R. Gao, B. A. Apgar, L. W. Martin, M. E. Bowden, J. B. Baxter, and S. A. Chambers. Visible light carrier generation in co-doped epitaxial titanate films. *Applied Physics Letters*, 106:092901, 2015.

[69] L. E. Rehn. Ion beams in high-temperature superconductivity research. *Nuclear Instruments and Methods in Physics Research B*, 64:161–168, 1992.

[70] X.L. Shia, H. Wua, Q. Liua, W. Zhoua, S. Lud, Z. Shaoa, M. Darguschc, and Z.G. Chen. $SrTiO_3$-based thermoelectrics: Progress and challenges. *Nano Energy*, 78:105195, 2020.

[71] K. Domen, A. Kudo, and T. Onishi. Mechanism of photocatalytic decomposition of water into H_2 and O_2 over $NiO-SrTi_{03}$. *Journal of catalysis*, 102:92–98, 1986.

[72] C.A Chang, B. Raya, D. K. Paul, D. Demydov, and . J. Klabunde. Photocatalytic reaction of acetaldehyde over $SrTiO_3$ nanoparticles. *Journal of Molecular Catalysis A: Chemical*, 281:99–106, 2008.

[73] M. S. Wrighton, A. B. Ellis, P. T. Wolczanski, D. L. Morse, H. B. Abrahamson, and D. S. Ginley. Strontium titanate photoelectrodes. efficient photoassisted electrolysis of water at zero applied potential. *Journal of the American Chemical Society*, 98:10:2774–2279, 1976.

[74] X. Chen, S. Shen, L. Guo, and S. S. Mao. Semiconductor-based photocatalytic hydrogen generation. *Chem. Rev.*, 110:6503–6570, 2010.

[75] F. E. Osterloh. Inorganic materials as catalysts for photochemical splitting of water. *Chem. Mater.*, 20:36–54, 2008.

[76] C. Wang, H. Qiu, T. Inoue, and Q. Yao. Highly active $SrTiO_3$ for visible light photocatalysis: A first-principles prediction. *Solid StateCommunications*, 181:5–8, 2014.

[77] R. Konta, T. Ishii, H. Kato, and A. Kudo. Photocatalytic activities of noble metal ion doped $SrTiO_3$ under visible light irradiation. *J. Phys. Chem. B*, 108:8992–8995, 2004.

[78] W. Wei1, Y. Dai1, H. Jin, and B. Huang. Density functional characterization of the electronic structure and optical properties of Cr-doped $SrTiO_3$. *Journal of Physics D: Applied Physics*, 42:055401, 2009.

[79] C. Collignon, X. Lin, C. W. Rischau, B. Fauque, and K. Behnia. Metallicity and superconductivity in doped strontium titanate. *Annual Review of Condensed Matter Physics*, 10:25–44, 2019.

[80] M. N. Gastiasoro, J. Ruhman, and R. M. Fernandes. Superconductivity in dilute $SrTiO_3$: A review. *Annals of Physics*, 417:168107, 2020.

[81] W. Luo, W. Duan, S. G. Louie, and M. L. Cohen. Structural and electronic properties of n-doped and p-doped $SrTiO_3$. *PHYSICAL REVIEW B*, 70:214109, 2004.

[82] A. C. L. S. Marques. Advanced si pad detector development and $SrTiO_3$ studies by emission channeling and hyperfine interaction experiments, 2009.

[83] J. Rhoa, S. Jung, S. Shin, J. Kwon, M. Kim, J. Song, and E. Choi. Blue and infrared cathodo luminescence induced by carbon-irradiation in $SrTiO_3$ single crystal. *Journal of Luminescence*, 130:1687–1689, 2010.

[84] R. He, S. Sun, M. Xu, F. Chen, S. Akhmadaliev, and S. Zhou. Planar optical wave guide in $SrTiO_3$ crystal fabricated by carbon ion irradiation. *Nuclear Instruments and Methods in Physics Research B*, 308:6–8, 2013.

[85] M. L. Crespillo, J. T. Graham, F. Agullo'-Lo'pez, Zhang, and W. J. Weber. Correlation between Cr^{3+} luminescence and oxygen vacancy disorder in strontium titanate under MeV ion irradiation. *The journal of physical chemistry*, 121:19758-19766, 2017.

[86] A. Solanki, J. Shrivastava, S. Upadhyay, V. Sharma, P. Sharma, P. Kumar, P. Kumar, K. Gaskell, V. R. Satsangi, R. Shrivastav, and S. Dass. Irradiation-induced modifications and pec response - a case study of $SrTiO_3$ thin films irradiated by 120 MeV Ag^{9+} ions. *international journal of hydrogen energy*, 36:5236–5245, 2011.

[87] T. Wang, M. Qiao, Y. Liu, T. Liu, and S. Xu. $SrTiO_3$ optical waveguides fabricated by carbon ion irradiation at various fluences. *Optics Communications*, 474:126168, 2020.

[88] L. D. Landau. On the theory of phase transitions. *Zh. Eksp. Teor. Fiz*, 7:19–32, 1937.

[89] R. Peierls. *Quelques propriétés typiques des corps solides*, pages 177–222. Number 3 in 5. Annales de l'institut Henri Poincaré, 1935.

[90] K.S. Novoselov, A.K. Geim1, S.V. Morozov, S.V. Dubonos, Y. Zhang, and D. Jiang. Room-temperature electric field effect and carrier-type inversion in graphene films. *Nature*, 2004.

[91] K. S. Novoselov, A. K. Geim, S. V. Morozov, D. Jiang, Y. Zhang, S. V. Dubonos, I. V. Grigorieva, and A. A. Firsov. Electric field effect in atomically thin carbon films. *Science*, 306:666–669, 2004.

[92] J. C. Meyer, A. K. Geim, M. I. Katsnelson, K. S. Novoselov, T. J. Booth, and S. Roth. The structure of suspended graphene sheets. *Nature*, 446:60–63, 2007.

[93] K. Zhang, N. J. Borys, B. M. Bersch, G. R. Bhimanapati, K. Xu, B. Wang, K. Wang, M. Labella, T. A. Williams, M. A. Haque, E. S. Barnard, S. Fullerton-Shirey, P. J. Schuck, and J. A. Robinson. Deconvoluting the photonic and electronic response of 2d materials: The case of MoS_2. *Sci Rep*, 7:16938, 2017.

[94] H. J. Conley, B. Wang, J. I. Ziegler, R. F. Haglund Jr S. T. Pantelides, and K. I. Bolotin. Bandgap engineering of strained monolayer and bilayer MoS_2. *Nano letters*, 13:3626–3630, 2013.

[95] Y. Gong, Z. Liu, A. R. Lupini, G. Shi, J. Lin, S. Najmaei, Z. Lin, A. L. Elías, A. Berkdemir, G. You, H. Terrones, M. Terrones, R. Vajtai, S. T. Pantelides, S. J. Pennycook, J. Lou, W. Zhou, and P. M. Ajayan. Band gap engineering and layer-by-layer mapping of selenium-doped molybdenum disulfide. *Nano lett*, 14:442–449, 2014.

[96] L. Liu, Y. Lu, and Jing Guo. On monolayer MoS_2 field-effect transistors at the scaling limit. *IEEE Transactions of electron devices*, 60:4133–4139, 2013.

[97] Áron Szabó, Reto Rhyner, and Mathieu Luisier. Ab initio simulation of single-and few layer MoS_2 transistors: Effect of electron-phonon scattering. *Physical Review B*, 92:035435, 2015.

[98] K. T. Lam, Z. Dong, and J. Guo. Performance limits projection of black phosphorous field-effect transistors. *IEEE Electron Device Letters*, 35:963–965, 2014.

[99] S. S. Sylvia, K. Alam, and R. K. Lake. Uniform benchmarking of low voltage van der waals fets. *IEEE Journal on Exploratory Solid-State Computational Devices and Circuits*, 2:28–35, 2016.

[100] S. K. Lim, S. C. Kang, T. J. Yoo, S. K. Lee H. J. Hwang, and B. H. Lee. Operation mechanism of a MoS_2/BP heterojunction FET. *Nanomaterials*, 8:797, 2018.

[101] J. S. Lee, C. S. Park, T. Y. Kim, Y. S. Kim, and E. K. Kim. Characteristics of p-type conduction in p-doped MoS_2 by phosphorous pentoxide during chemical vapor deposition. *Nanomaterials*, 9:1278, 2019.

[102] D. Andrzejewski, E. Hopmann, M. John, T. Kümmell, and G. Bacher. WS_2 monolayerbased light-emitting devices in a vertical p–n architecture. *Nanoscale*, 11:8372–8379, 2019.

[103] B. Radisavljevic, A. Radenovic, J. Brivio1, V. Giacometti, and A. Kis. Single-layer MoS_2 transistors. *Nature Nanotechnology*, 6:147–150, 2011.

[104] O. Lopez-Sanchez, D. Lembke, M. Kayci, A. Radenovic, and A. Kis. Ultrasensitive photodetectors based on monolayer MoS_2. *Nature Nanotechnology*, 8:497–501, 2013.

[105] J. Zhu, Z.C Wang, H. Dai, Q. Wang, R. Yang, H. Yu, M. Liao, J. Zhang, W. Chen, Z. Wei, N. Li, L. Du, D. Shi, W.Wang andL. Zang, Y. Jiang, and G. Zhang. Boundary activated hydrogen evolution reaction on monolayer MoS_2. *Nat. Commun*, 10:1348, 2019.

[106] L. Madauß, I. Zegkinoglou, H. V. Muiños, Y. W. Choi, S. Kunze, M. Q. Zhao, C. H. Naylor, P. Ernst, E. Pollmann, O. Ochedowski, H. Lebius, A. Benyagoub, B. Ban-d'Etat, A. T. C. Johnson, F. Djurabekova, B. R. Cuenya, and M. Schleberger. Highly active single-layer MoS_2 catalysts synthesized by swift heavy ion irradiation. *Nanoscale*, 10:22908, 2018.

[107] J. Kibsgaard, Z. Chen, B. N. Reinecke, and T. F. Jaramillo. Engineering the surface structure of MoS_2 to preferentially expose active edge sites for electrocatalysis. *Nature Materials*, 11:963–969, 2012.

[108] K. Zhang, T. Zhang, G. Cheng, T. Li, S. Wang, W. Wei, X. Zhou, W. Yu†, Y. Sun, P. Wang, D. Zhang, C. Zeng, X. Wang, W. Hu†, H. J. Fan, G. Shen, X. Chen, X. Duan, K. Chang, and N. Dai. Interlayer transition and infrared photodetection in atomically thin type-II $MoTe_2$/MoS_2.

[109] X. Wu, X. Luo, H. Cheng, R. Yang, and X. Chen. Recent progresses on ion beam irradiation induced structure and performance modulation of two dimensional materials. *Nanoscale. The Royal Society of Chemistry*, 15:8925, 2023.

[110] M. Lemme, L. Li, T. Palacios, and F. Schwierz. Two-dimensional materials for electronic applications. *MRS Bull*, 39:71–718, 2014.

[111] N. Glavin, R. Rao, V. Varshney, E. Bianco, A. Apte, and A. Roy. Emerging applications of elemental 2D materials. *Adv. Mater*, 32:1904302, 2020.

[112] M. Bernardi, M. Palummo, and J.C. Grossman. Extraordinary sunlight absorption and one nanometer thick photovoltaics using two-dimensional monolayer materials. *Nano Lett*, 13:3664–3670, 2013.

[113] M. L. Tsaiand S. H. Su, J. K. Chang, D. S. Tsai, C. H. Chen, C. I. Wu, L. J. Li, L. J. Chen, and J. H. He. Monolayer MoS_2 heterojunction solar cells. *ACS Nano*, 8:8317–8322, 2014.

[114] D. Jariwala, A. R. Davoyan, J. Wong, and H.A. Atwater. Van der waals materials for atomically-thin photovoltaics: Promise and outlook. *ACS Photonics*, 4:2962–2970, 2017.

[115] A. K. Geim and I. V. Grigorieva. Van der waals heterostructures. *Nature*, 499:419–425, 2013.

[116] X. Wu, X. Chen, R. Yang, J. Zhan, Y. Ren, and K. Li. Recent advances on tuning the interlayer coupling and properties in van der waals heterostructures. *Small*, 18:2105877, 2022.

[117] X. Hong, J. Kim, S. F. Shi, Y. Zhang, C. Jin, Y. Sun, S. Tongay, J. Wu, Y. Zhang, and F. Wang. Ultrafast charge transfer in atomically thin MoS_2 / WS_2 heterostructures. *Nature Nanotech*, 9:682–686, 2014.

[118] Y. Chen, S. Huang, X. Ji, K. Adepalli, K. Yin, X. Ling, X. Wang, J. Xue, M. Dresselhaus, J. Kong, and B. Yildiz. Tuning electronic structure of single layer MoS_2 through defect and interface engineering. *ACS Nano*, 12:2569–2579, 2018.

[119] C. Ataca, H. Sahin, and S. Ciraci. Stable, single-layer MX_2 transition-metal oxides and dichalcogenides in a honeycomb-like structure. *J.Phys.Chem. C*, 116:8983–8999, 2012.

[120] F. Wypych and R. Schöllhorn. $1\,T-MoS_2$, a new metallic modification of molybdenum disulfide. *J. Chem. Soc.,Chem. Commun*, page 1386, 1992.

[121] H. Zhu, Y. Wang, J. Xiao, M. Liu, S. Xiong, Z. J. Wong, Z. Ye, Y. Ye, X. Yin, and X. Zhang. Observation of piezoelectricity in free-standing monolayer MoS_2. *Nature nanotechnology*, 10:151–155, 2015.

[122] W. Zhao, R. M. Ribeiro, and G. Eda. Electronic structure and optical signatures of semiconducting transition metal dichalcogenide nanosheets. *Accounts of chemical research*, 48:91–99, 2014.

[123] S. Bertolazzi, J. Brivio, and A. Kis. Stretching and breaking of ultrathin MoS_2. *ACS Nano*, 5:9703–9709, 2011.

[124] L. Mattheiss. Band structures of transition-metal-dichalcogenide layer compounds. *Phys. Rev. B*, 8:3719–3740, 1973.

[125] M. Schleberger and J. Kotakoski. 2D material science: Defect engineering by particle irradiation. *Materials*, 11:1885, 2918.

[126] J. Albrecht, S. Leonhardt, R. Spolenak, U. Täffner, HU. Habermeier, and G. Schütz. Surface patterning of $SrTiO_3$ by 30 keV ion irradiation. *Surface science*, 547:L847–L852, 2003.

[127] M. Narasaki, Q. Y. Li, T. Ikuta, J. Miyawaki, and K. Takahashi. Modification of thermal transport in an individual carbon nanofiber by focused ion beam irradiation. *Carbon*, 153:539–544, 2019.

[128] Z. Li and F. Chen. Ion beam modification of two-dimensional materials: Characterization, properties, and applications. *Applied Physics Reviews*, 4:011103, 2017.

[129] O. Ochedowski, S.Akcöltekin, B. Ban-d'Etat, H. Lebius, and M. Schleberger. Detecting swift heavy ion irradiation effects with graphene. *Nucl. Instr. Meth. B*, 314:18–20, 2013.

[130] X. Wu, H. Zhao, and J. pei. Fabrication of nanopore in graphene by electron and ion beam irradiation: Influence of graphene thickness and substrate. *Computational Materials Science*, 102:258–266, 2015.

[131] C. A. Merchant, K. Healy, M. Wanunu, V. Ray, N. Peterman, J. Bartel, M. D. Fischbein, K. Venta, Z. Luo, A. T. C. Johnson, and M. Drndic. DNA translocation through graphene nanopores. *Nano letters*, 10:2915–2921, 2010.

[132] H. Qiu, A. Sarathy, J.P Leburton, and K. Schulten. Intrinsic step wise translocation of stretched ssDNA in graphene nanopores. *NanoLett*, 15:8322–8330, 2015.

[133] D. Cohen-Tanugi and J. C. Grossman. Water desalination across nanoporous graphene. *NanoLett*, 12:3602–3608, 2012.

[134] K. Sint, B. Wang, and P. Kra. Selective ion passage through functionalized graphene nanopores. *American Chemical Society*, 130:16448–16449, 2008.

[135] H. Vazquez, E. H. Åhlgren, O. Ochedowski, A. A. Leino, R. Mirzayev, R. Kozubek, H. Lebius, M. Karlušic, M. Jakšic, A. V. Krasheninnikov, J. Kotakoski, M. Schleberger, K. Nordlund, and F. Djurabekova. Creating nanoporous graphene with swift heavy ions. *Carbon*, 114:511, 2017.

[136] S. Kumar, A. Tripathi, F. Singh, S. A. Khan, V. Baranwa, and D. K. Avasthi. Purification/annealing of graphene with 100-MeV Ag ion irradiation. *Nanoscale Research Letters*, 9:126, 2014.

[137] O. Ochedowski, H. Bukowska, V. M. Freire Soler, L. Brökers, B. Ban-d'Etat, H. Lebius, and M. Schleberger. Folding two dimensional crystals by swift heavy ion irradiation. *Nucl. Instr. Meth. B*, 340:39–43, 2014.

[138] M. Temmen1, O. Ochedowski, B. K. Bussmann, M. Schleberger, M. Reichling, and T. R. J. Bollmann. Routes to rupture and folding of graphene on rough 6h-sic(0001) and their identification. *Beilstein journal of Nanotechnology*, 4:625–631, 2013.

[139] G. Binnig, C. F. Quate, and Ch. Gerber. Atomic force microscope. *Phys. Rev. Lett*, 56:930–033, 1986.

[140] C. V. Raman and K. S. Krishnan. A new type of secondary radiation. *Nature*, 121:501–502, 1928.

[141] A. C. Ferrari. Raman spectroscopy of graphene and graphite: Disorder, electron–phonon coupling, doping and nonadiabatic effects. *Solid State Commun*, 143:47–57, 2006.

[142] L. G. Cançado, A. Jorio, E. H. Martins Ferreira, F. Stavale, C. A. Achete, R. B. Capaz, M. V. O. Moutinho, A. Lombardo, T. S. Kulmala, and A. C. Ferrari. Quantifying defects in graphene via raman spectroscopy at different excitation energies. *ACS Nano*, 11.8:3190–3196, 2011.

[143] M. Bruna, A. K. Ott, M. Ijäs, D. Yoon, U. Sassi, and A. C. Ferrari. Doping dependence of the raman spectrum of defected graphene. *ACS Nano*, 8:7432–7441, 2014.

[144] C. Rice, R. J. Young, R. Zan, U. Bangert, D. Wolverson, T. Georgiou, R. Jalil, , and K. S. Novoselov. Raman-scattering measurements and first principles calculations of strain-induced phonon shifts in monolayer MoS_2. *Phys. Rev. B*, 87:081307, 2013.

[145] A. Das, S. Pisana, B. Chakraborty, S. Piscanec, S. K. Saha, U. V. Waghmare, K. S. Novoselov, H. R. Krishnamurthy, A. K. Geim, A. C. Ferrari, and A. K. Sood. Monitoring dopants by raman scattering in an electrochemically top-gated graphene transist. *Nature Nanotechnology*, 3:210–215, 2008.

[146] A. Cuenat, H. B. George, K.C. Chang, J. M. Blakely, and M. J. Aziz. Lateral templating for guided self-organization of sputter morphologies. *Advanced materials*, 17:2845–2849, 2005.

[147] D. Necas and P. Klapetek. Gwyddion: an open-source software for spm data analysis. *Cent. Eur. J. Phys*, 10:181–188, 2012.

[148] N. Otsu. A threshold selection method from gray-level histograms. *IEEE Trans. Syst. Man Cybern*, 9:62–66, 1979.

[149] E. S. Gadelmawla, M.M. Koura, T. M. A. Maksoud, I. M. Elewa, and H. H. Soliman. Roughness parameters. *Journal of Materials Processing Technology*, 123:133–145, 2002.

[150] A. Keller and S. Facsko. Ion-induced nanoscale ripple patterns on Si surfaces: Theory and experiment. *Materials*, 3(10):4811–4841, 2010.

[151] S.A. Mollick and P.D. Shipman D. Ghose. Anomalous patterns and nearly defect-free ripples produced by bombarding silicon and germanium with a beam of gold ions. *Appl. Phys. Lett*, 104:043103, 2014.

[152] R.L. Cunningham, P. Haymann, C. Lecomte, W.J. Moore, and J.J. Trillat. Etching of surfaces with 8 keV argon ions. *Appl. Phys*, 31:839–842, 1960.

[153] H. Zhou, Y. Wang, L. Zhou, R.L. Headrick, A.S. Ozcan, Y. Wang, G. Ozaydin, and K. F. Ludwig Jr. Wavelength tunability of ion-bombardment-induced ripples on sapphire. *Phys. Rev. B*, 75:155416, 2007.

[154] R.M Bradley and J. M. E. Harper. Theory of ripple topography induced by ion bombardment. *J. Vac. Sci. Technol.*, 6:2390–2396, 1988.

[155] Y. Kuramoto and T. Tsuzuki. Persistent propagation of concentration waves in dissipative media far from thermal equilibrium. *Prog. Theor. Phys*, 55:356–369, 1976.

[156] G. I. Sivashinsky. On self-turbulization of a laminar flame. *Acta Astronaut*, 6:569–591, 1979.

[157] S. Facsko, T. Bobek, A. Stahl, H. Kurz, and T. Dekorsy. Dissipative continuum model for self-organized pattern formation during ion-beam erosion. *Phys. Rev. B*, 69:153412, 2004.

[158] J. Munoz-Garcia, M. Castro, and R. Cuerno. Nonlinear ripple dynamics on amorphous surfaces patterned by ion beam sputtering. *Phys. Rev. Lett.*, 96:086101, 2006.

[159] H. Trinkaus. Dynamics of viscoelastic flow in ion tracks: origin of plastic deformation of amorphous materials. *Nucl. Instrument. Method. Phys. Res. Sect. B*, 146:204–216, 1998.

[160] W. Bolse. Self-organised nano-structuring of thin oxide-films under swift heavy ion bombardment. *Nucl. Instrument. Method. Phys. Res. Sect. B*, 244(1):8–14, 2006.

[161] R.S. Chauhan, D.C. Agarwal, S. Kumar, S.A. Khan, D. Kabiraj, I. Sulania, D. K. Avasthi, and W. Bolse. Nano/micro-structuring of oxide thin film under shi irradiation. *Vacuum*, 86(1):96–100, 2011.

[162] T. W. Simpson; I. V. Mitchell; J. C. McCallum; L. A. Boatner. Hydrogen catalyzed crystallization of strontium titanate. *J. Appl. Phys*, 76:2711–2718, 1994.

[163] L. Madauß, T. Foller, J. Plaß, P. V. Kumar, T. Musso, K. Dunkhorst, R. Joshi, and M. Schleberger. Selective proton transport for hydrogen production using graphene oxide membranes. *J. Phys. Chem. Lett.*, 11:9415-9420, 2020.

[164] L. Banszerus, H. Janssen, M. Otto, A. Epping, T. Taniguchi, K. Watanabe, B. Beschoten, D. Neumaier, and C. Stampfer. Identifying suitable substrates for high-quality graphene-based heterostructures. *2D Materials*, 4:025030, 2017.

[165] B. J. Robinson, C. E. Giusca, Y. T. Gonzalez, N. D. Kay, O. Kazakova, and O. V. Kolosov. Structural, optical and electrostatic properties of single and few layers MoS_2: effect of substrate. *2D matter*, 2:015005, 2015.

[166] D. Wang and R. Sundararaman. Substrate effects on charged defects in two-dimensional materials. *Phys. Rev. Materials*, 3:083803, 2019.

[167] Q. Li, L. Zhang, C. Li, J. He, Y. Wei, J. Zhao, R. Zhang, P. Wang, S. Fu, F. Chen, R. Peng, and M. Wang. Morphological evolution of monolayer MoS_2 single crystalline flakes. *J. Phys. Chem. C*, 126:3549–3559, 2022.

[168] A. C. Ferrari and D. M. Basko. Raman spectroscopy as a versatile tool for studying the properties of graphene. *Nat. Nanotechnol*, 8:235–246, 2013.

[169] M. Bruna, A. K. Ott, M. Ijäs, D. Yoon, U. Sassi, and A.C. Ferrari. Doping dependence of the raman spectrum of defected graphene. *ACS Nano*, 8,7:7432–7441, 2014.

[170] H. Nan, Z. Wang, W. Wang, Z. Liang, Y. Lu, Q. Chen, D. He, P. Tan, F. Miao, X. Wang, J. Wang, and Z. Ni. Strong photoluminescence enhancement of MoS_2 through defect engineering and oxygen. *American Chemical Society*, 8:5738–5745, 2014.

[171] J. Zhang, Y. Yu, P. Wang, C. Luo, X. Wu, Z. Sun, J. Wang, W. D. Hu, and G. Shen. Characterization of atomic defects on the photoluminescence in two-dimensional materials using transmission electron microscope. *InfoMat*, 1:85–97, 2019.

[172] V. Pankratov, J. Hoszowska, J. Dousse, M. Huttula, A. Kis, D. Krasnozhon, M. Zhang, and W. Cao. Vacuum ultraviolet excitation luminescence spectroscopy of few-layered MoS_2. *J. Phys.: Condens. Matter*, 28:015301, 2016.

[173] S. Tongay, J. Zhou, C. Ataca, K. Lo†, T. S. Matthews, J. Li, J. C. Grossman, and J. Wu. Thermally driven crossover from indirect toward direct bandgap in 2D semiconductors: Mose2 versus MoS_2. *American Chemical Society*, 12:5576–5580, 2012.

[174] Z. He, R. Zhao, and X. Chen et al. Defect engineering in single-layer MoS_2 using heavy ion irradiation. *ACS Appl Mater Interfaces*, 10:42524–42533, 2018.

[175] C. Huang, C. Chen, W. Wang, J. Fu, M. Xiang, Y. Xing, Q. Chen, H. Zeng, and X. Shao. Modulated photoluminescence of single-layer MoS_2 via nanostructured $SrTiO_3$ surface. *adv. Mater. Interfaces*, 9:2200383, 2022.

[176] H. Li, Q. Zhang, C.C.R. Yap, B.K. Tay, T.H.T. Edwin, A. Olivier, and D. Baillargeat. From bulk to monolayer MoS_2: Evolution of raman scattering. *Adv. Funct. Mater*, 22:1385–1390, 2012.

[177] C. Rice, R. J. Young, R. Zan, U. Bangert, D. Wolverson, T. Georgiou, R. Jalil, and K. S. Novoselov. Raman-scattering measurements and first-principles calculations of strain-induced phonon shifts in monolayer MoS_2. *Physical review B*, 87:081307, 2013.

[178] T. M. G. Mohiuddin, A. Lombardo, R. R. Nair, A. Bonetti, G. Savini, R. Jalil, N. Bonini, D. M. Basko, C. Galiotis, N. Marzari, K. S. Novoselov, A. K. Geim, and A. C. Ferrari. Uniaxial strain in graphene by raman spectroscopy: G peak splitting, grüneisen parameters, and sample orientation. *Phys. Rev. B*, 79:205433, 2009.

[179] N. Blanc, F. Jean, A. V. Krasheninnikov, G. Renaud, and J. Coraux. Strains induced by point defects in graphene on a metal. *Phys. Rev. Lett*, 111:085501, 2013.

[180] B. Chakraborty, A. Bera, D. V. S. Muthu, S. Bhowmick, U. V. Waghmare, and A. K. Sood. Symmetry-dependent phonon renormalization in monolayer MoS_2transistor. *Phys. Rev. B*, 85:161403, 2012.

[181] A. H. Castro Neto, F. Guinea, N. M. R. Peres, K. S. Novoselov, and A. K. Geim. The electronic properties of graphene. *Rev. Mod. Phys.*, 81:109, 2009.

[182] Y. Y. Hui, X. Liu, W. Jie, N. Y. Chan, J. Hao, Y-T. Hsu, L.-J. Li, W. Guo, and S. P.Lau. Exceptional tunability of band energy in a compressively strained trilayer MoS_2 sheet. *ACS Nano*, 7:7126–7131, 2012.

[183] D. Wu, H. Huang, X. Zhu, Y. He, Q. Xie, X. Chen, X. Zheng, H. Duan, and Y. Gao. E" raman mode in thermal strain fractured CVD-MoS_2. *Crystals*, 6:151, 2016.

[184] E. Scalise, M. Houssa, G. Pourtois, V.V. Afanas'ev, and A. Stesmans. First-principles study of strained 2d MoS_2. *Physica E: Low-dimensional Systems and Nanostructures*, 56:416–421, 2014.

[185] K. Yin, S. Huang, X. Chen, X. Wang, J. Kong, Y. Chen, and J. Xue. Generating sub-nanometer pores in single-layer MoS_2 by heavy- ion bombardment for gas separation: A theoretical perspective. *ACS Appl. Mater. Interfaces*, 10:28909-28917, 2018.

[186] H. P. Komsa, S. Kurasch, O. Lehtinen, and U. Kaiser A.V. Krasheninnikov. From point to extended defects in two-dimensional MoS_2: Evolution of atomic structure under electron irradiation. *Phys. Rev. B*, 88:035031, 2013.

[187] M. Matsunaga, A. Higuchi, G. He, T. Yamada P. Kruger, Y. Ochiai, Y. Gong, R. Vajtai, P.M. Ajayan, and J.P. Birdand N. Aoki. Nanoscale-barrier formation induced by low-dose electron-beam exposure in ultrathin MoS_2 transistors. *ACS Nano*, 10:9730-9737, 2016.

[188] S. Mignuzzi, A. J. Pollard, N. Bonini, B. Brennan, I. S. Gilmore, M. A. Pimenta, D. Richards, and D. Roy. Effect of disorder on raman scattering of single-layer MoS_2. *Physical review B*, 91:195411, 2015.

[189] A. P. Nayak, T. Pandey, and D. Voiry et al;. Pressure-dependent optical and vibrational properties of monolayer molybdenum disulfide. *Nano. Lett*, 15:346–353, 2014.

[190] A. Castellanos-Gomez, H. S. J. van der Zant, and G. A. SteelE. Folded MoS_2 layers with reduced interlayer coupling. *Nano research*, 7:572–578, 2014.

[191] X. Du, Y. Lee, Y. Zhang, T. Yu, K. Kim, and N. Liu. Electronically weak coupled bilayer MoS_2 at various twist angles via folding. *ACS Appl. Mater. Interfaces*, 13,19:22819–22827, 2021.

[192] X. Fan, C. H. Chang, W. T. Zheng, J. . Kuo, and D. J. Singh. The electronic properties of single-layer and multilayer MoS_2 under high pressure. *J. Phys. Chem. C*, 19:10189–10196, 2015.

[193] Z. Zhao, W. Zhang, Y. Zhang, H. Hao, S. Zhang, L. Tong, B. Peng, and N. Liu. Tuning bandstructure of folded MoS_2 through fluid dynamics. *Nano res*, 15:2734–2740, 2022.

[194] F. R. Negreiros, G. J. Soldano, S. Fuentes, T. Zepeda, M. José-Yacamán, and M. M. Mariscal. The unexpected effect of vacancies and wrinkling on the electronic properties of MoS_2 layers. *Phys. Chem*, 21:24731–24739, 2019.

[195] Y. Cheng, H. Song, H. Wu, P. Zhang, Z. Tang, and S. Lu. Defects enhance the electrocatalytic hydrogen evolution properties of MoS_2 based materials. *Chemistry – An Asian Journal*, 15:3123–3134, 2020.

[196] F. Ling, X. Liu, H. Jing, Y. Chen, W. Zeng, Y. Zhang, W. Kang, J. Liu, L. Fang, and M. Zhou. Optimizing edges and defects of supported MoS_2 catalysts for hydrogen evolution via an external electric field. *Phys. Chem. Chem. Phys*, 20:26083, 2018.

[197] T. X. Huang, X. Cong, S. S. Wu, K. Q. Lin, X. Yao, Y. H. He, J. B. Wu, Y. F. Bao, S. C. Huang, X. Wang, P. H. Tan, and B. Ren. Probing the edge-related properties of atomically thin MoS_2 at nanoscale. *Nature communications*, 10:5544, 2019.